ROLE OF PLASMA IN THE NUCLEATION AND GROWTH OF CARBON NANOFIBERS

THESIS SUBMITTED TO
DELHI TECHNOLOGICAL UNIVERSITY
FOR THE AWARD OF THE DEGREE OF

DOCTOR OF PHILOSOPHY

By

Mr. RAVI GUPTA
(2K15/PhD/AP/01)

Under the supervision of
PROF. (DR.) SURESH C. SHARMA

DEPARTMENT OF APPLIED PHYSICS
DELHI TECHNOLOGICAL UNIVERSITY
SHAHBAD DAULATPUR, MAIN BAWANA ROAD,
DELHI-110042, INDIA

JULY 2018

Dedicated

To

My Father

Delhi Technological University

(Govt. of National Capital Territory of Delhi)

Shahbad Daulatpur, Bawana Road, Delhi-110042

CERTIFICATE

This is to certify that the thesis entitled ***"Role of Plasma in the Nucleation and Growth of Carbon Nanofibers"*** submitted by **Mr. Ravi Gupta (2K15/PhD/AP/01)** to Delhi Technological University (DTU), Delhi, India for the degree of Doctor of Philosophy, is a bonafide record of the research work carried out by him under my supervision and guidance. The work embodied in this thesis has been carried out in the Plasma & Nano Simulation Lab, Department of Applied Physics, Delhi Technological University (DTU), Delhi, India. The work of this thesis is original and has not been submitted in parts or fully to any other Institute or University for the award of any other degree or diploma.

_____

Prof. (Dr.) Suresh C. Sharma
Supervisor
Head, Department of Applied Physics
Delhi Technological University
Shahbad Daulatpur, Bawana Road
Delhi-110042, India

Delhi Technological University
(Govt. of National Capital Territory of Delhi)
Shahbad Daulatpur, Bawana Road, Delhi-110042

CANDIDATE'S DECLARATION

I, herby certify that the thesis titled ***"Role of Plasma in the Nucleation and Growth of Carbon Nanofibers"*** submitted in the fulfilment of the requirements for the award of the degree of Doctor of Philosophy is an authentic record of my research work carried out under the supervision of **Prof. (Dr.) Suresh C. Sharma**. Any material borrowed or referred to is duly acknowledged.

_____

Ravi Gupta
(2K15/PhD/AP/01)
Delhi Technological University
Shahbad Daulatpur, Bawana Road
Delhi-110042, India

ACKNOWLEDGEMENTS

This Ph.D. thesis is the result of challenging journey and it would not have been possible to write this doctoral thesis without the support of kind people around me, to only some of whom it is possible to give particular mention here.

Foremost, I would like to give my gratitude to ***Prof. Suresh C. Sharma,*** Head, Department of Applied Physics, Delhi Technological University, Delhi, India for his supervision, valuable guidance, and genuine advice from the early stage of this research. His dedication, timely advice, meticulous scrutiny, scientific intuition and instinct have exceptionally inspired and enriched my growth as the student and research scholar. I owe him special thanks for enabling me to accomplish my Ph.D thesis on time.

My sincere thanks also goes to ***Hon'ble Prof. Yogesh Singh***, Vice Chancellor, DTU and officials of DTU for their precious support and providing ample research facilities to conduct this research. I would also like to acknowledge their financial support to attend the 18th International Conference on Physics of Highly Charged Ions (HCI-2018) held at UJK University, Kielce, Poland (September 2016).

I would also thank profusely ***Prof. Rinku Sharma*** for her originality that has triggered and nourished my maturity and benefitted me for long time. Moreover, I would also thank all other faculty and staff members of Department of Applied Physics, DTU for their help and cooperation throughout my research period.

I express my heart-felt gratitude to ***Ms. Neha Gupta*** (*Research Fellow*) for her constant motivation and support during the course of my Ph.D. thesis. Her scientific inputs, personal helps, moral support and encouragement have always made me feel at ease and enhance the quality of my research. I would also like to express huge and warm thanks to my other fellow lab mates in

Plasma & Nano Simulation Research Laboratory; ***Ms. Pratibha Malik, Ms. Jyotsna Panwar, Ms. Umang Sharma, Ms. Monika Yadav, Ms. Kavita Rani, Ms. Ruchi Sharma, Ms. Renu Kumari, Ms. Anshu Dahiya, and Ms. Suman Dahiya*** for the stimulating discussions, selfless support, and for all the fun we have had in the last four years. I also explicitly thank my colleagues ***Mr. Ajay Kumar, Mr. Rahul Pandey, Ms. Neha Gupta, Ms. Jaya Madan, Ms. Nisha Deopa, Ms. Sumandeep Kaur, Mr. Aman Prasad,*** and ***Mr. Abhishek Bhardwaj*** for all their selfless support.

I am indebted to some of my dear friends ***Mr. Apoorv Bhardwaj*** and ***Ms. Amrit Kaur*** for influencing me in a positive way and for their moral support and motivation, which drives me to give my best.

I would like to acknowledge all the teachers I learnt from since my childhood, I would not have been here without their guidance, blessings and support.

I would also like to thank ***Science and Engineering Research Board (SERB)–Department of Science and Technology (DST), Government of India*** for providing me with the necessary funding to attend the 44^{th} European Physical Society Conference on Plasma Physics held at Queen's University, Belfast, Northern Ireland (June 2017).

Last but not the least, I would like to pay high regards to my father ***Lt. Mr. Mukat Lal Gupta,*** my mother ***Mrs. Usha Gupta,*** my elder sisters ***Mrs. Ritu Goel, Mrs. Prapti Garg, and Mrs. Deepika Jindal*** for supporting me spiritually throughout writing this thesis and my life in general. Their cooperation, understanding, and sincere encouragement were the sustaining factors in accomplishing this thesis successfully.

Above all, I thank the Almighty and Balaji Maharaj for giving me the strength and patience to work through all these years so that today I can stand proudly with my head held high.

(Ravi Gupta)

ABSTRACT

Carbon nanofibers (CNFs) are the one dimensional carbon nanostructures in which graphene layers are inclined at some non-zero angle with respect to the growth axis. Vertically aligned carbon nanofibers (VACNFs) are the potential candidate in the applications of field emission devices, electronic sensors, and electron emission displays, etc. There are many synthesis routes available, however, plasma enhanced chemical vapour deposition (PECVD) are exclusively used to synthesize VACNFs at low temperatures. The present thesis aims to elucidate the deep insights of the nucleation and growth mechanism of the VACNFs in the reactive plasma environment through an analytical model developed which mainly incorporates two sub-models.

One is the plasma sheath model that accounts the excitation, dissociation and ionization of the gaseous sources due to applied plasma power and kinetics of the plasma species (electrons, positively charged ions, and neutral species); and the other one is the surface deposition model that incorporates the adsorption and dissociation of carbon bearing species (ionic and neutral species of hydrocarbons) over the catalyst nanoparticle active surface (free surface available for the adsorption of the plasma species) to generates building units (carbon species) via various surface processes (surface reaction), surface and bulk diffusion of carbon species over the catalyst nanoparticle surface, precipitation of the carbon species in the form of graphitic shells around the rear of the catalyst, etching of the walls of the CNFs, and vertical growth of the CNFs under the influence of the electric field induced in the plasma sheath. The solutions of the model equations have been carried out for experimentally determined initial conditions and glow discharge parameters. It is found that the plasma parameters, i.e., number density of ions and neutral species in the bulk plasma, insertion of nitrogen as the doping element, insertion of water and oxygen as the etchant gases, and plasma process parameters have great influence on the growth characteristics of the VACNFs. In addition, the plasma pre-treatment of the thin metal catalyst film to generate catalyst nanoparticles have also been studied and it is found that the plasma

parameters, plasma compositions and thickness of the metal catalyst film significantly affect the size and the surface concentration of the catalyst nanoparticles which ultimately affect the growth characteristics of the VACNFs. The good comparisons of the analytical results of the present thesis with the available experimental observations confirm the adequacy of the present model.

The present work of the thesis can be extended to fabricate the thin and long VACNFs for their potential applications in the field emitters as the field emission characteristics of the VACNFs depend on its geometrical characteristics, i.e., height and tip radius. Moreover, the present work can also be extended to investigate the growth of other carbon based nanostructures.

LIST OF PUBLICATIONS

International Journals

1. **Ravi Gupta**, Neha Gupta, and Suresh C. Sharma, Modeling to study the role of catalyst in the formation of graphitic shells during carbon nanofiber growth subjected to reactive plasma, *Phys. Plasmas* **25** (2018) 043504.

2. **Ravi Gupta** and Suresh C. Sharma, Modelling the effects of nitrogen doping on the carbon nanofiber growth via catalytic plasma-enhanced chemical vapour deposition process, *Contribution to Plasma Physics* (2018), DOI: 10.1002/ctpp.201700138.

3. **Ravi Gupta** and Suresh C. Sharma, Theoretical modeling to study the impact of different oxidizers (etchants) on the plasma-assisted catalytic carbon nanofiber growth, *Phys. Plasmas* **24** (2017) 073504.

4. **Ravi Gupta**, Suresh C. Sharma, and Rinku Sharma, Mechanisms of plasma-assisted catalyzed growth of carbon nanofibres: A theoretical modeling, *Plasma Sources Sci. Technol.* **26** (2017) 024006**.**

5. Suresh C. Sharma, Aarti Tewari, and **Ravi Gupta**, Role of plasma and doping elements on the growth and field emission properties of metallic carbon nanotube (CNT) tip placed over cylindrical surface, *Journal of Atomic, Molecular, Condensate and Nano Physics* **6 (3)** (2015) 195.

International peer reviewed proceedings

6. **Ravi Gupta**, Suresh C. Sharma, and Neha Gupta, Role of different etchants on the growth of catalyst nanoparticles during the plasma processing of the metal catalyst thin film, *Materials Today: Proceedings* **5** (2018) 15416.

7. **Ravi Gupta**, Suresh C. Sharma, and Neha Gupta, Role of carrier gas on the morphology of plasma grown carbon nanofibers (**accepted** in Indian Journal of Engineering and Material Sciences).

8. Neha Gupta, Suresh C. Sharma, and **Ravi Gupta**, Oxygen assisted growth of graphene sheet by PECVD process (**accepted** in Indian Journal of Pure and Applied Physics).

9. **Ravi Gupta**, Suresh C. Sharma, and Neha Gupta, Role of etchant on the morphology of plasma grown carbon nanofibers: Theoretical modeling, *44th EPS Conference on Plasma Physics* (2017) P2.304.

10. Neha Gupta, Suresh C. Sharma, and **Ravi Gupta**, Formalism to study the effect of hydrogen on the plasma-assisted growth and field emission properties of the graphene sheet, *44th EPS Conference on Plasma Physics*, (2017) P1.309.

11. Neha Gupta, Suresh C. Sharma, and **Ravi Gupta**, Modelling graphene sheet growth subjected to plasma containing negatively charged ions, *44th EPS Conference on Plasma Physics*, (2017) P4.418.

12. Umang Sharma, Suresh C. Sharma, **Ravi Gupta**, and Neha Gupta, Theoretical investigations to study the effects of C_2H_2/H_2 gas ratio on the multi-walled carbon nanotubes growth, *44th EPS Conference on Plasma Physics*, (2017) P4.418.

13. Neha Gupta, Suresh C. Sharma, and **Ravi Gupta**, Theoretical investigation on the effect of nitrogen doping on the growth and field emission properties of the plasma-grown graphene sheet, *IOP Conf. Series: Journal of Physics: Conf. Series* **836** (2017) 012010.

14. **Ravi Gupta**, Suresh C. Sharma, and Neha Gupta, Theoretical study to investigate the impact of plasma parameters on the catalyst nanoparticle growth, *IOP Conf. Series: Journal of Physics: Conf. Series* **1836** (2017) 012024.

15. Umang Sharma, Neha Gupta, **Ravi Gupta**, and Suresh C. Sharma, Analytical modeling to study the effect of hydrogen plasma on the growth of multi-walled carbon nanotubes, *IOP Conf. Series: Journal of Physics: Conf. Series* **836**, (2017) 012017.

Communicated papers

16. Ravi Gupta and Suresh C. Sharma, Parametric study of plasma characteristics and carbon nanofiber growth in PECVD system: Numerical modeling, *Plasma Sources Sci. Technol.* (2018).

CONTENTS

Page No.

Certificate……. i

Candidate's Declaration……. ii

Acknowledgement…… iii

Abstract…… v

List of Publications…….. vii

List of Figures…….. x

List of Tables…… xvii

Chapter 1: Introduction……. 1-38

1.1 Background……... 1

1.2 Structures of CNFs/CNTs……..... 1

1.3 Properties of CNFs/CNTs……. 4

1.3.1 Electrical Properties……...……... 4

1.3.2 Mechanical Properties……..……. 4

1.3.3 Thermal Properties…… 5

1.4 Applications of CNFs/CNTs……...…….. 5

1.4.1 Hydrogen storage devices…….…… 5

1.4.2 Field emission devices based on one dimensional carbon nanostructures……... 6

1.4.2.1 CNFs/CNTs as field effect transistors……. 6

1.4.2.2 CNFs/CNTs as flat panel display……. 7

1.5 CNFs/CNTs synthesis route…….……. 8

1.5.1 Laser ablation……...……. 8

1.5.2 Arc discharge……...……. 9

1.5.3 Chemical vapor deposition (CVD)……... 10

1.5.4 Plasma enhanced chemical vapor deposition (PECVD)…….. 12
1.5.4.1 MW-PECVD…… 14
1.5.4.2 RF-PECVD and ICPECVD……. 15
1.5.4.3 DC-PECVD…….. 16
1.6 Nucleation and growth mechanism of 1-D carbon nanostructures in the reactive plasma…… 17
1.6.1 Formation of plasma sheath…….. 19
1.6.2 Nucleation stage……..…….. 20
1.6.3 Surface deposition of reactive plasma species…….. 21
1.6.4 Growth of 1-D carbon nanostructures (CNFs/CNTs)……... 21
1.7 Parameters affecting the nucleation and growth of CNFs/CNTs……. 22
1.7.1 Impact of source precursors……...……... 22
1.7.1.1 Effect of carbon feedstock gases……... 22
1.7.1.2 Effect of etching gas…..……. 22
1.7.1.3 Effect of carrier gas…..…….. 23
1.7.2 Effect of gas proportions…...…… 24
1.7.3 Role of catalyst…….…… 24
1.7.4 Effect of gas pressure of the plasma reactor……. 25
1.7.5 Effect of plasma power……...…….. 26
1.7.6 Effect of temperature…… 26
1.8 Objectives and organization of the thesis……. 17
References…….. 30

Chapter 2: Plasma processing of the thin metal catalyst film…..……... 39-51
2.1 Brief outline of the chapter……. 39
2.2 Introduction……..... 39
2.3 Analytical Model……...……. 40
2.3.1 Balance equation of plasma species in the bulk plasma…….. 41
2.3.2 Plasma processing of the thin metal catalyst film……... 42
2.4 Results and discussion…… 44
References……... 50

Chapter 3: Mechanisms of plasma-assisted catalyzed growth of carbon nanofibers: A theoretical modeling……..……. 52-71

3.1 Brief outline of the chapter……. 52

3.2 Introduction…… 52

3.3 Analytical model……...……. 53

3.3.1 Charging of CNF……..…… 54

3.3.2 Particle balance equations for various plasma species……. 56

3.3.3 Growth rate equation of the carbon species generated over the catalyst surface……... 58

3.3.4 Growth rate equation of carbon nanofibers…….. 59

3.4 Results and discussion…… 61

References……... 69

Chapter 4: Modeling the effect of doping on the carbon nanofibers growth via catalytic PECVD process……..……. 72-100

4.1 Brief outline of the chapter……. 72

4.2 Introduction ……... 72

4.3 Analytical model……...……..... 74

4.3.1 Charging of N-CNF surface……..……..... 76

4.3.2 Number density equalization of electrons……...……. 77

4.3.3 Number density equalization of positively charged density……. 77

4.3.4 Number density equalization of neutral species density…….. 79

4.3.5 Growth rate equation of carbon species over the catalyst surface…… 80

4.3.6 Growth rate equation of N-CNF……..... 82

4.4 Results and discussion…… 85

References……... 96

Chapter 5: Theoretical modeling to study the impact of different oxidizers (etchants) on the plasma assisted catalytic carbon nanofiber growth…….. 101-126

5.1 Brief outline of the chapter……. 101

5.2 Introduction…… 101

5.3 Model……. 103

5.3.1 Charging rate equation of CNFs…….…….. 104

5.3.2 Kinetic equation of electron density…….…… 104

5.3.3 Kinetic equation of positively charged ions……. 105

5.3.4 Kinetic equation of neutral species……. ……. 106

5.3.5 Growth rate equation of carbon and hydrogen species generated over the catalyst surface……..…….. 107

5.3.6 Growth rate equation of carbon nanofibers…….……. 110

5.4 Results and discussion…… 111

References…… 124

Chapter 6: Modeling to study the role of catalyst in the formation of graphitic shells during carbon nanofiber growth subjected to reactive plasma……..... 127-155

6.1 Brief outline of the chapter……. 127

6.2 Introduction……..... 127

6.3 Model……. 128

6.3.1 Nanostructuring of the thin metal catalyst film…… 130

6.3.2 Restructuring of the catalyst particle during CNF growth……... 135

6.3.3 Growth of carbon nanofibers…… 137

6.3.4 Balance equation of neutral species……. 138

6.3.5 Balance equation of positively charged ions……..... 139

6.3.6 Balance equation of electrons……..……. 140

6.3.7 Charged developed over CNF surface…….. 141

6.4 Results and discussion…… 141

References……... 152

Chapter 7: Parametric study of the plasma characteristics and carbon nanofibers growth in the PECVD system: Numerical modeling…… 156-183

7.1 Brief outline of the chapter……. 156

7.2 Introduction…… 156

7.3 Model…….…… 158

7.3.1 Computational approach……...…… 158

7.3.2 Analytical approach……..…… 160

7.4 Results and discussion…… 169

References……..... 180

Chapter 8: Conclusion and future scope…….. 184-188

8.1 Conclusion…….…… 184

8.2 Future scope of the present work…… 187

Appendix A: Graphene layers (graphitic shells) inclination angle with the growth axis…….……..……. 189

LIST OF FIGURES

Fig. No. **Page No.**

Chapter: 1

1.1 (a) Herringbone carbon nanofibers and (b) Stacked carbon nanofibers..... 2

1.2 (a) Single-walled carbon nanotubes (CNTs) and (b) Multi-walled carbon nanotubes..... 3

1.3 Representation of atomic orbitals in sp^2 hybridized graphite..... 4

1.4 (a) Schematic of the carbon nanotubes based field effect transistors, and (b) schematic of the vertically aligned CNT serves as the channel of the field effect transistors..... 7

1.5 Schematic of the flat panel display consisting carbon nanotubes-epoxy stripes on cathode glass plate and phosphorus coated indium tin oxide stripes (ITO) on anode glass plate..... 7

1.6 Schematic of the Laser ablation technique to synthesize CNFs/CNTs..... 7

1.7 Schematic of the arc discharge method..... 9

1.8 Schematic of the chemical vapour deposition system..... 9

1.9 (a) Dissociation of hydrocarbon species on the catalyst (making large contact angle with the substrate surface) active surface to generate carbon species, (b) precipitation of the carbon species around the rear of the catalyst, and (c) deformation of the catalyst resulting in the less interaction with substrate and thus, leads to the tip growth..... 11

1.10 (a) Dissociation of hydrocarbon species on the catalyst (making small contact angle with the substrate surface) active surface to generate carbon species, (b) formation of the carbon layer all around the catalyst particle and (c) base growth of the CNFs/CNTs..... 12

1.11 Schematic of the MW-PECVD technique..... 15

1.12 Schematic of the inductively coupled plasma with (a) planar spiral antenna and (b) helical antenna..... 16

1.13 Schematic of the parallel plate DC-PECVD system..... 17

1.14 Schematic of the pin to plate DC-PECVD system..... 17

1.15 The complete picture of the growth mechanism of the 1-D carbon nanostructure growth (CNFs/CNTs) in the reactive plasma environment..... 18

1.16 Mechanism of the plasma sheath formation between bulk plasma region and substrate surface..... 20

Chapter: 2

2.1 Time variation of the catalyst nanoparticle diameter with time for different hydrogen ion number densities (where a, b, c, d and e correspond to $n_e = n_{ij0} = 10^{11}$, 10^{12}, 10^{13}, 10^{14}, 10^{15} cm^{-3}, respectively)..... 46

2.2 Time variation of the catalyst nanoparticle diameter with time for different input plasma power..... 47

2.3 Time variation of catalyst nanoparticle diameter for two different plasmas i.e. hydrogen plasma and hydrogen + nitrogen plasma……... 47

2.4 Surface concentration of the catalyst nanoparticles for two different plasmas i.e. hydrogen plasma and hydrogen + nitrogen plasma……... 48

2.5 Time variation of substrate temperature during the plasma processing (Plasma treatment) of the thin catalyst film in the plasma containing electrons and ions and neutrals of hydrogen..... 49

Chapter: 3

3.1 Schematic representation of the nucleation and the growth mechanism of carbon nanofiber under plasma; (a) deposition of thin catalyst film on the substrate, (b) formation of catalyst nanoparticles, (c) dissociation and adsoprtion of hydrocarbons and hydrogen on catalyst particle surface, (d) precipitation of carbons and shape change of catalyst particle, (e) detachment of catalyst particle from substrate, (f) growth of carbon nanofiber, and (g) scheme of the CNF considered..... 62

3.2 (i) The time evolution of CNF length for different catalyst nanoparticle size(where a, b, c, d and e correspond to D = 109.3, 96.34, 75.91, 61.95, 47.31 nm, respectively). (ii) The variation of the growth rate of CNF with catalyst nanoparticle size..... 64

3.3 The time variation of the CNF length for different hydrocarbon number density (where a, b, c, and d correspond to $n_{10} = 10^{11}$, 10^{12}, 10^{13}, 10^{14} cm^{-3}, respectively) at $n_{20} = 10^{15}$ cm^{-3} 65

3.4 (i) The time evolution of CNF tip diameter for different hydrogen number density in the growth atmosphere (where a, b, c, d and e correspond to $n_{20} = 10^{11}, 10^{12}, 10^{13}, 10^{14}, 10^{15}$ cm^{-3}, respectively). (ii) The time variation of inclination angle with CNF tip diameter and hydrogen density..... 66

3.5 The time variation of the CNF length for different hydrogen number density (where a, b, and c correspond to $n_{20} = 10^{13}, 10^{14}, 10^{15}$ cm^{-3}, respectively) at $n_{10} = 10^{13}$ cm^{-3} 68

Chapter: 4

4.1 Schematic of the plasma species (ions and neutrals) deposition during nitrogen-contained carbon nanofibers (N-CNFs) growth..... 75

4.2 The time variation of tip diameter for undoped CNF (growth of CNF in C_2H_2/H_2 gas plasma) and nitrogen-doped CNF (growth of CNF in C_2H_2/NH_3 plasma) at C_2H_2 flow rate=40 sccm, H_2 flow rate=80 sccm, and NH_3 flow rate=80 sccm. Other parameters are given in the text……... 88

4.3 The time variation of number density for (a) H and (b) H^+ in the plasma for undoped (growth of CNF in C_2H_2/H_2 gas plasma) and nitrogen-doped CNF (growth of CNF in C_2H_2/NH_3 plasma) at C_2H_2 flow rate=40 sccm, H_2 flow rate=80 sccm, and NH_3 flow rate=80 sccm. Other parameters are given in the text……..... 89

4.4 The time variation of height for undoped (growth of CNF in C_2H_2/H_2 gas plasma) and nitrogen-doped CNF (growth of CNF in C_2H_2/NH_3 plasma) at C_2H_2 flow rate=40 sccm, H2 flow rate=80 sccm, and NH_3 flow rate=80 sccm. Other parameters are given in the text……..... 90

4.5 Time variation of nitrogen density for (a) C_2H_2 and (b) C_2H for undoped (growth of CNF in C_2H_2/H_2 gas plasma) and nitrogen-doped CNF (growth of CNF in C_2H_2/NH_3 plasma) at C_2H_2 flow rate=40 sccm, H_2 flow rate=80 sccm, and NH_3 flow rate=80 sccm. Other parameters are given in the text……... 91

4.6 (a) The time variation of N-CNF height for different C_2H_2 gas flow rates in C_2H_2/NH_3 plasma, keeping NH_3 gas flow rate constant at 80 sccm. (b) N-CNFs growth rate as a function of C_2H_2/NH_3 ratio for variable C_2H_2 gas flow rate and constant NH_3 gas flow rate. Other parameters are given in the text…….. 92

4.7 Time variation of the number of carbon species per unit area generated on the

***Ravi Gupta**, Department of Applied Physics, Delhi Technological University, Delhi, India*

catalyst nanoparticle surface for different C_2H_2 gas flow rates in C_2H_2/NH_3 plasma, keeping NH_3 gas flow rate constant at 80 sccm. Other parameters are given in the text……..... 93

4.8 Time variation of N-CNF height for different NH_3 gas flow rates in C_2H_2/NH_3 plasma, keeping C_2H_2 gas flow rate constant at 40 sccm. Other parameters are given in the text……..... 94

4.9 Time variation of nitrogen density for (a) N^+, (b) HCN^+, (c) N, and (d) H for different NH_3 gas flow rates in C_2H_2/NH_3 plasma, keeping C_2H_2 gas flow rate constant at 40 sccm. Other parameters are given in the text……..... 95

4.10 N-CNF tip diameter as function of C_2H_2/NH_3 ratio for variable C_2H_2 gas flow rate and constant NH_3 gas flow rate. Other parameters are given in the text……... 95

Chapter: 5

5.1 Time evaluation of height of the CNF grown in different plasma mixtures..... 113

5.2 Time evaluation of generation of carbon species per unit area (n_C) on the catalyst nanoparticle surface as a function of different plasma mixtures..... 115

5.3 Temporal variation of blocking function (Ω_C) for different gas mixtures..... 116

5.4 Temporal variation of plasma species number density in different plasma mixtures for (a) C_2H_2, (b) C_2H, (c) C_4H_2, (d) $C_2H_2^+$, (e) C_2H^+, and (f) $C_4H_2^+$..... 116

5.5 Time evolution of diameter of CNF grown in three different plasma mixtures..... 117

5.6 Temporal variation of height of CNF grown in $C_2H_2+H_2+H_2O$ plasma as function of different water concentration (number density) in the plasma i.e., (a) 4.7×10^{10} cm^{-3}, (b) 5.5×10^{10} cm^{-3}, (c) 6.0×10^{10} cm^{-3}, (d) 6.5×10^{10} cm^{-3}, (e) 7.5×10^{10} cm^{-3}, and (f) 8.5×10^{10} cm^{-3}..... 117

5.7 Temporal variation of height of CNF grown in $C_2H_2+H_2+O_2$ plasma as function of different oxygen concentration (number density) in the plasma i.e., (a) 4.5×10^{10} cm^{-3}, (b) 6.0×10^{10} cm^{-3}, (c) 7.3×10^{10} cm^{-3}, (d) 8.0×10^{10} cm^{-3}, (e) 8.5×10^{10} cm^{-3}, and (f) 9.5×10^{10} cm^{-3}..... 119

5.8 (i) & (ii) Shows the temporal variation of carbon species number density (n_C) and hydrogen species number density (n_H), respectively, generated on the catalyst nanoparticle surface in $C_2H_2+H_2+H_2O$ plasma as function of different water concentration (number density) in the plasma i.e., (a) 4.7×10^{10} cm^{-3}, (b) 5.5×10^{10} cm^{-3},(c) 6.0×10^{10} cm^{-3}, (d) 6.5×10^{10} cm^{-3}, (e) 7.5×10^{10} cm^{-3}, and (f) 8.5×10^{10} cm^{-3}.

Ravi Gupta, Department of Applied Physics, Delhi Technological University, Delhi, India

(iii) Temporal variation of carbon species number density generated on the catalyst nanoparticle surface in C_2H_2+H_2+O_2 plasma as function of different oxygen concentration number density) in the plasma i.e., (a) 4.5×10^{10} cm^{-3}, (b) 6.0×10^{10} (c) 7.3×10^{10} cm^{-3}, (d) 8.0×10^{10} cm^{-3}, (e) 8.5×10^{10} cm^{-3}, and (f) 9.5×10^{10} cm^{-3}..... 121

5.9 Bottom to top approach, i.e., atom to atom operation of CNF growth in three different plasma gas mixture. (a) CNF growth in typical hydrocarbon (C_2H_2)/hydrogen (H_2) plasma, in which continuous dissociation of hydrocarbon species (neutrals and ions) on the catalyst nanoparticle surface generate the excess carbon species and the ultimately amorphous carbon layer is formed on the catalyst nanoparticle surface and terminates the CNF growth. (b) CNF growth in C_2H_2+H_2+H_2O plasma, in which water species etch the amorphous carbon from the catalyst surface by means of many chemical reactions and preserve the catalyst activity and enhance the CNF growth. (c) CNF growth in C_2H_2+H_2+O_2 plasma, in which oxygen species not only remove the amorphous carbon from the catalyst surface but also remove the excess hydrogen radicals (H) from the catalyst surface which act as the sink for carbon species and thus CNF grows with much higher rate as compared to growth in (a) and (b)..... 122

Chapter :6

6.1 Dependence of (a) catalyst nanoparticles number density and (b) size of catalyst nanoparticle on the catalyst thin film thickness during plasma pre-treatment..... 143

6.2 Growth time variation of (a) elongation produced in catalyst and (b) catalyst base and tip diameter for different catalyst film thickness..... 144

6.3 Growth time variation of number of carbon species generated on catalyst nanoparticle front face as the function of nanofilm thickness..... 146

6.4 Dependence of number of graphitic shells (graphene layers) formed during CNF growth on the catalyst film thickness..... 146

6.5 Growth time variation of CNF height for different catalyst film thickness..... 147

6.6 Growth time variation of blocking function (poisoning of catalyst) as the function of catalyst film thickness..... 147

6.7 Schematic of the restructuring of catalyst particle during CNF growth over (a) thick catalyst film (thickness around 10 nm or more), (b) thin catalyst film (thickness around 5 nm), and (c) ultrathin films (thickness around 2 nm or less).

The dotted arrows show the flux of hydrocarbons and hydrogen species on the catalyst and CNF walls..... 148

6.8 Schematic of the dependence of graphene layers inclination on the restructuring of the catalyst during CNF growth over (a) thick catalyst film (thickness around 10 nm or more), (b) thin catalyst film (thickness around 5 nm), and (c) ultrathin films (thickness around 2 nm or less)..... 149

6.9 Variation of (a) difference between catalyst tip and base diameter and (b) elongation produced in the catalyst with catalyst film thickness..... 150

Chapter: 7

7.1 Geometry of the model constructed in the COMSOL modeling suite..... 159

7.2 Electron density spatial distribution in the plasma obtained from the computational model for different gas pressures, i.e., (a) 50 mTorr, (b) 500 mTorr, and (c) 5 Torr..... 170

7.3 Electron temperature spatial distribution in the plasma obtained from the computational model for different gas pressures, i.e., (a) 50 mTorr, (b) 500 mTorr, and (c) 5 Torr..... 170

7.4 Variation of (a) electron density and (b) electron temperature with growth time in the plasma for different gas pressures, i.e., 50 mTorr, 500 mTorr, and 5 Torr keeping other parameters constant that are given in the text..... 171

7.5 Density distribution of the neutral species in the bulk plasma region (black dots) and near the substrate surface (red dots) obtained from the computational model for different gas pressures i.e., 50 mTorr, 500 mTorr, and 5 Torr..... 172

7.6 Temporal variation of the (a) CNF height, (b) CNF diameter, (c) surface concentration of carbon species on the catalyst surface n_C, (d) surface concentration of hydrogen radicals on the catalyst surface n_H, and (e) poisoning rate of the catalyst for different gas pressures i.e., 50 mTorr, 500 mTorr, 5 Torr, 50 Torr, and 500 Torr keeping other parameter constant that are given in the text..... 173

7.7 Electron density distribution in the plasma obtained from the computational model for different input plasma powers, i.e., (a) 200 W, (b) 500 W, and (c) 1000 W..... 176

7.8 Electron temperature spatial distribution in the plasma obtained from the computational model for different plasma powers, i.e., (a) 200 W, (b) 500 W, and

(c) 1000 W..... 176

7.9 Density distribution of the positively charged species (ions) in the bulk plasma region (black dots) and near the substrate surface (red dots) obtained from the computational model for different input plasma powers, i.e., 200W, 500W, and 1000W..... 177

7.10 Variation of (a) electron density and (b) electron temperature with growth time in the plasma for different gas pressures i.e., 50 mTorr, 500 mTorr, and 5 Torr keeping other parameters constant that are given in the text..... 178

7.11 Temporal variation of the (a) surface concentration of carbon species on the catalyst surface n_C, (b) surface concentration of hydrogen radicals on the catalyst surface n_H, (c) poisoning rate of the catalyst, (d) CNF height, and (e) CNF diameter for different input plasma powers i.e., 200 W, 500 W, and 1000 W..... 179

Appendix A

A.1 Geometrical representation of the deformed catalyst particle at the tip of the Carbon Nanofiber..... 189

LIST OF TABLES

Table No.		Page No.
Chapter 1		
1.1	The different sources of plasma excitation and operating parameters used for the plasma-enhanced chemical vapour deposition (PECVD) growths of CNFs/CNTs based on experimental works.....	13
Chapter 2		
2.1	Species considered in the present model.....	41
2.2	Parameters used in the present model.....	45
2.3	Initial number density of the various plasma species used in the present model...	45
Chapter 3		
3.1	Boundary conditions used in the present model.....	63
Chapter 4		
4.1	Plasma species considered in the present model.....	75
4.2	Ion-neutral reactions between various plasma species in the bulk plasma considered in the present model.....	78
4.3	Various surface processes and their corresponding reactions on the catalyst nanoparticle surface considered in the Eq. (4.12) where “ads” and “des” corresponds to the adsorption and desorption of plasma species to/from the catalyst surface, respectively.....	81
4.4	Various surface processes and their corresponding reactions on the catalyst nanoparticle surface considered in the Eq. (4.13) where “ads” and “des” corresponds to the adsorption and desorption of plasma species to/from the catalyst surface, respectively.....	83
4.5	The different sources of plasma excitation and process-related parameters used for the plasma-enhanced chemical vapour deposition (PECVD) growths of carbon nanofibers (CNFs)/CNTs based on experimental works.....	86
4.6	Parameters used in the present model.....	87
4.7	Number density of various plasma species considered in the present model.....	87
4.8	Estimation of field enhancement factor for undoped and nitrogen-doped carbon nanofibers (CNFs) from the result obtained in Figs 4.2 and 4.4……	90

Chapter 5

5.1 Plasma species considered in the present model. Species of type A and B are taken into account when CNF growth is investigated in type I plasma. However, additional species of type C are taken into account when CNF growth is examined in type II and type III plasmas..... 103

5.2 Boundary conditions used in the present model..... 112

Chapter 6

6.1 Plasma species considered in the present model..... 129

6.2 The surface reactions incorporated in the present model and their corresponding parameters, where pl= plasma and ad= adsorption..... 133

6.3 Ion-neutral reactions in the bulk plasma considered in the present model..... 140

6.4 (a)Initial values of number density of numerous plasma species considered in the present computation (b) Initial values of the various parameters considered in the present computation..... 142

Chapter 7

7.1 Species considered in the present model..... 158

7.2 Parameters fed into the computational model developed in the COMSOL Multiphysics modeling suite..... 159

7.3 Initial conditions fed into the analytical model..... 167

7.4 Initial number density of the species fed into the analytical model..... 168

1
INTRODUCTION

1.1 Background

Nanostructures are the materials in which atleast one of the dimension is less than 100 nm. Nanostructures are designed at the molecular level to explore their novel properties due to their ultra-small size (exceptionally high surface to volume ratio) which cannot be observed at their bulk counterpart. Nanostructures based on gold, carbon, alloys, and oxides can be synthesized, however, carbon based nanostructures have gained potential research interest from the past several years. Carbon, one of the most abundant elements on the earth and one of the most studied elements of the research history, has two stable allotropes, i.e., graphite (consisting stacked graphene sheets) and diamond. One-dimensional nanostructures based on the carbon gathered the much attention in the field of research across the globe. One-dimensional carbon nanostructures were synthesized early in 1978 by Abrahamson *et al.* [1] in the form of fiber carpet but came into notice when Iijima published the research article on the multiwalled carbon nanotubes [2].

1.2 Structures of CNFs/CNTs

One-dimensional carbon nanostructures are composed of the rolled graphene sheets and can be classified into two broad categories (i) carbon nanofibers (CNFs) and (ii) carbon nanotubes (CNTs). CNFs/CNTs are the cylindrical shaped graphitic filaments having diameter in nanometer regime and length in microns. Despite of external similar morphology, CNFs/CNTs differ in crystalline structure and diameters. The inclination of graphitic layers about the axis of the tube characterizes the divergence between CNFs and CNTs. In CNTs, graphitic sheets are parallel to the tube axis whereas, in CNFs, graphitic sheets

***Ravi Gupta**, Department of Applied Physics, Delhi Technological University, Delhi, India*

are tilted at some non-zero angle [3,4]. On the basis of the inclination of graphitic layers, CNFs are classified into two types [5,6]:

- Herringbone carbon nanofibers
- Stacked carbon nanofibers

In herringbone CNFs, the graphene sheets are inclined at any angle between 0^0 and 90^0 and in stacked CNFs graphene layers are inclined perpendicular to the tube axis as shown in Fig.1.1.

On the basis of the number of graphene layers, CNTs can be divided into two types:

- Single walled CNTs (SWCNTs)
- Multi walled CNTs (MWCNTs)

As per the name suggested and shown in Fig.1.2, SWCNTs are composed of only a single rolled graphene sheet with diameter of about 1 nm and MWCNTs are the concentric cylinders of SWCNTs with diameter of about several nm. The interspacing between two SWCNTs in MWCNTs is of 0.34 nm.

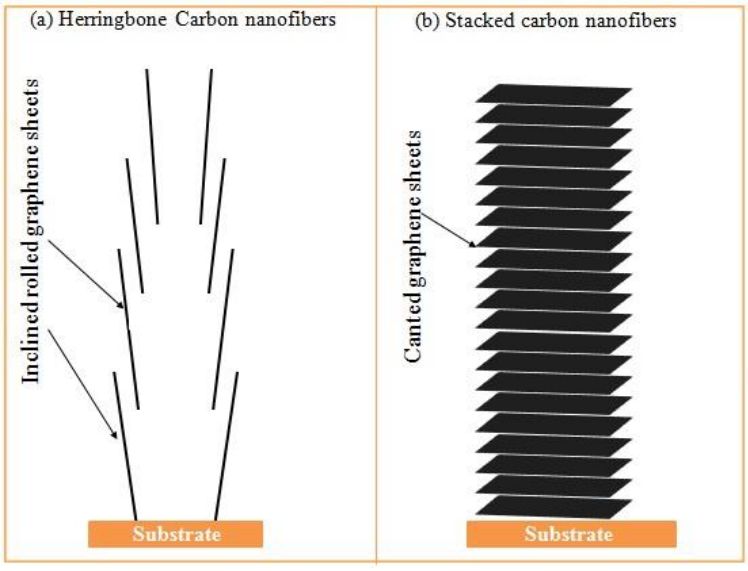

Fig.1.1. (a) Herringbone carbon nanofibers and (b) Stacked carbon nanofibers.

Ravi Gupta, Department of Applied Physics, Delhi Technological University, Delhi, India

In CNFs/CNTs, graphitic shells consist hexagonally arranged carbon atoms. The electronic configuration of carbon atom is $1s^2 2s^2 2p^2$. The inner two electrons occupy the 1s orbital whereas the valence electrons can occupy 2s and 2p orbitals i.e. they can attain sp, sp^2, and sp^3 hybrid orbitals. Three allotropes (diamond, graphite, and fullerenes) of carbon are possible depending upon the hybridization attained by the tetravalent valence electrons.

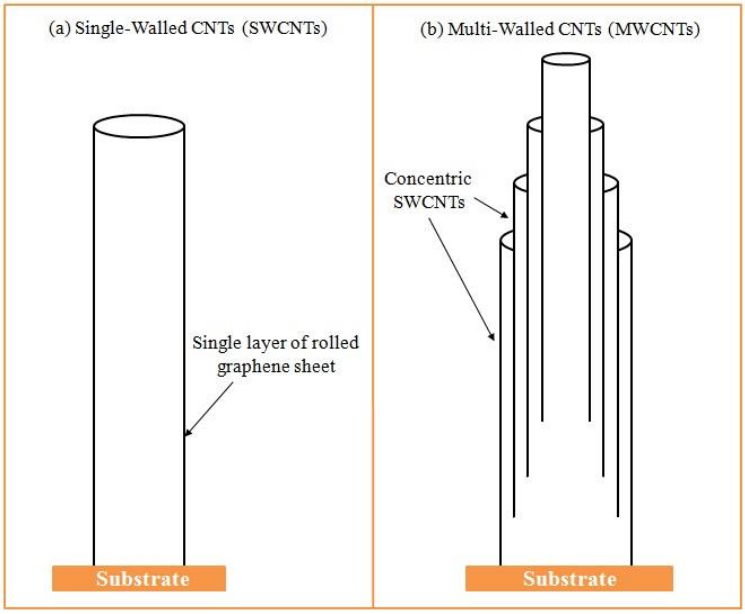

Fig.1.2: (a) Single-walled carbon nanotubes and (b) Multi-walled carbon nanotubes.

In diamond (crystalline form of carbon), the tetravalent electrons form four covalent bonds with other neighbouring carbon atoms using the s, p_x, p_y, and p_z orbitals and thus, forming sp^3 hybridization. However, in graphite (low crystalline allotrope) carbon atoms attain sp^2 hybridization, i.e., the three valence electrons form three strong planar σ bonds with other neighbouring atoms using s, p_x, and p_y planar orbitals as shown in Fig.1.3. The angular spacing between these orbitals is 120^0 due to which electrostatic repulsion between them is minimum. The remaining fourth valence electron forms weak π bond in the direction perpendicular to the plane. These valence electrons in π bonds are responsible for the interaction of stacked graphitic shells and are also responsible for the high electrical properties of the graphite [7-9].

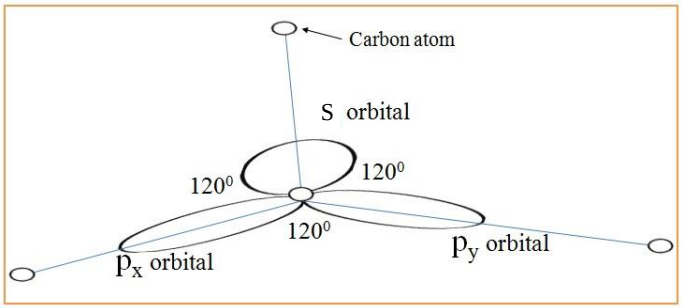

Fig.1.3. Representation of atomic orbitals in sp^2 hybridized graphite.

1.3 Properties of CNFs/CNTs

Owing to high surface to volume ratio, one dimensional carbon nanostructures CNFs/CNTs show promising electrical, mechanical, and thermal properties.

1.3.1 Electrical properties

The hollow structure and high aspect ratio make the charge carriers to transport in one dimension. Depending on the chirality and diameter of the CNFs/CNTs, they can be classified as metallic or semiconducting [10-11]. The energy band gap of CNFs/CNTs depends on their diameter [11]. The resistivity of the CNFs/CNTs at room temperature is found to be 10^{-6} **Ω** cm [12,13] which is much lower than the most conducting metals like silver and copper. The mobility of holes in semiconducting CNFs/CNTs is about 2×10^4 $cm^2\ V^{-1}\ s^{-1}$ which is higher than the mobility of electrons (1.5×10^3 $cm^2V^{-1}s^{-1}$) and holes (4.5×10^2 $cm^2V^{-1}s^{-1}$) in silicon. The CNFs/CNTs show much large current density, i.e., 10^7-10^9 A cm^{-2} [14,15].

1.3.2 Mechanical properties

In order to determine the mechanical strength of the solid material, one should know about the Young's modulus and tensile strength of the material. Young's modulus dictates the ability of the material to withstand under the linear extension/compression and tensile strength measures the resistance provided by the material under the breaking tension. The Young's modulus of the CNFs/CNTs is in the range of 0.7-1.8 TPa according to experimental studies [16-21] and 0.5-5 TPa according to theoretical studies [22] which

clearly show that CNFs/CNTs are much stronger and stiffer than steel having Young's modulus of about 0.18-0.2 TPa [23-24]. The tensile strength of the CNFs and CNTs is in the range of 11-200 GPa [19,20], however, the tensile strength of steel is about 0.38-1.55 GPa [23-24]. Moreover, CNFs/CNTs show highly elastic properties, they can recover from the extreme deformation (distortion greater than 90^0) without showing any plastic behaviour.

1.3.3 Thermal properties

The measuring scales to measure the thermal properties of any materials are specific heat and thermal conductivity. The heat conducting properties of CNFs/CNTs are better than the diamond. At room temperature, thermal conductivity of CNFs/CNTs is found to be 3000-6600 W/mK [25,26].

1.4 Applications of CNFs/CNTs

Vertically aligned CNFs/CNTs have numerous applications in the field of electron emission, nano electronics, etc. due to their high aspect ratio, high electrical conductivity and high mechanical strength.

1.4.1 Hydrogen storage devices

The structural diversity shown by one dimensional carbon nanostructures (CNFs/CNTs) gives rise to their application in hydrogen storage devices. Hydrogen is one of the most valuable energy source which can be easily produced with high percentage of utilization. One of the biggest disadvantage to use hydrogen as the source of energy is its storage. The storage of hydrogen (liquid hydrogen) is expensive and dangerous. CNFs/CNTs can absorb highly dense hydrogen at standard temperature and pressure (STP) conditions via H-bonding with van der Waals forces in CNFs/CNTs [27] and show hydrogen condensation of about 5-10% by weight. However, potassium and lithium doped CNTs show 14% and 20 % by weight hydrogen condensation, respectively [28].

1.4.2 Field emission devices based on one-dimensional carbon nanostructures

Field emission is the phenomenon to extract electrons from the material when sufficient electric field (greater than the work function of the material) is applied. Owing to the high aspect ratio (height to radius), tunnelling of electrons across the potential barrier make them promising candidates in the field emission devices. Fowler and Nordheim expressed [29] the relation between field emission current, applied electric field, and work function of the material;

$$I = \frac{q^3 E^2 \alpha}{8\pi h\phi t^2(y)} \times \exp\left[\frac{-8\pi v(y)\sqrt{2m_e\phi^3}}{3hqE}\right],$$

where I is the field emission current, E is the applied electric field, ϕ is the work function, α is the field area of the emission sites, $t(y)$ and $v(y)$ are the Nordheim functions, and all other symbols have their usual meaning. The field emission properties of any material can be characterized by the field enhancement factor. Generally, field enhancement factor (β) is proportional to the ratio of CNF/CNT height to the radius.

$$\beta \; \alpha \; h/r$$

The highly enhanced field emission property shown by the CNFs/CNTs comes from their geometry rather than their crystalline structure [30].

1.4.2.1 CNFs/CNTs as field effect transistors

CNFs/CNTs showing semiconducting behaviour are used as the channel in field effect transistors separated from gate by thin insulating film [31,32]. The schematic of the CNT based field effect transistors is shown in Fig. 1.4. These transistors, i.e., p-type CNFs/CNTs FET show very high transconductance and high carrier velocity. For 0.6 V gate voltage, they produce current density of 1500 A/m (current per unit gate width). However, p-type MOSFET (metal oxide semiconductor field effect transistor) shows approximate 500 A/m at the overdrive voltage.

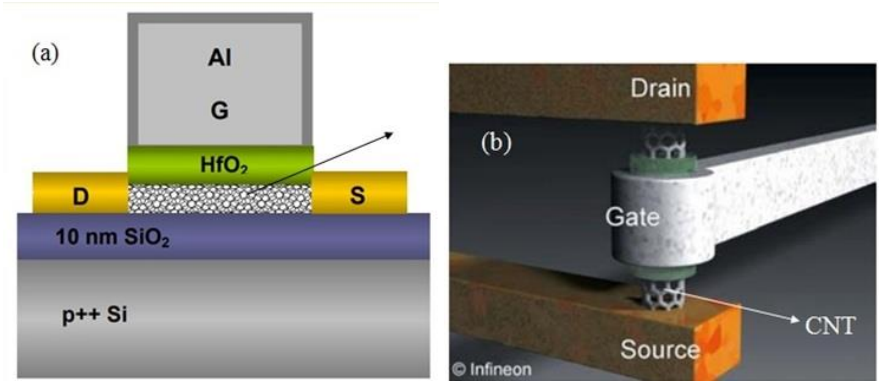

Fig.1.4. (a) Schematic of the carbon nanotubes based field effect transistors [31], and (b) schematic of the vertically aligned CNT serves as the channel of the field effect transistors [32].

1.4.2.2 CNFs/CNTs as flat panel display

The flat panel displays consisting CNFs/CNTs show wide range of operational temperature, they have very fast response rate, and consume very less power for ultra-high brightness. Generally, ±150 V pulse (230 V) is required to obtain a display of 76 μmA/mm^2 at 300 μm anode-cathode distance. The schematic of the CNT based flat panel display is shown in Fig. 1.5.

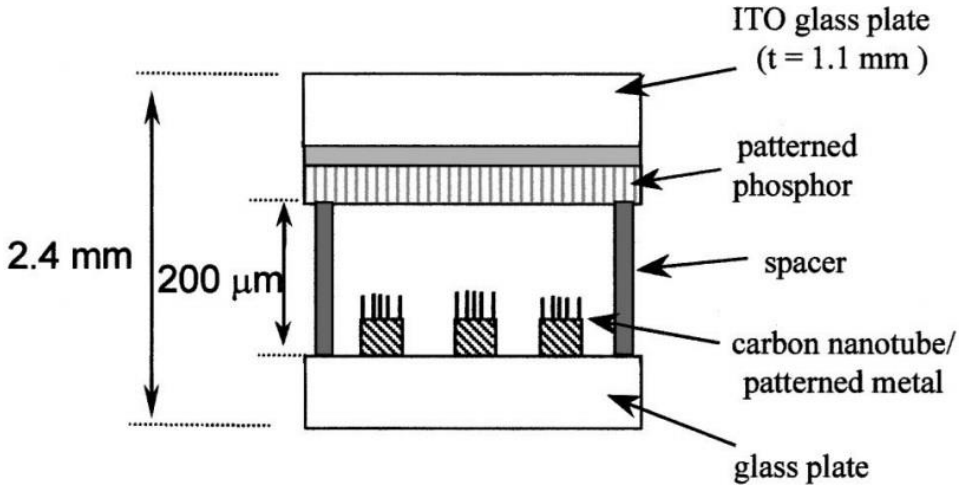

Fig.1.5. Schematic of the flat panel display consisting carbon nanotubes-epoxy stripes on cathode glass plate and phosphorus coated indium tin oxide stripes (ITO) on anode glass plate [33].

1.5 CNFs/CNTs Synthesis Routes

For industrial and research purpose, heterogeneity of the tube in terms of length, thickness, chiral angle, and inclination about the growth axis are the main aspect. There are many routes through which heterogeneous CNFs/CNTs can be synthesized but it is always necessary to adopt easy and cost effective methods. There are many synthesis routes but brief discussion of some of them which are generally used and widely known are as follows:

- Laser ablation
- Arc discharge
- Chemical vapour deposition (CVD)
- Plasma enhanced chemical vapour deposition (PECVD)

1.5.1 Laser ablation

Laser ablation also known as laser vaporization is developed in 1995 by Smalleys group [34] for the synthesis of fullerenes (zero dimensional carbon nanostructures) and applied for the synthesis of one dimensional carbon nanostructures in 1996 [35]. The schematic of the laser ablation method is shown in Fig. 1.6. As the name implies, a continuous laser pulsed (ND-YAG laser or CO_2 laser) is used to vaporize the piece of the graphite in a quartz reactor tube at 1200 ^{0}C with the flow of inert gas at controlled pressure [36]. The graphitic vapour generates the plume with metal catalyst nanoparticles which in turn facilitate the growth of CNFs/CNTs. The plume containing CNFs/CNTs and other by-products are collected on the collector via condensation. This method is especially known for the production of highly pure CNFs/CNTs with minimal defects density. Since solid graphite is vaporized at the atomic level thus, highly energetic laser pulse is required [37-39]. The diameters of the growing CNFs/CNTs can be deterministically controlled by suitably varying the furnace temperature, gas flow rate, and metal catalyst [38-42].

Ravi Gupta, Department of Applied Physics, Delhi Technological University, Delhi, India

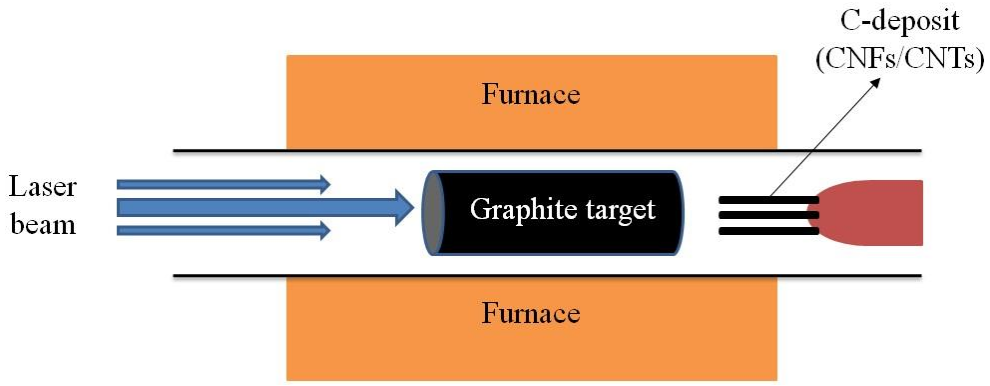

Fig. 1.6. Schematic of the laser ablation technique to synthesize CNFs/CNTs.

1.5.2 Arc discharge

Arc discharge or electric discharge is the first method used to reliably synthesize the MWCNTs and SWCNT. The schematic of the arc discharge method is shown in Fig. 1.7. In this method, electric arc discharge or plasma is generated between two graphite electrodes separated by the distance of 1 mm using low voltage (20 V) and high current (100 A) power source in the inert atmosphere of the Helium or Argon at high temperature and low pressure (100-1000 Torr) [43]. In this method, transition of solid carbon (graphite) to gas phase carbon occurs directly without involving the sublimation stage (liquid phase) due to the high temperature. The graphite with metal catalyst (generally Fe or Co) is taken as the anode and pure graphite is taken as the cathode. The electric discharge vaporizes the carbon from anode which in turn deposit at the cathode surface in the form of one dimensional carbon nanotubes (CNTs/CNFs). The presence of hydrogen in the growth atmosphere leads to the high crystalline product.

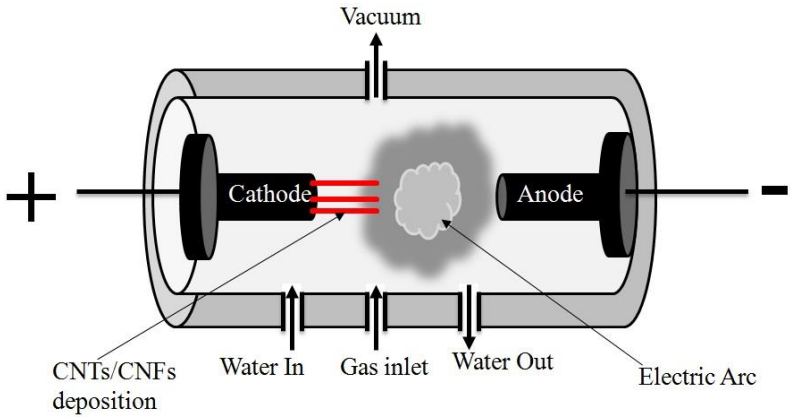

Fig.1.7. Schematic of the arc discharge method [44].

1.5.3 Chemical vapour deposition (CVD)

Chemical vapour deposition (CVD) is one of the parent to a family of many synthesis processes because of the availability of vast number of variations. In CVD, surface deposition of the solid material is caused via various surface reactions between gas phase carbon bearing species and substrate surface. Generally, metal catalyst thin film is deposited on the substrate to enhance the decomposition of the carbon bearing species. Since heat energy is the fuel for any reaction to occur, typical CVD system is precisely known as the thermal-CVD in which catalyst film placed over substrate surface is heated to high temperatures in the furnace. The Fig. 1.8 shows the schematic of the thermal CVD system. The applied heat energy fragments the metal catalyst film into many catalyst nanoislands or nanoparticles and these nanoislands act as the nucleation sites/seeds for the nanostructures growth. The carbon nanostructure growth process [45] via CVD is mainly divided into four fundamental stages;

(i) the carbon bearing gaseous species decompose and adsorb on the catalyst active surface to generate building units (carbon species) and hydrogen radicals via various intermediate processes,

(ii) the carbon species diffuse and dissolve through the catalyst surface towards the heated surface of the catalyst (rear surface) due to the temperature gradient,

(iii) precipitation of the carbon species at the rear surface of the catalyst nanoparticle, and

(iv) incorporation of carbon species into growing graphitic layers.

The catalyst nanoparticle remains either on the top of the tube or at the bottom of the tube during the growth depending upon the interaction between catalyst particle and substrate surface [47] as shown in Figs. 1.9 & 1.10. According to Baker [47], interaction between catalyst particle and substrate surface is characterized by the contact angle made by the catalyst particle with the substrate at constant operating conditions such as temperature,

Ravi Gupta, Department of Applied Physics, Delhi Technological University, Delhi, India

applied power etc. The small contact angle results in the strong interaction while large contact angles results in the weak interaction between them. When contact angle is large, then precipitation of carbon around the catalyst is so strong that it lifts up the catalyst particle and thus, leads to the tip growth [48] as shown in Fig. 1.9. However, when contact angle is small, precipitation of carbon around the catalyst is not able to overcome the interaction between catalyst and substrate and thus, leads to the base growth [49-51] as shown in Fig. 1.10.

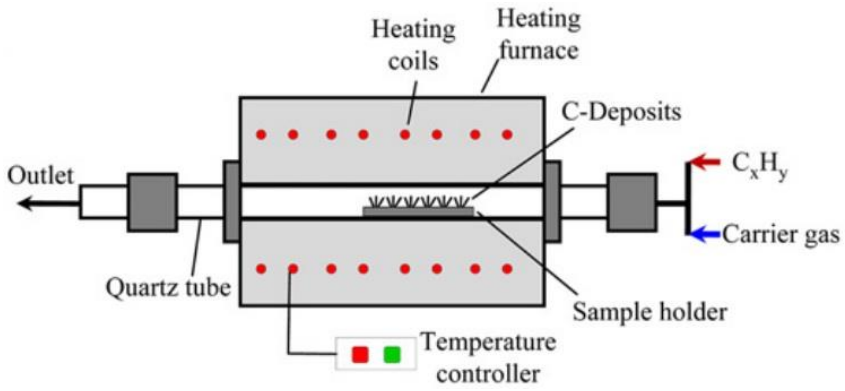

Fig. 1.8. Schematic of the chemical vapour deposition system [46].

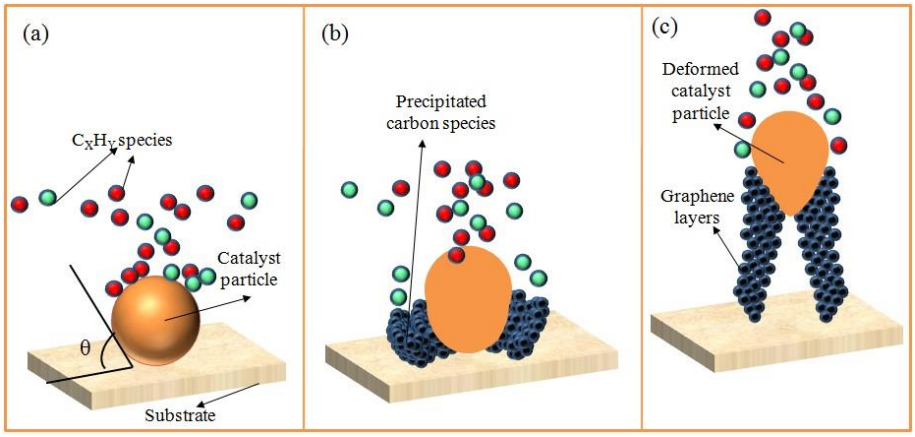

Fig.1.9. (a) Dissociation of hydrocarbon species on the catalyst (making large contact angle with the substrate surface) active surface to generate carbon species, (b) precipitation of the carbon species around the rear of the catalyst, and (c) deformation of the catalyst resulting in the less interaction with substrate and thus, leads to the tip growth.

Ravi Gupta, Department of Applied Physics, Delhi Technological University, Delhi, India

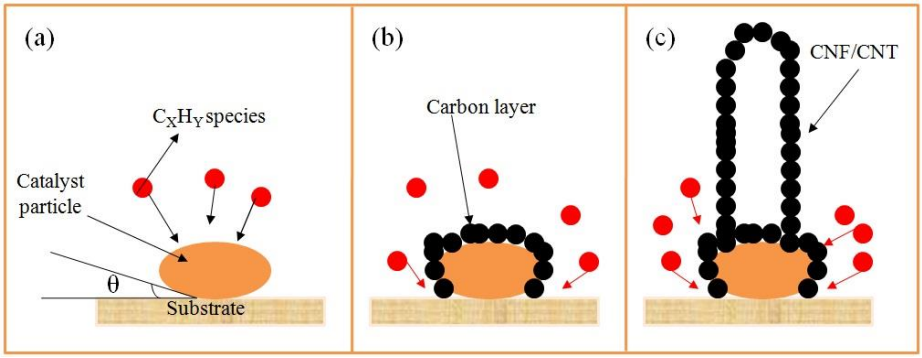

Fig.1.10. (a) Dissociation of hydrocarbon species on the catalyst (making small contact angle with the substrate surface) active surface to generate carbon species, (b) formation of the carbon layer all around the catalyst particle and (c) base growth of the CNFs/CNTs.

The number of graphitic layers can be controlled by the temperature of the system. At low temperature (600-900 ^{0}C), CNFs/MWCNTs are formed, however, at high temperature (900-1200 ^{0}C), SWCNTs are formed [52-59]. Other than temperature, nature of gases and catalyst are also important parameters to control the diameter and growth of the nanotubes. It is impossible to detach the catalyst particles from the nanotubes during the growth, thus high temperature or acidic washing post treatment is required. The CVD has an advantage over the other two synthesis routes discussed in Sec.1.5.1 and 1.5.2 because it offers the nanostructures with high purity and yield compared to other two methods.

1.5.4 Plasma enhanced chemical vapour deposition (PECVD)

In typical CVD (thermal CVD) system, thermal energy is used to activate the gaseous sources, however, as name suggested, plasma enhanced chemical vapour deposition is the technique in which gaseous sources (carrier gas, carbon source gas, and etching gas) are activated using the electron impact (collisions with other species) in the bulk plasma at low temperature and low pressure. In the plasma, gases are in the ionized state and decomposition of various plasma species (carbon bearing species and etching species) takes place in the non-equilibrium plasma known as the glow discharge. The main advantages of PECVD are; (i) it reduces the activation energy of the precursors for the decomposition and (ii) synthesis of the vertically oriented nanostructures. The strong electric field induced between the bulk plasma and

Table 1.1. The different sources of plasma excitation and operating parameters used for the plasma-enhanced chemical vapour deposition (PECVD) growths of CNFs/CNTs based on experimental works.

Source of plasma excitation	Gas mixture	Gas ratio (flow rate)	Pressure	Substrate temperature	Plasma power	Reference
DC	C_2H_2/NH_3	40/80 sccm	3 Torr	700 ^{0}C	123 W	[4]
DC	C_2H_2/NH_3	(0-76)/200 sccm	1.875 Torr	650 ^{0}C	--	[62]
DC	C_2H_2/NH_3	(0-150)/200 sccm	3.5 Torr	750 ^{0}C	--	[63]
DC	C_2H_2/NH_3	50/200 sccm	1.125 Torr	120-500 ^{0}C	--	[64]
DC	C_2H_2/NH_3	50/200 sccm	--	250 ^{0}C	20 W	[65]
DC	C_2H_2/NH_3	30/200 sccm	1.5 mbarr	200 ^{0}C	--	[66]
DC	C_2H_2/NH_3	50/200 sccm	0.7 mbarr	500 ^{0}C	20 W	[67]
MW	C_2H_2/NH_3	200 sccm	20 Torr	825 ^{0}C	--	[68]
MW	CH_4/NH_3	(150-240)/(60-150) sccm	21 Torr	650-1000 ^{0}C	--	[69]
ICP	CH_4/H_2	20/80 sccm	0.5-20 Torr	800-1000 ^{0}C	120 W	[70]
ICP	C_2H_4/H_2	(5-20)/(80-95) sccm	3 Torr	600-1000 ^{0}C	50-200 W	[71]
ICP	CH_4/H_2	50/50 sccm	1 Torr	500-650 ^{0}C	--	[72]
ICP	C_2H_2/H_2	(37.5-88)/(12-62.5) sccm	50 mTorr	700 ^{0}C	27 W	[73]
ICP	C_2H_2/H_2	15/85 sccm	20 mTorr	500 ^{0}C	400 W	[74]
RF	CH_4/H_2	0.4/20 sccm	5 Pa	400 ^{0}C	350 W	[75]
RF	C_2H_2/NH_3	5/20 sccm	--	450 ^{0}C	180 W	[76]

negatively biased substrate surface creates the charge separation region known as plasma sheath region, exert the alignment force on the nanostructures and direct the growth in vertical direction (perpendicular to the substrate) [60,61] and nanostructures grow in this plasma sheath region.

Currently, PECVD techniques are commercially used to synthesize the carbon based nanostructures because of its simplicity, controllability, and relatively low synthesis temperature and pressure. PECVD techniques are mainly characterized by the source of plasma energy used and the most widely used plasma sources include: microwave plasma enhanced chemical vapour deposition (MW-PECVD), inductively coupled plasma enhanced chemical vapour deposition (IC-PECVD), radio frequency plasma enhanced chemical vapour deposition (RF-PECVD), hot-filament plasma enhanced chemical vapour deposition system (HF-PECVD), and direct current plasma enhanced chemical vapour deposition system (DC-PECVD). The detailed overview of different sources of plasma excitation and process-related parameters used for the PECVD growth of CNFs/CNTs based on experimental works are summarized in Table 1.1.

1.5.4.1 MW-PECVD

MW-PECVD is the technique to generate high density plasma using 2.54 GHz microwave power generator. This method is effectively used to dissociate hydrogen molecule to generate hydrogen radicals. The effecting heating of the substrate to dissociate the gaseous sources is provided by the plasma. MW-PECVD technique is operated at low pressure and high microwave power to obtain sustainable plasma. If operated pressure is high enough or input microwave power is low enough then plasma becomes unstable. The operating parameters used in this method are given in Table 1.1. Srivastava *et al.* [77] used MW-PECVD technique to synthesize uniformly distributed dense carbon nanopetals. The schematic diagram of typical MW-PECVD system is shown in the Fig. 1.11.

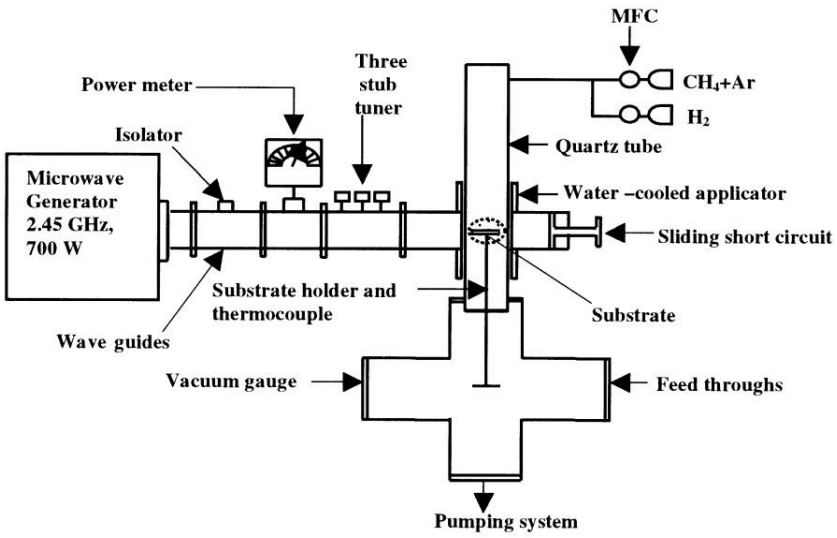

Fig. 1.11. Schematic of the MW-PECVD technique **[77].**

1.5.4.2 RF-PECVD and IC-PECVD

In this technique, radio frequency (13.56 MHz) voltage source is used to generate plasma. Generally two different types of RF-PECVD technique is used; (i) inductively coupled RF-PECVD and (ii) capacitively coupled RF-PECVD.

In inductively coupled RF-PECVD technique, inductive coils connected to radio frequency generator are used as the source of plasma. Generally, two types of coils are used as the coil antenna; planar and cylindrical. In planar type coil antenna, single turn metallic coil is used and in cylindrical type, coil in the spiral form having multiple turn is used as shown in Fig.1.12. When time varying current is passed through the coil, time varying magnetic field is generated around the coil. This time varying magnetic field induces the electric current in the gas, thereby, leading to the dissociation of gases and production of highly dense plasma. The parameters used in the IC-PECVD technique are given in Table 1.1.

In capacitively coupled RF-PECVD technique, circular parallel plate capacitor with the separation of 5 cm is used. RF voltage source is connected to the upper electrode and lower electrode is grounded. Inductively coupled PECVD is preferred over the capacitively coupled

PECVD because of the generation of high density plasma in the former case.

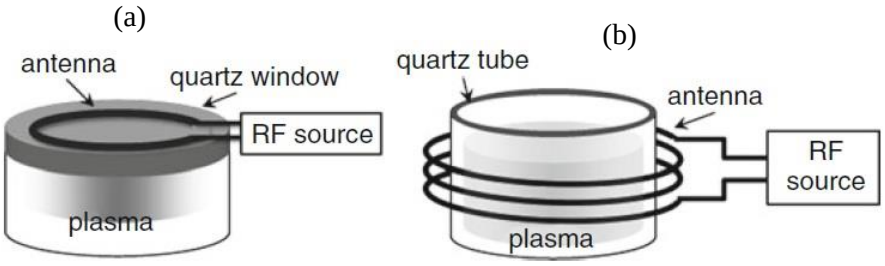

Fig.1.12. Schematic of the inductively coupled plasma with (a) planar spiral antenna and (b) helical antenna [78].

1.5.4.3 DC-PECVD

DC-PECVD synthesis of vertical aligned carbon nanostructures has been realized on two geometric setups: parallel plate and pin to plate [see Fig.1.13 & Fig.1.14]. In parallel plate method, a dc voltage is applied between planar cathode and anode across a space filled with low pressure gas for breakdown to occur. The gaseous ionization depends on the particular gas composition, pressure, and electrode distance [79]. The substrate is usually placed at the cathode or serves the cathode directly. The glow discharge that is initiated can be divided into eight regions, and is arranged from cathode to anode: Aston dark space, cathode glow, cathode dark space (cathode sheath), negative glow, Faraday space, positive column, anode glow, and anode dark space [80,81]. The electric field induced in the cathode sheath accelerate the ions towards the substrate surface and also exert the alignment force in the vertical direction. However, the pin to plate method is a non-uniform plasma source in which asymmetric electrodes i.e., tungsten tip and planar substrate are used. This method results in the non-uniformity in the morphology and structure of carbon nanostructures on the substrate. The conductive substrate is the primary requirement of this technique which is the main disadvantage of this technique.

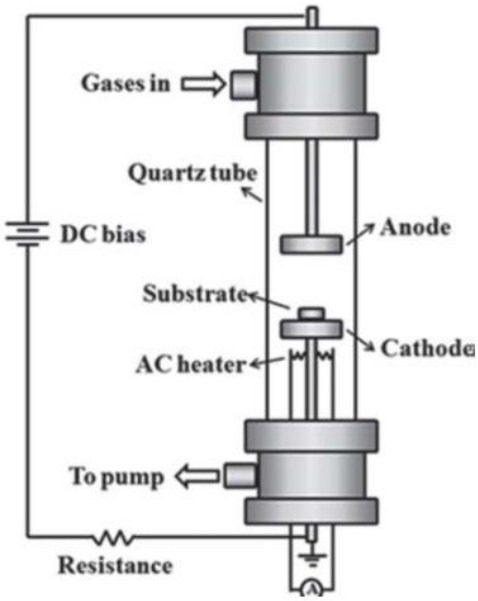

Fig.1.13. Schematic of the parallel plate DC-PECVD system [80].

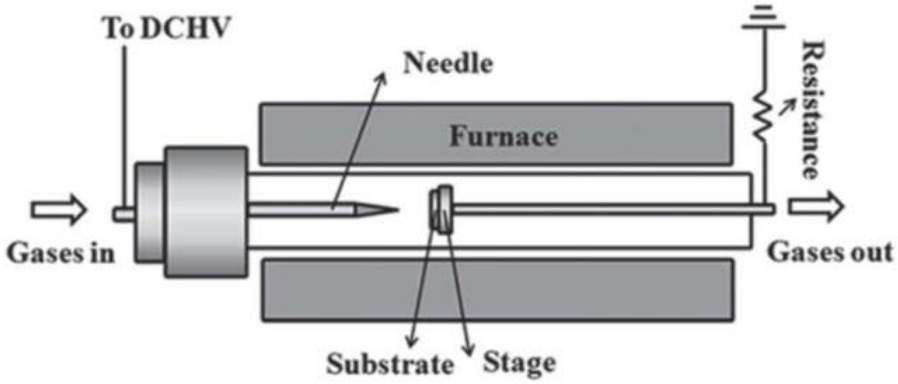

Fig. 1.14. Schematic of the pin to plate DC-PECVD system [80].

1.6 Nucleation and growth mechanism of 1-D carbon nanostructures in reactive plasma

Synthesis of 1-D carbon nanostructures (CNFs/CNTs) in reactive plasma mainly include five fundamental stages;

(i) ***Plasma excitation:*** activation of gaseous sources due to applied plasma power as discussed above in detail in Sec. 1.5.4.

(ii) ***Plasma sheath:*** formation of plasma sheath region between bulk plasma and substrate surface.

(iii) ***Nucleation stage:*** nucleation of the nanostructure over the nucleating seeds [82].

(iv) ***Surface deposition:*** deposition of reactive species (positively charged and neutral species) over the catalyst [83-84].

(v) ***Growth stage:*** finally, the growth of nanostructure in the reactive plasma [45,61].

The Fig.1.15. shows the complete picture of plasma excitation and growth mechanism of 1-D carbon nanostructures. All these stages include complex processes which are discussed in detail below.

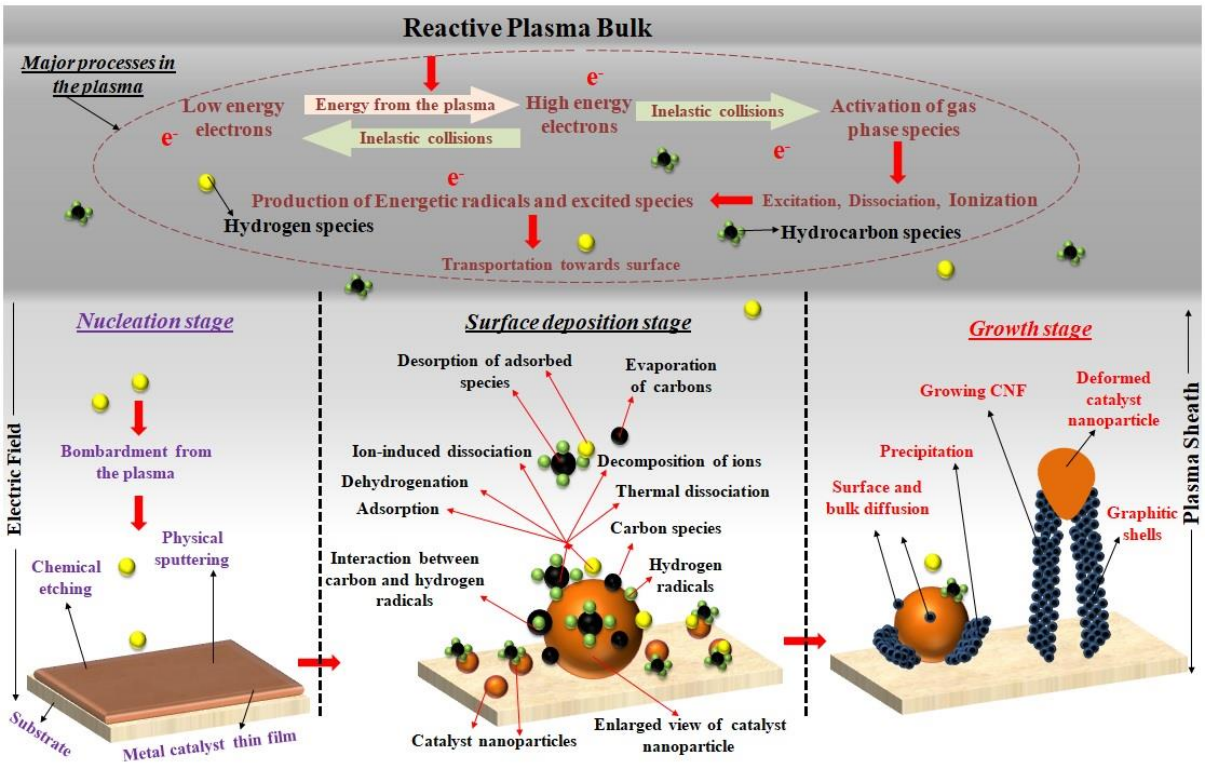

Fig. 1.15. The complete picture of the growth mechanism of the 1-D carbon nanostructure (CNFs/CNTs) growth in the reactive plasma environment. The dark grey space (the top most region) shows the reactive plasma bulk region and the red elliptical circle shows the major processes in the bulk plasma. The low energy electrons gain the energy from the plasma and collide with gaseous species. Thus, gas phase species gets activated and generate highly energetic (highly reactive) ions, neutrals, and free radicals via electron impact excitation, dissociation, and ionization of gaseous sources. The electric field in the plasma sheath transports these reactive species towards the substrate. The bottom of the figure shows the three stages (separated by black dashed bars) of the growth mechanism; the nucleation stage (written in purple ink), in which bombardment of the plasma species leads to the fragmentation of the thin metal catalyst film into many catalyst nanoparticles via various processes (written in purple ink); the surface deposition stage (written in black ink), in which hydrocarbons and hydrogen species get adsorb and dissociate over the catalyst nanoparticle active surface via various surface processes (written in black ink) to generate building units (also shown in the enlarged view of the catalyst nanoparticle); and the growth stage of the CNFs/CNTs (written in red ink), in which carbon species diffuse and precipitate in the form of graphitic shells that leads to the deformation of catalyst nanoparticle during the growth.

1.6.1 Formation of plasma sheath

In PECVD synthesis of the nanostructures, it is reasonable to divide the plasma into two separate regions, the bulk plasma and the plasma sheath. This is because, physics involved in two regions is entirely different. The bulk plasma is the region that contains the balanced charges of electrons and ions (quasi-charge-neutrality,) i.e., the region in which densities of electrons as well as positively charged ions are very high and substantially equal. The sheath region or plasma sheath is formed between the bulk plasma and wall or the boundaries of the chamber. In plasma sheath, the density of positively charged ions is slightly greater than the density of electrons.

The shielding occurs in the bulk plasma beyond the Debye length, have constant potential which is known as the plasma potential. Electrons and ions will be lost in the plasma when they strike to the chamber walls. Electrons make more collisions with the walls than the ions because electrons have high thermal velocity than ions. Thus, electron current to the walls are high enough to leave the plasma with net positive charges, which in turn increases the plasma potential and walls becomes negatively charged with respect to the plasma. Thus, an electric field is set up between the bulk plasma and the walls which provide the net flux of positive charge to the walls and offers the barrier for the electrons. This charge imbalance region is known as the plasma sheath [85] as shown in Fig.1.16 .

The formation of plasma sheath is the important stage in the plasma processing of the materials because substrate surface or surface of material also interacts with the plasma as the walls or boundaries of the reactor, moreover, nanostructures grow in this plasma sheath region. Generally, negatively biased substrate is placed below the bulk plasma to induce strong electric field between the bulk plasma and substrate surface and leads to the formation of strong plasma sheath region.

Ravi Gupta, Department of Applied Physics, Delhi Technological University, Delhi, India

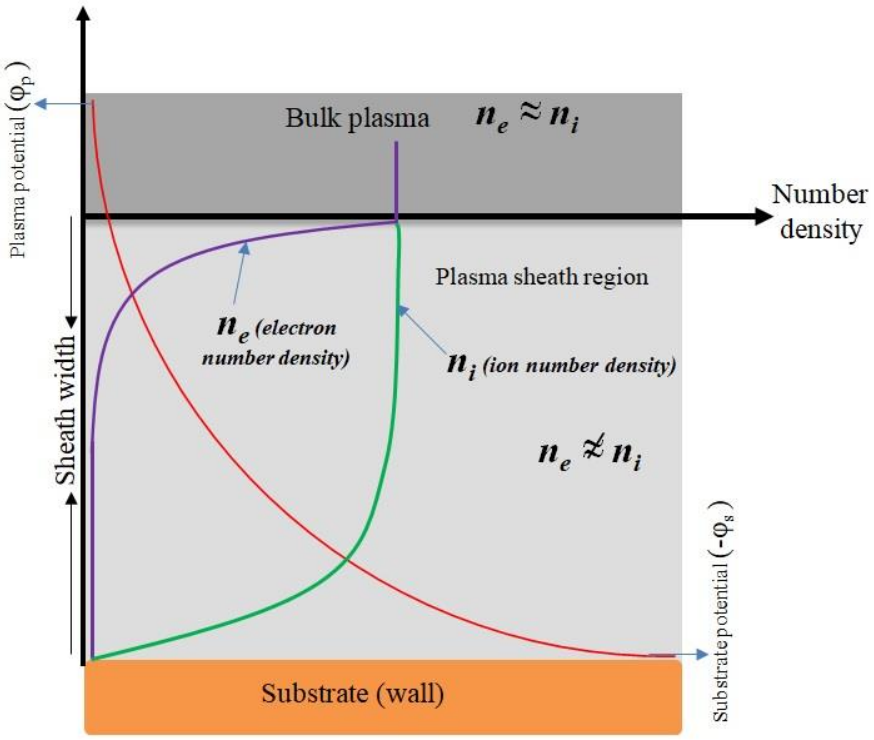

Fig. 1.16. Mechanism of the plasma sheath formation between bulk plasma region and substrate surface. The purple curve shows the rapid decay of the electron density in the sheath region. The green curve shows that the sheath region mainly comprises the positively charged ions. The red curve shows that plasma has constant potential and substrate or wall attain negative potential due to the loss of electrons near the walls.

1.6.2 Nucleation stage

Prior to the nanostructure growth over the catalyst-substrate surface, the plasma pre-treatment of the thin metal catalyst film (catalyst nanofilm) is highly necessary step. In this process, a predeposited catalyst nanofilm is subjected to reactive plasma that contains the highly energetic species of etching gas (generally, hydrogen or nitrogen is used for this purpose). The heavy bombardment of highly energetic etchant species (ions and radicals) leads to the physical sputtering and chemical etching of the catalyst nanofilm which ultimately results in the fragmentation of the catalyst nanofilm into the many catalyst nanoparticles as shown in Fig.1.15. However, in the typical CVD case, the thermal annihilation is performed for segregation purpose. These catalyst nanoparticles have peculiar ability to dissociate the carbon

feedstock gases over their active site to generate building species (carbon species) and thus, acts as the seeds/sites for the nanostructure nucleation.

1.6.3 Surface deposition of reactive plasma species

The reactive plasma species accelerates due to the induced electric field in the plasma sheath and reach to the catalyst-substrate surface with sufficient high energy and get adsorbed over the catalyst nanoparticle active sites (free surface available for adsorption). These adsorbed species dissociate over the catalyst nanoparticle surface via various complex processes (surface reactions [82-91]) such as; thermal dissociation of hydrocarbons, ion-induced dissociation of hydrocarbons, ion decomposition, desorption of adsorbed species, and evaporation of radicals to generate building species (carbon species) and etching species (hydrogen radicals) as shown in Fig.1.15.

1.6.4 Growth of 1-D carbon nanostructures (CNTs/CNFs)

These building species (carbon species) diffuse over and dissolve through catalyst nanoparticle surface and gets precipitated around the rear of the catalyst nanoparticle in the form of the carbon layers (graphene layers). These carbon layers exert substantial stress on the catalyst nanoparticle which can cause metal nanoparticle to deform [92-94]. Now, it is crucial to understand what stops the in plane growth of carbon condensation i.e., why carbon does not spread out over the whole substrate surface. The highly active atomic and ionic hydrogen etch the terminal carbons present at the edges of the graphitic nest and the carbon shadowed by the catalyst particle may contribute to the formation of graphitic shells around the catalyst particle and continuous supply of the carbon species leads to the vertical growth of existing graphitic shells. Due to the morphological changes in the catalyst nanoparticle during growth, the interaction between metallic catalyst nanoparticle and substrate decreases, and hence the catalyst particle gets lift off leading to the vertical growth of nanostructure as shown in Fig1.15.

Ravi Gupta, Department of Applied Physics, Delhi Technological University, Delhi, India

1.7 Parameters affecting the nucleation and growth of CNFs/CNTs

For the deterministically controlled growth of CNFs/CNTs, the proper knowledge of plasma parameters, PECVD operating parameters, source gases, etc., is highly crucial as these parameters significantly affect the characteristics of the reactive plasma and growth profile of the nanostructures. Some of the essential parameters are as follows;

1.7.1 Impact of source precursors

Generally, three types of the gases, i.e., carbon feedstock gas, etching gas, and carrier gas are introduced in the plasma chamber for CNFs/CNTs growth. Each type of gas has great impact on the growth characteristics of the CNFs/CNTs.

1.7.1.1 Effect of carbon feedstock gas

Most of the studies adopted the acetylene (C_2H_2) or methane (CH_4) as the carbon source gas in the PECVD system [95-98]. However, C_2H_2 is considered to be better carbon source gas over CH_4 [53] because;

- C_2H_2 species require less dissociation energy compared to the CH_4 species,
- C_2H_2 requires low temperature plasma processing than CH_4,
- CNFs/CNTs grown in C_2H_2 plasma show high growth rate and better vertical alignment compared to CH_4 plasma.

1.7.1.2 Effect of etching gas

During the growth of CNFs/CNTs, the removal of amorphous carbon layer to maintain the catalyst activity of the catalyst nanoparticles is inevitable and crucial process for the high quality growth. Generally, hydrogen, ammonia, and nitrogen are most commonly used etching gases. Atomic hydrogen (hydrogen radicals), highly excited nitrogen species are the most

commonly found etchants in the growth atmosphere. It is reported that ammonia gas is considered as the more effective source of atomic hydrogen rather and hydrogen gas [99]. However, nitrogen is considered to be the better etchant than hydrogen. Zhang *et al.* [100] introduced the small amount of O_2 in the C_2H_2/H_2 plasma and found the much enhanced growth of CNFs/CNTs due to the more effective control over the growth of amorphous carbon layer [101]. He *et al.* [53] found that small amount of water insertion in the C_2H_2/H_2 plasma leads to the better growth of CNFs/CNTs.

Role of etching gas is not only to remove amorphous carbon layer, it also segregates the catalyst nanofilm into many catalyst nanoparticles due to the physical sputtering and chemical etching of the film via heavy plasma environment. The hydrogen gas is used for plasma pre-treatment of the nanofilm, however, it is reported that insertion of small amount of nitrogen in the hydrogen plasma leads to the increase in number density and decrease in the size of the catalyst nanoparticle formed [102].

1.7.1.3 Effect of carrier gas

In PECVD process, the gaseous sources are activated by the electron impact reactions (excitation, dissociation, and ionization) between electrons and gaseous reactants. Thus, it is crucially important to retain the electron energy with high energy to stabilize and sustain the plasma which can be done to minimize the inelastic collisions in plasma responsible for the loss of the energy of electrons. Argon gas is used for this purpose, because argon has high excitation and ionization potential [103] due to which it interacts with electrons via elastic collisions and makes electrons capable to increase the ionization rate of the system. Moreover, the chemical reactions between argon and hydrocarbons in the bulk plasma lead to the formation of carbon dimers (C_2) in the bulk plasma [104] which increase the number of building species on the catalyst nanoparticle surface and consequently, increases the degree of graphitization.

1.7.2 Impact of gas proportions

The flow rates of gaseous sources or gas ratios (proportions) are the essential parameters to control the degree of graphitization, morphology, and the growth characteristics of the CNFs/CNTs. It was reported by Wu *et al.* [105] that by suitably increasing the hydrogen gas ratio in CH_4/H_2, different nanostructures deposits are obtained. Merkulov *et al.* [4] studied the effect of C_2H_2/NH_3 gas ratio on the growth and diameter of the vertically aligned CNFs and found the increase in growth rate and decrease in tip diameter with increase in C_2H_2/NH_3 gas ratio in the plasma. It is important to note that the optimum gas ratio to control the growth profiles of the CNFs/CNTs strictly depend on the many PECVD conditions. Thus it is not justified to mention the exact range for the high quality growth of the 1-D carbon nanostructures or other carbon based nanostructures.

1.7.3 Role of catalyst

The catalyst plays an indispensable role during the CNFs/CNTs growth in the reactive plasma. The resulting structure, number of graphene layers, alignment of graphene layers about the growth axis, and growth characteristics (height and diameter) of nanotubes/nanofibers strictly depend on the dynamics of the catalyst particle during PECVD growth process which ultimately depends on the thickness of the catalyst nanofilm. The catalyst nanoparticle undergoes geometrical reconstruction during PECVD growth process and the extent up to which catalyst nanoparticle can reconstruct itself decides the number and inclination of graphene layers. It is reported that the CNFs nucleated from small catalyst nanoparticles are lesser in diameter, grow faster, and contain few graphene layers which are almost parallel to the growth axis (or perpendicular to the substrate surface) [93,94]. Moreover, it is also reported that size of the catalyst nanoparticle can be effectively reduced by reducing the thickness of the catalyst nanofilm and by suitably varying the plasma processing conditions [48].

1.7.4 Effect of gas pressure of the plasma reactor

The gas pressure of the plasma reactor is one of the preliminary PECVD operating parameter which affects the plasma characteristics and consequently, affects the PECVD growth process. The gas pressure and mean free path of the electrons are inversely related to each other, thus, change in gas pressure affect the mean free path of the electrons which directly influences the temperature, energy and density of electrons in the bulk plasma. The gas pressure of the plasma reactor must be kept in the optimum range, if gas pressure is low enough then the mean free path of the electron may exceed the dimensions of the plasma system which leads to the sufficient loss of density and energy of electrons. On the other hand, if gas pressure is high enough then the mean free path becomes so small that number of collisions in plasma increases abruptly and leads to the significant loss of energetic electrons. Wei *et al.* [61] experimentally investigated the effect of pressure in the plasma on the CNF length and observed that the length of the CNF increases with increase in pressure (0-30 Torr) and decrease when pressure is increased further [61]. Wang *et al.* [106] investigated the growth of CNTs via PECVD technique at two different gas pressures, i.e., 15 Torr and 30 Torr and found that average length of the CNF grown at 30 Torr is smaller than that at pressure 15 Torr. Li *et al.* [107] have studied the effect of gas pressure on the structure and the growth of the CNTs via chemical vapour deposition (CVD) technique and observed that CNTs grow with shorter in length and larger in diameter at high pressures (50-760 Torr). Ganjipour *et al.* [108] observed the increase in CNTs diameter when gas pressure in the PECVD system is increased (0-500 Torr). Pint *et al.* [109] investigated the effect of pressure on the CNT growth via CVD process and found the increase in CNT height with increase in pressure (0-15 Torr). Chhowalla *et al.* [48] investigated the PECVD growth process conditions of the vertically aligned CNTs and observed the increase in the length of the CNTs with increase in the pressures (0-10 Torr). Hinkov *et al.* [110] found the increase in the growth rate of plasma grown single-walled CNTs with increase in the pressure (0-1000 mbar).

1.7.5 Effect of plasma power

Input plasma power is essential PECVD operating parameter to control the plasma characteristics i.e., electron temperature and density which are primary scale to measure the strength and stability of the plasma. The electrons gain the energy from the applied plasma power and collide with the gaseous species to activate them. The change in plasma characteristics affects the ionization and dissociation of gaseous species in the bulk plasma which further affects the growth characteristics of the CNFs/CNTs. Collison *et al.* [111] have experimentally found the increase in electron density and electron temperature when input plasma power is raised. Chang *et al.* [112] synthesized the CNTs at low temperature using microwave plasma and found the considerable reduction in the diameter of the CNT when input plasma power is raised (700-1000 W). Merkulov *et al.* [4] have found the reduction in the diameter of the CNFs when plasma power of the DC PECVD system is increased. Wei *et al.* [61] also observed the increase in the CNF length with an increase in the plasma power (0-2000 W).

1.7.6 Effect of temperature

The PECVD process is a low temperature process because thermal energy required to dissociate hydrocarbon species is provided by the plasma that contains highly energetic electrons and other activated positively charged and neutral species (molecules and radicals). The substrate temperature in the CVD system is the most important operating parameter as it directly affects the reaction over the catalyst nanoparticle surface (surface processes) to generate building species [113] and also affects the relative etching of the growing graphitic shells. The MW-PECVD system does not require external substrate heating because microwaves have primary characteristic of heating the material in contact. The RF-PECVD system does not require external heater because of its ability to generate highly dense and energetic plasma or it requires the low substrate heating. However, DC-PECVD system relies on the external substrate heating due to its limited input energy for glow discharge. At low temp fibers are formed and at high temp nanotubes are

formed [53]. It is reported that the high substrate heating leads to the higher growth of the CNFs/CNTs [90,95].

1.8 Objectives and organization of the thesis

From the literature studied, it can be seen that there is the correlation between the growth mechanism of the CNFs and CNTs and the growth conditions decide the nature of final nanostructure formed. The present work of the thesis aims to elucidate the role of plasma on the catalyst-assisted nucleation and growth of carbon nanofibers and also explain the deep insights of the correlation between CNFs/CNTS growth mechanism. The entire work of the present thesis is divided into eight chapters. The current chapter (chapter 1), incorporates the general introduction on the CNFs/CNTs based on extensive literature which motivated us to bring deep insights of the CNFs/CNTs growth mechanism into the notice of others. The major objectives of the thesis are outlined below:

- **In chapter 2,** the plasma kinetics based model is developed to elucidate the fragmentation mechanism of the thin metal catalyst film (catalyst nanofilm) into nanoparticles in the reactive plasma environment and effect of plasma parameters on the growth and number density of catalyst nanoparticles formed. The model considers the plasma processing of thin catalyst film, power equalization at the film surface, flux and kinetics of plasma species (electrons, ions, and neutrals), physical sputtering and chemical etching of the thin film.

- **In chapter 3,** a theoretical model is developed to study the nucleation and catalytic growth of carbon nanofiber (CNF) in the plasma environment. The model includes the charging of CNF, kinetics of plasma species (neutrals, ions and electrons), plasma pre-treatment of catalyst film, various processes unique to plasma exposed catalyst surface such as adsorption of neutrals; thermal dissociation of neutrals, ion induced dissociation, interaction between neutral species, stress exerted by the growing graphene layers and the growth of CNF. Numerical

calculations of model equations have been carried out for typical glow discharge plasma parameters.

- **In <u>chapter 4,</u>** an analytical model is developed to describe the effects of nitrogen doping on the growth of the carbon nanofibers (CNFs) and to elucidate the growth mechanism of nitrogen contained carbon nanofibers (N-CNFs) on the catalyst substrate surface through the plasma enhanced chemical vapour deposition (PECVD) process. The analytical model accounts the number density balance of electrons, positively charged and neutral species in the bulk plasma, generation of carbon species on the catalyst nanoparticle surface due to dissociation of hydrocarbons, and CNF growth due to diffusion and precipitation of carbon species and various other processes. The first-order differential equations have been solved for glow discharge plasma parameters for undoped CNFs (CNF growth in C_2H_2/H_2 plasma) and nitrogen doped CNFs (N-CNF growth in C_2H_2/NH_3 plasma).

- **In <u>chapter 5,</u>** an analytical model based accounting the various surface deposition processes and plasma sheath kinetics of the plasma species has been developed to investigate the effects of different plasmas (different etchants) on the catalyzed plasma aided growth of carbon nanofibers (CNFs). In particular, the model accounts the poisoning of the catalyst nanoparticle, i.e., the formation of the amorphous carbon layer on the catalyst active surface due to the continuous dissociation of incoming hydrocarbon species from the plasma. The effects of different oxidizers (H_2O and O_2) in the typical hydrocarbon/hydrogen plasma on the CNFs growth have also been studied.

- **In <u>chapter 6,</u>** a theoretical model to study the role of a metal catalyst nanofilm in the nucleation, growth, and resulting structure of carbon nanofibers (CNFs) in low-temperature hydrogen diluted acetylene plasma has been developed. The model incorporates the nanostructuring of thin catalyst films, growth of CNF, restructuring of catalyst nanoparticles during growth, and its repercussion on the resulting structure (alignment of rolled graphene sheets around catalyst nanoparticles) by taking into

account the plasma sheath formalization, kinetics of neutrals and positively charged species in reactive plasma, flux of plasma species onto the catalyst front surface, and numerous surface reactions for carbon generation. In order to examine the influence of the catalyst film on the growth of CNFs, the numerical solutions of the model equations have been obtained for experimentally determined initial conditions and glow discharge plasma parameters.

- **The chapter 7** aims to develop a numerical model to understand and optimize the process parameters for the growth of carbon nanofibers (CNFs) inside the plasma enhanced chemical vapor deposition (PECVD) system containing acetylene, hydrogen, and argon gases. Two-dimensional axis-symmetrical inductive couple plasma (ICP) module is implemented using COMSOL Multiphysics 5.2 simulation software to analyze the density profiles and temperatures of electrons, ions, and neutral species in the plasma at different gas pressures and input plasma powers. The plasma sheath equations and surface deposition model is accounted to study the fluxes and energies of the plasma species and growth characteristics of carbon nanofibers (i.e., poisoning of the catalyst nanoparticle, height, and diameter) at different gas pressures and input plasma powers.

- **The chapter 8** includes the conclusion and future scope of the present work. More importantly, the conclusions made in the present study are not only restricted to the growth of one-dimensional carbon nanostructures and may also extend to the plasma-assisted growth of other carbon nanostructures at low pressure and low temperature.

References

[1] J. Abrahamson, P. G. Wiles, Brian L. Rhoades, Carbon **37**, 1873 (1999).

[2] S. Iijima, Nature **354**, 56 (1991).

[3] V. I. Merkulov, A. V. Melechko, M. A. Guillorn, D. H. Lowndes, and M. L. Simpson, Chem. Phys. Lett. **361**, 492 (2002).

[4] V. I. Merkulov, D K Hensley, A. V. Melechko, M. A. Guillorn, D. H. Lowndes, and M. L. Simpson, J. Phys. Chem. B **106**, 10570 (2002).

[5] N. M. Rodriguez, A. Chambers, and R. T. K. Baker, Langmuir **11**, 3862 (1995).

[6] K. B. K. Teo, C. Singh, M, Chhowalla, and W. I. Milne, Encyclopaedia of nanoscience and nanotechnology **10**, 1 (2003).

[7] J. C. Meyer, A. K. Geim, M. Katsnelson, K. Novoselov, T. Booth, and S Roth, Nature **446**, 60 (2007).

[8] J. Meyer, A. Geim, M. Katsnelson, K. Novoselov, D. Obergfell, S. Roth, C. Girit, and A. Zettl, Solid State Communications **143**, 101 (2007).

[9] R. Haering, Canadian Journal of Physics **36**, 352 (1958).

[10] M. S. Dresselhaus, G. Dresselhaus, P. Eklund. Science of Fullerene and Carbon Nanotubes. Academic Press, New York (1996).

[11] R. Saito, G. Dresselhaus, M. S. Dresselhaus. Physical Properties of Carbon Nanotubes. Imperial College Press, London (1998).

[12] L. Forro and C. Schnonenberger, in "Carbon Nanotubes Synthesis, Structure, Properties and Applications" (M. S. Dresselghaus, G. Dresselhaus, and P. Avouris Eds.), p.329, Springer-verlag, Newyork, 2001.

[13] A. These, R. Lee, P. Nikolaev, H. J. Dai, P. Petit, J. Robert, C. H. Xu, Y. H. Lee, S. G. Kim, A. G. Rinzler, D.. T. Colbert, G. E. Scuseris, D. Tomanek, J. E. Fischer, and R. E. Smalley, Science **273**, 483 (1996).

[14] C. Schonenberger, A. Bachtold, C. Strunk, J. P. Salvetat, and L. Forro, Appl. Phys. A **69**, 283 (1999).

[15] W. A. De Heer and R. Martel, Phys. World 13, 49 (2000)

[16] Bhushan, B. Springer Handbook of Nanotechnology. Springer - Verlag. 2007.

[17] O'Connell, M. Carbon Nanotubes: Properties and Applications. CRC Press, Boca Raton, 2006.

[18] Geckelar K. E., and Rosenburg E., Functional Nanomaterials. American Scientific Publishers, California, 2006.

[19] E. W. Wong, P. E. Sheehann, and C. M. Lieber, Science **277**, 1971 (1997).

[20] M. F. Yu, O. Lourie, M. J. Dyer, K. Moloni, T. E. Kelly, and R. S. Ruoff, Science **287**, 637 (2000).

[21] M. F. Yu, B. S. Files, S. Arepalli, and R. S. Ruoff, Phys. Rev. Lett. **84**, 5552 (2000).

[22] Bates, H., Brand, O., Fedder, G., Hierold, C., Korvink, J., and Tabata, O. *Enabling Technology for MEMS and Nanodevices*. Weinheim, Germany, Wilely-VCH, 2004.

[23] "Properties of Stainless Steel". Australian Stainless Steel Development Association "Stainless Steel-17-7PH (Fe/Cr17/Ni 7) Material Information".

[24] W. D. J. Callister, Material Science and Engineering an introduction, (6^{th} ed. Wiley, New York 2003).

[25] S. Berber, Y. K. Kown, D. Tomanek, Phys. Rev. Lett. **84**, 4613 (2000).

[26] P. Kim, L. Shi, A. Majumdar, and P. L. MeEuen Phys. Rev. Lett. **87**, 215502 (2001).

[27] A. C. Dillon, K. M. Jones, T. A. Bekkedahl, C. H. Kiang, D. S. Bethune, and M. J. Heben, Nature **386**, 377 (1997).

[28] P. Chen, X Wu, J. Lin, and K. L. Tan, Science **285**, 91 (1999).

[29] R. H. Fowler and L. Nordheim, Proc. R. Soc. London Ser. A **119**, 173 (1928).

[30] T. M. Minea, S. Point, A. Granier, M. Touzeau, Appl. Phys. Lett. **85**, 1244 (2004).

[31] A. Javey, J. Guo, D. B. Farmr, Q. Wang, E. Yenilmez, R. G. Goprdon, M. Lundstrom, and H. Dai, Nano Lett. **4**, 1319 (2004).

[32] A. P. Graham, G. S. Duesberg, W. Hoenlein, F. Kreupl, M. Liebau, R. Martin, B. Rajasekharan, W. Pamler, R. Seidel, W. Steinhoegl, and E. Unger, Appl. Phys. A **80**, 1141 (2005).

[33] W. B. Choi, D. S. Chung, J. H. Kang, H.Y. Kim, Y. W. Jin, I. T. Han, Y. H. Lee, J. E. Jung, N. S. Lee, G. S. Park, and J. M. Kim, Appl. Phys. Lett. **75**, 3129 (1999).

[34] T. Guo, M. D. Diener, Y. Chai, M. J. Alford, R. E. Haufler, S. M. Mcclure, T. Ohno, J. H. Weaver, G. E. Scuseria, and R. E. Smalley, Science **257**, 1661 (1992).

[35] A. Thess, R. Lee, P. Nikolaev, H. J. Dai, P. Petit, J. Robert, C. Xu, Y. H. Lee, S. G. Kim, A. G. Rinzler, D. T. Colbert, G. E. Scuseria, D. Tomanek, J. E. Fischer, and R. E. Smalley, Science **273**, 483 (1996).

[36] K. Tanaka, T. Yamabe, and K. Fukui, *The Science and Technology of Carbon Nanotubes*. Elsevier, New York, 1999.

[37] A. A. Puretzky, D. B. Geohegan, X. Fan, and S. J. Pennycook, Appl. Phys. A **70**, 153 (2000).

[38] R. Sen, Y. Ohtsuka, T. Ishigaki, D. Kasuya, S. Suzuki, H. Kataura, and Y. Achiba, Chem. Phys. Lett. **332**, 467 (2000)

[39] F. Kokai, K. Takahashi, M. Yudasaka, and S. Iijima, J. Phys. Chem. B **104**, 6777 (2000).

[40] S. Bandow, S. Asaka, Y. Saito, A. M. Rao, L. Grigorian, E. Richter, and P. C. Eklund, Phys. Rev. Lett. **80**, 3779 (1998).

[41] H. Kataura, Y. Kumazawa, Y. Maniwa, Y. Ohtsuka, R. Sen, and S. Suzuki, Carbon **38**, 1691 (2000).

[42] H. Kataura, A. Kimura, Y. Ohtsuka, S. Suzuki, Y. Maniwa, T. Hanyu, and Y. Achiba, Jpn. J. Appl. Phys. Part 2 **37**, L616 (1998).

[43] O. Connell, M. *Carbon Nanotubes: Properties and Applications*. CRC Press, Boca Raton, 2006.

[44] M. P. A. T. Goswami, Materials & Design, **28**, 1477 (2007).

[45] G. B. Zheng, K. Kouda, H. Sano, Y. Uchiyama, Y. F. Shi, and H. J. Quan, Carbon **42**, 635 (2004).

[46] W. M. Merchan, A. V. Saveiliev, L. Kennedy, and W.C. Jimenez. Progress in Energy and Combustion Science **36**, 696 (2010).

[47] R. T. K. Baker, Carbon **27**, 315 (1989).

[48] M. Chhowalla, K B K Teo, C. Ducati, N. L. Rupesinghe, G. A. J. Amaratubga, A. C. Ferrari, D. Roy, J. Roberston, and W. I. Milne, J. Appl. Phys. **90**, 5308 (2001).

[49] S. S. Fan, M. G. Chapline, N. R. Franklin, T. W. Tombler, A. M. Cassell, and H. J. Dai, Science **283**, 512 (1999).

[50] C. Bower, O. Zhou, W. Zhu, D. J. Werder, and S. H. Jin, Appl. Phys. Lett. **77**, 2767 (2000).

[51] J. I. Sohn, S. Lee, Y. H. Song, S. Y. Choi, K. I. Cho, and K. S. Nam, Appl. Phys. Lett. **78**, 901 (2001).

[52] http://mrsec.wisc.edu/Edetc/SlideShow/slides/contents/nanotubes.html. [Accessed 30 04 2012].

[53] Z. B. He, J. –L. Maurice, C. S. Lee, A. Gohier, D. Pribat, P. Legagneux, and C. S. Cojocaru, Carbon **49**, 435 (2011).

[54] H. Dai, A. G. Rinzler, P. Nikolaev, A. Thess, D. T. Colbert, R. E. Smalley, Chem. Phys. Lett. **260**, 471 (1996)

[55] H. M. Cheng, F. Li, X. Sun, S. D. M. Brown, M. A. Pimenta, A. Marucci, G. Dreselhaus, and M. S. Dresselhaus, Chem. Phys. Lett. **289**, 602 (1998).

[56] B. C. Satish Kumar, A. Govindaraj, R. Sen, and C. N. R. Rao, Chem. Phys. Lett. **293**, 47 (1998).

[57] J. H. Hafner, M. J. Bronikowski, B. R. Azamian, P. Nikolaev, A. G. Rinzler, D. T. Colbert, K. A. Smith, and R. E. Smalley, Chem. Phys. Lett. **296**, 195 (1998).

[58] J. Kong, A. M. Cassell, and H. J. Dai, Chem. Phys. Lett. **292**, 567 (1998).

[59] E. Flahaut, A. Govindaraj, A. Peigney, C. Laurent, A. Rousset, and C. N. R. Rao, Chem. Phys. Lett. **300**, 236 (1999).

[60] V. I. Merkulov, A. V. Melechko, M. A. Guillorn, M. L. Simpson, D. H. Lowndes, J. H. Whealton, and R. J. Raridon, Appl. Phys. Lett. **80**, 4816 (2002).

[61] H. W. Wei, K. C. Leou, M. T. Wei, Y. Y. Lin, and C. H. Tsai, J. Appl. Phys. **98**, 044313 (2005).

[62] M. S. Bell, R. G. Lacerda, K. B. K. Teo, N. L. Rupesinghe, G. A. J. Amaratunga, W. I. Milne, M. Chhowalla, Appl. Phhys. Lett. **85**, 1137 (2004).

[63] S. Hofmann, C. Ducati, J. Robertson, B. Kleinsorge, Appl. Phys. Lett., **83**, 135 (2003).

[64] M. Cantoro, V. B. Golovkob, S. Hofmanna, D. R. Williamsa, C. Ducatic, J. Gengb, B. O. Boskovicc, B. Kleinsorgea, D. A. Jeffersonb, A. C. Ferraria, B. F. G. Johnsonb, J. Robertsona, Diamond Relat. Mater.**14**, 733 (2005).

[65] S. Hoffmann, C. Ducati, B. Kleinsorge, J. Robertson, Appl. Phys. Lett. **83,** 4661 (2003).

[66] S. Hofmann, M. Cantoro, M. Kaempgen, D. J. Kang, V. B. Golovko, H. W. Li, Z. Yang, J. Geng, W. T. S. Huck, B. F. G. Johnson, S. Roth, J. Robertson, Appl. Phys. A **81**, 1559 (2005).

[67] C. Bower, W. Zhu, S. Jin, O. Zhou, Appl. Phys. Lett. **77**, 830 (2000).

[68] H. Cui, O. Zhou, B. R. Stoner, J. Appl. Phys. **88**, 6072 (2000).

[69] L. Delzeit, I. McAninch, B. A. Cruden, D. Hash, B. Chen, J. Han, M. Meyyappan, J. Appl. Phys. **91**, 6027 (2002).

[70] K. Matthews, B. A. Cruden, B. Chen, M. Meyyappan, L. Delzeit, J. Nanosci. Nanotechnol. **2**, 475 (2002**)**.

[71] C. H. Weng, C. S. Yang, H. Lin, C. H. Tsai, K. C. Leou, J. Nanosci. Nanotechnol. **8**, 2526 (2008**)**.

[72] J. B. O. Caughman, L. R. Baylor, M. A. Guillorn, V. I. Merkulov, D. H. Lowndes, L. F. Allard, Appl. Phys. Lett. **83**, 1207 (2003**)**.

[73] Y. Y. Lin, H. W. Wei, K. C. Leou, H. Lin, C. H. Tung, M. T. Wei, C. Lin, C. H. Tsai, J. Vac. Sci. Technol. B **24**, 97 (2006**)**.

[74] Y. Shiratori, H. Hiraoka, Y. Takeuchi, S. Itoh, M. Yamamoto, Appl. Phys. Lett. **82**, 2485 (2003**)**.

[75] H. S. Kang, H. J. Yoon, C. O. Kim, J. P. Hong, I. T. Han, S. N. Cha, B. K. Song, J. E. Jung, N. S. Lee, J. M. Kim Chem, Phys. Lett. **349**, 196 (2001).

[76] B. G. Sumpter, V. Meunier, J. M. Romo-Herrera, E. Cruz-Silva, D. A. Cullen, H. Terrones, D. J. Smith, M. Terrones, ACS Nano **1**, 369 (2007).

[77] S. K. Srivastava, A. K. Shukla, V.D. Vankar, V. Kumar, Thin solid films, Thin solid films **492**, 124 (2005).

[78] M. Hiramatsu, M. Hori, *Carbon Nanowalls* (Springer, Vienna, 2010)

[79] F. Paschen, Ann. Phys. Chem. **273**, 69 (1889).

[80] Z. Bo, Y. Yang, J. Chen, K. Yu, J. Yan and K. Cen, Nanoscale **5**, 5180 (2013).

[81] M. Lieberman and A. Lichtenberg, Principles of Plasma Discharges and Materials Processing, John Wiley & Sons, Inc., New Jersey, 2005.

[82] H.Cui, X. Yang, M. L. Simpson, D. H. Lowndes, and M. Varela, Appl. Phys. Lett. **84**, 4077 (2004).

[83] C. S. Cojocaru, A. Senger, and F. L. Normand, J. Nanosci. Nanotechnol. **6**, 1 (2006).

[84] N. M. Rodriguez, J. Mater. Res. **8**, 3233 (1993).

[85] K. Ostrikov, and S. Xu, Plasma Aided Nanofabrication: From Plasma Sources to Nanoassembly (Wiley-VCH, Weinheim, Germany, 2007).

[86] I. Denysenko, N. A. Azarenkov, J. Phys, D: Appl. Phys. **44**, 174031 (2011).

[87] I. Denysenko, K. Ostrikov, J. Phys. D Appl. Phys. **42**, 015208 (2009).

[88] Z. Marvi, S. Xu, G. Foroutan, K. Ostrikov, Phys. Plasmas **22**, 013504 (2015).

[89] I. Denysenko, K. Ostrikov, Appl. Phys. Lett. **90**, 251501 (**2007)**.

[90] H. Mehdipour, K. Ostrikov, A. E. Rider, Nanotechnology **21**, 455605 (2010).

[91] I. Denysenko, K. Ostrikov, M. Y. Yu, N. A. Azarenkov, J. Appl. Phys.**102**, 074308 (2007).

[92] M. Cantoro, S. Hofmann, S. Pisana, C. Ducati, A. Parvez, A. C. Ferrari, and J. Robertson, Diamond Relat. Mater. **15**, 1029 (2006).

[93] S. Hofmann, M. Cantoro, B. Kleinsorge, C. Casiraghi, A. Parvez, J. Robertson, and C. Ducati, J. Appl. Phys. **98**, 034308 (2005).

[94] M. Yudasaka, R. Kikuchi, T. Matsui, Y. Ohki, S. Yoshimura, and E. Ota, Appl. Phys. Lett. **67** 2477 (1995).

[95] R. Loffler, M. Haffner, G. Visanesu, H. Weignad, X. Wang, D. Zhang, M. Fleischer, A. J. Meixner, J. Fortagh, and D. P. Kern, Carbon **49**, 4197 (2011).

[96] M. Dubosc, S. Casimirius, M. –P. Besland, C. Cardinaud, A. Granier, J. –L. Duvail, A. Gohier, T. Minea, V. Arnal, and J. Torres, Materials for Advanced Metallization **84**, 2501 (2007).

[97] D. Kim, S. H. Lim,, A. J. Guilley, C. S. Cojocaru, J. E. Bouree, L. Vila, J. H. Ryu, K. C. Park, and J. Jang, Thin Solid Films **516**, 706 (2008)

[98] S.-ichi Honda, M. Latayama, K. –Y Lee, T. Ikuno, S. Ohkura, K. Oura, H. Furuta, and Takashi, Jpn. J. Appl. Phys. **42**, L441 (2003).

[99] Y. S. Woo, D. Y. Jeon, I. T. Han, N. S. Lee, J. E. Jung, and J. M. Kim, Diamond Relat. Mater. **11**, 59 (2002).

[100] G. Zhang, D. Mann, L. Zhang, A. Javey, Y. Li, E. Yenilmez, Q. Wang, J. P. McVittie, J. Gibbons, and H. Dai, Proc. Natl. Acad. Sci. U.S.A **102**, 16141 (2005).

[101] Y. Kim, W. Song, S. Y. Lee, S. Shrestha, C. Jeon, W. C. Choi, M. Kim, and C. Y. Park, Jpn. J. Appl. Phys., Part **1 49**, 085101 (2010).

[102] S. C. Chang, T. C. Lin, T. S. Li, and S. H. Huang. Microelectron. J. **39** (2008) 1572.

[103] C. Yamabe, S. J. Buckman, and A. V. Phelps, Phys. Rev. A: At. Mol. Opt. Phys. **27**, 1345 (1983).

[104] K. Teii, S. Shimada, M. Nakashima and A. T. H. Chuang, J. Appl. Phys. **106**, 084303 (2009).

[105] Y. H. Wu, P. W. Qiao, T. C. Chong and Z. X. Shen, Adv. Mater. **114**, 64 (2002).

[106] B. B. Wang, S. Lee, X. Z. Xu, S. Choi, H. Yan, B. Zhang, and W. Hao, Applied surface science **236**, 6 (2004).

[107] W. Z. Li, J. G. Wen, Y. Tu, and Z. F. Ren, Appl. Phys. A **73**, 259 (2001).

[108] B. Ganjipour, S. Mohrajerzadeh, H. Hesamzadeh and A. Khodadadi, Fullerenes, nanotubes, and carbon nanostrcutures **13**, 365 (2005).

[109] C. L. Pint, N. Nicholas, S. T. Pheasant, J. G. Duque, A. N. G. P. Vasquez, G. Eres, M. Pasquali, and R. H. Hauge, J. Phys. Chem. C **112**, 14041 (2008).

[110] I. Hinkov, S. Farhat, and C. D. Scott, Carbon **43**, 2453 (2005).

[111] W. Z. Collison, T. Q. Ni, and M. S. Barnes, J. Vac. Sci. Technol. A **16**,100 (1998).

[112] S. C. Chang, T. C. Lin, C. Y. Pai, Microelectronics Journal **38,** 657 (2007).

[113] V. Krivchenko, P. Shevnin, A. Pilevsky, A. Egorov, N. Suetin, V. Sen, S. Evlashin and A. Rakhimov, J. Mater. Chem. **22**, 16458 (2012).

2

Plasma processing of the thin metal catalyst film

2.1 Brief outline of the chapter

In this chapter, an analytical model has been developed to describe the segregation of thin metal catalyst film into the many catalyst nanoparticles in the reactive plasma environment. The model incorporates the kinetics of the plasma species (charged and neutral species) and plasma processing of the thin film which includes the power balance at the film surface, physical sputtering of the catalyst film, and chemical etching of the catalyst film. The effect of plasma parameters and different plasma compositions (hydrogen plasma and hydrogen+nitrogen plasma) on the nucleation and growth of catalyst nanoparticle have been investigated.

2.2 Introduction

Plasma enhanced chemical vapor deposition (PECVD) is the commonly used technique to synthesize vertically aligned carbon nanostructures [1], in which graphitic structures are shaped from the disintegration of carbon-containing gases on the metallic catalyst nanoparticle surface [2].

Published work of the present chapter:

1. **Ravi Gupta,** Suresh C. Sharma, and Neha Gupta, Role of different etchants on the growth of catalyst nanoparticles during the plasma processing of the metal catalyst thin film, *Materials Today: Proceedings* **5,** 15416 (2018).
2. **Ravi Gupta,** Suresh C. Sharma, and Rinku Sharma, Mechanisms of plasma-assisted catalyzed growth of carbon nanofibres: A theoretical modeling, *Plasma Sources Sci. Technol.* **26**, 024006 (2017).
3. **Ravi Gupta,** Suresh C. Sharma, and Neha Gupta, Theoretical study to investigate the impact of plasma parameters on the catalyst nanoparticle growth, *IOP Conf. Series: Journal of Physics: Conf. Series* **1836**, 012024 (2017).

These catalyst nanoparticles act as the nucleation sites for the nucleation and growth of carbon nanostructures and can be formed on the substrate surface by plasma etching [3] or by thermal annealing [4] of pre-deposited thin metal catalyst film. The initial size of the catalyst nanoparticle influences the shape, alignment and crystalline structure of the nanostructure [5]. Amid plasma pre-treatment of the metal catalyst film, plasma parameters affect the catalyst particle size. Chang *et al.* [6] pre-treated the nickel catalyst thin film with hydrogen plasma to segregate it into nanoparticles and found that catalyst particle size decreases with increase in plasma power. Other than plasma parameters, plasma compositions also influence the growth characteristics of the catalyst particle. Yang *et al.* [7] utilized hydrogen, nitrogen and oxygen plasma for pretreatment and reported the formation of nickel nitride that can enhance the growth of nanostructures. Chang *et al.* [8] pre-treated catalyst film with hydrogen+nitrogen plasma and found that hydrogen+nitrogen proportion has giant impact on the morphology of the catalyst particle.

So far only thermodynamics based models are available to depict the size of the catalyst nanoparticle obtained from the thin catalyst film. In this chapter, we have devised the plasma based model to elucidate the growth mechanism of catalyst nanoparticle resulting from the etching and sputtering of the thin film in the reactive plasma, i.e., plasma treatment of the thin catalyst film.

2.3 Analytical model

An analytical model to explain the effect of plasma pre-treatment of the metal catalyst thin film on the growth of the catalyst nanoparticle has been developed. The present model considers the two different plasmas (i) hydrogen plasma and (ii) hydrogen+nitrogen plasma. The species considered in these plasma compositions are listed in Table 2.1. The electric field due to plasma sheath is assumed to be in vertically downward direction, i.e., from bulk plasma region to substrate surface. To determine the energies and fluxes of the plasma species the plasma sheath Eqs. (2.1)-(2.3) are taken into account [9,10].

$$\text{Continuity equation: } \left(\hat{i}\frac{\partial}{\partial x}+\hat{j}\frac{\partial}{\partial y}+\hat{k}\frac{\partial}{\partial z}\right).(n_{0k}\overrightarrow{v_{0k}}) = f_{0i}n_{0e}\ , \tag{2.1}$$

Ravi Gupta, Department of Applied Physics, Delhi Technological University, Delhi, India

Ion-Momentum balance equation: $M_{0k} n_{0k} v_{0k} \frac{dv_{0k}}{dz} = e n_{0k} E - M_{0k} n_{0k} f_{0kn} v_{0k}$, (2.2)

Poisson equation: $\frac{d^2\phi(x)}{dz^2} = -4\pi \sum q_{0k} \Omega_{0k} n_{0k}$, (2.3)

where k refers to either electron (e) or charged species, n_{0k}, M_{0k}, v_{0k}, q_{0k}, and f_{0i} are number density, mass, fluid velocity, charge, and ionization frequency of k^{th} species, respectively. E is the electric field, f_{0kn} is the collision frequency, Ω_{0k} is the k^{th} ion to electron number density ratio, ϕ is the electrostatic potential, $\sum_k \Omega_{0k} = 1$, and $0 < \Omega_{0k} < 1$.

Table 2.1. Species considered in the present model.

	Hydrogen plasma	Hydrogen+nitrogen plasma
Ionic species	H^+,	H^+, N^+
Neutral species	H	H, N

2.3.1 Balance equation of plasma species in the bulk plasma

$$\frac{\partial n_e}{\partial t} = \sum_j \beta_j n_j - \sum_j \alpha_j n_e n_{ij} - \gamma_e \frac{n_a}{\lambda_d} \left(I_{\text{ef}} \right), \quad (2.4)$$

$$\frac{\partial n_{ij}}{\partial t} = \beta_j n_j - \alpha_j n_e n_{ij} - \frac{n_a}{\lambda_d} \left(I_{ijf} \right), \quad (2.5)$$

$$\frac{\partial n_j}{\partial t} = \alpha_j n_e n_{ij} - \beta_j n_j + \frac{n_a}{\lambda_d} \left(1 - \gamma_{ij}\right) \left(I_{ijf} \right) - \frac{n_a}{\lambda_d} \gamma_j \left(I_{jf} \right) + IF_j - OF_j, \quad (2.6)$$

where n_e, n_j, and n_{ij} are the number density of electrons, neutrals, and ions, respectively in the bulk plasma (j refers to the ions or neutral species of hydrogen or nitrogen). I_{ef}, I_{ijf}, and I_{jf} are the collection currents at the metal catalyst film surface due to electrons, ions, and neutral species, respectively [11]. β_j is the coefficient of ionization of positively charged ions, α_j is the coefficient of recombination of positively charged ions and electrons, n_a is the surface concentration of catalyst nanoparticles, λ_d is the plasma sheath width. γ_e, γ_j, and γ_{ij} are the sticking coefficient of electrons, neutrals and ions,

Ravi Gupta, *Department of Applied Physics, Delhi Technological University, Delhi, India*

respectively. IF_j and OF_j are the inflow and outflow rates of the j^{th} species into/from the plasma chamber, respectively.

The Eq. (2.4) represents the rate of electron number density variation in the reactive plasma system on account of ionization of neutral atoms (first term), recombination of electrons and ions (second term), and electron collection current on the film surface (last term).

The Eq. (2.5) represents the rate of positively charged species number density variation in the reactive plasma due to ionization of neutral atoms (first term), electron-ion recombination (second term), and ion collection current at the film surface (last term).

The Eq. (2.6) is the particle balance equation for neutrals that represents the growth rate of neutral atom number density in the plasma system. First and third terms show the increase in growth rate of neutral density due to electron-ion recombination and neutralization of ions collected at the film surface, respectively. The second and fourth terms symbolize the decay rate of neutral density due to ionization and accumulation of neutrals on the film surface, respectively.

2.3.2 Plasma processing of the thin metal catalyst film

Catalyst nanoparticles are the nucleating seeds for the carbon nanostructure nucleation and growth. Their number density and size strongly influence the growth characteristics and resulting structure of the nanostructures. These nucleating seeds are formed by the plasma pre-treatment of the predeposited thin metal catalyst film over the silicon substrate. The heavy bombardment of plasma species (ions and neutrals) from dense plasma fragments the thin film into many nanoislands (nanoparticle). The morphological characteristics and number density of these nanoparticles strongly depend on plasma parameters and plasma compositions. The general power balance at the surface of the catalyst film placed over the silicon substrate in the presence of plasma is given by the following equation [12].

$$\dot{E}_{in} = \dot{E}_{gain} + \dot{E}_{loss}, \tag{2.7}$$

$$\dot{E}_{in} = A_f \sigma \left[\in_{env} (T_{env})^4 - \in_f (T_S)^4 \right] + \left[I_{ef} \varepsilon_e^f + \sum_j I_{ijf} \varepsilon_{ij}^f + \sum_j I_{jf} \varepsilon_j^f \right] + \frac{3}{2} k_B T_S \sum_j (1-\gamma_{ij}) I_{ijf}, \tag{2.8}$$

$$\dot{E}_{gain} = \frac{d}{dt}\left(m_f C_f T_S\right) = A_f C_f \rho_f \left[d_f \frac{dT_s}{dt} + T_s n_a \frac{d}{dt}\left(\frac{1}{6}\pi D^3\right)\right], \tag{2.9}$$

$$\dot{E}_{loss} = \sigma A_f \left(\in_f T_s^4 - \in_{env} T_{env}^4 \right) + \delta_{ef} (1-\gamma_e)\left(\varepsilon_{ef}^S - \frac{3}{2} k_B T_S \right) I_{ef} + \left[\upsilon_0 \sigma_{ads} U_B + y_d (E_i)(1-\theta_t) \sum_{ij} J_{ij} \right] A_f, \tag{2.10}$$

where $\dot{E}_{in}$, $\dot{E}_{gain}$ and $\dot{E}_{loss}$ are the total input plasma power, power gained, and power loss during plasma pre-treatment, respectively. A_f is the area of the metal catalyst film, $\sigma\left(=5.67\times10^{-5} \text{ ergs cm}^{-2} \text{ s}^{-1} \text{ K}^{-4}\right)$ is the Stefan's constant, $\in_{env} (\approx 1)$ is the emissivity of the environment, $\in_f$ (=0.12 for Nickel) is the emissivity of the material of the metal catalyst film, T_S is the substrate temperature, T_{env} is the temperature of the plasma environment, ε_e^f, ε_{ij}^f, and ε_j^f are the mean energies collected by metal catalyst film surface due to electrons, ions, and neutral atoms, respectively [13] and given by $\varepsilon_k^f = \left[\left(\frac{2-Z\gamma_k}{1-Z\gamma_k}\right) - Z\gamma_k\right] k_B T_k$ and $\gamma_k = \frac{E_b}{k_B T_k}$, where *k* can be ion, electron or neutral atom. E_b is the energy barrier at the catalyst film surface, m_f is the mass of the catalyst film, d_f is the thickness of the film, $C_f \left(= 0.104 \text{ cal g}^{-1}\ {}^0C^{-1}\right)$ is the specific heat of the film, ρ_f is the density of catalyst film material, *D* is the diameter of the catalyst nanoparticle, $\delta_{ef} = 2\left(m_e / m_f\right)$ is the fraction of energy lost during the collision with film, $\varepsilon_{ef}^S \left(= 2k_B T_e\right)$ is the mean energy of electrons collected by the surface film [13],

***Ravi Gupta**, Department of Applied Physics, Delhi Technological University, Delhi, India*

υ_0 is the number of sites available, $\sigma_{ads}\left(=6.8\times10^{-16}\ \text{cm}^2\right)$ is the cross section for the reaction of atomic hydrogen [14], $J_j = n_j\left(k_BT_j/m_j\right)^{1/2}$ is the neutral atom flux, $J_{ij} = n_{ij}\left(k_BT_e/m_{ij}\right)^{1/2}$ is the ion flux [15], U_B (= 3.74 eV for the nickel) is the surface binding energy of the material (sputter target), y_d is the sputtering yield [16], and θ_t is the total surface coverage.

The Eq. (2.7) represents the power equalization over the film surface during plasma processing the thin metal catalyst film. The first term of the Eq. (2.8) denotes the input energy per unit time towards the film surface due to the heat radiation per unit time towards the surface of the film from the surrounding, the second term represents the energy per unit time collected by the film surface due to electrons, ions and neutral atoms, and the last term is the energy received per unit time due to the formation of neutrals at the film surface.

The Eq. (2.9) represents the power gained during the nanostructuring of the thin film. The applied plasma power fragments the catalyst film into the catalyst nanoparticles [17]. During this plasma treatment, the temperature of the substrate increases and attains the constant value after some time [18]. Similarly to the power input, various processes contribute to the power loss (power out) during plasma pre-treatment of the catalyst film. The first term of Eq. (2.10) represents the radiative energy per unit time from the surface to the surrounding. The remaining terms denote the energy loss due to sticking and elastic collision of electrons with the surface, energy loss due to chemical etching, and physical sputtering of the thin metal catalyst film [19], respectively. The surface concentration of the catalyst particle can be evaluated using the mass conservation of the catalyst film and catalyst nanoparticles.

2.4 Results and discussion

This plasma-based model correlates the thickness of the film, plasma parameters, diameter and number density of the catalyst nanoparticles. With the

Ravi Gupta, Department of Applied Physics, Delhi Technological University, Delhi, India

aid of Mathematica software, we have solved the first order differential equations simultaneously for the default set of glow discharge parameters and initial conditions listed in Table 2.2 and Table 2.3.

Table 2.2. Parameters used in the present model.

Parameter	Description	Initial Value
T_{e0}	Electron temperature	1.7 eV
T_{i0}	Ion temperature	2200 K
T_{n0}	Neutral temperature	2000 K
T_S	Substrate temperature	410 ^{0}C
m_{ij}	Mass of ion ≈mass of neutral	
	$H^+ \approx H$	1 amu
	$H_2^+ \approx H_2$	2 amu
	$N^+ \approx N$	7 amu
	$N_2^+ \approx N_2$	14 amu
ρ_{ct}	Density of catalyst Cu	8.96 g/cm^3
α_{j0}	Coefficient of recombination of electrons and ions	1.12×10^{-7} cm^3/sec
A_f	Area of the catalyst film	1 cm^2
$\dot{E}_{in}$	Input plasma power	80 W
d_f	Thickness of the catalyst film	10 nm
γ_e	Sticking coefficient of electrons	1
γ_{ij}	Sticking coefficient of ions	1
γ_j	Sticking coefficient of neutrals	1

Table 2.3. Initial number density of the various plasma species used in the present model.

Species	Plasma compositions	
	Hydrogen plasma	**Hydrogen+ nitrogen plasma**
e$^-$	10^{11} cm^{-3}	10^{11} cm^{-3}
H$^+$	10^{11} cm^{-3}	0.6×10^{11} cm^{-3}
H	10^{13} cm^{-3}	10^{13} cm^{-3}
N$^+$		0.2×10^{11} cm^{-3}
N		0.35×10^{13} cm^{-3}

Figure 2.1 illustrates the time evolution of catalyst nanoparticle size (diameter) obtained from the thin catalyst film for different hydrogen ion number density. From Fig. 2.1, it can be seen that the size of the catalyst nanoparticles increases with time and attains saturation value when film gets completely transformed into the catalyst nanoparticles. This figure also indicates the decrease in catalyst nanoparticle size with increase in hydrogen ion number density. This is attributable to the fact that on increasing the hydrogen ion number density, the heavy ion bombardment on the catalyst film surface takes place which in turn increases the effective etching and sputtering of the film surface, and consequently, results in smaller catalyst nanoparticle size.

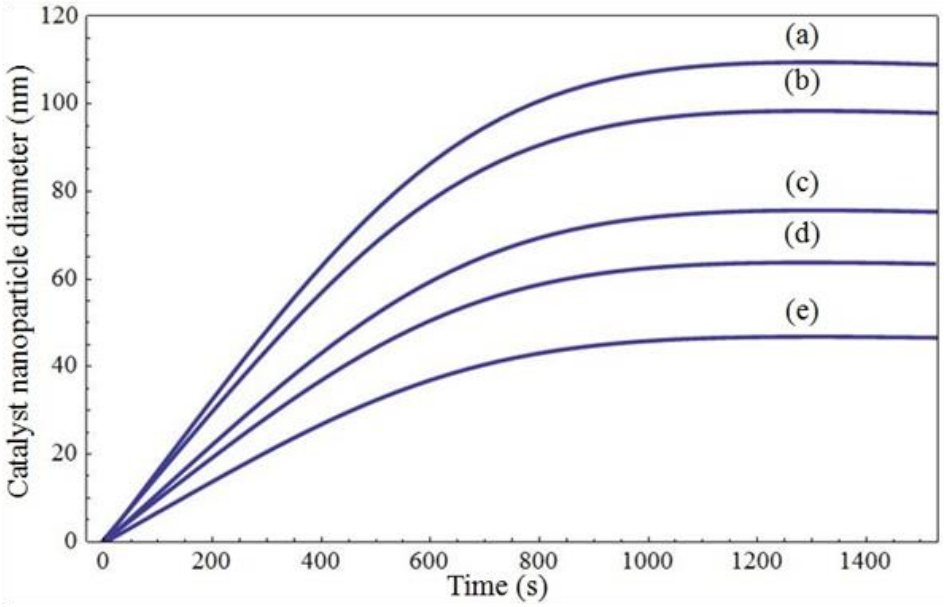

Fig. 2.1. Time variation of the catalyst nanoparticle diameter with time for different hydrogen ion number densities (where a, b, c, d and e corresponds to $n_e = n_{ij0} = 10^{11}$, 10^{12}, 10^{13}, 10^{14}, 10^{15} cm^{-3}, respectively).

The Fig. 2.2 shows variation of catalyst nanoparticle diameter with plasma power. As plasma power increases, the catalyst nanoparticle diameter decreases. This is because with increase in input plasma power, highly energetic plasma species (electrons, ions, and neutrals) are created in the reactive plasma which ultimately leads to higher etching and sputtering of the catalyst thin film resulting in the lesser catalyst nanoparticle diameter. Srivastava *et al.* [18] claimed that on increasing the plasma power, the density of the energetic plasma species increases. In this chapter, we devised a model to relate the density of plasma species with input plasma power during plasma processing of thin

catalyst film. Thus, the theoretical findings of Figs. 2.1 & 2.2 are in compliance with the experimental observations of Chang *et al.* [6], Srivastava *et al.* [18], and Abdi *et al.* [20].

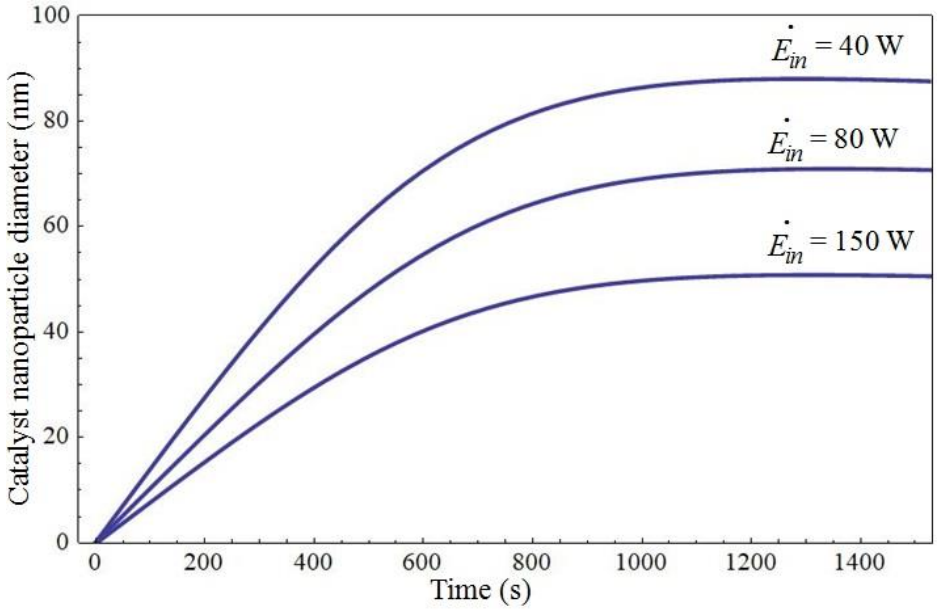

Fig. 2.2. Time variation of the catalyst nanoparticle diameter with time for different input plasma power.

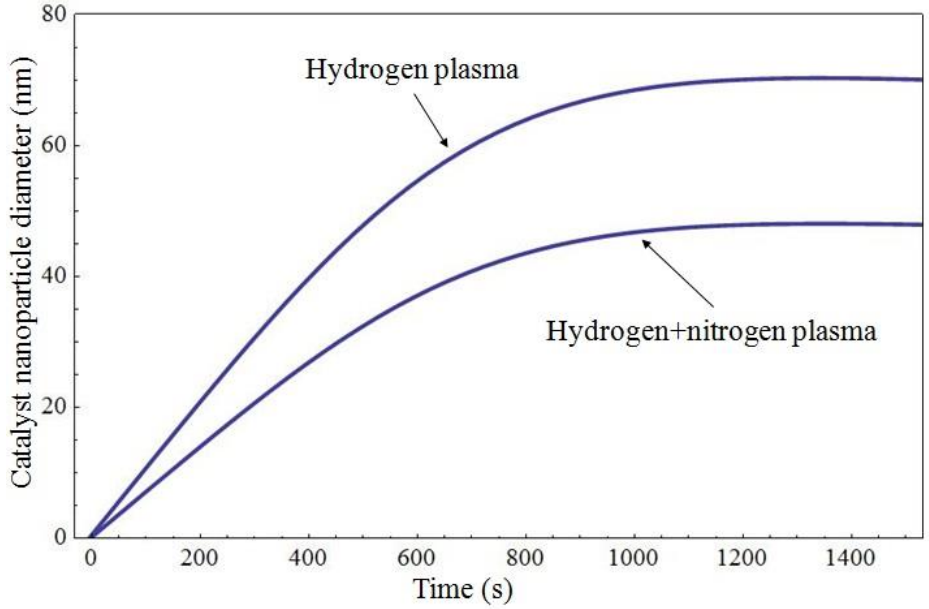

Fig. 2.3. Time variation of catalyst nanoparticle diameter for two different plasmas, i.e., hydrogen plasma and hydrogen + nitrogen plasma.

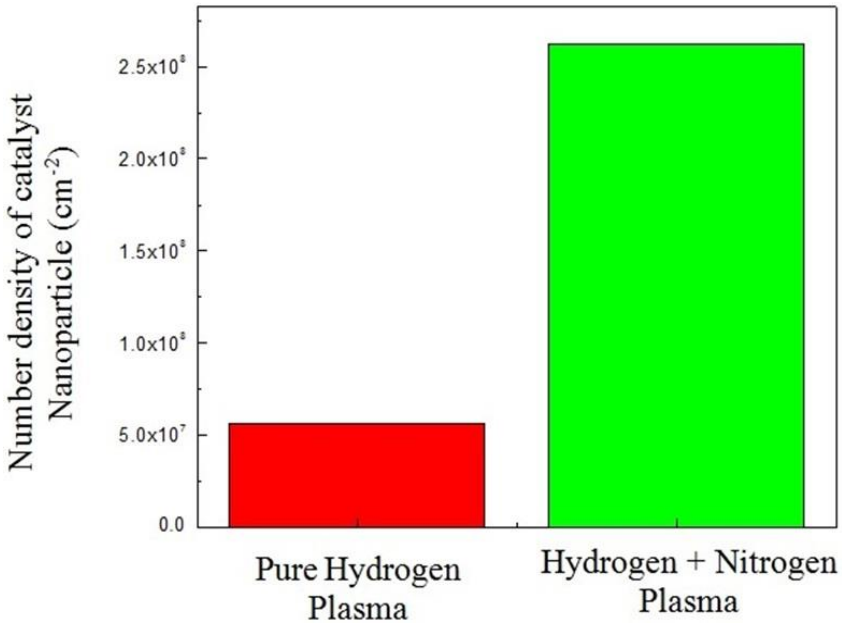

Fig. 2.4. Surface concentration of the catalyst nanoparticles for two different plasmas, i.e., hydrogen plasma and hydrogen + nitrogen plasma.

Figure 2.3 shows the time advancement of catalyst particle diameter obtained from plasma pre-treatment for two different plasma compositions. From Fig. 2.3, it can be seen that one can obtain lesser particle size when hydrogen + nitrogen plasma is utilized contrasted to the pure hydrogen plasma. This is imputable to the fact that nitrogen is more massive than hydrogen and also acts as the etching agent which leads to the higher etching and sputtering of the catalyst film and results in the lesser particle size. The Fig. 2.4 represents that number of catalyst particles per unit area increases when nitrogen is introduced in the pre-treatment process. This can be clarified in the way that particles with lesser diameters are formed when hydrogen+nitrogen plasma is used (cf. Fig. 2.3) and consequently, more particles are formed. These theoretical findings comply with the experimental observations of Chang *et al.* [8].

The Fig. 2.5 shows the temporal variation of substrate temperature during the plasma pre-treatment of the thin catalyst film. The substrate temperature increases during the plasma treatment and achieves the saturation after sometime. The highly energetic plasma species transfer their energy to the film surface during the bombardment and collision processes with the film surface and thus, increase the film surface/substrate temperature. These

theoretical findings are in good agreement with the experimental observations of Srivastava *et al.* [18] and Poa *et al.* [21].

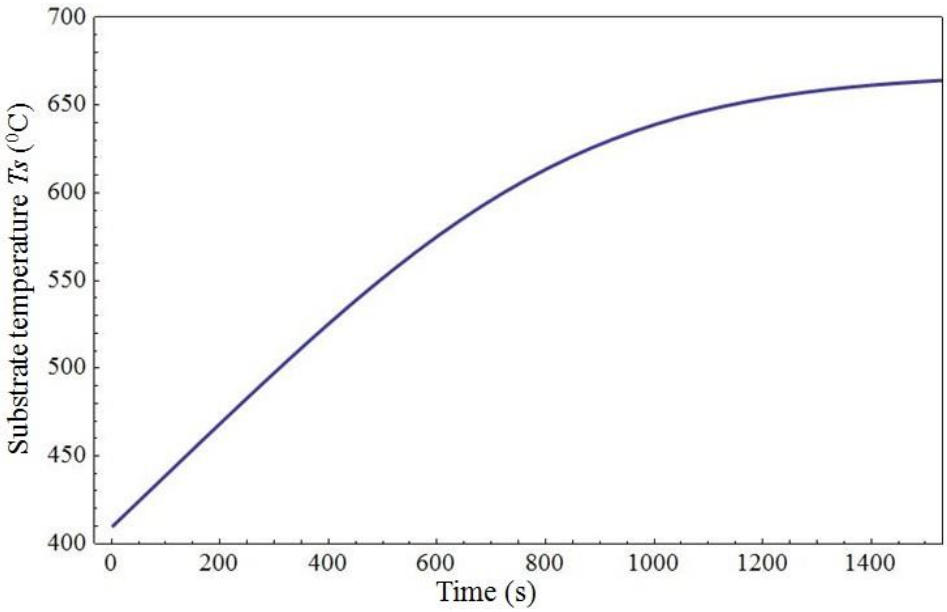

Fig. 2.5. Time variation of substrate temperature during the plasma processing (plasma treatment) of the thin catalyst film in the plasma containing electrons and ions, and neutrals of hydrogen.

References

[1] P. Nath and P.K. Sarker, Constr. Build. Mater. **66,** 163 (2014).

[2] N. M. Rodriguez, J. Mater. Res. **8**, 3233 (1933).

[3] M. Yudasaka, R. Kikuchi, T. Matsui, Y. Ohki, S. Yoshimura, and E. Ota, Appl. Phys. Lett. **67,** 2477 (1995).

[4] C. H. P. Pao, S. J. Henley, G. Y. Chen, A. A. D. T. Adikaari, G. E. Giusca, and S. R. P. Silvaa, J. Appl. Phys. **97**, 114308 (2005).

[5] R. T. Yang and J. P. Chen, J. Catal. **115**, 52 (1989).

[6] S. C. Chang, T. C. Lin, and C. Y. Pai, Microelectron. J. **38**, 657 (2007).

[7] D. J. Yang, Q. Zhang, and S. F. Yoon, Surf. Coat. Technol. **167**, 288 (2003).

[8] S. C. Chang, T. C. Lin, T. S. Li, and S. H. Huang, Microelectron. J.**39**, 1572 (2008).

[9] H. Mehdipour, K. Ostrikov, and A. E. Rider, Nanotechnology **21**, 455605 (2010).

[10] M. A. Lieberman, and A. J. Lichtenberg, *Principles of Plasma Discharges and Material Processing* (Wiley Interscience Publication, USA, 1994).

[11] S. C. Sharma and N. Gupta, Phys. Plasmas **22**, 123517 (2015).

[12] H. Kersten, H. Deutsch, H. Steffen, G. M. W. Kroesen, and R. Hippler, Vacuum **63,** 385 (2001).

[13] M. S. Sodha and S. Guha, A. Simon, and W. B. Thomson, *Physics of Colloidal Plasmas* (John Wiley & Sons, New York, pp. 219, 1971).

[14] I. Denysenko and K. Ostrikov, J. Phys. D: Appl. Phys. **42,** 015208 **(**2009).

[15] S. Hofmann, G. Csanyi, A. C. Ferrari, M. C. Payne, and J. Robertson, Phys. Rev. Lett. **95**, 036101 (2005).

[16] R. T. K. Baker, M. A. Barber, R. J. Waite, P. S. Harris, and F. S. Feates, J. Catal. **26**, 51 (1972).

[17] H. Cui, X. Yang, M. L. Simpson, D. H. Lowndes, and M. Varela, Appl. Phys. Lett. **84**, 20 (2004).

[18] S. K. Srivastava, A. K. Shukla, V. D. Vankar, and V. Kumar, Thin Solid Films. **492**, 12 (2005).

[19] N. V. Mantzaris and E. Gogolides, J. Appl. Phys. **79**, 3718 (1996).

[20] Y. Abdi, E. Arzi, and S. Mohajerzadeh, Eur. Phys. J. Appl. Phys. **44**, 149 (2008).

[21] C. H. P. Poa, S. J. Henley, G. Y. Chen, A. A. D. T. Adikaari, C. E. Giusca, and S. R. P. Silva, J.Appl. Phys. **97,** 114308 (2005).

3

Mechanisms of plasma-assisted catalyzed growth of carbon nanofibers: A theoretical modeling

3.1 Brief outline of the chapter

In the present chapter, we try to provide the in-depth study of nucleation and the deterministic growth of vertically aligned carbon nanofibers (VACNFs) accounting the plasma sheath effects, kinetics of plasma species (electrons, ions, and neutrals), adsorption and dissociation of the hydrocarbon species over the catalyst surface via various complex processes, and growth of CNF in the plasma environment. In particular, we solve the simultaneous coupled kinetic equations to analyze the effect of plasma species on the size of the catalyst nanoparticle and the growth of carbon nanofiber.

3.2 Introduction

The growth of carbon nanofibers (CNFs), carbon nanotubes (CNTs) and related carbon nanostructures have gained heightened research and commercial interest for the last few decades. It has been observed that nanostructures produced via plasma based processes exhibit various miraculous electrical, physical and optical properties and, as a result, applications in electronics specially field emission devices [1-3], mechanics, biochemistry and several others [4].

Published work of the present chapter:

1. **Ravi Gupta,** Suresh C. Sharma, and Rinku Sharma, Mechanisms of plasma-assisted catalyzed growth of carbon nanofibres: A theoretical modeling, *Plasma Sources Sci. Technol.* **26**, 024006 (2017).
2. **Ravi Gupta**, Suresh C. Sharma, and Neha Gupta, Role of etchant on the morphology of plasma grown carbon nanofibers: Theoretical modeling, 44th EPS Conference on Plasma Physics P2.304 (2017).

The orientation of graphite basal planes with respect to the growth axis characterizes the divergence between CNFs and CNTs, and dictates their properties. The CNFs are composed of graphitic funnels whereas concentric cylinders exist in CNTs [5]. In general, graphitic planes are aligned along the growth axis in CNTs, i.e., inclination angle $\theta = 0$ and are inclined at some non-zero angle to the growth axis in the case of CNFs. Diameter, height, shape and orientation of the vertically aligned carbon nanofibers (VACNFs) must be externally controlled for various practical applications [6-7]. The low temperature plasma enhanced chemical vapor deposition technique favours the disciplined growth of VACNFs as several parameters, such as ions, neutrals, and electrons fluxes from the plasma, plasma power, gas mixture ratio in plasma, and temperature have intense effect on the VACNFs growth [5, 8-10].

3.3 Analytical model

The present model considers the following scenario towards elucidating the nucleation and the growth mechanism of carbon nanofibers in the plasma.

I. The pre-etching of catalyst film in the presence of plasma segregates the catalyst film into discrete islands (nanoparticles) [11]. These catalyst nanoparticles act as the fundamental sites for the nucleation and growth of CNFs. The initial geometry of catalyst nanoparticle can greatly affect the configuration of resulting carbon nanostructure [12].

II. Carbon precursors i.e., hydrocarbon gases and hydrogen are adsorbed and decomposed via various processes on the catalyst nanoparticle surface to produce carbon species and active hydrogen radicals. These carbon species dissolve and diffuse (surface as well as bulk) through catalyst nanoparticles and ultimately precipitate at the rear of the catalyst nanoparticle to form carbon nanofiber [13-14].

III. Following this carbon precipitation, graphene layers form around the catalyst nanoparticle. These growing graphene layers exert significant stress on the catalyst particle resulting in the deformation of its shape [15].

IV. The carbon nanofiber grows vertically due to alignment force induced by electric field provided by the plasma sheath [16].

Including these elementary processes, we have developed the theoretical model considering the reactive plasma of $Ar + H_2 + C_2H_2$ gas mixture containing electrons, positively charged ions of acetylene ($C_2H_2^+$) and hydrogen (H^+) denoted as ions of type 1 and 2, respectively, and neutrals of acetylene C_2H_2 (type 1) and hydrogen H (type 2), nickel (Ni) catalyst film placed over silicon (Si) substrate surface and the sheath configuration near the substrate surface. The electric field within the sheath is assumed along the z- direction. Following Tewari and Sharma [17], Mehdipour *et al.* [18], and Lieberman *et al.* [19], the equations to investigate the sheath kinetics are

$$\text{Continuity equation: } \left(\hat{i}\frac{\partial}{\partial x}+\hat{j}\frac{\partial}{\partial y}+\hat{k}\frac{\partial}{\partial z}\right).(n_{0k}\overrightarrow{v_{0k}}) = f_{0i}n_{0e}\ , \tag{3.1}$$

$$\text{Ion-Momentum balance equation: } M_{0k}n_{0k}v_{0k}\frac{dv_{0k}}{dz} = en_{0k}E - M_{0k}n_{0k}f_{0kn}v_{0k}, \tag{3.2}$$

$$\text{Poisson equation: } \frac{d^2\phi(x)}{dz^2} = -\,4\pi\sum q_{0k}\Omega_{0k}n_{0k}, \tag{3.3}$$

where k refers to either electron, $C_2H_2^+$ or H^+, n_{0k} is their number density, M_{0k} is their mass in plasma, v_{0k} is their fluid velocity, f_{0i} is the ionization frequency, E is the electric field, f_{0kn} is the collision frequency, Ω_{0k} is the k^{th} ion to electron number density ratio, q_{0k} is the charge of the species, ϕ is the electrostatic potential, $\sum_k \Omega_{0k} = 1$, and $0 < \Omega_{0k} < 1$.

3.3.1 Charging of the CNF

The Eq. (3.4) describes the charge developed on the CNF surface due to accretion of positively charged ions and electrons on the surface of the CNF. The effects of collisional processes and dissipative losses have not been accounted in this equation since plasmas are considered here to be thermodynamically open systems [20, 21].

$$\dot{q} = \sum_{j=1}^{2} \left(I_{ij}\right)_{tip} + \sum_{j=1}^{2} \left(I_{ij}\right)_{cur} - \gamma_e \left[\left(I_e\right)_{tip} + \left(I_e\right)_{cur} \right] \tag{3.4}$$

where q is the charge over the whole CNF including tip as well as curved surface which can be expressed as q = Ze, where Z is the charge number and e is the electronic charge. For negatively charged nanoparticles/nanostructures, Z may vary from -1 to -100. $(I_{ij})_{tip}$ and $(I_{ij})_{cur}$ are the ion collection currents at the tip and curved surface of the CNF and given by,

$$\left(I_{ij}\right)_{tip} = \frac{\pi d^2}{4} \left(\frac{8 k_B T_{ij}}{\pi m_{ij}} \right)^{1/2} n_{ij}(x)[1 - q\alpha_i] \exp\left[\frac{-E_b}{k_B T_S} \right] \exp\left[\frac{-eU_S}{k_B T_S} \right], \tag{3.5}$$

$$\left(I_{ij}\right)_{cur} = n_{ij}(x) \frac{d \times h}{2} \left(\frac{2\pi k_B T_{ij}}{m_{ij}} \right)^{1/2} \times \left\{ \frac{2}{\sqrt{\pi}} \left(\frac{eV_s}{k_B T_{ij}} \right)^{1/2} + \exp\left[\frac{eV_s}{k_B T_{ij}} \right] erfc\left[\left(\frac{eV_s}{k_B T_{ij}} \right)^{\frac{1}{2}} \right] \right\}$$
$$\times \exp\left[\frac{-E_b}{k_B T_s} \right] \exp\left[\frac{-eU_s}{k_B T_s} \right], \tag{3.6}$$

where d is the diameter of the CNF tip, h is the height of the CNF, T_{ij} is the ion temperature, m_{ij} is the mass of ion (subscript j refers to 1 or 2 type of positively charged ion species as explained earlier), k_B is the Boltzmann constant, $\alpha_i = \left(\frac{2e^2}{d\ k_B T_s} \right)$, V_S is the surface potential of the curved surface of the CNF, U_S is the substrate bias, E_b is the energy barrier for bulk diffusion, T_S is the substrate or catalyst nanoparticle temperature, $n_{ij}(x) = n_{ij0}\left(1 - \frac{2e\phi(x)}{m_{ij} v_{i0}^2}\right)^{-1/2}$ is the ion density in the plasma sheath; $\phi(x)$ is the electrostatic potential; n_{ij0} is the initial ion density in plasma sheath; v_{i0} is the ion velocity at any point within the plasma and $\phi(x) = \phi_0 \exp\left(-\frac{|x|}{\lambda_d}\right)$; ϕ_0 is the negative potential at the surface; $\lambda_d = \sqrt{\frac{k_B T_e}{n_e e^2}}$ is the Debye length. $(I_e)_{tip}$ and $(I_e)_{cur}$ are the electron collection currents at the tip and curved surface of the CNF and given by,

$$(I_e)_{tip} = \pi \frac{d^2}{4}\left(\frac{8k_B T_e}{\pi m_e}\right)^{1/2} n_e(x)\exp\left[q\alpha_e + \frac{eU_S}{k_B T_S}\right], \quad (3.7)$$

$$\left(I_e\right)_{cur} = n_e(x)\frac{d}{2}h\left(\frac{2\pi k_B T_e}{m_e}\right)^{1/2} \exp\left[\frac{eV_S}{k_B T_e} + \frac{eU_S}{k_B T_S}\right], \quad (3.8)$$

where $n_e(x) = n_{e0}\exp\left[\frac{|e|\phi(x)}{k_B T_e}\right]$ is the electron density in plasma sheath, n_{e0} is the initial electron density in plasma sheath, T_e is the electron temperature, m_e is the mass of an electron, $\alpha_e = \left(\frac{2e^2}{d\ k_B T_e}\right)$, and γ_e is the sticking coefficient of electrons which describes the probability of electrons adsorption to a surface i.e., ratio of number of electrons adsorb to a surface to the number of electrons impinge upon the surface [22].

3.3.2 Particle balance equations for various plasma species

$$\dot{n_e} = \sum_{j=1}^{2}\beta_j n_j - \sum_{j=1}^{2}\alpha_j n_e n_{ij} - \gamma_e n_{cnf}\left[(I_e)_{tip} + (I_e)_{cur}\right], \quad (3.9)$$

$$\dot{n_{i1}} = \beta_1 n_1 - \alpha_1 n_e n_{i1} - n_{cnf}\left[(I_{i1})_{tip} + (I_{i1})_{cur}\right] - J_{ai1} + J_{desp1}\ , \quad (3.10)$$

$$\dot{n_{i2}} = \beta_2 n_2 - \alpha_2 n_e n_{i2} - n_{cnf}\left[(I_{i2})_{tip} + (I_{i2})_{cur}\right] - J_{ai2} + J_{desp2} + J_{thd}\ , \quad (3.11)$$

$$\dot{n_j} = \alpha_j n_e n_{ij} - \beta_j n_j + n_{cnf}\left(1-\gamma_{ij}\right)\left[\left(I_{ij}\right)_{tip} + \left(I_{ij}\right)_{cur}\right] - n_{cnf}\gamma_j\left[\left(I_j\right)_{tip} + \left(I_j\right)_{cur}\right], \quad (3.12)$$

where β_j is the coefficient of ionization of the constituent neutral atoms due to external field, n_j is the number density of neutral atom, n_e is the electron number density, n_{ij} is the ion number density, $\alpha_j(T_e) = \alpha_{j0}\left(\frac{300}{T_e}\right)^k cm^3/\sec$ is the coefficient of recombination of electrons and positively charged ions, $k = -1.2$ is a constant, γ_{ij} is the ion sticking coefficient, γ_j is the sticking

coefficient of neutral atoms, and j refers to either 1 or 2 type of positively charged ions and neutrals. $J_{aij} = \frac{p_i}{(2\pi m_{ij} k_B T_{ij})^{1/2}} \times \frac{n_{ij}}{j_{ij}}$ is the adsorption flux onto the catalyst substrate surface, p_i is the partial pressure of adsorbing species, $J_{desp} = j_{ij} \nu \exp\left(-\frac{\varepsilon_{ai}}{k_B T_{ij}}\right)$ is the desorption flux from the catalyst-substrate surface, ε_{ai} is the adsorption energy, j_{ij} is the ion flux on the catalyst substrate surface, ν is the thermal vibrational frequency $J_{thd} = j_H \nu \exp\left(\frac{-\delta\varepsilon_{th}}{k_B T_s}\right)$ is the flux of type 2 ion (namely hydrogen) on account of thermal dehydrogenation, $\delta\varepsilon_{th}$ is the activation energy of thermal dehydrogenation, j_H is the hydrogen ion flux at catalyst-substrate surface [17]. $(I_j)_{tip}$ and $(I_j)_{cur}$ are neutral collection current at the tip and curved surface of the CNF and given by:

$$\left(I_j\right)_{tip} = n_j(x)\pi \frac{d^2}{4}\left(\frac{8k_B T_j}{\pi m_j}\right)^{1/2}, \tag{3.13}$$

$$\left(I_j\right)_{cur} = n_j(x)\pi \frac{d}{2} h\left(\frac{2\pi k_B T_j}{m_j}\right)^{1/2}, \tag{3.14}$$

where T_j is the neutral atom temperature and m_j is the mass of the neutral atom.

Equation (3.9) indicates the balance of electron number density in the plasma system on account of ionization of neutral atoms, recombination of electrons and ions, and electron collection current on the CNF surface. The first term on the right-hand side of Eq. (3.9) refers to the gain in electron density per unit time due to ionization of neutral atoms; second and third terms represent the rate of decrease of electron density due to electron-ion recombination and electron collection current at the CNF surface, respectively.

Equations (3.10) and (3.11) describe the balance of positively charged ion species in the plasma system due to ionization of neutral atoms, electron-ion recombination, ion collection current at the surface of CNF, their adsorption, desorption, and thermal dehydrogenation. The first term on the right hand side describes the gain in ion density per unit time on account of ionization of neutral atoms. The second and the third terms represent the rate of decrease in positively charged ion density due to electron-ion recombination and ion collection current at the surface of the CNF (tip as well as curved surface), respectively. The fourth and fifth terms indicate adsorption and desorption of ions to/from the catalyst-substrate surface, respectively. One additional term in Eq. (3.11), i.e., the last term represents the increase of hydrogen ion number density in plasma because of thermal dehydrogenation of hydrocarbon ions since at temperature (> 400 K), dehydrogenation process (removal of hydrogen) becomes possibly an important factor [23, 24].

Equation (3.12) is the particle balance equation for neutrals of type 1 and 2 which indicates the growth rate of neutral atom number density. First and third terms show the increase in growth rate of neutral density due to electron-ion recombination and neutralization of ions collected at the surface of CNF, respectively. The second and fourth terms symbolize the decay rate of neutral density due to ionization and accumulation of neutrals on the surface of CNF, respectively.

3.3.3 Growth rate equation of the carbon species generated over the catalyst surface

$$\dot{n}_C = J_1(1-\theta_t) + 2n_{C_2H_2}\upsilon\exp\left(\frac{-\delta E_i}{k_B T_S}\right) + \frac{2n_{C_2H_2}J_{i1}y_d}{\upsilon_0} + \frac{J_C}{\pi D} - \frac{J_2\sigma_{ads}J_H}{\upsilon} - n_{C_2H_2}\upsilon\exp\left(\frac{-\delta E_i}{k_B T_S}\right) - \frac{J_{i1}\sigma_{ads}J_{i2}}{\upsilon}, \quad (3.15)$$

where n_C is the number of carbon species per unit area generated on the catalyst surface, $\sigma_{ads}\left(=6.8\times10^{-16}\ \mathrm{cm}^2\right)$ is the cross section for the reaction of

atomic hydrogen [31], $J_j = n_j\left(k_BT_j/m_j\right)^{1/2}$ is the neutral atom flux, $J_{ij} = n_{ij}\left(k_BT_{ij}/m_{ij}\right)^{1/2}$ is the hydrogen ion flux [23], $J_\alpha = \left(n_\alpha v_{th\alpha}/4\right)$ is the flux of impinging species (where $\alpha = C,H$) [23], $n_{C_2H_2} = \theta_{C_2H_2}\upsilon_0$ is the number density per unit area of C_2H_2 radicals [23], $\upsilon_0\left(=1.3\times10^{15}\ \text{cm}^{-2}\right)$ is the number of adsorption sites per unit area [23], and $\delta E_i\left(=1.87\ \text{eV}\right)$ is the thermal energy barrier.

The Eq. (3.15) describes the generation of carbon species per unit area on the catalyst surface via various complex processes such as adsorption of hydrocarbons (first term), thermal dissociation of hydrocarbons (second term), ion induced dissociation of hydrocarbons (third term), and the direct carbon flux towards catalyst surface (fourth term) [23]. The Eq. (3.15) also includes the processes which are responsible for the carbon loss from the catalyst surface. These processes are; loss of carbon due to interaction of neutral hydrocarbons with the neutral hydrogen (fifth term), carbon evaporation (sixth term), and ion-ion recombination (last term), i.e., hydrocarbon ion and hydrogen ion recombination [23].

3.3.4 Growth rate equation of carbon nanofibers

$$\frac{d}{dt}\left[\pi\left(D^2-d^2\right)h\right] = \left[\frac{D_S n_C\times\left(\pi D^2\right)}{\upsilon\times\left(\pi D\right)} + \frac{D_b n_C\times\pi D}{2\upsilon} + 4kn_C\times\pi D^2\right]\times\left(\frac{p}{\rho_{cnf}I_{i1}}\right)$$
$$+ J_2\left(1-\theta_t\right) + J_2\exp\left(\frac{-\delta E_{th}}{k_BT_S}\right) + \frac{n_{C_2H_2}J_{i2}y_d}{\upsilon_0} + n_{C_2H_2}\nu\exp\left(\frac{-\delta E_i}{k_BT_S}\right)$$
$$+ J_{i2} - J_2\exp\left(\frac{-E_{aH}}{k_BT_S}\right) + \frac{16D_m m_{cat}}{\rho_{cat}\times\pi D^2}, \qquad (3.16)$$

where d is the inner diameter of the CNF, h is the height of the CNF, $D_S = D_{S0}\exp\left(-E_S/k_B T_S\right)$ is the surface diffusion coefficient, D_{S0} is the constant, E_S (=0.3 eV) is the energy barrier for diffusion of carbon species on the catalyst surface [25], $D_b = D_{b0}\exp\left(-E_b/k_B T_S\right)$ is the bulk diffusion coefficient, D_{b0} is the constant, E_b (=1.6 eV) is the energy barrier for bulk diffusion of carbon species through catalyst nanoparticle [25], $D_m = D_{m0}\exp\left(-E_{SD}/k_B T_S\right)$ is the diffusion coefficient of metal atoms [26], D_{m0} is the constant, E_{SD} is the activation energy of self-diffusion of metal atoms, $p(\approx 20\ GPa)$ is the pressure exerted by graphene layers on catalyst nanoparticle [27], $k = A_k\exp\left(-\delta E_{inc}/k_B T_S\right)$ is the incorporation speed of carbon species into the graphene layers [28], A_k is constant, δE_{inc} is the energy barrier for diffusion of carbon species along the CNF-catalyst interface, ρ_{cnf} is the density of CNF, E_{aH} (=1.8 eV for hydrogen) is the desorption energy, m_{cat} is the mass of the metal catalyst particle, and ρ_{cat} is the density of metal catalyst particle.

The Eq. (3.16) accounts the various processes to elucidate the growth mechanism of carbon nanofiber on the metal catalyst surface. The first and second term in first bracket of RHS represent the surface and bulk diffusion of carbon species through the catalyst surface, respectively. These diffusion processes significantly depend on the catalyst nanoparticle temperature. For lower catalyst temperatures, surface diffusion process dominates the CNF growth whereas at higher catalyst temperatures, the CNF growth is mainly due to the bulk diffusion process and at intermediate temperature both the processes contribute to the CNF growth [29, 30]. However, in the present chapter, we have considered both surface and bulk diffusion process in the CNF growth since the temperature of catalyst nanoparticle is assumed to be constant. The third term represents the precipitation or incorporation of C species around the catalyst nanoparticle, i.e. realization of graphene layers around the catalyst

nanoparticle. These carbon layers exert substantial stress on the catalyst nanoparticle which can cause metal nanoparticle to deform. The catalyst nanoparticle no longer exhibited the spherical shape and appeared alike either truncated cone or teardrop. Now the question arises what stops the in plane growth of carbon condensation i.e., why carbon does not spread out over the whole substrate surface. The highly active atomic hydrogen and hydrogen ion etch the terminal carbons present at the edges of the graphitic nest and the carbon shadowed by the catalyst particle may contribute to the formation of graphitic shells around the catalyst particle or carbon nanofiber. Therefore, the Eq. (3.16) also incorporate the adsorption of hydrogen atom on the catalyst surface [25] (fourth term), incoming flux of hydrogen ion due to thermal dehydrogenation of hydrocarbon ions [18] (fifth term), ion induced decomposition of hydrogen [31] (sixth term), flux of H-atoms due to thermal dissociation of hydrocarbons [31] (seventh term), direct flux due to hydrogen ion decomposition [32] (eight term), and desorption of H-atom from the catalyst surface (ninth term) [25]. The last term corresponds to the metal diffusion [13] which is also responsible for the change of the catalyst particle morphology. Due to this morphological change and continuous carbon supply, interaction between metallic catalyst nanoparticle and substrate decreases and hence the catalyst particle gets lift off leading to the vertical growth of carbon nanofiber.

3.4 Results and discussion

The Fig. 3.1 shows the schematic of different stages of nucleation and growth of carbon nanofiber on the catalyst substrate surface in presence of plasma. The growth pattern considered in Fig. 3.1 is similar to the growth of single- and multi-walled carbon nanotubes (SWCNTs & MWCNTs). The Fig. 3.1(a) shows the initial stage in which thin catalyst film is deposited on the silicon substrate and kept in the plasma environment. We assume that the catalyst nanoparticles with spherical morphology are formed due to plasma etching [Fig. 3.1(b)]. In Fig. 3.1(c), the dissociation and adsorption of the carbon gas precursor (C_2H_2) as well as hydrogen on the catalyst surface is shown. The carbon species diffuse through bulk and surface of the catalyst particle and ultimately precipitate in the form of graphene layers at the rear surfaces of the catalyst nanoparticle [Fig.

3.1(c)]. These graphene layers exert significant pressure on the catalyst particle resulting in the shape change of catalyst particle [Fig. 3.1(d)]. The interaction (bonding force) between the catalyst nanoparticle and substrate is not so strong [33] and thus the catalyst nanoparticle is pushed up away from the substrate as the graphene layers precipitate out of the catalyst particle. Now, the active hydrogen and hydrogen ions etch the terminal carbons present at the edges of the graphitic nest and the carbon shadowed by the catalyst nanoparticle lead to the formation of new graphene layers [Fig. 3.1(e)]. Due to the plasma sheath effect, the vertical growth continues [18, 34] and the catalyst particle changes it shape continuously, and finally transforms to pear drop like shape [Fig. 3.1(f)]. The geometrical structure of the resulting CNF is shown in Fig. 3.1(g), where h is the height of the CNF, *D* is the initial diameter of the catalyst nanoparticle and d is the tip diameter or the inner diameter of the CNF.

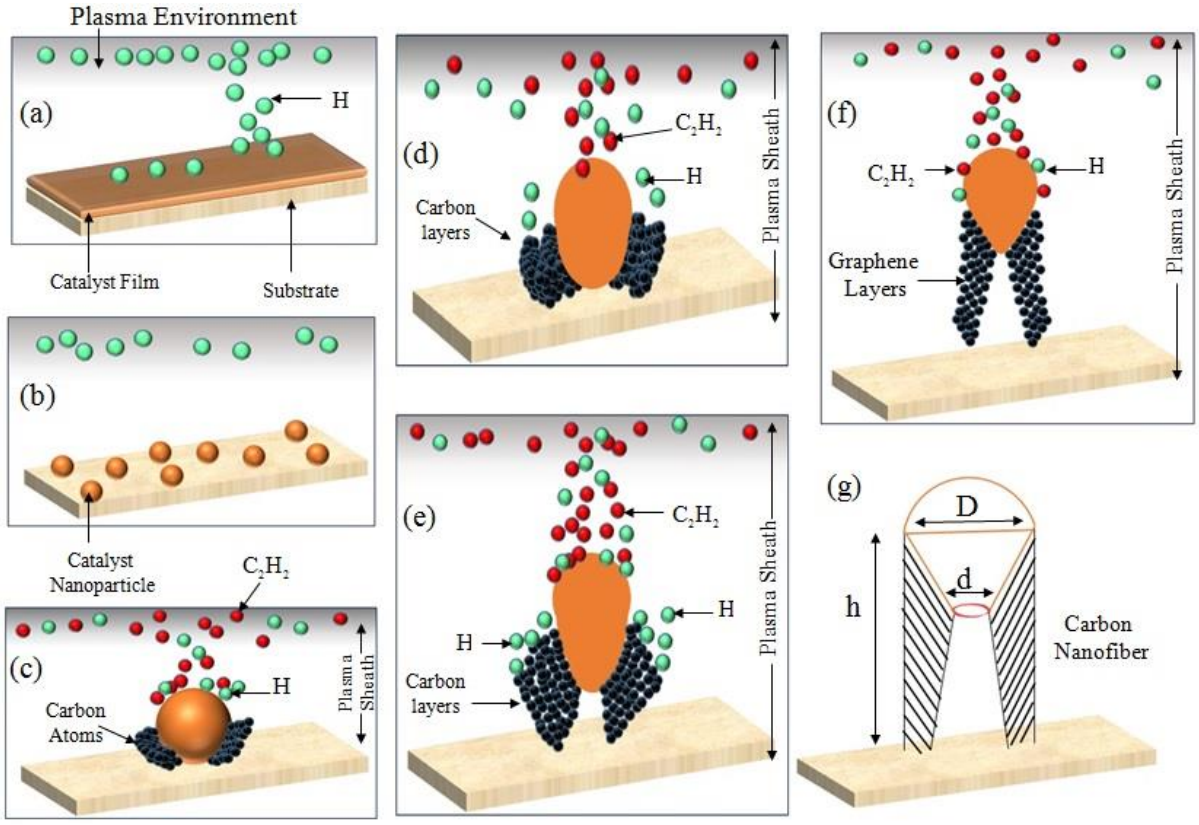

Fig. 3.1. Schematic representation of the nucleation and the growth mechanism of carbon nanofiber under plasma; (a) deposition of thin catalyst film on the substrate, (b) formation of catalyst nanoparticles, (c) dissociation and adsoprtion of hydrocarbons and hydrogen on catalyst particle surface, (d) precipitation of carbons and shape change of catalyst particle, (e) detachment of catalyst particle from substrate, (f) growth of carbon nanofiber, and (g) scheme of the CNF considered.

Using MATHEMATICA software, the first order differential Eqs. (3.1) - (3.16) have been solved simultaneously with appropriate boundary conditions listed in Table 3.1.

Table 3.1. Boundary conditions used in the present model.

Parameter	Description	Initial Value
n_{e0}	Electron number density	$10^{12}\ cm^{-3}$
n_{i10}	Ion density of type 1	$0.3n_{e0}$
n_{i20}	Ion density of type 2	$0.7n_{e0}$
n_{10}	Neutral atom density of type 1	$10^{13}\ cm^{-3}$
n_{20}	Neutral atom density of type 2	$10^{15}\ cm^{-3}$
T_{e0}	Electron temperature	2 eV
T_{i0}	Ion temperature	2500 K
T_{n0}	Neutral temperature	2000 K
T_s	Substrate temperature	400 ^{0}C
$\alpha_{10} \approx \alpha_{20}$	Coefficient of recombination of electrons and ions	1.12×10^{-7} cm^3/sec
γ_e	Sticking coefficient of an electron	1
γ_{ij}	Sticking coefficient of ions	1
γ_j	Sticking coefficient of neutrals	1
θ_t	Total surface coverage	0.01

The etching gas density n_{20} is assumed to be the greater than the hydrocarbon gas density n_{10} in order to avoid the poisoning of the catalyst nanoparticle, i.e., formation of the thin layer of amorphous carbon on the front surface (surface which is exposed towards the bulk plasma) of the catalyst nanoparticle. The poisoning of catalyst nanoparticle blocks the active surface for the decomposition of incoming hydrocarbons, and stops the carbon nanofiber growth due to the loss of catalytic activity [35, 36].

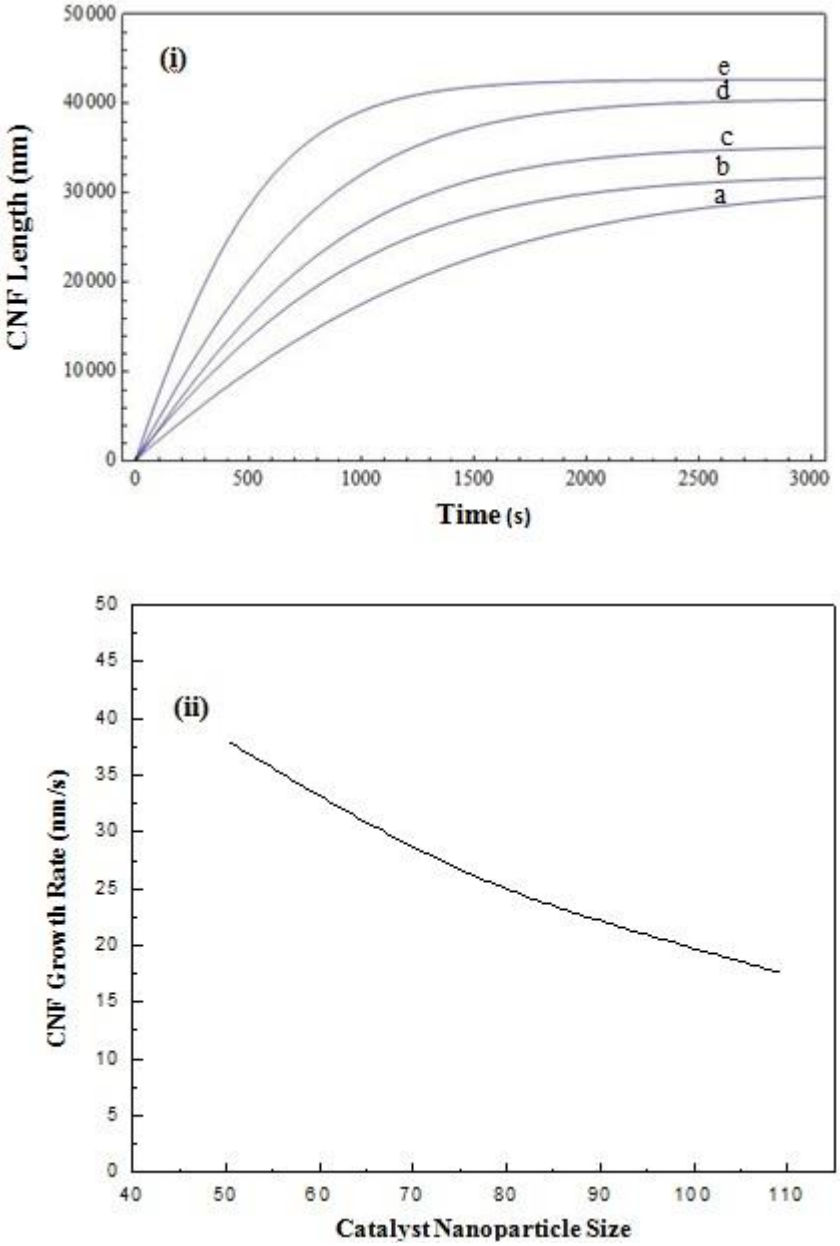

Fig. 3.2. (i) The time evolution of CNF length for different catalyst nanoparticle size(where a, b, c, d and e correspond to D = 109.3, 96.34, 75.91, 61.95, 47.31 nm, respectively). (ii) The variation of the growth rate of CNF with catalyst nanoparticle size.

The variation of CNF length to the growth time for different catalyst nanoparticle size is shown in the Fig. 3.2(i). It can be seen from the Fig. 3.2(i) that as the catalyst nanoparticle size is increased, the growing CNF of shorter length is observed. This signifies that one can get thick and shorter CNFs with large catalyst nanoparticles. The dependence of CNF length on the catalyst nanoparticle size during the growth can also be interpreted in terms of the

growth rate (CNF length per unit deposition time) of CNF as shown in Fig. 3.2(ii). The growth rate of CNF is decreased as catalyst nanoparticle size is increased. This happens because for large catalyst nanoparticle size, the carbon species diffusion path increases and therefore the growth of CNF is slowed down. These results are in good agreement with the experimental observations shown by Jong *et al.* [32].

The Fig. 3.3 shows the variation of CNF length for different hydrocarbon number density $\left(n_{10} = 10^{11},\ 10^{12},\ 10^{13},\ 10^{14}\ \text{cm}^{-3}\right)$ in the plasma. The Fig. 3.3 indicates that greater the hydrocarbon (C_2H_2) number density in the plasma larger would be the CNF length. This is explainable to the fact that with increasing number density of hydrocarbons, the dissociation of hydrocarbons at the catalyst nanoparticle surface increases resulting in greater diffusion of carbon species through the catalyst which consequently increases the CNF length. The results of the Fig. 3.3 are in accordance with the experimental observations of Matthews *et al.* [9].

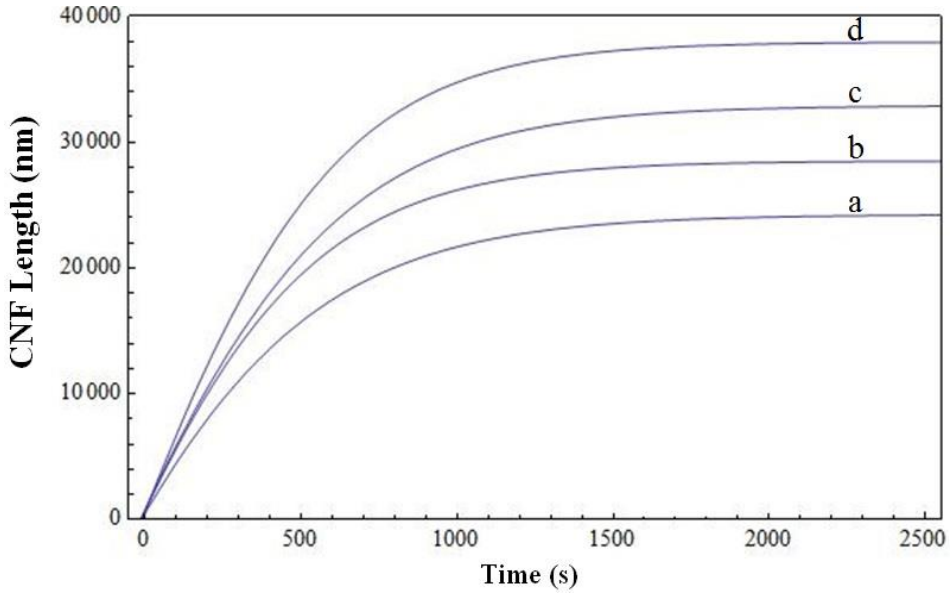

Fig. 3.3. The time variation of the CNF length for different hydrocarbon number density (where a, b, c, and d corresponds to $n_{10} = 10^{11},\ 10^{12},\ 10^{13},\ 10^{14}\ \text{cm}^{-3}$, respectively) at $n_{20} = 10^{15}\ \text{cm}^{-3}$.

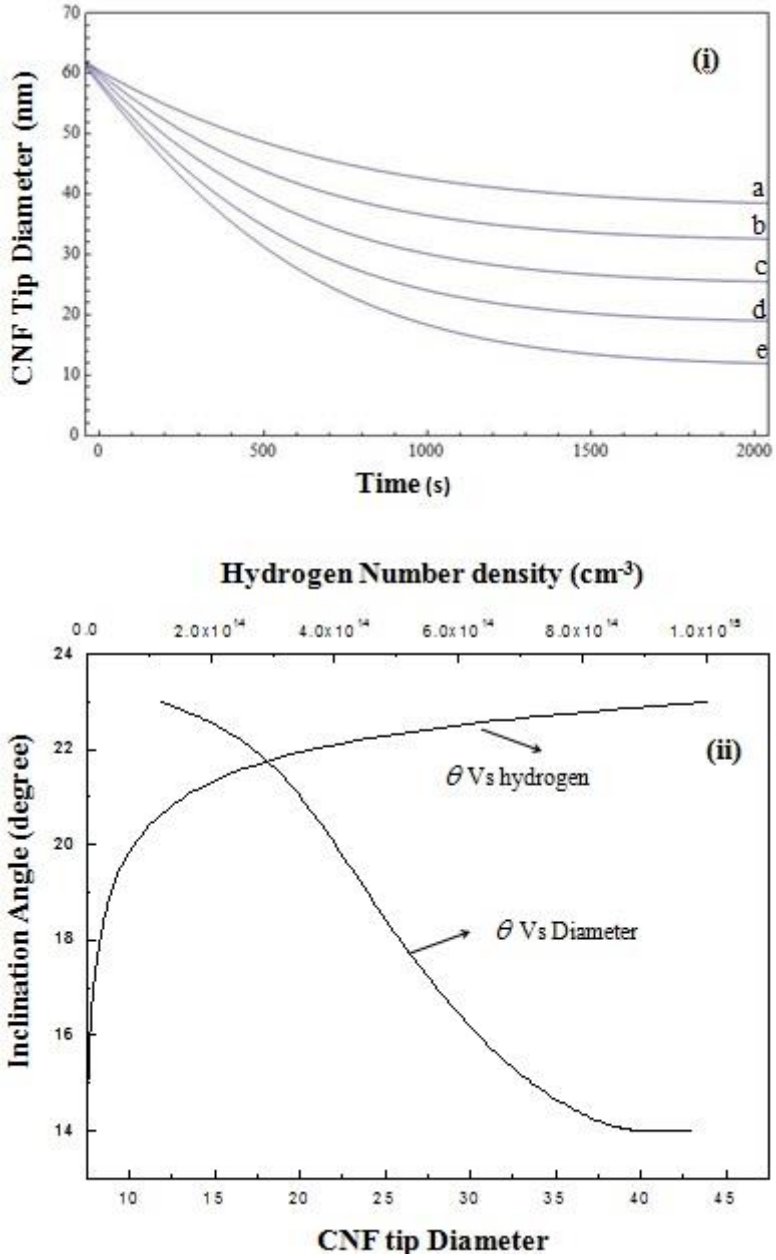

Fig. 3.4. (i) The time evolution of CNF tip diameter for different hydrogen number density in the growth atmosphere (where a, b, c, d and e corresponds to $n_{20} = 10^{11},\ 10^{12}, 10^{13},\ 10^{14}, 10^{15}\ \text{cm}^{-3}$, respectively). (ii) The time variation of inclination angle with CNF tip diameter and hydrogen density.

The Fig. 3.4(i) shows the time evolution of the CNF tip diameter (CNF inner diameter) for different hydrogen number density (i.e., $n_{20} = 10^{11},\ 10^{12}, 10^{13},\ 10^{14}, 10^{15}\ \text{cm}^{-3}$). From Fig. 3.4(i), it can be seen that as the deposition time is increased, the inner diameter of the CNF is decreased. This

happens because the growing graphene layers exert significant stress on the catalyst nanoparticle which results in the change of the catalyst nanoparticle shape and consequently the decrease in the diameter of the base of the catalyst nanoparticle is observed. This is in good agreement with the experimental observations of Poa *et al.* [37]. Furthermore, in the Fig. 3.4(i), it has been shown that increase in hydrogen content $n_{20}(=10^{11}, 10^{12}, 10^{13}, 10^{14}, 10^{15}\ \text{cm}^{-3})$ in the growth atmosphere decrease the inner diameter of the CNF. Two possibilities exist in this context; (i) more hydrogen adsorption over the metal catalyst particle surface weakens the metal-metal bond [14] which leads to the induced diffusion of metal atoms and consequently the base diameter of the catalyst nanoparticle or the inner diameter of the CNF tip is decreased, (ii) the abundance supply of hydrogen can terminate the large number of dangling bonds at the edges of the graphene layers and thus prevents the condensation reaction which leads to the formation of new graphene layers. Now catalyst nanoparticle experiences more stress due to these layers and this leads to decrease in catalyst particle size. Now, one can think that the catalyst nanoparticle size and the relative inclination of graphene layers must be correlated (See Appendix A). The Fig. 3.4(ii) shows the dependence of angle between the graphene layers and fiber axis on the catalyst nanoparticle base size as well as on the amount of hydrogen in the growth environment. It can be inferred from Fig. 3.4(ii) that increase and decrease of the hydrogen concentration and catalyst nanoparticle size, respectively, would tend to tilt the graphene layers away from the growth axis or fiber axis. The above observations are in compliance with the works of Cui *et al.* [11], Nolan *et al.* [38], and Murayama and Maeda [39].

The role of atomic hydrogen on the CNF growth has also been investigated in the present chapter. In Fig. 3.5(i), time variation of CNF length for different hydrogen number density ($n_{20} = 10^{13}, 10^{14}, 10^{15}\ \text{cm}^{-3}$) is shown. As can be seen from Fig. 3.5(i), the CNF length decreases with increase in hydrogen atom number density in the plasma. This may be ascribed to the fact that with increase in the hydrogen atom number density, interaction between hydrogen and hydrocarbon on the catalyst nanoparticle surface [fifth term of the

Eq. (3.15)] increases resulting in the decrease in number (per unit area) of carbon species n_c generated on the catalyst nanoparticle surface as shown in Fig. 3.5(ii). This leads to loss of carbon diffusion on the catalyst nanoparticle surface resulting in decrease of CNF length and eventually, the decrease in CNF growth rate. The similar trend has been observed by other researchers [18, 23].

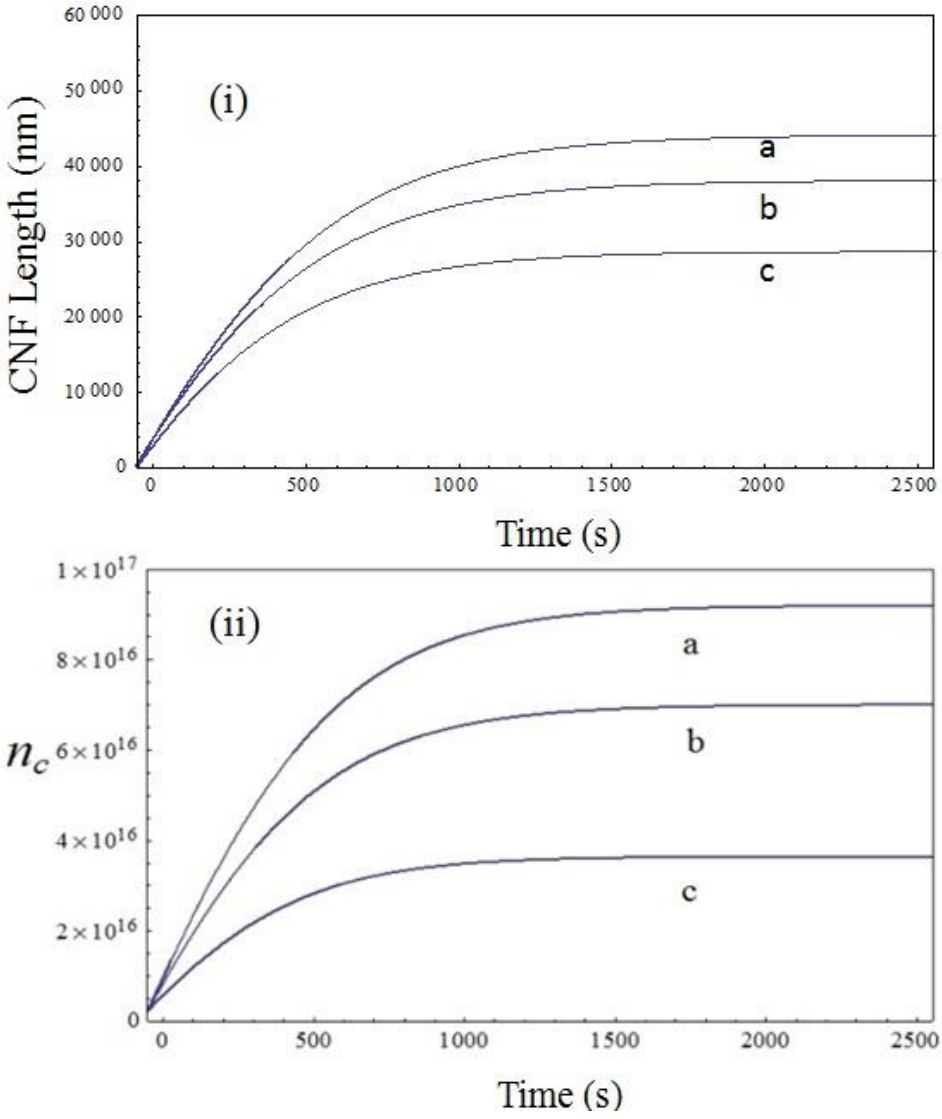

Fig. 3.5. The time variation of the CNF length for different hydrogen number density (where a, b, and c corresponds to $n_{20} = 10^{13}, 10^{14}, 10^{15}$ cm^{-3}, respectively) at $n_{10} = 10^{13}$ cm^{-3}.

References

[1] V. I. Merkulov, D. H. Lowndes, and L. R. Baylor, J. Appl. Phys. **89,** 1933 (2001).

[2] M. A. Guillorn, A. V. Melechko, V. I. Merkulov, E. D. Ellis, C. L. Britton, M. L. Simpson, D. H. Lowndes, and L. R. Baylor, Appl. Phys. Lett. **79,** 3506 (2001).

[3] H. Murakami, M. Hirakawa, C. Tanaka, and H. Yamakawa, Appl. Phys. Lett. **76,** 1776 (2000).

[4] M. S. Dresselhaus, G. Dresselhaus, and P. Avouris, *Carbon Nano-tubes: Synthesis, Structure, Properties and Applications* (Berlin Springer) (2001).

[5] V. I. Merkulov, A. V. Melechko, M. A. Guillorn, D. H. Lowndes, and M. L. Simpson, Chem. Phys. Lett. **361,** 492 (2002).

[6] V. I. Merkulov, D. H. Lowndes, Y. Y. Wei, G. Eres, and E. Voelkl, Appl. Phys. Lett. **76,** 3555 (2000).

[7] Z. F. Ren, Z. P. Huang, D. Z. Wang, J. G. Wen, J. W. Xu, J. H. Wang, L. E. Calvet, J. Chen, J. F. Kelmic, and M. A. Reed, Appl. Phys. Lett. **75,** 1086 (1999).

[8] V. I. Merkolov, D. K. Hensley, A. V. Melechko, M. A. Guillorn, D. H. Lowndes, and M. L. Simpson, J. Phys. Chem. B **106,** 10570 (2002).

[9] K. Matthews, B. A. Cruden, B. Chen, M. Meyyappan, and L. Delzeit, J. Nanosci. Nanotect. **2,** 475 (2002).

[10] H. Zhanbing, J. L. Maurice, A. Gohier, C. S. Lee, D. Pribat, and C. S. Cojocaru, Chem. Mater. **23**, 5379 (2011).

[11] H. Cui, X. Yang, M. L. Simpson, D. H. Lowndes, and M. Varela, Appl. Phys. Lett. **84,** 20 (2004).

[12] M. S. Kim, N. M. Rodriguez, and R. T. K. Baker, J. Catal. **134,** 253 (1992).

[13] C. S. Cojocaru, A. Senger, and F. L. Normand, J. Nanosci. Nanotech. **6,** 1 (2006).

[14] N. M. Rodriguez, J. Mater. Res. **8,** 3233 (1993).

[15] G. B. Zheng, K. Kouda , H. Sano, Y. Uchiyama, Y. F. Shi, and H. J. Quan, Carbon **42,** 635 (2004).

[16] H. W. Wei, K. C. Leou, M. T. Wei, Y. Y. Lin, and C. H. Tsai, J. Appl. Phys. **98,** 044313 (2005).

[17] A. Tewari and S. C. Sharma, Phys. Plasmas **21**, 063512 (2014).

[18] H. Mehdipour, K. Ostrikov, and A. E. Rider, Nanotechnology **21,** 455605 (2010).

[19] M. A. Lieberman and A. J. Lichtenberg, Principles of Plasma Discharges and Material Processing (Wiley Interscience Publications, USA, 1994).

[20] K. N. Ostrikov, S. V. Viladimirov, M. Y. Yu, and G. E. Morfill, Phys. Plasmas **7**, 461 (2000).

[21] S. V. Viladimirov, K. N. Ostrikov, and M. Y. Yu, Phys. Rev. E **58** (6), 8046 (1998).

[22] A. V. Keudell and W. Moller, J. Appl. Phys. **75**, 7718 (1994).

[23] I. Denysenko, and K. Ostrikov, J. Phys. D: Appl. Phys. **42,** 015208 (2009).

[24] L. Vattuone, Y. Y. Yeo, R. Kose, and D. A. King, Surf. Sci. **447,** 1 (2000).

[25] I. Denysenko and N. A. Azarenkov**,** J. Phys. D: Appl. Phys. **44,** 17403 (2011).

[26] See http://www.matter.org.uk/matscicdrom/manual/df.html for metal atom diffusion coefficient.

[27] M. Yudasaka, R. Kikuchi, T. Matsui, Y. Ohki, S. Yoshimura, and E. Ota, Appl. Phys. Lett. **67,** 2477 (1995).

[28] O. A. Louchev, T. Laude, Y. Sato, and H. Kanda, J. Chem. Phys. **118**, 7622 (2003).

[29] I. Denysenko and K. Ostrikov, Appl. Phys. Lett. **90,** 251501 (2007).

[30] S. Hofmann, G. Csanyi, A. C. Ferrari, M. C. Payne, and J. Robertson, Phys. Rev. Lett. **95,** 036101 (2005).

[31] I. Denysenko, K. Ostrikov, M. Y. Yu, and N. A. Azarenkov, J. Appl. Phys. **102**, 074308 (2007).

[32] K. P. D. JONG and J. W. GEUS, CATAL. Rev. Sci. Eng. **42,** 481 (2000).

[33] R. T. K. Baker, M. A. Barber, R. J. Waite, P. S. Harris, and F. S. Feates, J. Catal. **26**, 51 (1972).

[34] V. I. Merkulov, A. V. Melechko, M. A. Guillorn, M. L. Simpson, D. H. Lowndes, J. H. Whealton, and R. J. Raridon, Appl. Phys. Lett. **80**, 4817 (2002).

[35] S. Hofmann, M. Contoro, B. Kleinsorge, C. Casiraghi, A. Parvez, J. Robertson, and C. Ducati, J. Appl. Phys. **98,** 034308(2005).

[36] C. Veríssimo, S. A. Moshkalyov, A. C. S. Ramos, J. L. Gonçalves, O. L. Alvesc, and J. W. Swart, J. Braz. Chem. Soc. **17**, 1124 (2006).

[37] C. H. P. Poa, S. J. Henley, G. Y. Chen, A. A. D. T. Adikaari, C. E. Giusca, and S. R. P. Silvaa, J. Appl. Phys. **97,** 114308 (2005).

[38] P. E. Nolan, D. C. Lynch, and A. H. Cutler, J. Phys. Chem. B **102**, 4165 (1998).

[39] H. Murayama, and T. Maeda, Nature **345,** 791(1990).

4

Modeling the effects of nitrogen doping on the carbon nanofibers growth via catalytic PECVD process

4.1 Brief outline of the chapter

In this chapter, the effects of nitrogen doping on the growth of CNFs i.e. the growth of the nitrogen contained carbon nanofibers (N-CNFs) and their field emission properties through the plasma kinetics-based model have been explained. The model used in previous chapter relies on selected absorbed species; however, one of the main advantages of plasma-based growth is the ability to generate the highly reactive plasma species, which significantly affect CNF growth. Therefore, in the present chapter, numerous additional species of the reactive plasma have been accounted. Moreover, the basic growth mechanisms of CNFs in the presence of reactive plasma remains the same, but to point out the consequent effects of nitrogen doping, many additional terms and equations have been incorporated in the present chapter.

4.2 Introduction

The growth of carbon nanofibers (CNFs) is an unexpectedly developing field of nanotechnology. Within the purview of a catalyst, diverse techniques can be utilized to synthesize CNFs, such as electric arc discharge, laser ablation, pyrolysis of organic precursor, and plasma-enhanced chemical vapour deposition (PECVD). The PECVD technique gathers continually growing interest because of its capability to grow vertically aligned CNFs at low temperatures.

Published work of the present chapter:

1. **Ravi Gupta** and Suresh C. Sharma, Modelling the effects of nitrogen doping on the carbon nanofiber growth via catalytic plasma-enhanced chemical vapour deposition process. *Contribution to plasma physics, (2018),* DOI: 10.1002/ctpp.201700138.

This is possible because the electric field existing within the plasma sheath aids the CNFs' growth in the vertical direction [1] and by substituting high thermal energy required in the growth process by dissociation of hydrocarbon precursors induced in plasma [2].

The growth and synthesis of nitrogen-doped CNFs/nitrogen-contained carbon nanofibers (N-CNFs) receives constantly developing interest as the incorporation of nitrogen into the CNF grid leads to extraordinary physical and chemical properties [3,4]. Along with doping, catalysed growth is essential to control the characteristics of the resulting CNF by properly selecting the reaction conditions [5]. Merkulov *et al.*[6] synthesized the isolated N-CNFs and observed that nitrogen concentration in the plasma environment strictly affects the growth rate, tip diameter, and nitrogen content in the resulting CNF. It is also observed that, by the proper selection of the gas ratio, that is, hydrocarbon to ammonia, the morphology of the N-CNFs can be controlled [7]. Saidin *et al.*[8] observed a decrease in CNF diameter and increase in CNF growth rate when the ammonia gas flow rate is increased in reactive plasma. Moreover, Teo *et al.*[9] observed the change in CNF shape on increasing the gas ratio. One of the most promising utilizations of CNFs is in the field emission devices [10]. The superior field emission obtained from CNFs/CNTs (carbon nanotubes) comes from their geometry rather than their crystalline structure [2]. Therefore, decent field emitters must have a high aspect ratio structure. CNFs hosting small diameters and comparatively excessive lengths can generate a high electric field (field enhancement) at the tip surface of the emitters to reap superior field emission; therefore, the greater the field enhancement factor of the emitter, the larger would be the field emission of electrons. Doping of CNFs with heteroatoms is essential for their practical applications [11]. Nitrogen atoms substitute carbon atoms in the graphene layers (graphene matrix of CNFs) and thus, enhance the n-type electrical conductivity [12]. Kimura *et al.*[10] synthesized N-CNFs using the microwave plasma chemical vapour deposition (MW-PECVD) technique and observed the reduction in turn on field and increment in the field-enhancement factor when N-CNFs are utilized as field emitters.

4.3 Analytical model

The present analytical model elucidates the effects of nitrogen doping on the growth and field emission properties of CNFs, i.e., the growth mechanism of N-CNFs in the reactive plasma composed of acetylene (C_2H_2) and ammonia (NH_3). In reality, the C_2H_2/NH_3 plasma mixture contains a large number of species [13,14] (ions and neutrals). However, following the experimental studies of Bell *et al.*[15] and Merkulov *et al.*[16], the plasma species accounted in the present model are listed in Table 4.1. Fig 4.1 shows the schematic of deposition of these plasma species and N-CNF growth mechanism considered in the present model. The nickel catalyst nanoparticle placed over the silicon substrate is considered to be the nucleation site for N-CNFs' nucleation. When a negatively biased substrate surface with a catalyst nanoparticle is subjected to the reactive plasma, an electric field $\vec{E}$ is induced between the bulk plasma and the substrate surface as a result of a charge separation region known as the plasma sheath. This induced electric field is assumed to be in a vertically downward direction, i.e., from bulk plasma to substrate surface. The motion of ions is governed by this induced electric field, whereas neutrals have a random motion. At very low temperatures, it has been observed that no CNF grows when a small negative potential is applied to the substrate or a positive potential is applied to the substrate [17]. To investigate the sheath structure, fluxes, and energies of these plasma species, the following sheath equations are considered [18].

$$\frac{d}{dx} n_k u_{kx} = \nu_i n_e \ , \tag{4.1}$$

$$M_k n_k u_{kx} \frac{du_{kx}}{dx} = e n_k \frac{d\phi}{dx} - M_k n_k \nu_{kn} u_{kx}, \tag{4.2}$$

$$\frac{d^2\phi}{dx^2} = -\ 4\pi e \sum \Omega_k n_k, \tag{4.3}$$

where Eqs. (4.1)-(4.3) denotes continuity equation, ion-momentum balance equation, and Poisson's equation, respectively; *k* refers to either electron or ions that are considered in the present model, n_k is their number density, M_k is their mass in plasma, u_{kx} is their fluid velocity, ν_i is the ionization frequency, E is

the electric field, ν_{kn} is the collision frequency, Ω_k is the k^{th} ion to electron number density ratio, ϕ is the electrostatic potential, $\sum_k \Omega_k = 1$, and $0 < \Omega_k < 1$.

Table 4.1. Plasma species considered in the present model.

Type	Ions	Neutrals
a	$C_2H_2^+$, C_2H^+	C_2H_2, C_2H
b	H_2^+, H^+	H_2, H,
c	NH_3^+, NH_4^+, NH_2^+, HCN^+, N^+	NH_3, NH_4, NH_2, HCN, N,

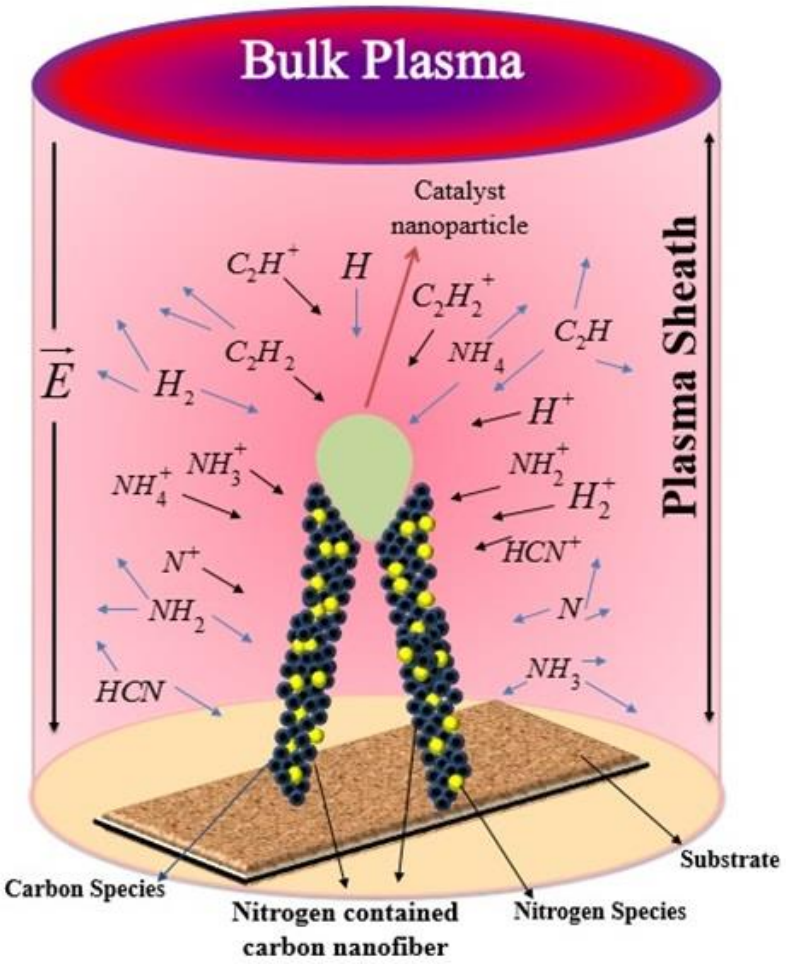

Fig. 4.1. Schematic of the plasma species (ions and neutrals) deposition during nitrogen-contained carbon nanofibers (N-CNFs) growth.

The presumptions of the present model are as follows: (a) negatively biased substrate is considered; (b) temperature of substrate and catalyst nanoparticle is considered to be the same; (c) the Maxwellian distribution of electrons, as well as ions, is considered; and (d) in the plasma sheath region, the electron number density is considered to be less than the ion number density, i.e., $n_i(x) > n_e(x)$.

The elementary processes considered to study the effects of nitrogen insertion/doping on the growth of CNFs in the reactive plasma are:

1. Generation of carbon species on the catalyst nanoparticle surface (which is exposed to plasma) due to the dissociation of hydrocarbons on the catalyst nanoparticle surface [19].

2. Surface and bulk diffusion of carbon species through the catalyst nanoparticle and formation of graphene layers around the catalyst nanoparticle [20].

3. Transformation and deformation of catalyst nanoparticle shape due to stress exerted by these graphene layers [21].

4. Etching of nanofiber side walls and tip by the etchants present in the plasma.

5. Vertical growth due to alignment force provided by the electric field induced by plasma sheath [22].

4.3.1 Charging of the N-CNF surface

The following equation describes the charge developed on the N-CNF surface due to the accumulation of electrons and positively charged ions on the surface, considering plasmas to be the thermodynamically open system [23,24].

$$\dot{q} = \sum_{a=1}^{2}\left[\left(I_{ia}\right)_{tip} + \left(I_{ia}\right)_{cur}\right] + \sum_{b=1}^{2}\left[\left(I_{ib}\right)_{tip} + \left(I_{ib}\right)_{cur}\right] + \sum_{c=1}^{5}\left[\left(I_{ic}\right)_{tip} + \left(I_{ic}\right)_{cur}\right] - \gamma_e\left[\left(I_e\right)_{tip} + \left(I_e\right)_{cur}\right], \quad (4.4)$$

where q is the charge over the entire CNF (i.e., tip and curved surface), and $\left(I_{ij}\right)_{tip}$ and $\left(I_{ij}\right)_{cur}$ are the ion collection currents at the CNF tip and the curved

surface, respectively (where *j* refers to the ions of type *a*, *b*, and *c*). $(I_e)_{tip}$ and $(I_e)_{cur}$ are the electron collection currents at the CNF tip and the curved surface,[23–25], respectively.

4.3.2 Number density equalization of electrons

$$\dot{n_e} = \sum_{a=1}^{2} \beta_a n_a + \sum_{b=1}^{2} \beta_b n_b + \sum_{c=1}^{5} \beta_c n_c - \sum_{a=1}^{2} \alpha_a n_e n_{ia} - \sum_{b=1}^{2} \alpha_b n_e n_{ib} - \sum_{c=1}^{5} \alpha_c n_e n_{ic} - \gamma_e n_{ncnf} \left[(I_e)_{tip} + (I_e)_{cur} \right], \quad (4.5)$$

where β_j is the coefficient of ionization of neutral atoms [26], α_j is the coefficient of recombination of electrons and positively charged ions, and γ_e is the sticking coefficient of electrons.

Equation (4.5) indicates the time evolution of electron number density in the plasma. The first three terms of Eq. (4.5) correspond to increase in electron number density per unit time due to ionization of neutral species of type *a*, *b*, and *c*, respectively. The next three terms represent the decrease in electron number density per unit time due to recombination of electrons with ions of type *a*, *b*, and *c*, respectively. The last term represents the decrease in electron density in the plasma due to the electron collection current at the CNF surface.

4.3.3 Number density equalization of positively charged ions

$$\dot{n_{ia}} = \beta_a n_a - \alpha_a n_e n_{ia} - n_{ncnf} \left[(I_{ia})_{tip} + (I_{ia})_{cur} \right] - J_{aia} + J_{despa} + \sum_{\ell ab} k_\ell n_a n_{ib}, \quad (4.6)$$

$$\dot{n_{ib}} = \beta_b n_a - \alpha_b n_e n_{ib} - n_{ncnf} \left[(I_{ib})_{tip} + (I_{ib})_{cur} \right] - J_{aib} + J_{despb} + \sum_{mbc} k_m n_b n_{ic} - \sum_{\ell ab} k_\ell n_a n_{ib} + J_{thd}, \quad (4.7)$$

$$\dot{n_{ic}} = \beta_c n_c - \alpha_c n_e n_{ic} - n_{ncnf} \left[(I_{ic})_{tip} + (I_{ic})_{cur} \right] - J_{aic} + J_{despc} - \sum_{pbc} k_p n_b n_{ic}, \quad (4.8)$$

Ravi Gupta, Department of Applied Physics, Delhi Technological University, Delhi, India

where J_{aij} and J_{despj} are the ion adsorption flux and ion desorption flux onto/from the catalyst substrate surface, respectively (*j* refers to the ions of type *a*, *b*, and *c*). k_l, k_m, and k_p are the reaction rate coefficients of ion-neutral reactions, and J_{thd} is the hydrogen flux due to thermal dehydrogenation.

Table 4.2. Ion-neutral reactions between various plasma species in the bulk plasma considered in the present model.

Reaction	Reaction Rate (cm^3/s)	Reference
$NH_3^+ + H_2 \rightarrow NH_4^+ + H$	4.00×10^{-13}	[14]
$NH_3^+ + H_2 \rightarrow NH_3 + H_2^+$	9.63×10^{-13}	[14]
$NH_3^+ + H_2 \rightarrow NH_3 + H^+ + H$	8.46×10^{-10}	[14]
$NH_3^+ + H_2 \rightarrow H_2^+ + NH_2 + H$	2.18×10^{-9}	[14]
$NH_3^+ + H_2 \rightarrow H^+ + NH_2 + H_2$	6.8×10^{-9}	[39]
$NH_3^+ + H_2 \rightarrow H^+ + H + NH_3$	8.46×10^{-10}	[39]
$NH_2^+ + H_2 \rightarrow NH_2 + H_2^+$	1.0×10^{-9}	[14]
$H_2^+ + NH_2 \rightarrow NH_2^+ + H_2$	5.00×10^{-10}	[14]
$H_2^+ + NH_2 \rightarrow NH_3^+ + H$	5.00×10^{-11}	[14]
$H_2^+ + NH_3 \rightarrow NH_3^+ + H_2$	5.70×10^{-9}	[14]
$H_2^+ + NH_3 \rightarrow NH_4^+ + H$	5.00×10^{-11}	[14]
$H^+ + NH_3 \rightarrow NH_3^+ + H$	5.00×10^{-11}	[14]
$H^+ + NH_2 \rightarrow NH_2^+ + H$	5.00×10^{-11}	[14]
$H_2^+ + C_2H_2 \rightarrow C_2H_2^+ + H_2$	5.30×10^{-9}	[14]
$H^+ + C_2H_2 \rightarrow C_2H^+ + H_2$	4.30×10^{-9}	[14]
$H^+ + C_2H \rightarrow C_2H^+ + H$	1.50×10^{-9}	[40]
$H_2^+ + C_2H \rightarrow C_2H_2^+ + H$	1.00×10^{-9}	[40]

In Eqs. (4.6)–(4.8), various processes are taken into account to equalize the number density of ions in the reactive plasma, such as gain in ion density per

unit time on account of ionization of neutral atoms (first term), decrease in positively charged ion number density due to electron–ion recombination (second term), and ion collection current at the surface of the CNF (third term), adsorption (fourth term) and desorption of ions (fifth term) to/from the catalyst–substrate surface, and increase and decrease in ion number density due to ion-neutral reactions between different plasma species (sixth and seventh term). The main ion-neutral reactions considered in the present model are listed in Table 4.2. The last term of Eq. (4.7) indicates the increase in hydrogen ion number density due to thermal dehydrogenation.

4.3.4 Number density equalization of neutral species

$$\dot{n}_a = \alpha_a n_e n_{ia} - \beta_a n_a + n_{ncnf}\left(1-\gamma_{ia}\right)\left[\left(I_{ia}\right)_{tip} + \left(I_{ia}\right)_{cur}\right] - n_{ncnf}\gamma_a\left[\left(I_a\right)_{tip} + \left(I_a\right)_{cur}\right] - \sum_{\ell ab} k_\ell n_a n_{ib} + IF_a - OF_a, \quad (4.9)$$

$$\dot{n}_b = \alpha_b n_e n_{ib} - \beta_b n_b + n_{ncnf}\left(1-\gamma_{ib}\right)\left[\left(I_{ib}\right)_{tip} + \left(I_{ib}\right)_{cur}\right] - n_{ncnf}\gamma_b\left[\left(I_b\right)_{tip} + \left(I_b\right)_{cur}\right] + \sum_{\ell ab} k_\ell n_a n_{ib} - \sum_{mbc} k_m n_b n_{ic} + IF_b - OF_b, \quad (4.10)$$

$$\dot{n}_c = \alpha_c n_e n_{ic} - \beta_c n_c + n_{ncnf}\left(1-\gamma_{ic}\right)\left[\left(I_{ic}\right)_{tip} + \left(I_{ic}\right)_{cur}\right] - n_{ncnf}\gamma_c\left[\left(I_c\right)_{tip} + \left(I_c\right)_{cur}\right] + \sum_{pbc} k_p n_b n_{ic} + IF_c - OF_c, \quad (4.11)$$

where $\left(I_j\right)_{tip}$ and $\left(I_j\right)_{tcur}$ are neutral atom collection currents at the tip and the curved surface of CNF, respectively (*j* refers to the neutrals atoms of type *a*, *b*, and *c*). In Eqs. (4.9)–(4.11), the processes taken into account to equalize the neutral atom number density are: increase in neutral atom number density due to electron–ion recombination (first term) and neutralization of ions collected at the N-CNFs surface (third term), the decay rate of neutral atom density due to ionization of neutrals (second term) and accumulation of neutrals on the N-CNF surface (fourth term), and increase and decrease in neutral atom number density due to the ion-neutral reactions between

different plasma species (fifth and sixth term) that are listed in Table 4.2. Moreover, the last two terms represent the j^{th} species inflow rate [$IF_j = 4.4\times10^{17}\times f\ /V$] into the plasma chamber and j^{th} species outflow rate [$OF_j = R_p\times n_a/V$] from the plasma chamber, where f is the inlet flow of corresponding gas, V *is* the volume of the chamber ($\approx 2 \times 104$ cm^3), and Rp is the pumping rate [29].

4.3.5 Growth rate of carbon species over the catalyst surface

At the initial stage, applied plasma power dissociates the input gases and creates highly energetic ions and electrons, which further breaks the catalyst's thin film into many catalyst nanoparticles, and these catalyst nanoparticles act as the fundamental sites for the nucleation and growth of CNFs [30]. At this nucleation stage, numerous carbon species (N_c) are generated on the catalyst nanoparticle front surface (plasma-exposed surface) via various surface processes that are discussed in Eq. (4.12). In the present model, the catalyst nanoparticle size (D) is assumed to be 100 nm.

$$\begin{aligned}\dot{N}_C = &\sum_{a=1}^{2} J_a(1-\theta_t) + 2\sum_{a=1}^{2} n_{sa}\upsilon\exp\left(\frac{-\delta E_{td}}{k_B T_S}\right) + 2\sum_{a=1}^{2}\frac{n_{sa}y_d}{\upsilon_0}\sum_{a=1}^{2} J_{ia} \\ &+ \sum_{a=1}^{2} J_{ia} + J_C - \sum_{a=1}^{2}\frac{J_a\sigma_{ads}J_b}{\upsilon} - \frac{N_c\sigma_{ads}J_b}{\upsilon} \\ &- N_c\upsilon\exp\left(\frac{-\delta E_{ev}}{k_B T_S}\right) - n_{sa}\upsilon\exp\left(\frac{-\delta E_{dhc}}{k_B T_S}\right), \end{aligned} \qquad (4.12)$$

where $n_{sj}\left(=\theta_j\upsilon_0\right)$ is the surface concentration of neutral atoms [31,32], θ_j is the surface coverage by the respective species, $\upsilon_0\left(=1.3\times10^{15}\ \text{cm}^{-2}\right)$ is the adsorption sites per unit area, $J_j\left(=n_j v_{th}/4\right)$ is the flux of neutral impinging species on the catalyst nanoparticle surface from the plasma, $J_{ij}\left[=n_{ij}\left(k_B T_e/m_{ij}\right)^{1/2}\right]$ is the ions flux on the catalyst nanoparticle surface from the plasma [32], υ is the thermal vibration frequency,

Ravi Gupta, *Department of Applied Physics, Delhi Technological University, Delhi, India*

$\sigma_{ads}\left(=6.8\times10^{-16}\ \text{cm}^2\right)$ is the cross section for the interaction among the various species [32], δE_{td} (=2.1 eV) is the hydrocarbons dissociation energy, δE_{ev} (= 1.8 eV) is the carbon evaporation energy, and δE_{dhc} (=1.8 eV) is the hydrocarbon desorption energy [33]. The explanation of various terms as well as their corresponding surface reactions involved in the Eq. (4.12), are listed in Table 4.3.

Table 4.3. Various surface processes and their corresponding reactions on the catalyst nanoparticle surface (refs 31–36) considered in the Eq. (4.12) where "ads" and "des" corresponds to the adsorption and desorption of plasma species to/from the catalyst surface, respectively.

Functional term	Explanation and reactions involved
$J_a(1-\theta_t)$	adsorption of hydrocarbons $C_2H_{2(plasma)} \rightarrow C_2H_{2(ads)}$, $C_2H_{(plasma)} \rightarrow C_2H_{(ads)}$.
$n_{sa}\upsilon\exp\left(\frac{-\delta E_{td}}{k_B T_S}\right)$	thermal dissociation of hydrocarbons $C_2H_{2(ads)} \rightarrow 2C_{(ads)} + 2H_{(ads)}$, $C_2H_{(ads)} \rightarrow 2C_{(ads)} + H_{(ads)}$.
$\frac{n_a y_d}{\upsilon_0} J_{ia}$	ion induced dissociation of hydrocarbons $C_2H_2^+ + C_2H_{2(ads)} \rightarrow 2C_{(ads)} + H_{2(plasma)} + C_2H_2^+$, $C_2H^+ + C_2H_{(ads)} \rightarrow 2C_{(ads)} + H_{(ads)} + C_2H^+$, $C_2H_2^+ + C_2H_{(ads)} \rightarrow 2C_{(ads)} + H_{(ads)} + C_2H_2^+$, $C_2H^+ + C_2H_{2(ads)} \rightarrow 2C_{(ads)} + H_{2(plasma)} + C_2H^+$.
J_{ia}	ion decomposition $C_2H_2^+ \rightarrow 2C_{(ads)} + H_{2(plasma)}$, $C_2H^+ \rightarrow 2C_{(ads)} + H_{(ads)}$.
J_C	direct carbon flux towards catalyst surface
$\frac{J_a\sigma_{ads}}{\upsilon} J_b$	interaction with atomic hydrogen from plasma $C_2H_{2(ads)} + H_{(plasma)} \rightarrow C_2H_{3(plasma)}$, $C_2H_{(ads)} + H_{(plasma)} \rightarrow C_2H_{2(plasma)}$.
$\frac{N_c\sigma_{ads}}{\upsilon} J_b$	interaction with atomic hydrogen $C_{(ads)} + H_{(plasma)} \rightarrow CH_{(plasma)}$.
$N_c\upsilon\exp\left(\frac{-E_{ev}}{k_B T_S}\right)$	evaporation of carbon $C_{(ads)} \rightarrow C_{(evaporation)}$.
$n_{sa}\upsilon\exp\left(\frac{-E_{dhc}}{k_B T_S}\right)$	desorption of hydrocarbons $C_2H_{2(ads)} \rightarrow C_2H_{2(des)}$, $C_2H_{(ads)} \rightarrow C_2H_{(des)}$.

Ravi Gupta, Department of Applied Physics, Delhi Technological University, Delhi, India

4.3.6 Growth rate equation of N-CNF

$$\frac{d}{dt}\left[\pi\left(D^2-d^2\right)h\right]=\left[\begin{matrix}\frac{D_s N_C}{\upsilon}D+\frac{D_b N_C}{2\upsilon}\pi D\\ +4kN_C\pi D^2\end{matrix}\right]\times\left(1-\Omega_c\right)\times\left(\frac{P}{\rho_{ncnf}I_{ia}}\right)+\frac{16D_m m_{cat}}{\rho_{cat}\times\pi D^2}$$
$$+\left[\begin{matrix}\sum_{b=1}^{2}J_b\left(1-\theta_t\right)+\sum_{b=1}^{2}J_b\exp\left(\frac{-E_{th}}{k_BT_S}\right)+\sum_{a=1}^{2}\frac{n_{sa}y_d}{\upsilon_0}\sum_{b=1}^{2}J_{ia}\\ +\sum_{b=1}^{2}J_{ib}+\sum_{a=1}^{2}n_{sa}\upsilon\exp\left(\frac{-\delta E_{td}}{k_BT_S}\right)-\sum_{b=1}^{2}n_{sb}\exp\left(\frac{-E_{dH}}{k_BT_S}\right)\\ +\sum_{c=1}^{3}\theta_c\left(J_{ic}y_d+\upsilon_0\upsilon\exp\left(\frac{-\delta E_{td}}{k_BT_S}\right)\right)\end{matrix}\right]\frac{\pi D^2}{4\sum_{b=1}^{2}n_{ib}}$$
$$+\left(\sum_{c=1}^{2}\gamma_a I_a++\sum_{c=1}^{5}\gamma_c I_c\right)\pi D^2 h, \qquad (4.13)$$

where D is the catalyst nanoparticle diameter, d is the CNF tip diameter, h is the CNF height, $D_S=D_{S0}\exp\left(-E_S/k_BT_S\right)$ is the surface diffusion coefficient, $D_{S0}=a^2\nu$, a (=0.34 nm) is the carbon atoms' interatomic distance, E_S (=0.3 eV) is the energy barrier for carbon species diffusion through the catalyst nanoparticle surface [31], $D_b=D_{b0}\exp\left(-E_b/k_BT_S\right)$ is the bulk diffusion coefficient, $D_{b0}=D\nu/2\pi$, E_b (=1.6 eV) is the energy barrier for carbon species bulk diffusion through catalyst nanoparticle [31], P(≈20 GPa) is the pressure exerted by graphene layers on catalyst nanoparticle, $k=A_k\exp\left(-\delta E_{inc}/k_BT_S\right)$ is the carbon species incorporation speed in the graphene layers [13], $A_k=a\nu$, δE_{inc} (=0.4 eV) is the carbon species energy barrier to diffuse along the nanofiber–catalyst interface, ρ_{cnf} is the nanofiber density, m_{cat} is the mass of the metal catalyst particle, and ρ_{cat} is the density of metal catalyst nanoparticle. $D_m=D_{m0}\exp\left(-E_{SD}/k_BT_S\right)$ is the metal atoms' diffusion coefficient [31], δE_{td} (=1.87 eV) is the energy for thermal

dehydrogenation of hydrocarbons [33]. δE_{dH} (=1.8 eV) is the hydrogen species desorption energy.

Table 4.4. Various surface processes and their corresponding reactions on the catalyst nanoparticle surface (refs 31–36) considered in the Eq. (4.13) where "ads" and "des" corresponds to the adsorption and desorption of plasma species to/from the catalyst surface, respectively.

Functional term	Explanation and reactions involved
$\frac{D_s N_C}{\upsilon}\pi D$	surface diffusion of carbon species through catalyst nanoparticle
$\frac{D_b N_C}{\upsilon}\pi D$	bulk diffusion of carbon species through catalyst nanoparticle
$4kN_C\pi D^2$	incorporation of the carbon species in the form of graphene layers.
$\frac{D_m m_{cat}}{\rho_{cat}\times\pi D^2}$	metal atoms self-diffusion
$J_b\left(1-\theta_t\right)$	hydrogen adsorption on the catalyst nanoparticle surface $H_{(plasma)} \rightarrow H_{(ads)}$, $H_{2(plasma)} \rightarrow H_{2(ads)}$.
$J_b \exp\left(\frac{-E_{th}}{k_B T_S}\right)$	hydrogen ion incoming flux due to hydrocarbon ions thermal dehydrogenation
$\frac{n_{sa} y_d}{\upsilon_0} J_{ib}$	generation of hydrogen due to ion induced decomposition of hydrocarbons $C_2H^+ + C_2H_{(ads)} \rightarrow 2C_{(ads)} + H_{(ads)} + C_2H^+$, $C_2H_2^+ + C_2H_{(ads)} \rightarrow 2C_{(ads)} + H_{(ads)} + C_2H_2^+$.
J_{ib}	direct hydrogen ion flux
$n_{sa}\upsilon\exp\left(\frac{-\delta E_{td}}{k_B T_S}\right)$	the flux of H atom due to thermal dissociation of hydrocarbons $C_2H_{2(ads)} \rightarrow 2C_{(ads)} + 2H_{(ads)}$, $C_2H_{(ads)} \rightarrow 2C_{(ads)} + H_{(ads)}$.
$\theta_c J_{ic} y_d$	generation of hydrogen due to ion induced dissociation of ammonia $NH_3^+ + NH_{3(ads)} \rightarrow 2N_{(ads)} + 3H_{(ads)} + NH_3^+$, $NH_4^+ + NH_{4(ads)} \rightarrow 2N_{(ads)} + 4H_{(ads)} + NH_4^+$, $NH_2^+ + NH_{2(ads)} \rightarrow 2N_{(ads)} + 2H_{(ads)} + NH_2^+$.
$\theta_c\upsilon_0\upsilon\exp\left(\frac{-\delta E_{td}}{k_B T_S}\right)$	generation of hydrogen due to thermal decompositions of ammonia $NH_{3(ads)} \rightarrow C_{(ads)} + 3H_{(ads)}$, $NH_{4(ads)} \rightarrow C_{(ads)} + 4H_{(ads)}$, $NH_{2(ads)} \rightarrow C_{(ads)} + 2H_{(ads)}$.
$n_{sb}\exp\left(\frac{-E_{dH}}{k_B T_S}\right)$	hydrogen desorption from the catalyst nanoparticle surface $H_{(ads)} \rightarrow H_{(des)}$.

Ravi Gupta, Department of Applied Physics, Delhi Technological University, Delhi, India

$\gamma_a I_a$	Sticking of hydrocarbon neutrals on the CNF surface
$\gamma_c I_c$	Sticking of ammonia neutrals on the CNF surface

All complex processes involved in Eq. (4.13) to describe the growth mechanism of N-CNFs on the catalyst nanoparticle are listed in Table 4.4. The surface and bulk diffusion of carbon species significantly affect the growth of nanostructures, and their relative contribution depends on the catalyst nanoparticle temperature. At high temperatures, bulk diffusion dominates, and at low temperatures, surface diffusion dominates, whereas at intermediate temperatures, both are significant for growth [31,34,37–39]. Therefore, in the present paper, we have taken both the diffusion processes into account because the temperature of the catalyst nanoparticle is assumed to be constant through the growth process. The dissociation of hydrocarbons and the diffusion of carbon species is a key step for nanostructure growth. The growth of nanostructures terminates when the dissociation rate of hydrocarbons on the catalyst nanoparticle surface decreases because of the formation of the continuous carbon layer on the catalyst nanoparticle surface, which consequently prevents the diffusion of carbon species. Thus, term $(1-\Omega c)$, related to amorphous carbon deposition, is taken into account, where $\Omega c = n_c \times \pi D^2$.

Moreover, the realization of these carbon species in the form of a graphene layer is taken into account. Now, the continuously formed graphene layers around the catalyst nanoparticle due to continuous diffusion of carbon species exerts significant pressure on the catalyst nanoparticle and results in the catalyst nanoparticle shape deformation; therefore, the pressure term (outside the first bracket) is taken into account in Eq. (4.13). The catalyst nanoparticle shape deformation is an important process behind the inclination of graphene layers around catalyst nanoparticles during nanofiber growth. Therefore, the change in catalyst nanoparticle shape due to the metal atoms' self-diffusion is also taken into account. Due to continuous carbon supply, both vertical as well as in-plane growth of carbon precipitation continuous, but in-plane growth stops as a result of etching of terminal carbons by the

active hydrogen radicals and ions. Moreover, due to the presence of nitrogen in the reactive plasma, nitrogen incorporation is also taken into account in this equation. Nitrogen insertion/doping in the CNF lattice significantly affects the physical structure and growth of CNFs.

4.4 Results and discussion

In the present chapter, an analytical model has been used to describe the N-CNF growth (i.e., the effects of nitrogen doping on the CNF growth) and its field emission properties through the catalyst-assisted PECVD process. The analytical model incorporates the charging of N-CNFs; kinetics of plasma species (electron, ions, and neutrals); surface as well as bulk diffusion, accretion, and adsorption of carbon species on the catalyst nanoparticle surface; sticking of nitrogen atoms on the catalyst nanoparticle surface; incorporation of carbon species in the form of graphene layers around the catalyst nanoparticle; and vertical growth due to the plasma sheath effect.

The numerical solutions of the first-order, simultaneous differential Eqs. (4.1)–(4.13) given in Sec. 4.3 have been solved using MATHEMATICA software for experimentally determined boundary conditions and the glow discharge plasma parameters. The detailed overview of different sources of plasma excitation and process-related parameters, such as plasma power, gas pressure, substrate temperature, and plasma composition, used for the PECVD growth of CNFs/CNTs based on experimental works have been summarized in Table 4.5. Following Merkulov *et al.*[6] and Mao and Bogaerts [14], the process parameters and boundary conditions used in the present study are listed in Tables 4.6 and 4.7. Moreover, other parameters used in the present model are: $m_{ia} = m_a$ =26 and 25 a.m.u. for C_2H_2 and C_2H, respectively; $m_{ib} = m_b$ =2 and 1 a.m.u. for H_2 and H, respectively; $m_{ic} = m_c$ =17 a.m.u., 18 a.m.u., 16 a.m.u., 14 a.m.u., and 27 a.m.u. for NH_3, NH_4, NH_2, N, and HCN, respectively; atomic mass of nickel (m_{cat})=58.69 a.m.u.; density of catalyst nickel (ρ_{ct})=8.96 g/cm^3); coefficient of recombination of electrons and ions ($\alpha_{a0} \approx \alpha_{b0} \approx \alpha_{c0}$)=1.12 × 10^7 cm^3/s; κ =−1.2; sticking coefficient of electrons (γ_e)=1; sticking coefficient of ions ($\gamma_{ia} = \gamma_{ib} = \gamma_{ic}$)=1; and sticking coefficient of neutral atoms ($\gamma_a = \gamma_b = \gamma_c$)=1.

Table 4.5. The different sources of plasma excitation and process-related parameters used for the plasma-enhanced chemical vapour deposition (PECVD) growths of carbon nanofibers (CNFs)/CNTs based on experimental works.

Source of plasma excitation	Gas mixture	Gas ratio (flow rate)	Pressure	Substrate temperature	Plasma power	Reference
Direct-current (dc)	C_2H_2/NH_3	40/80 sccm	3 Torr	700 ^{0}C	123 W	[6]
dc	C_2H_2/NH_3	(0-76)/200 sccm	1.875 Torr	650 ^{0}C	--	[15]
dc	C_2H_2/NH_3	(0-150)/200 sccm	3.5 Torr	750 ^{0}C	--	[41]
dc	C_2H_2/NH_3	50/200 sccm	1.125 Torr	120-500 ^{0}C	--	[42]
dc	C_2H_2/NH_3	50/200 sccm	--	250 ^{0}C	20 W	[43]
dc	C_2H_2/NH_3	30/200 sccm	1.5 mbarr	200 ^{0}C	--	[44]
dc	C_2H_2/NH_3	50/200 sccm	0.7 mbarr	500 ^{0}C	20 W	[45]
(Micro-wave) MW	C_2H_2/NH_3	200 sccm	20 Torr	825 ^{0}C	--	[46]
MW	CH_4/NH_3	(150-240)/(60-150) sccm	21 Torr	650-1000 ^{0}C	--	[47]
Inductive coupled plasma (ICP)	CH_4/H_2	20/80 sccm	0.5-20 Torr	800-1000 ^{0}C	120 W	[48]
ICP	C_2H_4/H_2	(5-20)/(80-95) sccm	3 Torr	600-1000 ^{0}C	50-200 W	[49]
ICP	CH_4/H_2	50/50 sccm	1 Torr	500-650 ^{0}C	--	[50]
ICP	C_2H_2/H_2	(37.5-88)/(12-62.5) sccm	50 mTorr	700 ^{0}C	27 W	[51]
ICP	C_2H_2/H_2	15/85 sccm	20 mTorr	500 ^{0}C	400 W	[52]
RF	CH_4/H_2	0.4/20 sccm	5 Pa	400 ^{0}C	350 W	[53]
RF	C_2H_2/NH_3	5/20 sccm	--	450 ^{0}C	180 W	[54]

Table 4.6. Parameters used in the present model.

Parameter	value
pressure	3 Torr
plasma power	123 Watt
substrate Temperature	700 ^{0}C
C_2H_2 gas flow rate	40 sccm
H_2 gas flow rate	80 sccm
NH_3 gas flow rate	80 sccm
electron temperature	2.2 eV
ion temperature	2200 K
neutral temperature	2000 K
substrate potential	-300 V

Table 4.7. Number density of various plasma species considered in the present model.

Number density of various species	Value	
	Undoped CNF (C_2H_2/H_2 gas mixture)	**Nitrogen doped CNF (C_2H_2/NH_3 gas mixture)**
n_{e0}	10^{10} cm^{-3}	10^{10} cm^{-3}
$C_2H_2^+$	0.645 n_{e0},	0.55 n_{e0},
C_2H^+	0.05 n_{e0}	0.04 n_{e0},
H_2^+	0.34 n_{e0}	0.05 n_{e0}
H^+	0.01 n_{e0}	0.05 n_{e0}
C_2H_2	0.5×10^{14} cm^{-3}	0.5×10^{14} cm^{-3}
C_2H	0.2×10^{11} cm^{-3}	0.2×10^{11} cm^{-3}
H_2	10^{15} cm^{-3}	10^{15} cm^{-3}
H	0.2×10^{14} cm^{-3}	0.1×10^{14} cm^{-3}
NH_3^+		0.09 n_{e0}
NH_4^+		0.1 n_{e0}
NH_2^+		0.1 n_{e0}
HCN^+		0.01 n_{e0}
N^+		0.01 n_{e0}
NH_3		0.5×10^{15} cm^{-3}
NH_4		0.5×10^{13} cm^{-3}
NH_2		0.5×10^{13} cm^{-3}
HCN		0.2×10^{12} cm^{-3}
N		0.9×10^{11} cm^{-3}

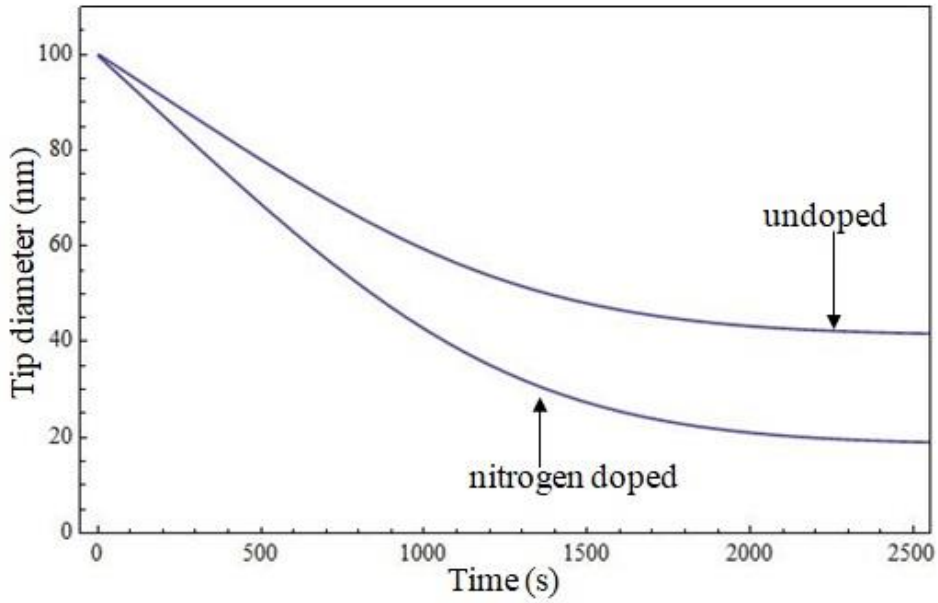

Fig. 4.2. The time variation of tip diameter for undoped CNF (growth of CNF in C_2H_2/H_2 gas plasma) and nitrogen-doped CNF (growth of CNF in C_2H_2/NH_3 plasma) at C_2H_2 flow rate=40 sccm, H_2 flow rate=80 sccm, and NH_3 flow rate=80 sccm. Other parameters are given in the text.

Fig. 4.2 shows the time variation of tip diameter for undoped (growth of CNF in C_2H_2/H_2 gas plasma) and nitrogen-doped CNF (growth of CNF in C_2H_2/NH_3 plasma). The tip diameter of both undoped and nitrogen-doped CNFs decreases with growth time. This can be easily explained by the fact that the diameter of catalyst nanoparticles at the tips of vertically aligned CNFs decreases during growth due to the stress exerted by growing graphene layers on the catalyst particles and self-diffusion of metal atoms of the catalyst [36]. Moreover, from Fig. 4.2, it can also be seen that the tip diameter *d* of the CNF decreases rapidly in the case of nitrogen-doped CNFs compared to the undoped CNFs. This reduction in tip diameter on account of nitrogen doping can be clarified with various facts. One such clarification is that, on ammonia insertion in the plasma, the amount of atomic hydrogen species (H and H^+) in the plasma increases (cf. Fig 4.3), and consequently, the etching of CNFs increases. Moreover, on ammonia addition, many additional etchant species, that is, atomic nitrogen and cyanide species (N, N^+, HCN^+), form in the plasma. Thus, the relative etching of CNFs on account of nitrogen increases compared to undoped CNFs.

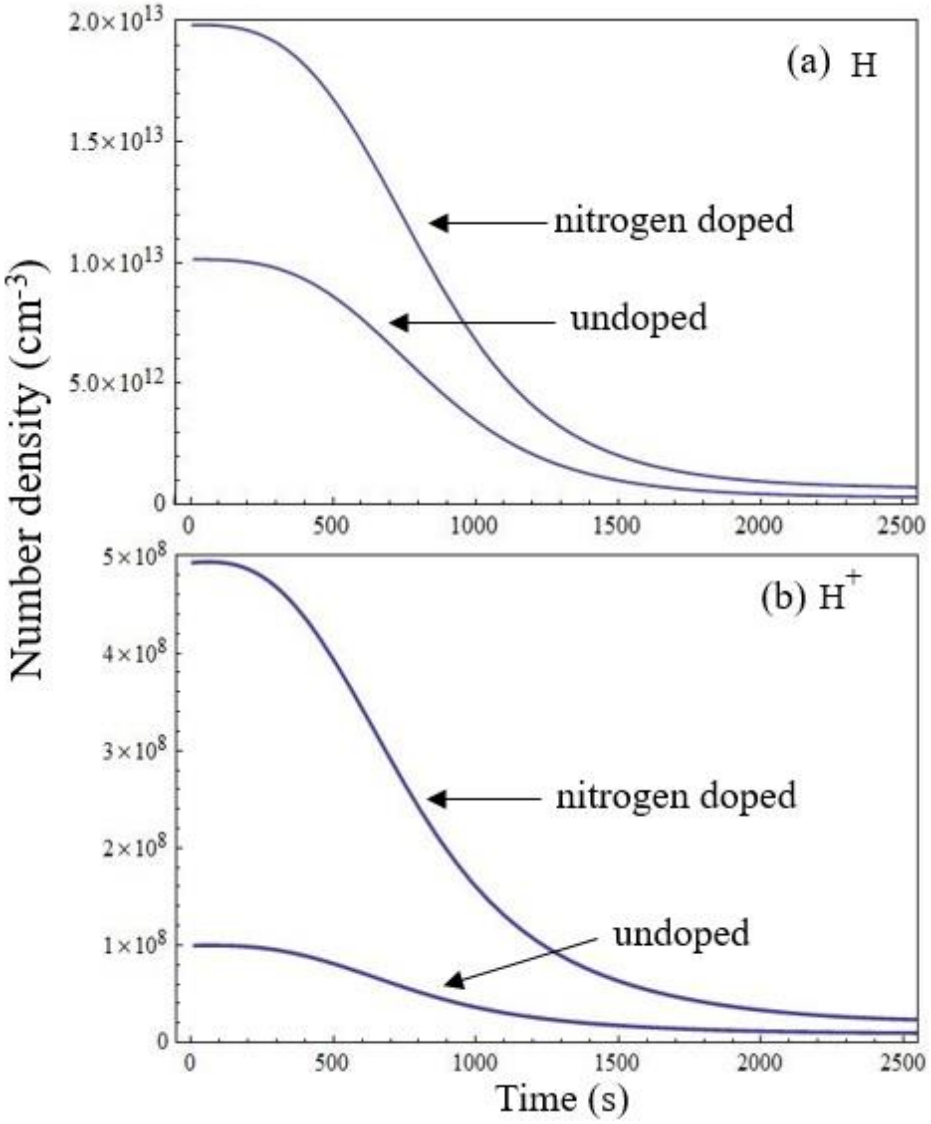

Fig. 4.3. The time variation of number density for (a) *H* and (b) H^+ in the plasma for undoped (growth of CNF in C_2H_2/H_2 gas plasma) and nitrogen-doped CNF (growth of CNF in C_2H_2/NH_3 plasma) at C_2H_2 flow rate=40 sccm, H_2 flow rate=80 sccm, and NH_3 flow rate=80 sccm. Other parameters are given in the text.

As nitrogen doping has been taken into account, the height of CNFs decreases, as can be seen from Fig. 4.4. On ammonia addition, ammonium ions are formed in the plasma, which contains pentavalent nitrogen. Therefore, the incorporation of nitrogen in the CNF lattice generates more electrons, and consequently, the ionization of neutral hydrocarbon increases. This suppresses the concentration of hydrocarbon neutrals available for growth (cf. Fig. 4.5). Moreover, hydrocarbon ions in the plasma form cyanide species on reacting with ammonia. Thus, these cyanide species also decrease the concentration of carbon species available for growth. A similar effect of nitrogen doping on the

diameter and height was observed by Sumpter *et al.*[54] in their nitrogen-mediated growth of bamboo-shaped carbon nanotubes (CNFs).

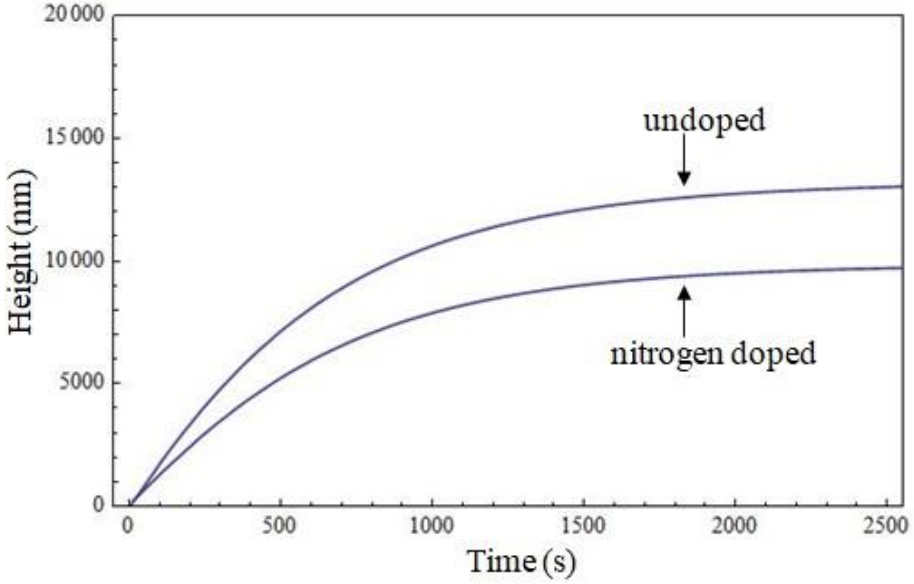

Fig. 4.4. The time variation of height for undoped (growth of CNF in C_2H_2/H_2 gas plasma) and nitrogen-doped CNF (growth of CNF in C_2H_2/NH_3 plasma) at C_2H_2 flow rate=40 sccm, H2 flow rate=80 sccm, and NH_3 flow rate=80 sccm. Other parameters are given in the text.

The superior field emission from carbon nanostructures (CNTs and CNFs) comes from their geometry rather than their crystalline structure [11], and therefore, field emission is primarily characterized by the field enhancement factor β *(=h/r),* where *h* is the height of the CNF and *r* is the CNF tip radius, which signifies the electric field amplification at the tip of the emitter. Thus, from the results obtained, we have estimated the variation in the field enhancement factor for undoped CNFs and N-CNFs. From Table 4.8, it can be seen that the field enhancement factor is much larger for nitrogen-doped CNFs as compared to Undoped CNFs. Kimura *et al.*[10] experimentally observed improved field emission from nitrogen-treated CNFs.

Table 4.8. Estimation of field enhancement factor for undoped and nitrogen-doped carbon nanofibers (CNFs) from the result obtained in Figs 4.2 and 4.4.

CNFs	Height (nm)	Tip Diameter (nm)	Field Enhancement Factor
Undoped	13105	43.8	299.2
Nitrogen Doped	10031	21.1	475.4

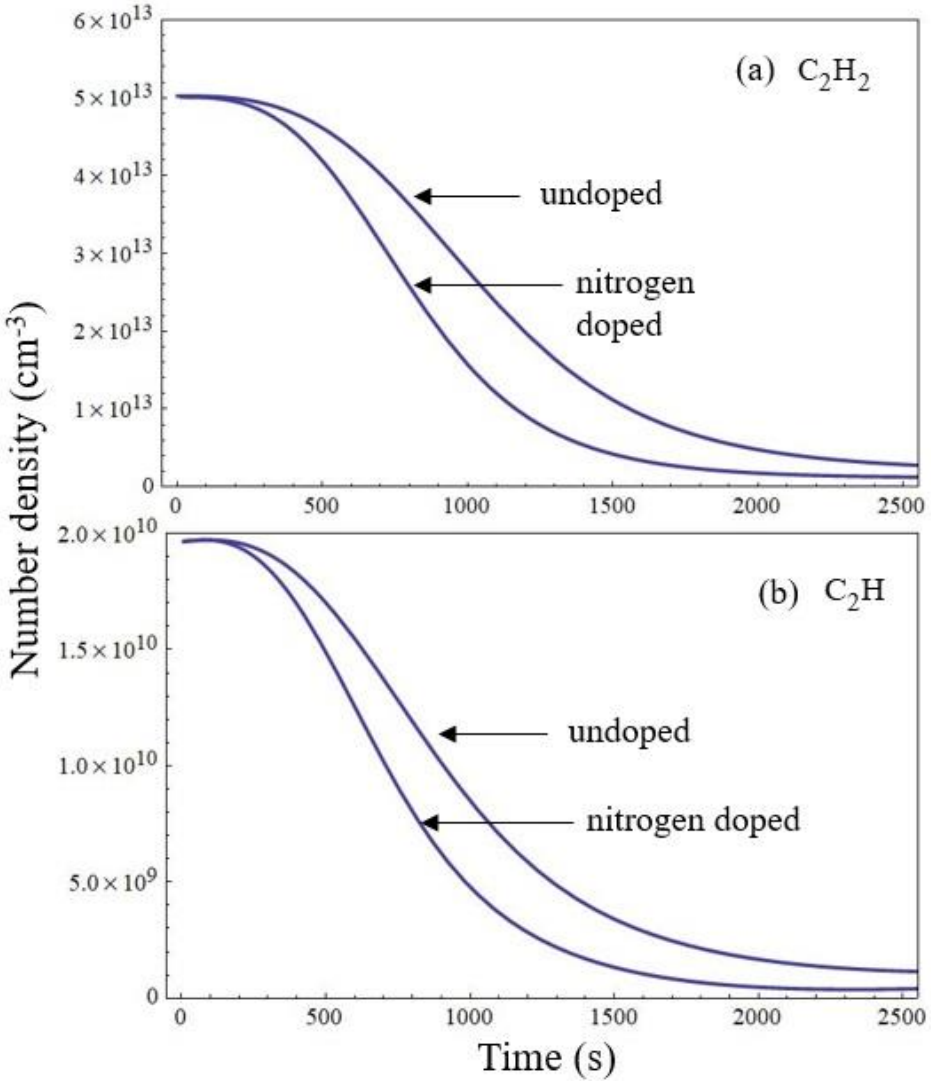

Fig. 4.5. Time variation of nitrogen density for (a) C_2H_2 and (b) C_2H for undoped (growth of CNF in C_2H_2/H_2 gas plasma) and nitrogen-doped CNF (growth of CNF in C_2H_2/NH_3 plasma) at C_2H_2 flow rate=40 sccm, H_2 flow rate=80 sccm, and NH_3 flow rate=80 sccm. Other parameters are given in the text.

Moreover, we have also observed that the relative concentration of hydrocarbon and nitrogen (ammonia) in the plasma significantly affects the N-CNFs growth and structure. Fig. 4.6(a) shows the time variation of N-CNF height at different hydrocarbon (i.e., C_2H_2) gas flow rates, and Fig. 4.6(b) shows the N-CNFs growth rate (height of N-CNFs per unit deposition time) as a function of hydrocarbon (i.e., C_2H_2) to nitrogen feedstock gas (ammonia) ratio in C_2H_2/NH_3 plasma.

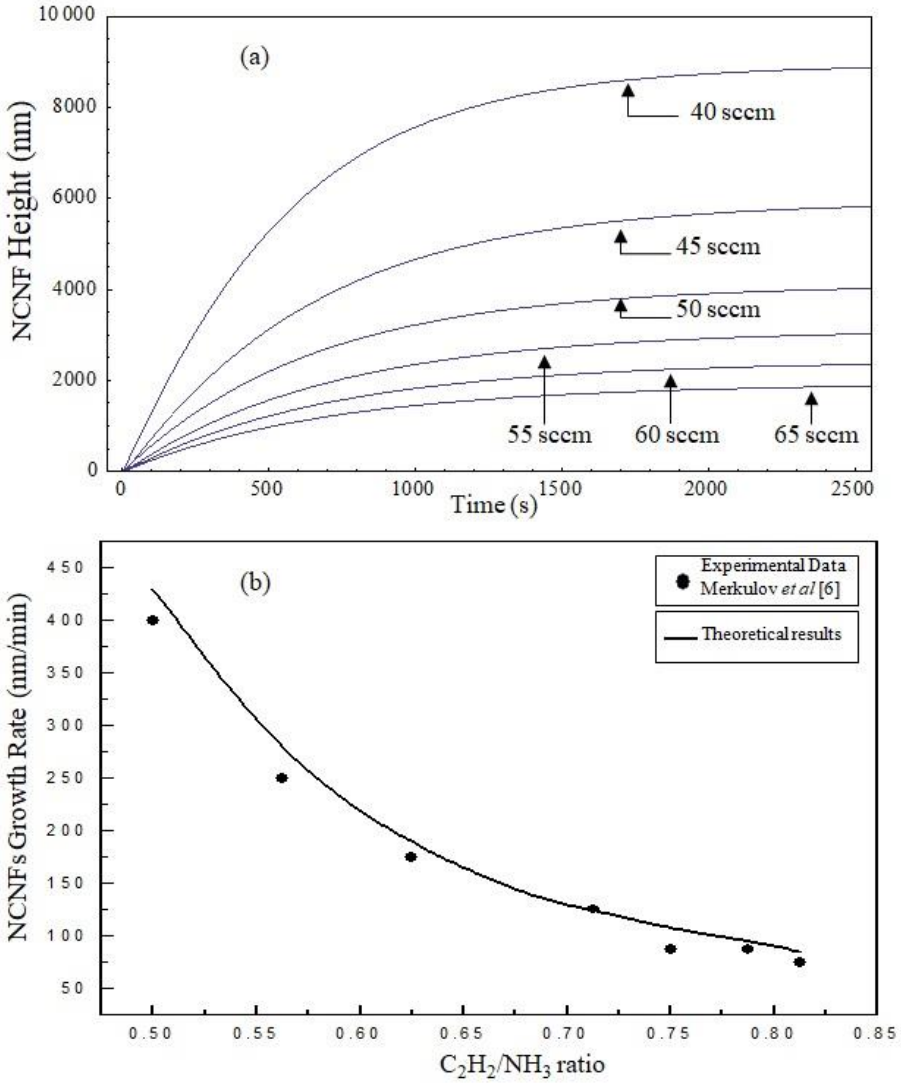

Fig. 4.6. (a) The time variation of N-CNF height for different C_2H_2 gas flow rates in C_2H_2/NH_3 plasma, keeping NH_3 gas flow rate constant at 80 sccm. (b) N-CNFs growth rate as a function of C_2H_2/NH_3 ratio for variable C_2H_2 gas flow rate and constant NH_3 gas flow rate. Other parameters are given in the text.

The results demonstrated in Fig. 4.6 are obtained for a fixed ammonia gas flow rate and variable acetylene gas flow rate. As can be seen, N-CNF height decreases when C_2H_2 gas flow rate increases, that is, N-CNFs growth rate decreases with increase in C_2H_2/NH_3 ratio. This result is somewhat surprising because one would think that higher carbon supply content would lead to a higher growth rate. However, the reverse trend is followed in reality. This astonishing growth of N-CNFs can be explained in many ways. One possible explanation is the poisoning of the catalyst particle. As C_2H_2 gas flow rate increases, carbon species generated on the catalyst nanoparticle surface increase

(cf. Fig. 4.7), which leads to the formation of a thin amorphous carbon layer on the catalyst nanoparticle surface, which blocks the diffusion of carbon species through catalyst nanoparticles. Thus, N-CNFs grow at a lower rate due to loss of catalytic activity of nanoparticles. The curve obtained in Fig. 4.6(b) is compared with the experimental data of Merkulov *et al.*[6].

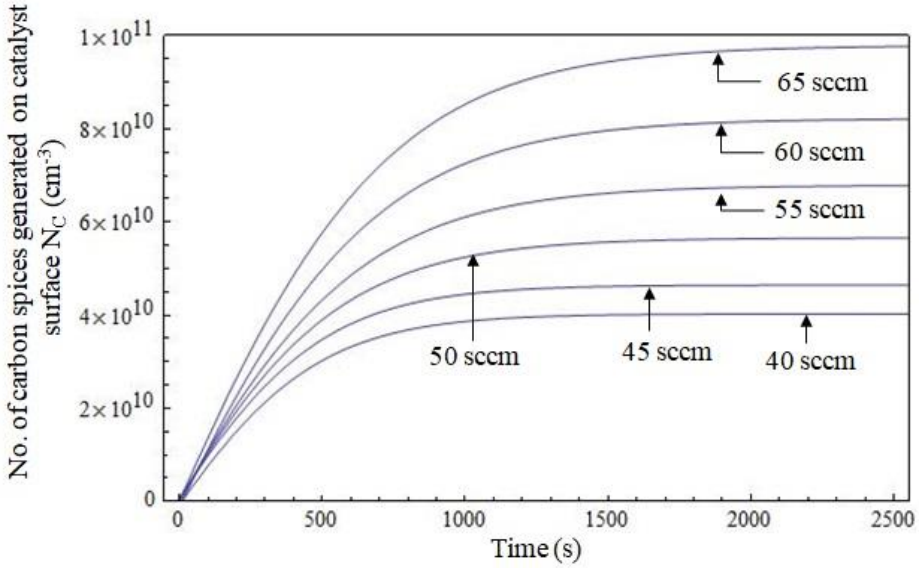

Fig. 4.7. Time variation of the number of carbon species per unit area generated on the catalyst nanoparticle surface for different C_2H_2 gas flow rates in C_2H_2/NH_3 plasma, keeping NH_3 gas flow rate constant at 80 sccm. Other parameters are given in the text.

One can see from this figure that the N-CNFs growth rate curve fits best with the experimental data of Merkulov *et al.*[6] in the broad range of C_2H_2/NH_3 ratios. However, one might wonder whether the same trend is to be followed if the NH_3 flow rate is varied, keeping the C_2H_2 flow rate constant. Fig. 4.8 shows the time variation of N-CNFs height for different ammonia gas flow rates. From Fig. 4.8, it can be seen that N-CNF height increases with increase in ammonia gas flow rate, and therefore, N-CNF growth rate increases with the decrease in C_2H_2/NH_3 ratio. This is imputable to the fact that number density of etchant species (i.e., N, N^+, HCN^+) increases in the reactive plasma as NH_3 gas flow rate increases [cf. Fig. 4.9a–4.9c]. Moreover, reactions between hydrocarbons, hydrogen, and ammonia in the reactive plasma produce a large amount of active hydrogen (cf. Table 4.2). Thus, the number density of active hydrogen increases in the plasma, with an increase in NH_3 flow rate [cf. Fig. 4.9d]. Therefore, these

species etch the amorphous carbon layer formed on the catalyst surface and contributes to the higher growth rate.

In Fig. 4.10, the dependence of N-CNF tip diameter as a function of C_2H_2/NH_3 ratio is shown for the PECVD case. From Fig. 4.10, it can be seen that the N-CNFs tip diameter decreases with decrease in C_2H_2/NH_3 ratio; that is, reduction in N-CNFs tip diameter is observed when either C_2H_2 content is decreased or NH_3 content is increased in reactive plasma. If the C_2H_2 gas flow rate increases, carbon deposition on the catalyst nanoparticle surface (which is at the tip of the N-CNFs) increases, and consequently, N-CNFs tip diameter increases. However, when the NH_3 inflow rate increases, that is, C_2H_2/NH_3 ratio decreases, the number of etchant species, as explained above, increases in the reactive plasma, and therefore, the relative etching of catalyst nanoparticles increases, and N-CNFs tip diameter decreases. From Fig. 4.10, one can also see that the dependence of N-CNFs tip diameter on C_2H_2/NH_3 ratio fits better with the experimental data of Merkulov *et al.*[6] A similar effect of the C_2H_2/NH_3 ratio on the tip diameter was observed by Saidin *et al.*[8].

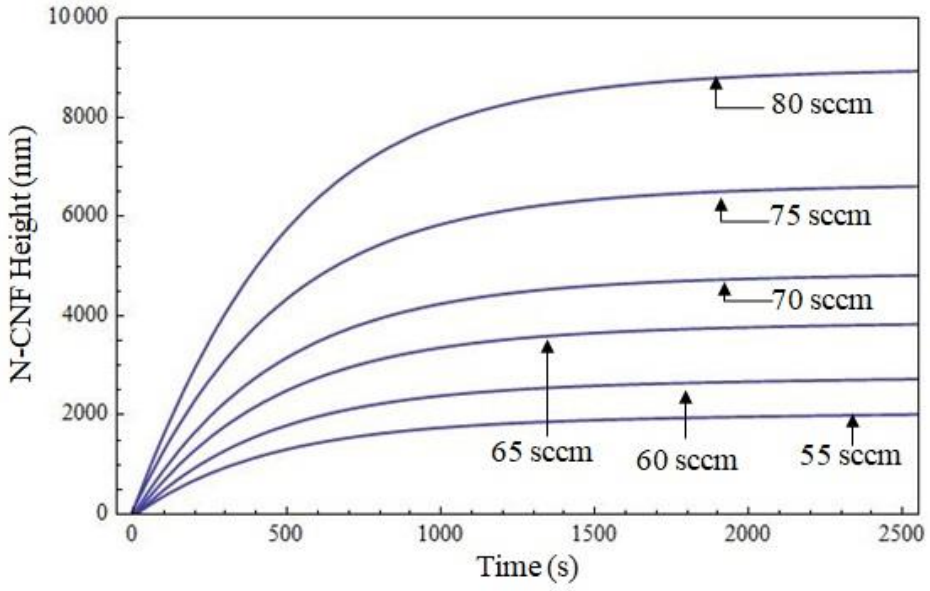

Fig. 4.8. Time variation of N-CNF height for different NH_3 gas flow rates in C_2H_2/NH_3 plasma, keeping C_2H_2 gas flow rate constant at 40 sccm. Other parameters are given in the text.

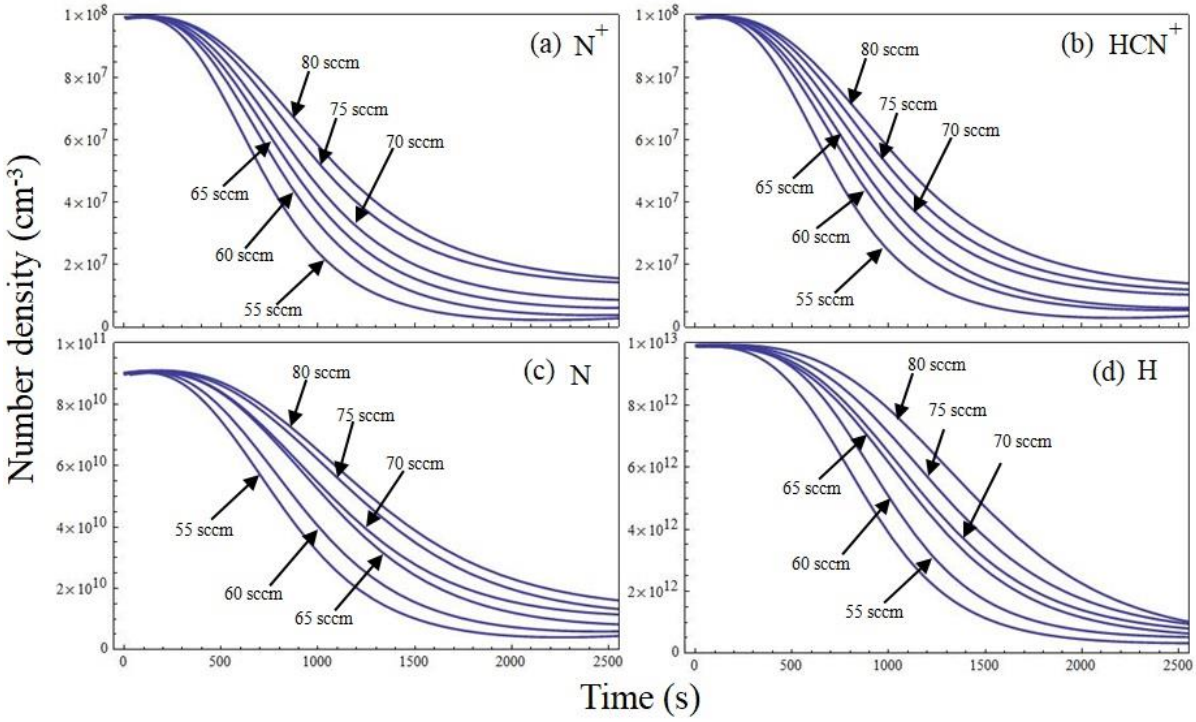

Fig. 4.9. Time variation of nitrogen density for (a) N^+, (b) HCN^+, (c) N, and (d) H for different NH_3 gas flow rates in C_2H_2/NH_3 plasma, keeping C_2H_2 gas flow rate constant at 40 sccm. Other parameters are given in the text.

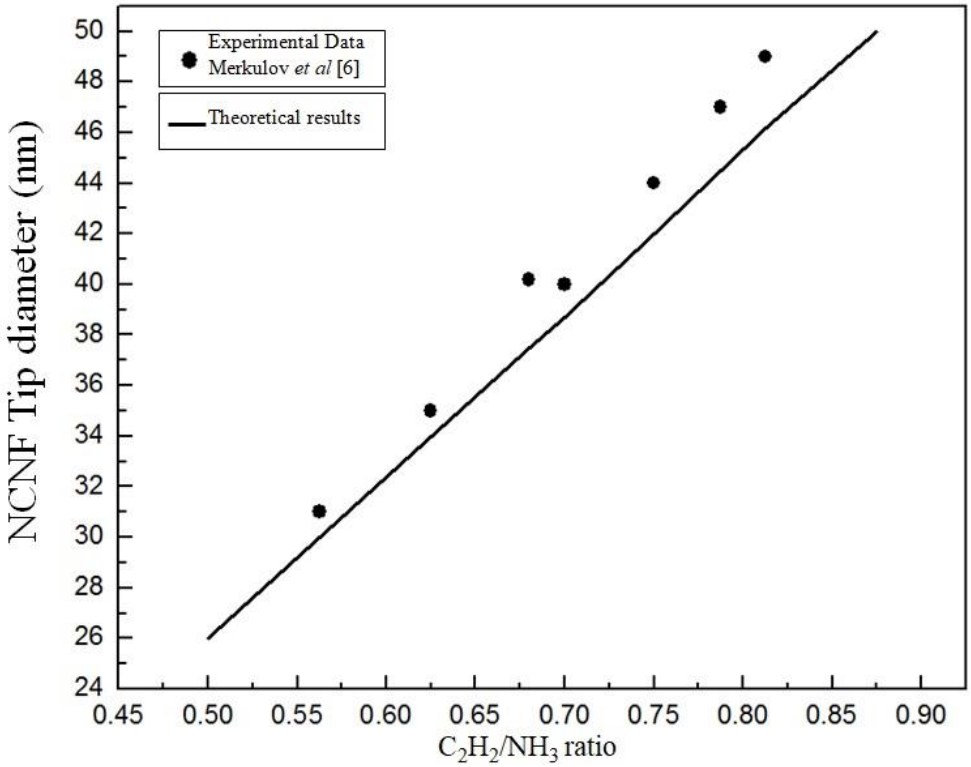

Fig. 4.10. N-CNF tip diameter as function of C_2H_2/NH_3 ratio for variable C_2H_2 gas flow rate and constant NH_3 gas flow rate. Other parameters are given in the text.

References

[1] V. I. Merkulov, A. V. Melechko, M. A. Guillorn, D. H. Lowndes, and M. L. Simpson, Appl. Phys. Lett. **79,** 2970 (2001).

[2] T. M. Minea, S. Point, A. Granier, and M. Touzeau, *Appl. Phys. Lett.*, **85,** 1244 (2004).

[3] P. Serp, M. Corrias, and P. Kalch, Appl. Catal. A **253**, 337 (2003).

[4] K. P. De Jong and J. W. Geus, *Catal.* Rev. Sci. Eng. **42**, 48 (2009).

[5] O. Y. Podyacheva, Z. R. Ismagilov, A. E. Shalagina, V. A. Ushakov, A. N. Shmakov, S. V. Tsybulya, V. V. Kriventsov, and A. V. Ischenko, Carbon **48**, 2792 (2010).

[6] V. I. Merkulov, D. K. Hensley, A. V. Melechko, M. A. Guillorn, D. H. Lowndes, and M. L. Simpson, J. Phys. Chem B **106**, 10570 (2002).

[7] V. I. Merkulov, A. V. Melechko, M. A. Guillorn, D. H. Lowndes, and M. L. Simpson, Appl. Phys. Lett. **80**, 476 (2002).

[8] M. A. R. Saidin, A. F. Ismail, S. M. Sanip, P. S. Goh, M. Aziz, and M. Tanemura, Thin Solid Films **520**, 2575 (2012).

[9] K. B. K. Teo, S. B. Lee, M. Chhowalla, V. Semet, V. T. Binh, O. Groening, M. Castignolles, A. Loiseau, G. Pirio, P. Legagneux, D. Pribat, D. G. Hasko, H. Ahmed, G. A. J. Amaratunga, and W. I. Milne, Nanotechnology **14**, 204 (2003).

[10] C. Kimura, Y. Yamamuro, H. Aoki, and T. Sugino, Diamond Relat. Mater. **16**, 1383 (2007).

[11] J. W. G. Wildoer, L. C. Venema, A. G. Rinzler, R. E. Smalley, and C. Dekker, Nature **391**, 59 (1998).

[12] Z. R. Ismagilov, A. E. Shalagina, O. Y. Podyacheva, A. V. Ischenko, L. S. Kibis, A. I. Boronin, Y. Chesalov, D. I. Kochubey, A. I. Romanenko, O. B. Anikeeva, T. I. Buryakov, and E. N. Tkachev, Carbon **47**, 1992 (2009).

[13] M. Mao, J. Benedikt, A. Consoli, and A. Bogaerts, J. Phys. D Appl. Phys. **41**, 225201 (2008).

[14] M. Mao and A. Bogaerts, J. Phys. D Appl. Phys. **43** (205), 201 (2010).

[15] M. S. Bell, R. G. Lacerda, K. B. K. Teo, N. L. Rupesinghe, G. A. J. Amaratunga, W. I. Milne, and M. Chhowalla, Appl. Phys. Lett. **85**, 1137 (2004).

[16] V. I. Merkulov, M. A. Guillon, D. H. Lowndes, M. L. Simpson, and E. Voelkl, Appl. Phys. Lett. **79**, 1178 (2001).

[17] I. Denysenko and N. A. Azarenkov, J. Phys. D: Appl. Phys. **44**, 174031 (2011).

[18] M. A. Lieberman and A. J. Lichtenberg, Principles of Plasma Discharges and Material Processing (*Wiley Interscience Publications*, USA, 1994).

[19] C. S. Cojocaru, A. Senger, and F. L. Normand, J. Nanosci. Nanotech. **6**, 1 (2006).

[20] N. M. Rodriguez, J. Mater. Res. **8**, 3233 (1993).

[21] G. B. Zheng, K. Kouda, H. Sano, Y. Uchiyama, Y. F. Shi, and H. J. Quan, Carbon **42**, 635 (2004).

[22] H. W. Wei, K. C. Leou, M. T. Wei, Y. Y. Lin, and C. H. Tsai, J. Appl. Phys. **98**, 044313 (2005).

[23] K. N. Ostrikov, S. V. Viladimirov, M. Y. Yu, and G. E. Morfill, Phys. Plasmas, **7**, 461 (2000).

[24] S. V. Viladimirov, K. N. Ostrikov, and M. Y. Yu, Phys. Rev. E **58**, 8046 (1998).

[25] A. V. Keudell and W. Moller, J. Appl. Phys. **75**, 7718 (1994).

[26] M. S. Sodha, S. Misra, and S. K. Mishra, Phys. Plasmas **17**, 113705 (2010).

[27] D. B. Hash, M. S. Bell, K. B. K. Teo, B. A. Cruden, W. I. Milne, and M. Meyyappan, Nanotechnology **16**, 925 (2005).

[28] UMIST. http://www.udfa.net/

[29] I. B. Denysenko, S. Xu, J. D. Long, P. P. Rutkevych, N. A. Azarenkov, and K. Ostrikov, J. Appl. Phys. **95**, 2713 (2004).

[30] H. Cui, X. Yang, M. L. Simpson, D. H. Lowndes, and M. Varela, Appl. Phys. Lett. **84**, 20 (2004).

[31] I. Denysenko and N. A. Azarenkov, J. Phys. D: Appl. Phys. **44,** 174031 (2011).

[32] I. Denysenko and K. Ostrikov, J. Phys. D Appl. Phys. **42**, 015208 (2009).

[33] Z. Marvi, S. Xu, G. Foroutan, and K. Ostrikov, Phys. Plasmas **22**, 013504 (2015).

[34] I. Denysenko and K. Ostrikov, Appl. Phys. Lett. **90,** 251501 (2007).

[35] H. Mehdipour, K. Ostrikov, and A. E. Rider, Nanotechnology **21**, 455605 (2010).

[36] I. Denysenko, K. Ostrikov, M. Y. Yu, and N. A. Azarenkov, J. Appl. Phys. **102**, 074308 (2007).

[37] M. Yudasaka, R. Kikuchi, T. Matsui, Y. Ohki, S. Yoshimura, and E. Ota, Appl. Phys. Lett. **67**, 2477 (1995).

[38] O. A. Louchev, T. Laude, Y. Sato, and H. Kanda, J. Chem. Phys. **118**, 7622 (2003).

[39] S. Hofmann, G. Csanyi, A. C. Ferrari, M. C. Payne, and J. Robertson, Phys. Rev. Lett. **95**, 036101 (2005).

[40] M. Chhowalla, K. B. K. Teo, C. Ducati, N. L. Rupesinghe, G. A. J. Amaratunga, A. C. Ferrari, D. Roy, J. Robertson, and W. I. Milne, J. Appl. Phys. **90**, 5308 (2001).

[41] S. Hofmann, C. Ducati, J. Robertson, and B. Kleinsorge, Appl. Phys. Lett. **83**, 135 (2003).

[42] M. Cantoro, V. B. Golovkob, S. Hofmanna, D. R. Williamsa, C. Ducatic, J. Gengb, B. O. Boskovicc, B. Kleinsorgea, D. A. Jeffersonb, A. C. Ferraria, B. F. G. Johnsonb, and J. Robertsona, Diamond Relat. Mater. **14**, 733 (2005).

[43] S. Hoffmann, C. Ducati, B. Kleinsorge, and J. Robertson, Appl. Phys. Lett. **83**, 4661 (2003).

[44] S. Hofmann, M. Cantoro, M. Kaempgen, D. J. Kang, V. B. Golovko, H. W. Li, Z. Yang, J. Geng, W. T. S. Huck, B. F. G. Johnson, S. Roth, and J. Robertson, Appl. Phys. A **81**, 1559 (2005).

[45] C. Bower, W. Zhu, S. Jin, and O. Zhou, Appl. Phys. Lett. **77**, 830 (2000).

[46] H. Cui, O. Zhou, and B. R. Stoner, J. Appl. Phys. **88**, 6072 (2000).

[47] L. Delzeit, I. McAninch, B. A. Cruden, D. Hash, B. Chen, J. Han, and M. Meyyappan, J. Appl. Phys. **91**, 6027 (2002).

[48] K. Matthews, B. A. Cruden, B. Chen, M. Meyyappan, and L. Delzeit, J. Nanosci. Nanotechnol. **2**, 475 (2002).

[49] C. H. Weng, C. S. Yang, H. Lin, C. H. Tsai, and K. C. Leou, J. Nanosci. Nanotechnol. **8**, 2526 (2008).

[50] J. B. O. Caughman, L. R. Baylor, M. A. Guillorn, V. I. Merkulov, D. H. Lowndes, and L. F. Allard, Appl. Phys. Lett. **83**, 1207 (2003).

[51] Y. Y. Lin, H. W. Wei, K. C. Leou, H. Lin, C. H. Tung, M. T. Wei, C. Lin, and C. H. Tsai, J. Vac. Sci. Technol. B **24**, 97 (2006).

[52] Y. Shiratori, H. Hiraoka, Y. Takeuchi, S. Itoh, and M. Yamamoto, Appl. Phys. Lett. **82**, 2485 (2003).

[53] H. S. Kang, H. J. Yoon, C. O. Kim, J. P. Hong, I. T. Han, S. N. Cha, B. K. Song, J. E. Jung, N. S. Lee, and J. M. Kim, Chem, Phys. Lett. **349**, 196 (2001).

[54] B. G. Sumpter, V. Meunier, J. M. Romo-Herrera, E. Cruz-Silva, D. A. Cullen, H. Terrones, D. J. Smith, and M. Terrones, ACS Nano **1**, 369 (2007).

5

Theoretical modeling to study the impact of different oxidizers (etchants) on the plasma-assisted catalytic carbon nanofiber growth

5.1 Brief outline of the chapter

In this chapter, we attempt to present the kinetic model to compare the effects of utilizing oxygen and water as the etching gases, on the plasma assisted catalyzed growth of vertically aligned CNFs accounting the plasma sheath effects and various surface processes including the formation of the amorphous carbon layer on the catalyst surface and poisoning of the catalyst nanoparticle. The first order kinetic differential equations have been assessed simultaneously and their results in the view of time evaluation analysis are discussed.

5.2 Introduction

Rolled graphene sheets in the form of one-dimensional carbon nanostructures, i.e., carbon nanofibers (CNFs) and carbon nanotubes (CNTs) have attracted great interest for applications in field emission devices inferable from their exceptional electrical properties [1-3]. Catalyst-assisted plasma enhanced chemical vapor deposition (PECVD) process is thought to be the most promising growth technique to grow vertically aligned CNFs/CNTs [4-6]. In PECVD growth process, a thin layer of metal catalyst is deposited over the substrate surface, and upon plasma processing in the presence of etching gas, granulated into the metal catalyst nanoparticles [7].

Published work of the present chapter:

1. **Ravi Gupta** and Suresh C. Sharma, Theoretical modeling to study the impact of different oxidizers (etchants) on the plasma-assisted catalytic carbon nanofiber growth, *Phys. Plasmas* **24,** 073504 (2017).

Each catalyst nanoparticle serves as the nucleation seed for the CNFs/CNTs growth by decomposing the carbon precursors over its active surface coming from the reactive plasma that comprises a carbon source gas and an etching gas [8, 9]. Catalyst activity during the growth, i.e., catalyst lifetime influences the CNFs/CNTs growth rate and catalyst lifetime decreases due to the formation of the amorphous carbon layer on the catalyst surface. Removal of amorphous carbon is one of the major concerns to enhance the CNFs/CNTs growth rate.

Etching gas etches the amorphous carbon layer formed on the active surface and retains the activity of the catalyst. Usually, hydrogen and nitrogen are utilized as the etching gases [10-12]. In the catalytic chemical vapor deposition growth process, it is observed that introducing a small amount of oxidizer such as H_2O and O_2 can colossally expand the CNFs/CNTs growth rates. The presence of water vapours in the growth atmosphere amplifies the catalyst lifetime and preserves the catalyst action because of which CNFs/CNTs growth time and their length increments [13-15]. Besides, water vapors were also found to change their structure from multiwall to more slender nanotubes [16]. A few reviews have shown the possibility to grow ultra long CNFs/CNTs via plasma enhanced CVD process within sight of oxidizers [13, 17-21]. It is accounted for that high concentration of hydrogen radicals in PECVD process act as the sink for carbon species and thus suppresses the number of carbon species accessible for precipitation in the form of graphene layers around the catalyst nanoparticle. Oxygen in PECVD process keeps up the deterministic control over carbon to hydrogen ratio by scavenging these hydrogen radicals and also removes the amorphous carbon layer formed on the catalyst nanoparticle and in this manner supports the considerably higher CNF/CNT growth [20]. Kim *et al.*[21] investigated the role of water and oxygen on the growth of vertically aligned CNTs and found that addition of oxygen and water in the hydrocarbon/hydrogen plasma increased the CNTs growth rate up to thrice and twice, respectively, than that of CNT grown in typical hydrocarbon/hydrogen plasma. For the future industrial fabrication, it is vital to see how is the presence

of oxidizers and their relative level in the plasma influence the CNFs/CNTs growth.

5.3 Model

In this work, we have adopted the following scenario to enlighten the role of different plasmas on the growth of carbon nanofibers (CNFs). (i) We have accounted the CNF growth in hydrocarbon + hydrogen ($C_2H_2+H_2$) plasma, hydrocarbon + hydrogen + water ($C_2H_2+H_2+H_2O$) plasma, and hydrocarbon + hydrogen + oxygen ($C_2H_2+H_2+O_2$) plasma denoted as type I, type II, and type III plasmas, respectively. These plasma compositions contain electrons, singly ionized positively charged ions, radicals, and neutrals that are listed in Table 5.1. (ii) The nucleation of CNFs is considered on the nickel metal catalyst nanoparticles placed over the negatively biased substrate surface. (iii) The temperature of the metal catalyst nanoparticle and the substrate is assumed to be the same. (iv) The sheath electric field due to space charge separation is assumed along the direction perpendicular to the substrate surface. (v) The Maxwellian distribution of ions and electron is assumed. (vi) It is assumed that the ion number density is greater than the electron number density in the plasma sheath region. (vii) To investigate the structure of plasma sheath and the dynamics of plasma particles (electrons, ions, radicals, and neutrals), the sheath kinetics given in Ref. [22-24] are considered in the present chapter. Using the assumptions mentioned above, the main equations used in the model are:

Table 5.1. Plasma species considered in the present model. Species of type A and B are taken into account when CNF growth is investigated in type I plasma. However, additional species of type C are taken into account when CNF growth is examined in type II and type III plasmas.

Type	X	Y	Z	
			II plasma	III plasma
Ions	$C_2H_2^+$, $C_4H_2^+$, C_2H^+, CH^+	H_2^+, H^+	H_2O^+, OH^+, O^+	OH^+, O^+
Neutrals	C_2H_2, C_4H_2	H_2	H_2O	O_2
Radicals	CH, C_2H	H	OH, O	OH, O

5.3.1 Charging rate equation of CNFs

$$\partial_t(q) = \sum_X \left(I_{\text{tip-}iX} + I_{\text{cur-}iX}\right) + \sum_Y \left(I_{\text{tip-}iY} + I_{\text{cur-}iY}\right) + \sum_{Z=1}^{2} \left(I_{\text{tip-}iZ} + I_{\text{cur-}iZ}\right) - \gamma_e \left(I_{\text{tip-e}} + I_{\text{cur-e}}\right), \quad (5.1)$$

where q is the charge developed on CNFs surface, $I_{\text{tip-}ij}$ and $I_{\text{cur-}ij}$ are the ion collection currents at the tip and the curved surface of CNFs, respectively [see chapter 3], j refers to X, Y, and Z type of positively charged ions, $I_{\text{tip-e}}$ and $I_{\text{cur-e}}$ are the electron collection currents at the tip and the curved surface of CNFs [see chapter 3], respectively, and γ_e is the electron sticking coefficient at the CNF surface. The positively charged ions of type X and Y are taken into account when plasma of type I is considered. However, additional species of type Z are taken into account when plasma of type II and III are considered. From Table 5.1, it can be seen that species of type Z are different for plasma of type II and III, respectively. In Eq. (5.1), the first three terms denote the charge developed on the CNFs surface due to the accumulation of positively charged ions and the last term indicates the reduction in charge on account of the accumulation of electrons from the plasma at the CNFs surface. It is assumed that all the ions, incident on the CNF surface transfer their charge and get neutralized.

5.3.2 Kinetic equation of electron density

$$\partial_t(n_e) = \sum_{X=1} \beta_X n_X + \sum_Y \beta_Y n_Y + \sum_Z \beta_Z n_Z - \sum_{X=1} \alpha_X n_e n_{iX} - \sum_{Y=1} \alpha_Y n_e n_{iY} - \sum_{Z=1} \alpha_Z n_e n_{iZ} - \gamma_e \frac{n_{cnf}}{\lambda_d}\left(I_{\text{tip-e}} + I_{\text{cur-e}}\right), \quad (5.2)$$

where β_j is the coefficient of ionization of neutral atoms [25], α_j is the coefficient of recombination of electrons and positively charged ions [26], n_e is the electron number density, n_{ij} is the ion number density (i.e., number of ions per unit volume), n_j is the neutral atom density, n_{cnf} is the number

density (i.e., number of CNFs per unit area) of CNFs, and $\lambda_d \left(=3\times10^{-3}\text{cm}\right)$ is the plasma sheath width.

The Eq. (5.2) indicates the growth of electron number density in the reactive plasma. The first three terms of Eq. (5.2) denotes the gain in electron number density per unit time due to ionization of neutral atoms. The last four terms of Eq. (5.2) indicates the electron number density decay rate due to electron-ion recombination and electron collection current at the CNFs surface, respectively.

5.3.3 Kinetic equation of positively charged ions

$$\partial_t(n_{iX}) = \beta_X n_X - \alpha_X n_e n_{iX} - \frac{n_{cnf}}{\lambda_d}\left(I_{\text{tip-}iX} + I_{cur\text{-}iX}\right) + \sum_{\ell XY} k_\ell n_X n_{iY} - \sum_{QYX} k_Q n_Y n_{iX}, \quad (5.3)$$

$$\partial_t(n_{iY}) = \beta_Y n_Y - \alpha_Y n_e n_{iY} - \frac{n_{cnf}}{\lambda_d}\left(I_{\text{tip-}iY} + I_{\text{cur-}iY}\right) + \sum_{QYX} k_Q n_Y n_{iX} - \sum_{\ell XY} k_\ell n_X n_{iY}, \quad (5.4)$$

$$\partial_t(n_{iZ}) = \beta_Z n_Z - \alpha_Z n_e n_{iZ} - \frac{n_{cnf}}{\lambda_d}\left(I_{\text{tip-}iZ} + I_{\text{cur-}iZ}\right), \quad (5.5)$$

where k_j is the ion-neutral reaction rate coefficient. Eqs. (5.3) – (5.5) refer to the growth rate of positively charged ions of type *X*, *Y*, and *Z*, respectively in the plasma on account of gain in the ion number density per unit time due to ionization of neutral atoms (first term), decay rate of positively charged ion number density due to electron-ion recombination (second term) and ion collection current at the CNF surface (third term), increase/decrease in ion number density due to reaction between positively charged ions and neutrals in the plasma, these reactions have different reaction rate coefficients (fourth & fifth terms).

5.3.4 Kinetic equation of neutral species

$$\partial_t(n_X) = \alpha_X n_e n_{iX} - \beta_X n_X + \frac{n_{cnf}}{\lambda_d}(1-\gamma_{iX})\left(I_{\text{tip-}iX} + I_{cur-iX}\right) - \frac{n_{cnf}}{\lambda_d}\gamma_X\left(I_{\text{tip-}X} + I_{cur-X}\right) + IF_X - OF_X - J_{\text{ai-x}} + J_{\text{desp-x}} - \sum_{\ell XY} k_\ell n_X n_{iY} + \sum_{QYX} k_Q n_Y n_{iX}, \quad (5.6)$$

$$\partial_t(n_Y) = \alpha_Y n_e n_{iY} - \beta_Y n_Y + \frac{n_{cnf}}{\lambda_d}(1-\gamma_{iY})\left(I_{\text{tip-}iY} + I_{cur-iY}\right) - \frac{n_{cnf}}{\lambda_d}\gamma_Y\left(I_{\text{tip-}Y} + I_{cur-Y}\right) + IF_Y - OF_Y - J_{\text{ai-Y}} + J_{\text{desp-Y}} + J_{\text{thd}} - \sum_{QYX} k_Q n_Y n_{iX} + \sum_{\ell XY} k_\ell n_X n_{iY}, \quad (5.7)$$

$$\partial_t(n_Z) = \alpha_Z n_e n_{iZ} - \beta_Z n_Z + \frac{n_{cnf}}{\lambda_d}(1-\gamma_{iZ})\left(I_{\text{tip-}iZ} + I_{cur-iZ}\right) - \frac{n_{cnf}}{\lambda_d}\gamma_Z\left(I_{\text{tip-}Z} + I_{cur-Z}\right) + IF_Z - OF_Z - J_{\text{ai-}Z} + J_{\text{desp-Z}}, \quad (5.8)$$

where γ_{ij} is the ion sticking coefficient, $J_{\text{ai-j}}$ is the adsorption flux on the catalyst substrate surface, $J_{\text{desp-j}}$ is the desorption flux from the catalyst substrate surface, J_{thd} is the hydrogen ion flux due to thermal dehydrogenation, $I_{\text{tip-j}}$ and $I_{cur-\text{j}}$ are the neutral atom collection currents at the tip and curved surface of the CNF [see chapter 3], $IF_j\left(=4.4\times10^{17}\times f_j/V\right)$ and $OF_j\left(=R_p\times n_j/V\right)$ are the j^{th} species inflow rate and outflow rate into/from the plasma chamber, respectively. f_j is the inlet flow of corresponding gas, $V\left(\approx 2\times10^4\ \text{cm}^3\right)$ is the volume of the chamber, and R_p is the pumping rate [27]. Eqs. (5.6) – (5.8) refer to the growth of neutral atoms number density of type *X*, *Y*, and *Z* in the plasma on account of gain in neutral atom number density per unit time due to electron-ion recombination (first term), decay rate of neutral atom number density due

to ionization (second term), gain in neutral density per unit time due to neutralization of ions collected at the CNF surface (third term), decay in neutral atom number density due to accretion of neutrals at the CNF surface (fourth term), inflow and outflow rate of neutral species from plasma chamber (fifth & sixth term), adsorption of ions to the catalyst surface (seventh term) and desorption of ions from the catalyst surface (eighth term). The ninth term of Eq. (5.7) corresponds to increase in hydrogen ion number density in the plasma due to thermal dehydrogenation [28,29]. The remaining terms correspond to the increase and decrease in neutral atoms number density due to the reaction between ions and neutrals in the plasma as mentioned above.

5.3.5 Growth rate equation of carbon and hydrogen species generated over the catalyst surface

$$\begin{aligned}\partial_t(n_C) = \Bigg[& \sum_X J_X(1-\theta_t) + \sum_X n_{sX}\upsilon \exp\left(\frac{-\delta E_{td}}{k_B T_S}\right) + \sum_{iX}\left(\sum_X \frac{n_{sX} y_d}{\upsilon_0}\right) J_{iX} + \sum_{iX} J_{iX} \\ & + J_C + \sum_{iY}\left(\sum_{iX} \frac{J_{iX}\sigma_{ads}}{\upsilon}\right) J_{iY} - \sum_Y \left(\sum_X n_{sX}\sigma_{ads}\right) J_Y \\ & - n_C \upsilon \exp\left(\frac{-\delta E_{ev}}{k_B T_S}\right) - \sum_X n_X \upsilon \exp\left(\frac{-\delta E_{dhc}}{k_B T_S}\right) - n_C \sigma_{ads} \upsilon n_H \\ & - \sum_\gamma n_C \sigma_{ads} J_\gamma - \frac{1}{(\pi D)} \sum_{goc} k_g n_O n_C \Bigg] \times \frac{d\Omega_C}{dt}, \end{aligned} \quad (5.9)$$

$$\begin{aligned}\partial_t(n_H) = & \sum_Y J_Y(1-\theta_t) + \sum_{iX}\left(\sum_X \frac{n_{sX} y_d}{\upsilon_0}\right) J_{iX} + \sum_Y n_{sY} \exp\left(\frac{-\delta E_{td}}{k_B T_S}\right) \\ & + \sum_{iY} J_{iY} - \sum_Y n_{sY} \upsilon \exp\left(\frac{-\delta E_{dH}}{k_B T_S}\right) - n_C \sigma_{ads} \upsilon n_H \\ & - \sum_Y n_{sY} \sigma_{ads} J_Y - \sum_Y n_{sY} \sigma_{ads} J_{iY}, \end{aligned} \quad (5.10)$$

where $J_j\left(=\frac{n_j v_{th}}{4}\right)$ is the flux of neutral impinging species on the catalyst nanoparticle surface from the plasma, $n_{sj}\left(=\theta_j \upsilon_0\right)$ is the surface

concentration of neutral atoms [28, 30], θ_j is the surface coverage by the respective species, υ_0 is the adsorption sites per unit area, $J_{ij}\left(=n_{ij}\sqrt{k_B T_{ij}/m_{ij}}\right)$ is the ions flux on the catalyst nanoparticle surface from the plasma [28], where j denotes the species of type X, Y, Z, and carbon species. υ is the thermal vibration frequency, n_C and n_H are the number of carbon species and hydrogen radicals per unit area, respectively, generated on the catalyst nanoparticle surface, n_O is the flux of water/oxygen species impinge to the catalyst nanoparticle surface, $\sigma_{ads}\left(=6.8\times10^{-16}\,\mathrm{cm}^2\right)$ is the cross section for the interaction among the various species [28], $\delta E_{td}(=2.1\,eV)$ is the hydrocarbons dissociation energy, $\delta E_{\mathrm{ev}}(=1.8\ \mathrm{eV})$ carbon evaporation energy, $\delta E_{dhc}\left(=1.8\ \mathrm{eV}\right)$ is the hydrocarbon desorption energy, $\delta E_{th}\left(=1.87\ \mathrm{eV}\right)$ is the energy for thermal dehydrogenation of hydrocarbons, $\delta E_{dH}(=1.8\ \mathrm{eV})$ is the hydrogen atom desorption energy [31].

The nucleation of the CNF is a fundamental stage of synthesizing the CNFs and the catalyst nanoparticles placed over the substrate surface act as the nucleation sites for the growth of CNFs. The hydrocarbons and other species from the plasma dissociate on the catalyst nanoparticle surface to generate carbon species. These carbon species diffuse through the catalyst particle surface and precipitates at the rear of the catalyst nanoparticle and hence, nucleates the CNF [8, 9]. Thus, the number of carbon species generated on the catalyst nanoparticle surface is the one of the most remarkable growth determining factor. Due to continuous dissociation of hydrocarbons and generation of carbon species, a thin carbon film known as amorphous carbon layer is formed on the catalyst nanoparticle surface which prevents the further dissociation of hydrocarbons and diffusion of carbon species through the catalyst and thus leads to the poisoning of catalyst nanoparticle and stops the CNFs growth [32]. The Eq. (5.9) represents the number of carbon species per unit area (n_C) generating on catalyst nanoparticle on accounting various surface processes i.e., hydrocarbons

adsorption on the catalyst nanoparticle surface (first term), thermal dissociation of hydrocarbons (second term), ion induced dissociation of hydrocarbons (third term), ion dissociation (fourth term), direct carbon flux towards catalyst surface (fifth term) [28], and generation of carbon species due to hydrocarbon ions and hydrogen ions interaction i.e. ion-ion interaction (sixth term). Moreover, many processes lead to the loss of carbon species such as; loss of hydrocarbons neutrals due to interaction with hydrogen (seventh term), carbon evaporation (eight term), and desorption of hydrocarbons neutrals from catalyst nanoparticle surface [31]. The last three terms denote the loss of carbon species due to interaction with atomic hydrogen generated on the catalyst nanoparticle surface, interaction with the species of type Z and due to reaction with water/oxygen molecules, respectively. These interactions act as the sink for carbon species that may otherwise form amorphous carbon layer on the catalyst nanoparticle surface. Moreover, the term $\frac{d\Omega_c}{dt}\left(=1-n_c\pi D^2\right)$ is the blocking term that denotes the blocking of hydrocarbons dissociation on the catalyst nanoparticle surface when the number of carbon species $\left(n_c\right)$ generated on the catalyst nanoparticle surface increases rapidly and forms the amorphous carbon layer.

In the plasma-assisted catalytic growth process, the relative number density of carbon species $\left(n_c\right)$ and hydrogen radicals $\left(n_H\right)$ generated on the catalyst nanoparticle surface have significant implications for the CNF growth. Therefore, the model accounts the various processes responsible for the generation of hydrogen species or radicals on the catalyst nanoparticle surface discussed in Eq. (5.10) such as; hydrogen adsorption on catalyst nanoparticle surface [30] (first term), hydrogen produced due to ion-induced dissociation and thermal dissociation of hydrocarbons (second & third term) [31], and direction hydrogen ion flux (fourth term). However, there are many other surface processes which are responsible for the loss of hydrogen species such as; desorption of hydrogen radicals from catalyst nanoparticle surface (fifth term), interaction of hydrogen radicals with carbon species

(sixth term), and interaction of adsorbed hydrogen with incoming hydrogen neutrals and ions from the plasma (seventh & eight term) [31].

5.3.6 Growth rate equation of carbon nanofibers

$$\partial_t(\pi d^2 h) = \left[D_s + D_b + k\nu D\right] \times \frac{P(4\pi D) n_C}{\nu \rho_{cnf} I_{ix}} + \left[\frac{D_m}{\pi D^2} + n_H \left(\pi D^2\right) \sum_y I_{iy} + \sum_z \left(\gamma_z I_z + \gamma_{iz} I_{iz}\right) \right] \times \frac{m_{cat}}{\rho_{cat}}, \quad (5.11)$$

where D is the catalyst nanoparticle diameter, d is the CNF tip diameter, h is the CNF height, $D_S \left[= D_{S0} \exp\left(-\varepsilon_S / k_B T_S\right)\right]$ is the surface diffusion coefficient, $D_{S0} = a_0^2 \nu$, $a_0 (= 0.34\ nm)$ is the carbon atoms inter-atomic distance, ε_S (=0.3 eV) is the energy barrier for carbon species diffusion through the catalyst nanoparticle surface [30], $D_b \left[= D_{b0} \exp\left(-\varepsilon_b / k_B T_S\right)\right]$ is the bulk diffusion coefficient, $D_{b0} = \nu D / 2\pi$, ε_b (=1.6 eV) is the energy barrier for carbon species bulk diffusion through catalyst nanoparticle [30], P ($\approx 20\ GPa$) is the pressure exerted by graphene layers on catalyst nanoparticle [33], $k = A_k \exp\left(-\delta\varepsilon_{inc} / k_B T_S\right)$ is the carbon species incorporation speed into the graphene layers [34], $A_k = a_0 \nu$, $\delta\varepsilon_{inc} (= 0.4\ eV)$ is the carbon species energy barrier to diffuse along the nanofiber-catalyst interface, ρ_{cnf} is the nanofiber density, m_{cat} is the mass of the metal catalyst particle, and ρ_{cat} is the density of metal catalyst nanoparticle. $D_m = D_{m0} \exp\left(-\varepsilon_{SD} / k_B T_S\right)$ is the metal atoms diffusion coefficient [35], D_{m0} is the constant, ε_{SD} is the metal atoms self-diffusion activation energy.

The catalyzed CNF growth through PECVD process is dynamical and complex process during which carbon species generated on the catalyst

nanoparticle surface (as discussed in Eq. (5.9)) diffuse through the catalyst and ultimately precipitate to form graphene layers around rear surface of the catalyst nanoparticle and forms the CNF. Therefore, the terms in the first square bracket of Eq. (5.11) represents the surface as well as bulk diffusion of carbon species through catalyst nanoparticle and incorporation of carbon species to form graphene layers, respectively. Due to continuous dissociation of hydrocarbons and diffusion of carbon species, carbon precipitation grows in vertical as well planar direction. During the growth catalyst nanoparticle undergoes the shape transformation due to compressive stress exerted by the continuously adding graphene layers. Therefore, the pressure term is also taken into account outside the first bracket. Moreover, self-diffusion of the metal catalyst nanoparticle atoms is also an important factor for catalyst nanoparticle shape transformation (first term in the second square bracket). Continuous supply carbon species results in the continuous vertical as well planar growth. However, to stop the planar growth, hydrogen plays an important role. Highly reactive atomic hydrogen and ions act as the etchants and etch the terminal carbons. However, the carbons under the shadow of the catalyst nanoparticle remain protected. Thus, new graphene layers form in between the catalyst particle and existing graphene layers and support the vertical growth. The second term in the second square bracket denotes the etching of CNF by the hydrogen species. The last term in the second square bracket represents the sticking of atoms and ions of type 'Z' that also act as the good etchants and etch the CNF tip as well as side walls.

5.4 Results and discussion

Using the analytical equations presented in Sec. 5.3, we will investigate and analyze how the different plasma compositions affect the CNF growth rate and structure. To understand the better insight of such effects, we varied the types of neutrals and ions for various plasma compositions and their initial concentration in the reactive plasma and simultaneously solved the first order differential Eqs. (5.1) – (5.11) using Mathematica Software for typical glow discharge plasma parameters and appropriate boundary conditions at t=0 listed in Table 5.2 and other parameters used in the present model are as follows; $m_{iX} = m_X$ = 26 amu,

25 amu, 50 amu for, C_2H_2, C_2H, and C_4H_2 respectively, $m_{iY} = m_Y$ =2 amu, 1 amu for H_2 and H, respectively, $m_{iZ} = m_Z$ =18 amu, 32 amu, 17 amu, 16 amu

Table 5.2. Boundary conditions used in the present model.

Term	Description	Value
n_e	Electron density	1.5×10^{12} cm^{-3}
n_{iX}	Hydrocarbon ion density	
	$C_2H_2^+$	0.12 n_e
	C_2H^+	0.1 n_e
	$C_4H_2^+$	0.08 n_e
n_{iY}	Hydrogen ion density	
	H_2^+	0.35 n_e
	H^+	0.35 n_e
n_{iZ}	Oxygen/water ion density	
	H_2O^+	0.001 n_e
	OH^+	0.001 n_e
	O^+	0.001 n_e
n_X	Hydrocarbon neutral density	
	C_2H_2	1.4×10^{13} cm^{-3}
	C_2H	1.2×10^{13} cm^{-3}
	C_4H_2	1.0×10^{13} cm^{-3}
n_Y	Hydrogen neutral density	
	H_2	5.6×10^{14} cm^{-3}
	H	5.6×10^{14} cm^{-3}
n_Z	Oxygen/water neutral density	
	H_2O	5×10^{10} cm^{-3}
	O_2	5×10^{10} cm^{-3}
	OH	5×10^{10} cm^{-3}
	O	5×10^{10} cm^{-3}
T_e	Electron temperature	2.5 eV
T_i	Ion temperature	2500 K
T_n	Neutral temperature	2000 K
T_S	Substrate temperature	800 K

for H_2O, O_2, OH, and O,respectively, atomic mass of nickel m_{cat} = 58.69 amu, density of catalyst nickel ρ_{ct} (= 8.96 g/cm^3), coefficient of recombination

of electrons and ions $\alpha_X \approx \alpha_Y \approx \alpha_Z$ (= 1.12×10^{-7} cm^3/sec), κ = -1.2, substrate temperature T_S = 800 K, sticking coefficient of electrons $\gamma_e(=1)$, sticking coefficient of ions $\gamma_{iX} = \gamma_{iY} = \gamma_{iZ}(=1)$, sticking coefficient of neutral atoms acetylene $\gamma_X = \gamma_Y = \gamma_Z(=1)$, acetylene gas ($C_2H_2$) inflow rate = 50 sccm, hydrogen gas (H_2) inflow rate = 100 sccm.

In Fig. 5.1, the variation of the CNF height with growth time for different plasmas is shown. From the Fig. 5.1, one can see that CNF grown in $C_2H_2+H_2+O_2$ plasma attains maximum height followed by CNF grown in $C_2H_2+H_2+H_2O$ and $C_2H_2+H_2$ plasma. To understand why CNF growth rate is maximum in the $C_2H_2+H_2+O_2$ plasma and minimum in $C_2H_2+H_2$ plasma, we have plotted the curves of the number of carbon species per unit area generated on the catalyst nanoparticle surface as a function of growth time for different plasmas (cf. Fig. 5.2).

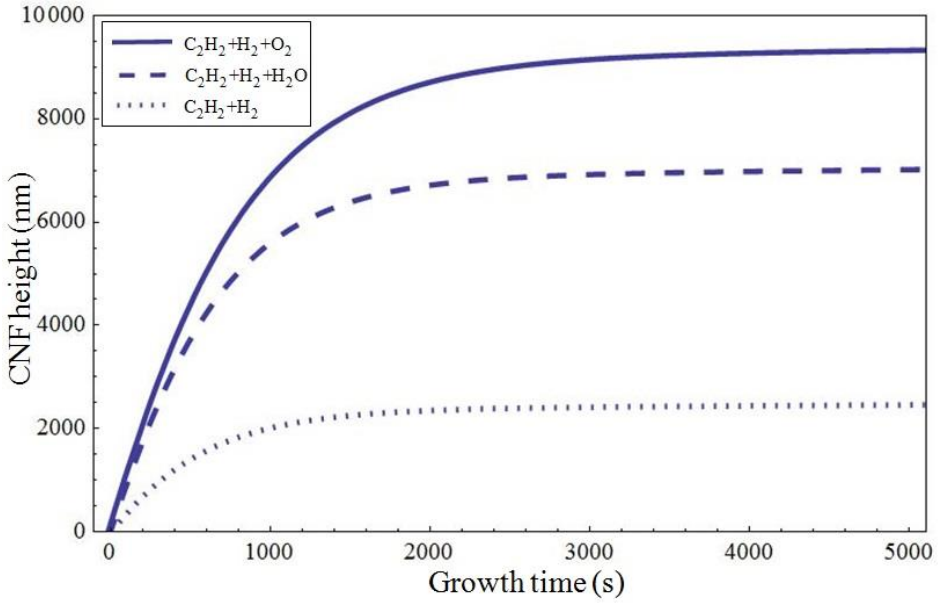

Fig. 5.1. Time evaluation of height of the CNF grown in different plasma mixtures.

From Fig. 5.2, one can see that the rate at which carbon species generated on the catalyst nanoparticle surface is maximum for $C_2H_2+H_2+O_2$ plasma followed by $C_2H_2+H_2+H_2O$ and $C_2H_2+H_2$ plasma. In $C_2H_2+H_2$ plasma, CNF growth continues due to continuous dissociation of hydrocarbons

on the front surface of catalyst nanoparticle to generate carbon species and due to continuous diffusion of these carbon species through the catalyst. Atomic hydrogen etches the amorphous carbon from the catalyst surface and maintains the catalyst activity for further dissociation of hydrocarbons coming from the plasma and contributes to the continuous CNF growth. During the growth, the number of carbon species generated on the catalyst nanoparticle surface increases continuously due to which etching of amorphous carbon by hydrogen becomes less effective, this leads to cover the catalyst nanoparticle surface with amorphous carbon layer and block the further dissociation of incoming hydrocarbons from the plasma. Thus, CNF growth terminates due to the poisoning of catalyst nanoparticle. However, in $C_2H_2+H_2+H_2O$ plasma, water acts as the catalyst enhancer, i.e., water molecules enhance and preserve the catalyst activity during the CNF growth. Water molecules etch away the amorphous carbon layer covering the catalyst nanoparticle by means of $C+H_2O \rightarrow CO+H_2$ [11] with large reaction rate coefficient and thus maintain catalyst activity that increases the hydrocarbons dissociation on the catalyst surface. Therefore, the number of carbon species generated on the catalyst surface increases (cf. Fig. 5.2) and results in the much-enhanced CNF growth as compared to $C_2H_2+H_2$ plasma. Furthermore, the addition of water vapours in the plasma not only removes the carbonaceous impurities (amorphous carbon) from the catalyst surface but also increase the number of hydrogen radicals on the catalyst surface $\left(C+H_2O \rightarrow CO+H_2\right)$. These highly reactive hydrogen radicals interact with carbon species on the catalyst surface and act as a sink for carbon species that may otherwise be diffused through the catalyst to contribute in the CNF growth. However, $C_2H_2+H_2+O_2$ plasma affords highly productive CNF growth; this is because of the two important roles played by the oxygen; (i) removal of amorphous carbon from the catalyst surface by converting carbon species into CO species by the means of various reactions [20,36] and thus prevents catalyst poisoning, (ii) removal of the highly reactive hydrogen radicals i.e., $\left(H+O_2 \rightarrow OH+O\right)$ with large reaction rate $k_g = 10^{17}\,\mathrm{cm}^3/\mathrm{mol.s}$ [20,36] that prevents the sinking of carbon species due to carbon-hydrogen interaction. These highly effective contributions of oxygen continuously increase the

hydrocarbons dissociation on the catalyst surface to generate the maximum number of carbon species on the catalyst surface (cf. Fig. 5.2) and results in the much higher CNF growth compared to $C_2H_2+H_2+H_2O$ and $C_2H_2+H_2$ plasma. During the growth, the concentration of oxygen species in the plasma decreases (as their concentration is about 1% of the hydrocarbon species) and formation of amorphous carbon on the catalyst surface increases. Consequently, dissociation of hydrocarbon species on the catalyst surface decreases which ultimately drives the CNF growth in the saturation region.

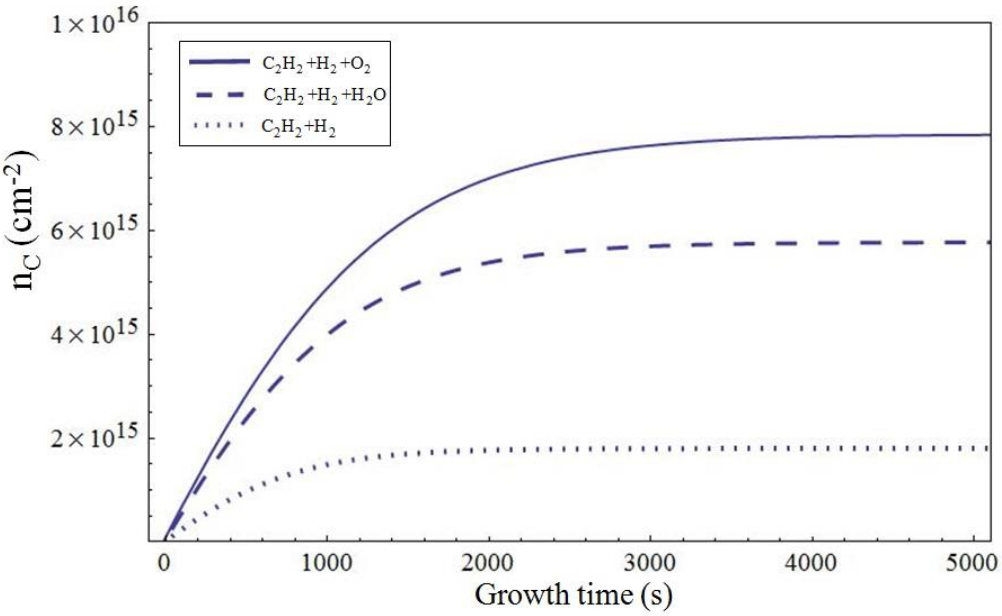

Fig. 5.2. Time evaluation of generation of carbon species per unit area (n_C) on the catalyst nanoparticle surface as a function of different plasma mixtures.

To make it clear that how different plasmas maintain catalyst activity during the growth; we have plotted the curves of blocking function Ω_C as a function of growth time for various plasma mixtures in Fig. 5.3 which shows that blocking function attains the saturation (i.e., the situation when catalyst particle is completely covered with the amorphous carbon film) quickly in the case of $C_2H_2+H_2$ plasma and blocks the further dissociation of incoming hydrocarbons from the plasma on the catalyst surface. Thus, catalyst particle lost its activity, and therefore, more hydrocarbon species remained undissociated in plasma as can be seen from Fig. 5.4. However, in $C_2H_2+H_2+H_2O$ plasma, blocking function slowly attains the saturation, and

thus catalyst particle maintains its activity for the much longer time. This leads to more dissociation of hydrocarbons on the catalyst surface and therefore, the fewer number of undissociated hydrocarbons left in the plasma (cf. Fig. 5.4).

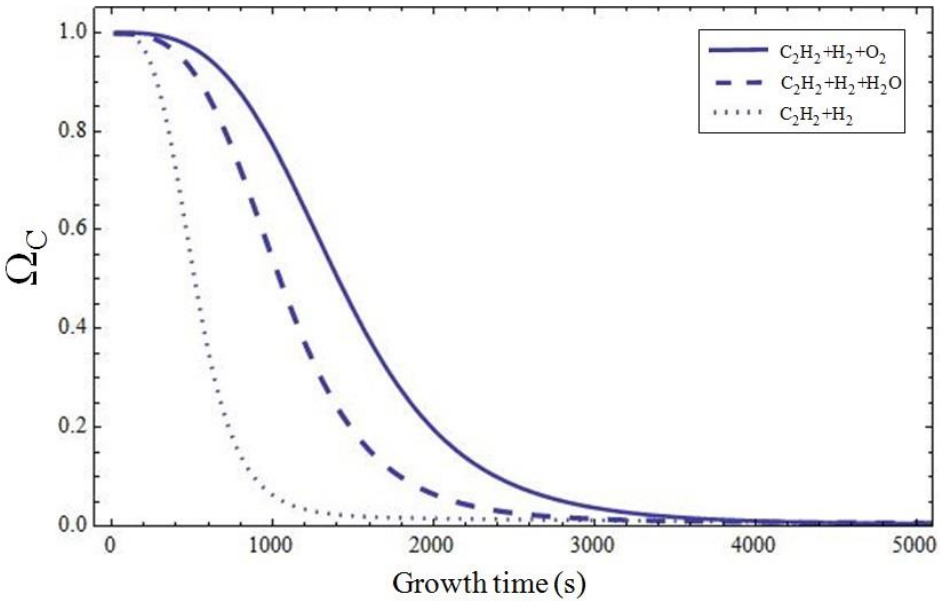

Fig. 5.3. Temporal variation of blocking function (Ω_C) for different gas mixtures.

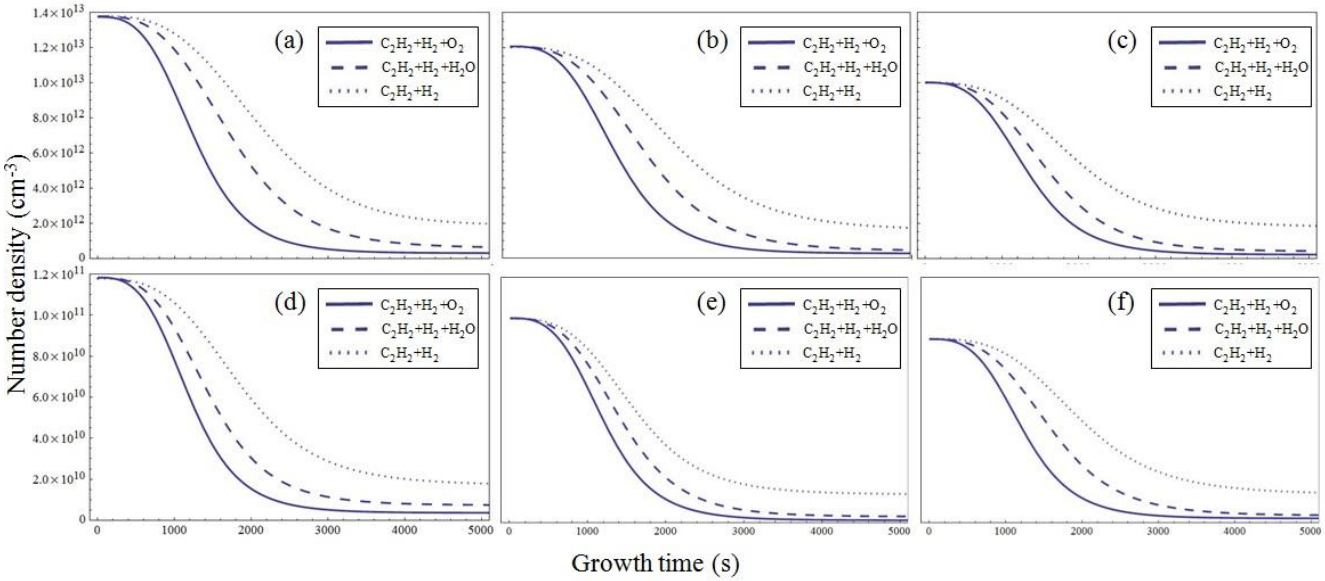

Fig 5.4. Temporal variation of plasma species number density in different plasma mixtures for (a) C_2H_2, (b) C_2H, (c) C_4H_2, (d) $C_2H_2^+$, (e) C_2H^+, and (f) $C_4H_2^+$.

In $C_2H_2+H_2+O_2$ plasma, blocking function attains the saturation at the slowest rate and thus maintains the high catalyst activity due to which much more hydrocarbons dissociate on the catalyst surface, and therefore, least number of hydrocarbons remained undissociated in the plasma that can be seen

from Fig. 5.4. From the results obtained in Fig. 5.1, the calculated CNF growth rates (i.e., saturated height per unit time taken to achieve saturation) are 1.52 nm/s, 3.315 nm/s, and 4.34 nm/s for $C_2H_2+H_2$, $C_2H_2+H_2+H_2O$, and $C_2H_2+H_2+O_2$, respectively. This shows that on the addition of water and oxygen in the reactive plasma, CNFs grow with much higher rates (almost double).

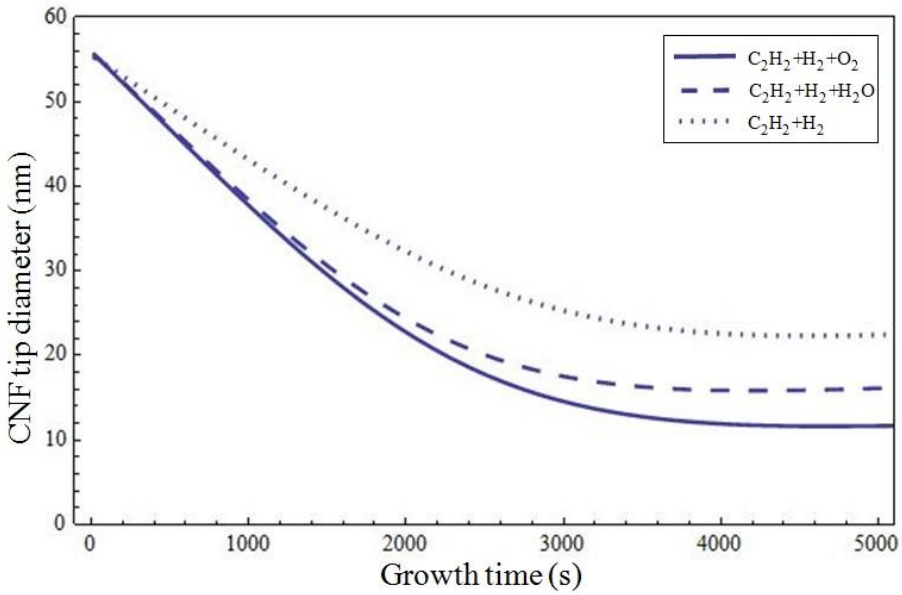

Fig. 5.5. Time evolution of diameter of CNF grown in three different plasma mixtures.

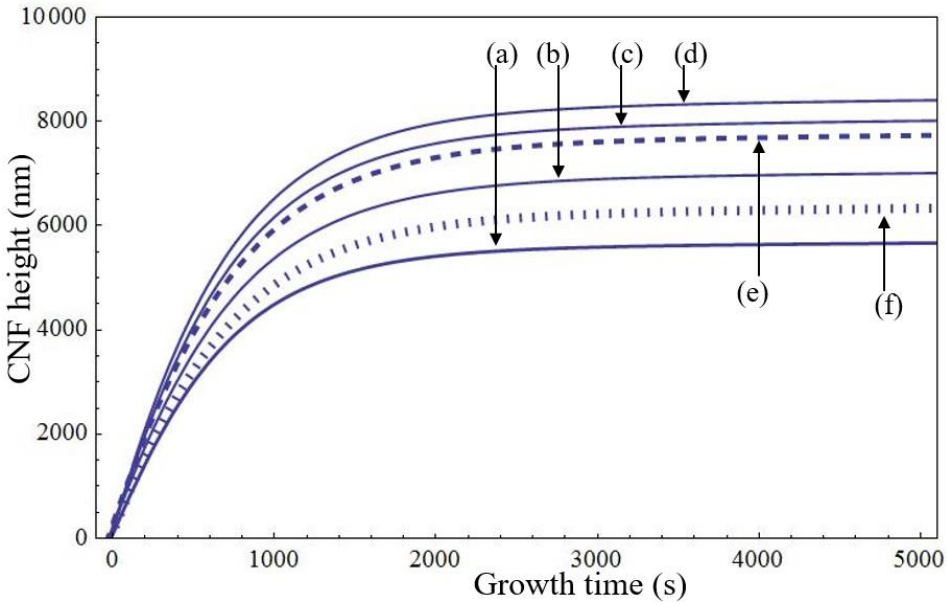

Fig. 5.6. Temporal variation of height of CNF grown in $C_2H_2+H_2+H_2O$ plasma as function of different water concentration (number density) in the plasma i.e., (a) 4.7×10^{10} cm^{-3}, (b) 5.5×10^{10} cm^{-3}, (c) 6.0×10^{10} cm^{-3}, (d) 6.5×10^{10} cm^{-3}, (e) 7.5×10^{10} cm^{-3}, and (f) 8.5×10^{10} cm^{-3}.

Fig. 5.5 shows the time evolution of the CNF tip diameter for the different plasmas. From the Fig. 5.5, it can be seen that CNF tip diameter decreases with the growth time. This can be understood from the catalyst particle shape and size transformation which remained on the tip of the CNF during the growth. Due to compressive stress applied by the continuously formed graphene layers around the catalyst particle, the shape of the catalyst particle changes continuously to teardrop like shape from the initial spherical shape that causes the remarkable reduction in the rear size of the catalyst particle. Moreover, hydrogen acts as the etchant and etches the CNF side walls as well as the tip which results in the reduction in CNF tip diameter. From Fig. 5.5, one can also see that CNF tip diameter is least for the $C_2H_2+H_2+O_2$ plasma followed by the $C_2H_2+H_2+H_2O$ and $C_2H_2+H_2$ plasma. The significant reduction in CNF tip size during the growth in $C_2H_2+H_2+H_2O$ plasma in contrast with the $C_2H_2+H_2$ plasma is attributed to the fact that the number of hydrogen radicals augments on the catalyst nanoparticle surface by means of $C+H_2O \rightarrow CO+H_2$, thus relative etching of the CNF increases which results in the reduction in the CNF tip diameter. Moreover, OH species formed in the $C_2H_2+H_2+H_2O$ plasma also act as the etchants and etch the CNF and reduce the CNF tip diameter. However, CNF tip diameter is least in the $C_2H_2+H_2+O_2$ plasma among all the three plasma mixtures. In $C_2H_2+H_2+O_2$ plasma, CNF grows for the much longer time in contrast to other plasmas, in this way; relative etching of the CNF by etchants (hydrogen radicals and OH species) is higher which brings about the lesser tip diameter.

A family of time evolution curves discussed above reveals that CNF can be grown with much higher rate and with lesser tip diameter when H_2O/O_2 is added to the hydrocarbon + hydrogen plasma. The kinetics of water/oxygen assisted catalytic CNF growth must be accurately known to synthesize the highly efficient CNFs for their practical applications in field emission devices. The CNF growth can be deterministically controlled by suitably varying the growth parameters. The water/oxygen level in the plasma is one of the most significant growth parameters. In Fig. 5.6, the time evolution of the CNF growth

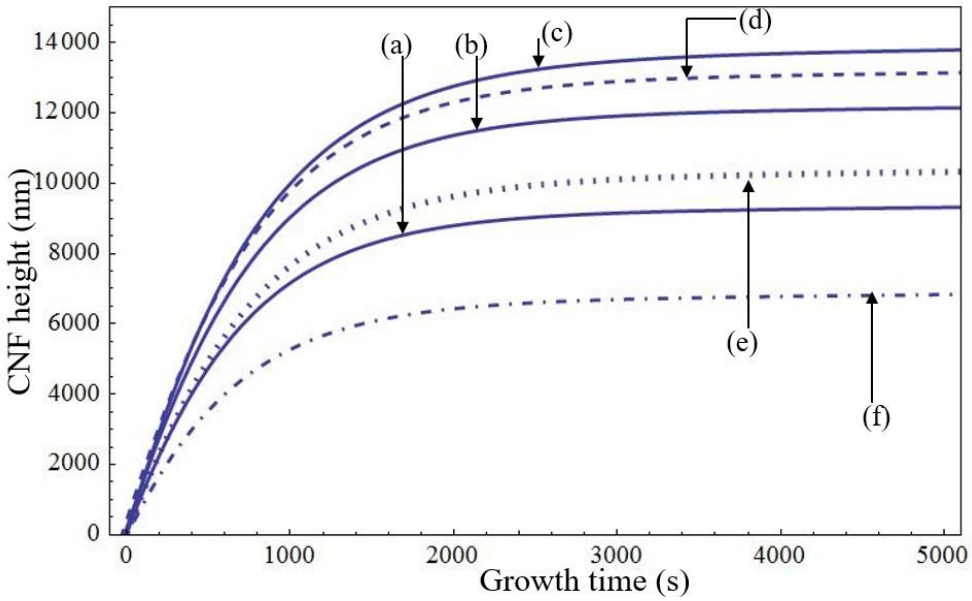

Fig. 5.7. Temporal variation of height of CNF grown in C_2H_2+H_2+O_2 plasma as function of different oxygen concentration (number density) in the plasma i.e., (a) 4.5×10^{10} cm^{-3}, (b) 6.0×10^{10} cm^{-3}, (c) 7.3×10^{10} cm^{-3}, (d) 8.0×10^{10} cm^{-3}, (e) 8.5×10^{10} cm^{-3}, and (f) 9.5×10^{10} cm^{-3}.

has been carried out at different water concentration, i.e., different water molecules number density in the reactive plasma. The curves plotted in Fig. 5.6 exhibits the complex behavior: as water number density increases up to 6.51×10^{10} cm^{-3} (which is about 1% of the hydrocarbon species number density in the plasma), the CNF height, i.e., CNF growth rate increases, but with further increase in water concentration CNF height decreases significantly. The increase in the CNF growth rate till 6.51×10^{10} cm^{-3} exemplifies the effect of water in maintaining the catalyst activity. Beyond this water level, CNF growth dropped steadily, which is due to the rapid increase in the hydrogen species on the catalyst surface [cf. Fig. 5.8(i)]. These hydrogen species ruin the carbon diffusion and precipitation, and thus retards the growth process. Moreover, with the high water level in the plasma, the oxidation of carbons from the catalyst surface increases by means of $C+H_2O\rightarrow CO+H_2$, therefore, the number of carbon species available for growth decreases significantly [cf. Fig. 5.8(ii)]. Thus last three terms of Eq. (5.9) becomes dominants over the all other terms responsible for carbon generation due to which water loses its primary characteristic. Likewise, the effect of oxygen level in the plasma on the CNF growth has been seen in Fig. 5.7 which indicates that CNF height increases up

to optimum oxygen concentration i.e., 7.3×10^{10} cm^{-3}. This is due to the fact that adequate measure of oxygen expels the amorphous carbon from the catalyst surface and accordingly preserve and enhance the catalyst activity which is its essential trademark. But beyond this ideal level, oxygen species oxidizes the carbon from catalyst surface (last two terms of Eq. (5.9) becomes dominants) and act as the sink for carbon species [cf. Fig. 5.8(iii)] that may otherwise form graphene layers and may contribute to the growth. Hence, oxygen setbacks its essential characteristic and poisons the growth process. Thus, one can interpret the results of Figs. 5.6 – 5.8 that H_2O/O_2 enhance the CNF growth with the large extent when their relative concentration is almost 1% of the hydrocarbon species in the reactive plasma.

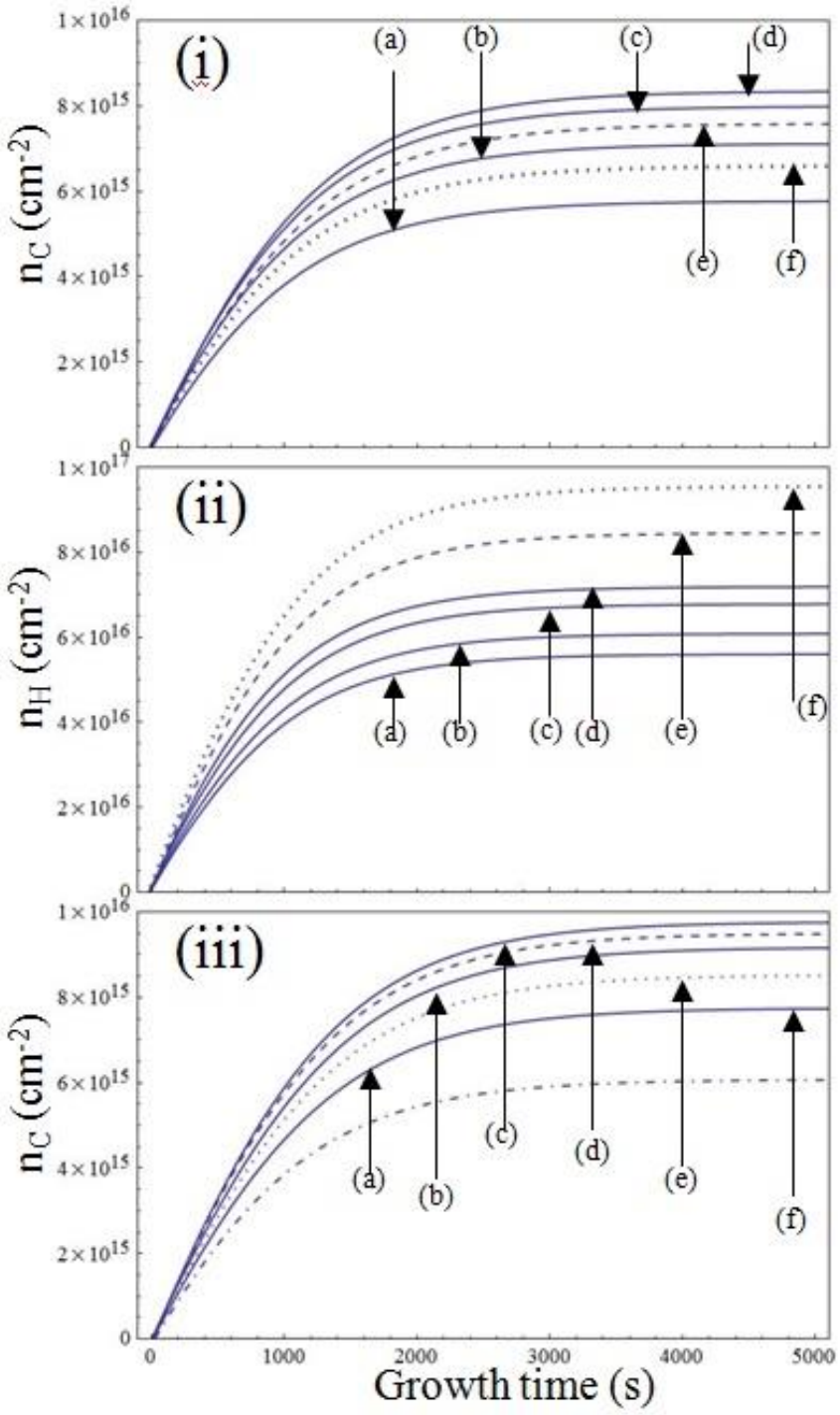

Fig. 5.8. (i) & (ii) Shows the temporal variation of carbon species number density (n_C) and hydrogen species number density (n_H), respectively, generated on the catalyst nanoparticle surface in C_2H_2+H_2+H_2O plasma as function of different water concentration (number density) in the plasma i.e., (a) 4.7×10^{10} cm^{-3}, (b) 5.5×10^{10} cm^{-3},(c) 6.0×10^{10} cm^{-3}, (d) 6.5×10^{10} cm^{-3}, (e) 7.5×10^{10} cm^{-3}, and (f) 8.5×10^{10} cm^{-3}. (iii) Temporal variation of carbon species number density generated on the catalyst nanoparticle surface in C_2H_2+H_2+O_2 plasma as function of different oxygen concentration number density) in the plasma i.e., (a) 4.5×10^{10} cm^{-3}, (b) 6.0×10^{10} (c) 7.3×10^{10} cm^{-3}, (d) 8.0×10^{10} cm^{-3}, (e) 8.5×10^{10} cm^{-3}, and (f) 9.5×10^{10} cm^{-3}.

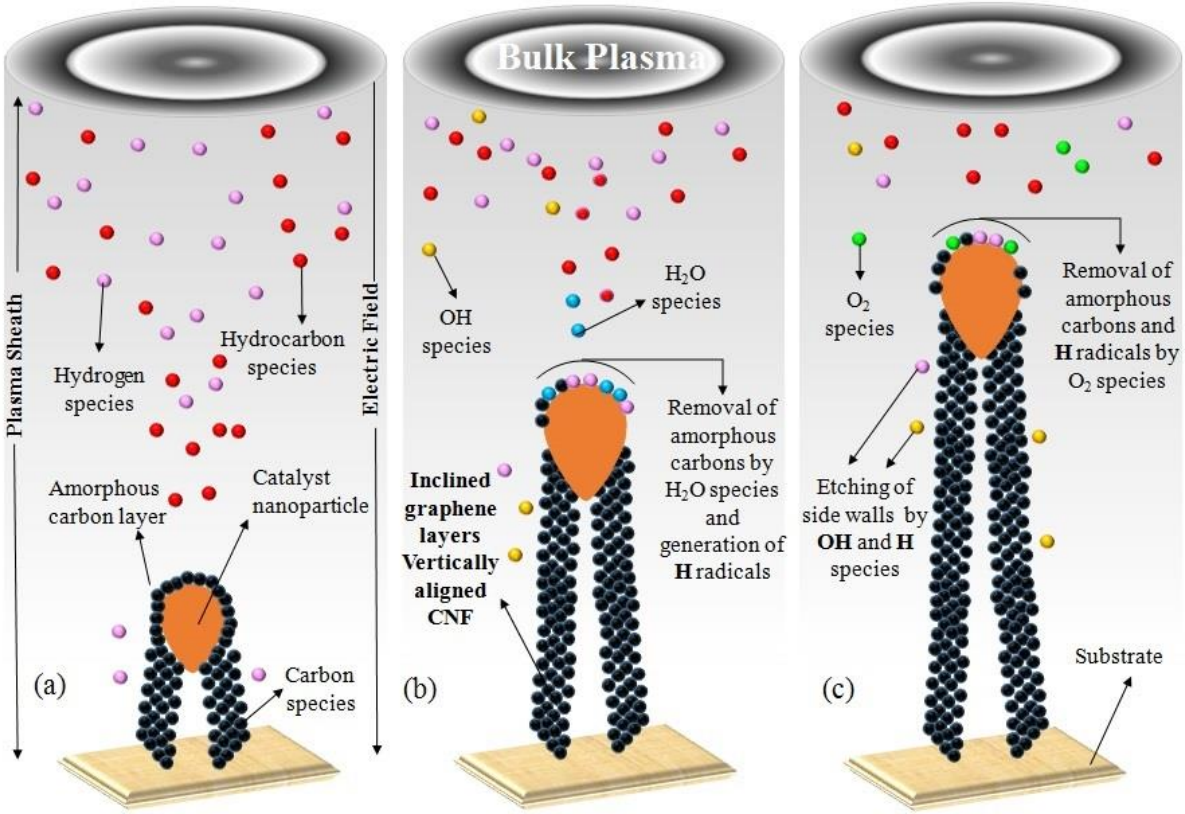

Fig. 5.9. Bottom to top approach, i.e., atom to atom operation of CNF growth in three different plasma gas mixture. (a) CNF growth in typical hydrocarbon (C_2H_2)/hydrogen (H_2) plasma, in which continuous dissociation of hydrocarbon species (neutrals and ions) on the catalyst nanoparticle surface generate the excess carbon species and the ultimately amorphous carbon layer is formed on the catalyst nanoparticle surface and terminates the CNF growth. (b) CNF growth in C_2H_2+H_2+H_2O plasma, in which water species etch the amorphous carbon from the catalyst surface by means of many chemical reactions and preserve the catalyst activity and enhance the CNF growth. (c) CNF growth in C_2H_2+H_2+O_2 plasma, in which oxygen species not only remove the amorphous carbon from the catalyst surface but also remove the excess hydrogen radicals (H) from the catalyst surface which act as the sink for carbon species and thus CNF grows with much higher rate as compared to growth in (a) and (b).

5.4.1 Comparison with available experimental observations

In our analytical model, we have investigated the effects of different plasmas (i.e., $C_2H_2+H_2$, $C_2H_2+H_2+H_2O$, and $C_2H_2+H_2+O_2$) on the growth and tip diameter of the vertically aligned CNFs. The theoretical results obtained from our model are in good agreement with the available experimental observation, as follows. Hata *et al.* [13], Yoshihara *et al.* [14], Yun *et al.* [15], Hussain *et al.* [16] has observed the increase in CNTs growth rate (CNF height per unit

deposition time) on the addition of water in the CVD growth process. He *et al.* [37] observed the much enhanced CNF growth and more elongation in catalyst nanoparticle in the presence of water in acetylene/hydrogen plasma mixture. Zhang *et al.* [20] revealed that CNF growth rate increases when oxygen is added to the hydrocarbon/hydrogen reactive plasma. Kim *et al.* [21] compared the growth of CNTs in above three plasma mixtures found that growth rate is maximum in $C_2H_2+H_2+O_2$ plasma followed by $C_2H_2+H_2+H_2O$, and $C_2H_2+H_2$ plasma. Futaba *et al.* [38] observed the increase in CNT growth rate up to some optimum water level in growth atmosphere and found the decrease in growth beyond that level. The effect of insertion of small amount of water/oxygen in the PECVD growth process on the CNF growth can also be seen from the schematic Fig. 5.9.

References

[1] W. A. Heer, A. Chatelain, and D. Ugarte, Science **270**, 1179 (1995).

[2] S. Fan, M. G. Chapline, N. R. Franklin, T. W. Tombler, A. M. Cassell, and H. Dai, Science **283**, 512 (1999).

[3] T. Y. Tsai, C. Y. Lee, N. H. Tai, and W. H. Tuan, Appl. Phys. Lett. **95**, 013107 (2009).

[4] V. I. Merkulov, A. V. Melechko, M. A. Guillorn, M. L. Simpson, D. H. Lowndes, J. H. Whealton, and R. J. Raridon, Appl. Phys. Lett. **80,** 4816 (2002).

[5] H.W. Wei, K. C. Leou, M. T. Wei , Y. Y. Lin, and C. H. Tsai, J. Appl. Phys. **98**, 044313 (2005).

[6] M. Meyyappan, L. Delzeit, A. Cassell, and D. Hash, Plasma Sources Sci. Technol. **12,** 205 (2003).

[7] H. Cui, X. Yang, M. L. Simpson, D. H. Lowndes, and M. Varela, Appl. Phys. Lett. **84,** 4077 (2004).

[8] C. S Cojocaru, A. Senger, and F. L. Normand, J. Nanosci. Nanotechnol. **6,** 1 (2006).

[9] N. M. Rodriguez, J. Mater. Res. **8,** 3233 (1993).

[10] D. H. Seo, S. Kumar, A. E. Rider, Z. Han, and K. Ostrikov, Opt. Mat. Express **2**, 700 (2012).

[11] T. M. Minea, S. Point, A. Granier, and M. Touzeau, . Appl. Phys. Lett. **85,** 1244 (2004).

[12] L. Valentini, J. M. Kenny, L. Lozzi, and S. Santucci, J. Appl. Phys. **92,** 6188 (2002).

[13] K. Hata, D. N. Futaba, K. Mizuno, T. Namai, M. Yumura, and S. Iijima, Science **306** , 1362 (2004).

[14] N. Yoshihara, H. Ago, and M. Tsuji, J Phys. Chem. C **111,** 11577 (2007).

[15] Y. Yun, V. Shanov, Y. Tu, S. Subramaniam, and M. J. Schulz, J. Phys. Chem. B **110,** 23920 (2006).

[16] S. Hussain, R. Amade, and E. Bertran, Mater. Chem. Phys. **148,** 914 (2014).

[17] L. Song, G. Toth, R. Vajtai, M. Endo, and P. M. Ajayan, Carbon **50,** 5521 (2012).

[18] L. Kurzepa, A. L. Raus, J. Patmore, and K. Koziol, Adv. Funct. Mater. **24,** 619 (2014).

[19] C. Zhang, Y. Fu, Q. Chen, and Y. Zhang, Front. Mater. Sci. China **2**, 37 (2008).

[20] G. Zhang, D. Mann, L. Zhang, A. Javey, Y. Li, E. Yenilmez, Q. Wang, J. P. McVittie, J. Gibbons, and H. Dai PNAS **102**, 16141 (2005).

[21] Y. Kim, W. Song, S. Y. Lee, S. Shrestha, C. Jeon, W. C. Choi, M. Kim, and C. Y. Park, Jpn. Appl. Phys. **49,** 085101 (2010).

[22] H. Mehdipour, K. Ostrikov, and A. E. Rider, Nanotechnology 21, 455605, (2010).

[23] M. A. Lieberman, and A. J. Lichtenberg, Principles of Plasma Discharges and Material Processing (*New York:Wiley-Interscience*, 1994).

[24] S. C. Sharma and N. Gupta, Phys. Plasmas. **22,** 1235117 (2015).

[25] M.S. Sodha, S. Misra, and S. K. Mishra, Phys. Plasmas **17,** 113705 (2010).

[26] M. S. Sodha, S. Misra, S. K. Misra, and S. Srivastava, J. Appl. Phys. **107,** 103307 (2010).

[27] I. B. Denysenko, S. Xu, J. D. Long, P. P. Rutkevych, N. A. Azarenkov, and K. Ostrikov, J. Appl. Phys. **95,** 2713 (2004).

[28] I. Denysenko, and K. Ostrikov, J. Phys. D: Appl. Phys. **42,** 015208 (2009).

[29] L. Vattuone,Y. Y. Yeo, R. Kose, and D. A. King, Surf. Sci. **447,** 1 (2000).

[30] I. Denysenko, and N. A. Azarenkov, J. Phys. D: Appl. Phys. **44,** 174031 (2011).

[31] Z. Marvi, S. Xu, G. Foroutan, and K. Ostrikov, Phys. Plasmas **22,** 013504 (2015).

[32] V. I. Merkulov, D. K. Hensley, A. V. Melechko, M.A. Guillorn, D. H. Lowndes, and M. L. Simpson, J. Phys. Chem B **106**, 10570 (2002).

[33] M. Yudasaka, R. Kikuchi, T. Matsui, Y. Ohki, S. Yoshimura, and E. Ota, Appl. Phys. Lett. **67,** 2477 (1995).

[34] O. A. Louchev, T. Laude, Y. Sato, and H. Kanda, J. Chem. Phys. **118,** 7622 (2003).

[35] See (http://matter.org.uk/matscicdrom/manual/df.html) for metal atom diffusion coefficient

[36] C. Benndorf, P. Joeris, and R. Kroger, Pure Appl. Chem. **66,** 1195 (1994).

[37] Z. B. He, J. L. Maurice, C. S. Lee, A. Gohier, D. Pribat, P. Legagneux, and C. S. Cojocaru, CARBON **49,** 435 (2011).

[38] D. N. Futaba, K. Hata, T. Yamada, K. Mizuno, M. Yumura, and S. Iijima, Phys. Rev. Lett. 056104 (2005).

6

Modeling to study the role of catalyst in the formation of graphitic shells during carbon nanofiber growth subjected to reactive plasma

6.1 Brief outline of the chapter

In this chapter, we endeavour to explore the roles of catalyst on the dissociation of plasma species on catalyst nanoparticles surface in the plasma enhanced chemical vapor deposition (PECVD) process and its repercussions on the growth of the CNFs/CNTs, on the dynamics of catalyst nanoparticles during the PECVD growth of CNFs/CNTs, and on the alignment of graphitic shells about the growth axis by the numerical model that includes many time-dependent equations governing the nanostructuring of nanofilm, deformation of nanoparticle during the growth, the formation of graphitic shells (rolled graphene sheets around the nanoparticle), and growth of resulting nanostructure. Additionally, the model includes the sheath kinetics of electrons, neutral and charged species in the hydrogen-diluted acetylene plasma and many surface deposition processes responsible for the carbon nanomaterials growth. The results of the numerical modeling that elucidate the dependence of one-dimensional carbon nanomaterials growth on the catalyst and their comparison with the existing experimental observations have been discussed.

6.2 Introduction

One dimensional carbon nanomaterials such as carbon nanotubes (CNTs) and carbon nanofibers (CNFs) constructed in an orientation perpendicular to the substrate surface, exhibit high aspect ratios (length to diameter).

Published work of the present chapter:

1. **Ravi Gupta**, Neha Gupta, and Suresh C. Sharma, Modeling to study the role of catalyst in the formation of graphitic shells during carbon nanofiber growth subjected to reactive plasma, *Phys. Plasmas* **25,** 043504 (2018).

The characteristics are particularly advantageous in field emission devices [1-3]. The entirely selective growth of vertically oriented CNFs/CNTs can be achieved on the predeposited metal catalyst film over the substrate by applying plasma [4-6]. It is necessary to control the CNF/CNT structure, aspect ratio, and degree of graphitization for their potential applications in field emission devices. However, it is hard to accomplish such high-level growth without the precise knowledge of the roles of the catalyst in the plasma enhanced chemical vapor deposition process. The nanostructuring (formation of nanoislands/nanoparticles) of predeposited ultra-thin metal catalyst film (nanofilm) to initiate the CNF/CNT nucleation can be achieved by plasma pretreatment or thermal annealing. The nucleation seeds thus formed influence the nature, growth, and graphitization of nucleating carbon nanostructure. The transformation of nanofilm into nanoparticles not only depends on the process parameters but also on the nature and thickness of the nanofilm. In particular, nickel, cobalt, and iron are the most effective catalysts used for CNF/CNT growth; however, nickel shows much-enhanced growth followed by cobalt and iron for typical CVD case [7]. The nanostructuring of thick nanofilm prompts the formation of large nanoislands and growth of thick and shorter CNFs. However, reduction in nanofilm thickness results in the growth of thin and longer CNFs [8-10]. The electrical conductivity and field emission efficiency of CNFs/CNTs significantly rely on the arrangement and number of graphitic shell [11, 12] and can also be enhanced by the thickness of the nanofilm [13].

6.3 Model

This section describes the indispensable role of catalyst on the plasma-assisted growth of CNFs. As explained in the previous chapters, we consider the nucleation and the growth of CNF on the nickel catalyst nanoparticle in the plasma containing the ionized gas mixture of hydrocarbon gas and etchant gas. However, in the present chapter, we study the dynamics of the metal catalyst used to nucleate the carbon nanofibers through PECVD process in the presence of C_2H_2/H_2 gas mixture. The present model considers the predeposited nickel nanofilm over the silicon substrate placed in the plasma chamber of inner diameter 32 cm and 23 cm in height [14].

Table 6.1. Plasma species considered in the present model.

Type	Neutral species	Positively charged Ions
A	C_2H, C_2H_2, C_2H_3, C_4H_2, C_4H_3, C_6H_2, C_6H_4	C_2H^+, $C_2H_2^+$, $C_2H_3^+$, $C_4H_2^+$, $C_4H_3^+$, $C_6H_2^+$, $C_6H_4^+$
B	H, H_2	H^+, H_2^+

The Table 6.1 details the positively charged and neutral species considered in the present computation from the experimental observations of literature specifying the plasma chemistry of the acetylene and hydrogen gas mixture [14-19]. Generally, C_2H_2 contained plasma consist $C_{2x}H_y$ species [where x=1 to 5 and y=1,2]. However, in the present model, we consider the $C_{2x}H_y$ species of type x=1 to 3 because higher species have the primary characteristic of sputtering and etching of the amorphous carbon layer formed on the catalyst front face during the growth. The plasma assisted CNF growth is strongly affected by the fluxes and energies of the hydrocarbon and etchant species in the plasma sheath region formed between bulk plasma and substrate maintained at negative potential *Us*. The fluxes and energies of plasma species can be controlled by the plasma parameters and the electric field (assumed to be in the vertical direction) induced in the plasma sheath region. To investigate the sheath structure, fluxes, and energies of the plasma species, a conventional fluid approach (sheath model) has been accounted in the present model [20, 21] that incorporates ionization of neutrals and ion-neutral collisions, however, electron-ion collisions are not accounted in the sheath model. The temperature of electrons and ions are assumed to be constant throughout the sheath. The number density and speed of the charged species (electrons and ions) are evaluated by the continuity Eqs. (6.1 & 6.2) and momentum Eqs. (6.3 & 6.4);

$$\frac{d}{dz}(n_k u_{kz}) = \nu_{ion} n_e \ , \tag{6.1}$$

$$\frac{d}{dz}(n_e u_{ez}) = \sum_k \nu_{ion} n_e \ , \tag{6.2}$$

$$M_k u_{kz} \frac{du_{kz}}{dz} = e\frac{d\phi}{dz} - m_k \nu_{col} u_{kz}, \tag{6.3}$$

$$0 = e\frac{d\phi}{dz} - m_e \nu_{col} u_{ez}, \tag{6.4}$$

where *k* refers to the positively charged species considered in the present model, n_j, m_j, and u_j are the number density, mass, and speed of the plasma species (*j*=e and *k* for electrons and positively charged ions, respectively), ϕ is the sheath potential, $\nu_{ion}(=\gamma_{ik}\Omega_k n_n)$ is the ionization frequency of the neutrals due to the collision with electrons, γ_{ik} is the ionization potential of the k^{th} ion, Ω_k is the k^{th} ion to electron number density ratio, $\sum_k \Omega_k = 1$, and $0 < \Omega_k < 1$, n_n is the number density of neutral atoms. However, the electron impact excitation and dissociation of the neutrals have not been accounted in the present plasma sheath model. ν_{col} is the collision frequencies of positively charged ions with neutrals. To determine the electric potential within the sheath, Poisson's equation (Eq. 6.5) has been considered in the present model.

$$\frac{d^2\phi}{dx^2} = 4\pi e(n_e - \sum \Omega_k n_k), \tag{6.5}$$

6.3.1 Nanostructuring of the thin metal catalyst film

Prior to carbon nanostructure growth, the predeposited thin metal (Nickel) catalyst film (nanofilm) is pre-treated with the low-temperature hydrogen plasma. The heavy plasma bombardment sinters the nanofilm into the many catalyst nanoislands (nanoparticles) which later initiates the CNF/CNT nucleation. The nucleation density (surface number density of nanoparticles) and nucleation seed size (nanoparticle size) can be deterministically controlled by reasonably varying the plasma conditions and initial nanofilm thickness and can be evaluated using the equation given underneath;

$$\begin{aligned}\frac{\partial}{\partial t}\left(m_{cf} C_{cf} T_s\right) &= A_{cf} C_{cf} t_{cf} \rho_{cf} T_s \frac{1}{n_{ct}} \frac{\partial n_{ct}}{\partial t} \\ &= \left[I_{ef} \varepsilon_e^f + I_{iBf} \varepsilon_{i2}^f + I_{Bf} \varepsilon_2^f \right] + \frac{3}{2} k_B T_S (1-\gamma_{iB}) I_{iBf} \\ &\quad + \upsilon_0 \sigma_{ads} J_2 U_B A_f + J_{i2} y_d(E_i)(1-\theta_t) A_f, \end{aligned} \tag{6.6}$$

where A_{cf} is the area of the metal catalyst film, T_S is the substrate temperature, m_{cf} is the mass of the catalyst film, t_{cf} is the thickness of the film, $C_{cf}\left(=0.104 \text{ cal g}^{-1}\ {}^{0}C^{-1}\right)$ is the specific heat of the film, ρ_{cf} is the density of catalyst film material, n_{ct} is the number of catalyst nanoparticle per unit area, υ_0 is the number of sites available, $J_j\left(=\frac{n_j v_{th}}{4}\right)$ and $J_{ij}=n_{ij}\left(k_B T_e / m_{ij}\right)^{1/2}$ are the neutral and ion flux, respectively [22], U_B(= 3.74 eV for the nickel catalyst) is the surface binding energy of the material (sputter target), y_d is the sputtering yield [23], and θ_t is the total surface coverage. ε_e^f, ε_{i2}^f, and ε_2^f are the mean energies collected by metal catalyst film surface due to electrons, ions, and neutral atoms, respectively [24] and given by $\varepsilon_k^f=\left[\left(\frac{2-Z\gamma_k}{1-Z\gamma_k}\right)-Z\gamma_k\right]k_B T_k$ and $\gamma_k=\frac{E_b}{k_B T_k}$, where k can be ion, electron or neutral atom. E_b is the energy barrier at the catalyst film surface, I_{i2f}, I_{2f}, and I_{ef} are the collection currents at the metal catalyst film surface due to ions and neutrals of type B, and electrons, respectively [25].

The Eq. (6.6) indicates the plasma-controlled nanostructuring of the thin metal catalyst nanofilm (segregation of nanofilm into many nanoparticles) by considering the energy balance at the nanofilm surface. In the LHS part of Eq. (6.6), the substrate temperature, specific heat and mass-volume density of the catalyst material is assumed to be constant. Thus, $\frac{\partial}{\partial t}\left(m_{cf}C_{cf}T_s\right)=C_{cf}T_s\rho_{cf}\frac{\partial}{\partial t}(V)$. Since the number of the nanoparticles and their size is continuously changing during the plasma processing of the nanofilm, therefore, volume V is replaced by the total volume of the nanoparticles i.e., $\frac{\partial}{\partial t}\left(m_{cf}C_{cf}T_s\right)=C_{cf}T_s\rho_{cf}A_{cf}\frac{\partial}{\partial t}\left(V' n_{ct}\right)$, where

$V'\left(=\pi D^3/12\right)$ is the volume of the each catalyst nanoparticles and D is the diameter of the nanoparticles (assuming here that all the nanoparticles formed are uniform in size with the hemispherical in shape). The plasma processing of the thin film initially segregates the nanofilm into large nanoislands and the continuous bombardments of energetic plasma species fragment the islands into many catalyst nanoparticles. Thus, the number density of the nanoparticles (number of nanoparticles per unit film area) as a function of processing time has been evaluated $\left[\frac{\partial}{\partial t}\left(m_{cf}C_{cf}T_s\right)=C_{cf}T_s\rho_{cf}A_{cf}V'\frac{\partial}{\partial t}\left(n_{ct}\right)\right]$ instead of nanoparticles size which is later evaluated using the mass balance condition between the nanofilm and nanoparticles $\left[A_{cf}t_{cf}=V'n_{ct}A_{cf}\right]$. Thus, reduced LHS of the Eq. (6.6) can be written as $\frac{\partial}{\partial t}\left(m_{cf}C_{cf}T_s\right)=C_{cf}T_s\rho_{cf}t_{cf}A_{cf}\frac{1}{n_{ct}}\frac{\partial}{\partial t}\left(n_{ct}\right)$. However, the RHS part of the Eq. (6.6) accounts the energy of the incident plasma species (first term of RHS), power gained by the film surface due to the formation of neutrals at the surface (second term), etching of the nanofilm by plasma species (third term), and physical sputtering (fourth term) of the nanofilm.

After pre-treatment, these nanoparticles are subjected to hydrogen diluted hydrocarbon plasma to initiate the growth of CNFs. The peculiar ability of these catalyst nanoparticles to form graphene layers around them is believed to be related with their catalytic activity for the decomposition of the hydrocarbon species to generate carbon and hydrogen species via various surface reactions [26-27] (see Table 6.2) and complex processes incorporated in the underneath equations.

$$\frac{\partial n_C}{\partial t}=\Bigg[\sum_A J_A(1-\theta_t)+\sum_A n_{sA}\upsilon\exp\left(\frac{-\delta E_{td}}{k_BT_S}\right)+\sum_{iA}\left(\sum_A\frac{n_{sA}y_d}{\upsilon_0}\right)J_{iA}+\sum_{iA}J_{iA}+J_C$$
$$+\sum_{iB}\left(\sum_{iA}\frac{J_{iA}\sigma_{ads}}{\upsilon}\right)J_{iB}-\sum_B\left(\sum_A n_{sA}\sigma_{ads}\right)J_B-n_C\upsilon\exp\left(\frac{-\delta E_{ev}}{k_BT_S}\right)$$
$$-\sum_A n_A\upsilon\exp\left(\frac{-\delta E_{dhc}}{k_BT_S}\right)-n_C\sigma_{ads}\upsilon n_H\Bigg]\times\frac{d\Omega_C}{dt}, \qquad (6.7)$$

Table 6.2. The surface reactions incorporated in the present model and their corresponding parameters, where pl= plasma and ad= adsorption.

Functional term	Explanation	Reaction involved
$J_A(1-\theta_t)$	adsorption of hydrocarbons on the catalyst nanoparticle surface	$C_{2X}H_{Y(pl)} \rightarrow C_{2X}H_{Y(ad)}$
$n_{sA}\upsilon \exp\left(\frac{-\delta E_{td}}{k_B T_S}\right)$	thermal dissociation of hydrocarbons	$C_{2X}H_{Y(ad)} \rightarrow 2XC_{(ad)} + YH_{(ad)}$
$\frac{n_A y_d}{\upsilon_0} J_{iA}$	ion induced dissociation of hydrocarbons	$C_{2X}H_Y^{+} + C_{2X}H_{Y(ad)} \rightarrow 2X\,C_{(ad)} + H_{Y(pl)} + C_{2X}H_Y^{+}$
J_{iA}	ion decomposition	$C_{2X}H_Y^{+} \rightarrow 2X\,C_{(ad)} + H_{2(pl)}$
$\frac{J_A \sigma_{ads}}{\upsilon} J_B$	loss of adsorbed hydrocarbons due to interaction with atomic hydrogen from plasma	$C_{2X}H_{Y(ad)} + H_{(pl)} \rightarrow C_{2X}H_{Y'(pl)}$
$\frac{n_C \sigma_{ads}}{\upsilon} J_B$	loss of generated carbon species at interaction with atomic hydrogen	$C_{(ad)} + H_{(pl)} \rightarrow CH_{(pl)}$
$n_C \upsilon \exp\left(\frac{-E_{ev}}{k_B T_S}\right)$	evaporation of carbon	$C_{(ad)} \rightarrow C_{(evaporation)}$
$n_{sa}\upsilon \exp\left(\frac{-E_{dhc}}{k_B T_S}\right)$	desorption of hydrocarbons	$C_{2X}H_{Y(ad)} \rightarrow C_{2X}H_{Y(ds)}$
$J_B(1-\theta_t)$	hydrogen adsorption on the catalyst nanoparticle surface	$H_{(pl)} \rightarrow H_{(ad)}$ $H_{2(pl)} \rightarrow H_{2(ad)}$
$\frac{n_{sA} y_d}{\upsilon_0} J_{iB}$	generation of hydrogen due to ion-induced decomposition of hydrocarbons	$C_{2X}H_Y^{+} + C_{2X'}H_{Y'(ad)} \rightarrow 2X\,C_{(ad)} + YH_{(ad)} + C_{2X'}H_{Y'}^{+}$
$n_{sB} \exp\left(\frac{-E_{dH}}{k_B T_S}\right)$	hydrogen desorption from the catalyst nanoparticle surface	$H_{(ad)} \rightarrow H_{(ds)}$

$$\frac{\partial n_H}{\partial t} = \sum_B J_B(1-\theta_t) + \sum_{iA}\left(\sum_A \frac{n_{sA} y_d}{\upsilon_0}\right) J_{iA} + \sum_B n_{sB}\upsilon \exp\left(\frac{-\delta E_{td}}{k_B T_S}\right) + \sum_{iB} J_{iB}$$
$$- \sum_B n_{sB}\upsilon \exp\left(\frac{-\delta E_{dH}}{k_B T_S}\right) - n_C \sigma_{ads} \upsilon n_H - \sum_B n_{sB}\sigma_{ads} J_B - \sum_B n_{sB}\sigma_{ads} J_{iB}, \quad (6.8)$$

where n_C and n_H are the surface number density of carbon and hydrogen

species, respectively, generated on the catalyst nanoparticle front face. $n_{sj}\left(=\theta_j \upsilon_0\right)$ is the surface number density of neutral atoms [22, 26, 28], θ_j is the surface coverage by the corresponding species, υ_0 is the adsorption sites per unit area, υ is the thermal vibration frequency, $\sigma_{ads}\left(=6.8\times10^{-16}\text{cm}^2\right)$ is the cross section for the interaction among various species [22], $\delta E_{td}\,(=2.1\,eV)$ is the hydrocarbons dissociation energy, $\delta E_{\text{ev}}(=1.8\text{ eV})$ carbon evaporation energy, $\delta E_{dhc}\left(=1.8\text{ eV}\right)$ is the hydrocarbon desorption energy, $\delta E_{th}\left(=1.87\text{ eV}\right)$ is the energy for thermal dehydrogenation of hydrocarbons, $\delta E_{dH}\,(=1.8\text{ eV})$ is the hydrogen atom desorption energy [29].

The dissociation of the hydrocarbon species on the front active surface of the catalyst is the complex process which is discussed in detail in the Eq. (6.7) that incorporates the adsorption of neutral hydrocarbon species on the catalyst surface (first term), thermal and ion induced dissociation of hydrocarbons (second & third term), ion dissociation (fourth term), direct carbon flux towards catalyst surface (fifth term) [22], and generation of carbon species due to the interaction between hydrocarbon ions and hydrogen ions i.e., ion-ion interaction (sixth term), loss of hydrocarbons neutrals due to interaction with hydrogen (seventh term), carbon evaporation (eight term), and desorption of hydrocarbons neutrals from catalyst surface (ninth term) [29], and interaction between carbon and hydrogen species generated on the catalyst nanoparticle surface (tenth term). The continuous generation of carbon species due to the progressive dissociation of hydrocarbons leads to the formation of the amorphous carbon layer on catalyst active surface. This amorphous carbon layer poisons the catalyst activity and blocks the further dissociation of the hydrocarbon species. Thus, the term $\frac{d\Omega_c}{dt}\left(=1-n_c\pi D^2\right)$ indicative of the catalyst poisoning rate has also been accounted in the Eq. (6.7), where Ω_c is blocking function which represents the poisoning of the catalyst particle and depends on the number of carbon species generated on the catalyst and the growth time.

The Eq. (6.8) indicates the hydrogen species generation rate on the catalyst surface on accounting the adsorption of hydrogen on catalyst nanoparticle surface [26] (first term), ion-induced dissociation and thermal dissociation of hydrocarbons (second & third term) [29], direct hydrogen ion flux (fourth term), loss of hydrogen due to desorption of hydrogen radicals from catalyst nanoparticle surface (fifth term), the interaction of hydrogen radicals with carbon species (sixth term), and interaction of adsorbed hydrogen with incoming hydrogen neutrals and ions from the plasma (seventh & eight term) [31]. The Eq. (6.8) does not account the poisoning rate of the catalyst this is because both Eqs. (6.7) and (6.8) are simultaneous coupled equations and both account the terms corresponding to the interaction between the carbon and hydrogen species generated on the catalyst surface. Therefore, if catalyst poisoning leads to the saturation of n_C, this further leads to the saturation of n_H.

6.3.2 Restructuring of the catalyst particle during CNF growth

$$\frac{\partial S}{\partial t}=\left[\begin{array}{c} D_S \exp\left(\frac{-E_S}{k_B T_S}\right)+D_b \exp\left(\frac{-E_b}{k_B T_S}\right)+ \\ A_k \exp\left(\frac{-\delta E_{inc}}{k_B T_S}\right)\frac{\rho_{cat}\pi D}{m_{cat}} \end{array}\right]\times\frac{P n_c}{\rho_{cat}\nu I_{iA}}+D_m\left(\frac{-E_{SD}}{k_B T_S}\right), \quad (6.9)$$

where $S\left[=\frac{\pi}{6}\left(\ell d+\ell b+d^2+b^2\right)\right]$ is the surface area of the catalyst nanoparticle that remains at the top of the CNF during the growth. ℓ, d, and b are the length, base diameter, and tip diameter of the elongated or deformed catalyst nanoparticle, respectively. $D_S\left(=a_0^2\nu\right)$ is the surface diffusion coefficient, $a_0(=0.34\ nm)$ is the carbon atoms inter-atomic distance, E_S (=0.3 eV) is the energy barrier for carbon species diffusion through the catalyst surface [26], $D_b\left(=\nu D/2\pi\right)$ is the bulk diffusion coefficient, E_b (=1.8 eV) is the energy barrier for carbon species bulk diffusion through catalyst nanoparticle [26], P ($\approx 20\ GPa$) is the pressure exerted by graphene layers on catalyst nanoparticle [31], $A_k\left(=a_0\nu\right)$ is the

carbon species incorporation speed into the graphene layers [31], $\delta E_{inc}\left(=0.4\ eV\right)$ is the carbon species energy barrier to diffuse along the nanofiber-catalyst interface, m_{ct} is the mass of the metal catalyst particle, and ρ_{ct} is the density of metal catalyst nanoparticle. D_m is the metal atoms self-diffusion coefficient [32], E_{SD} is the metal atoms self-diffusion activation energy.

The plasma assisted catalyzed growth of CNF is the dynamic process, in which catalyst particle undergoes shape transformation (deformation). The growth, as well as alignment of the graphitic shells around the catalyst nanoparticle unequivocally, relies upon the degree up to which the catalyst nanoparticle can restructure itself during the CNF/CNT growth. Subsequently, it is critically vital to think about how the catalyst nanoparticle experiences shape change and what are factors in charge of this. The Eq. (6.9) represents the rate of change of the surface area of the catalyst nanoparticle. However, it is assumed that the volume of the catalyst nanoparticle remains invariant during the growth i.e., the initial volume of the hemispherical particle must be equal to the final volume of the peer drop shaped particle, i.e., $D^3=\left(d^2+3b^2+bd\right)\ell$. One of the major factors for the catalyst deformation is the varying compressive stress exerted by the growing graphitic shells around the catalyst. Thus, to evaluate the change in surface area of the catalyst during the growth, it is necessary to account all the processes that are responsible for the precipitation and the growth of graphitic shells. Thus, Eq. (6.9) accounts the surface and the bulk (first &second term) diffusion of the carbon species generated on the active surface of the catalyst that eventually precipitates around the rear of the catalyst nanoparticle to frame graphitic shells (third term) and subsequently exert significant pressure on the catalyst nanoparticle (multiplication term outside the first bracket). Moreover, the self-diffusion of the metal atoms (last term) along the growth direction is an additional critical factor for the catalyst particle elongation.

6.3.3 Growth of carbon nanofibers

$$\frac{\partial N_g}{\partial t} = \left(\begin{array}{c} D_S \exp\left(\frac{-E_S}{k_B T_S}\right) + D_b \exp\left(\frac{-E_b}{k_B T_S}\right) \\ + A_k \exp\left(\frac{-\delta E_{inc}}{k_B T_S}\right) \pi D \end{array} \right) \times n_c S - n_H \mathrm{S}, \qquad (6.10)$$

$$\frac{\partial}{\partial t}\pi(D^2 - d^2)h = \left[\begin{array}{c} \left\{ \begin{array}{c} D_S \exp\left(\frac{-E_S}{k_B T_S}\right) + D_b \exp\left(\frac{-E_b}{k_B T_S}\right) \\ + A_k \exp\left(\frac{-\delta E_{inc}}{k_B T_S}\right) \times D \end{array} \right\} \times n_C \\ + n_H \left(\pi D^2\right) \sum_B I_{iB} \end{array} \right] \times \frac{m_{ct}}{\rho_{ct}}, \quad (6.11)$$

The Eq. (6.10) illustrates the rate of graphitization, i.e., number of graphitic shells formed (N_g) around the catalyst nanoparticle during CNF growth, however, the Eq. (6.11) relates the dimensions (i.e., CNF tip diameter and height) of the plasma grown CNF with the number of carbon and hydrogen species generated on the catalyst nanoparticle surface. The first three terms of Eqs. (6.10) & (6.11) denote the surface diffusion, bulk diffusion, and precipitation of carbon species around the catalyst particle, respectively. However, the last term of both the equations denotes the decrease in a number of graphene layers due to etching of side walls of CNF, i.e., removal of precipitated carbon due to the interaction with hydrogen species. During the growth, etching of the CNF by hydrogen species leads to the decrease in a number of graphene layers formed and thus decrease in CNF diameter. Therefore, the etching term has been subtracted in Eq. (6.10). However, the highly active hydrogen species etch the terminal carbons present at the edges of the graphitic nest and the carbon shadowed by the catalyst particle may contribute to the vertical growth of graphitic shells and thus leads to the higher growth of the CNF. Therefore, etching term has been added in Eq. (6.11).

6.3.4 Balance equation of neutral species

$$\frac{\partial n_A}{\partial t} = \alpha_A n_e n_{iA} - \beta_A n_A + \frac{n_{cnf}}{\lambda_d}(1-\gamma_{iA})\left(I_{\text{tip-}iA} + I_{cur-iA}\right) - \frac{n_{cnf}}{\lambda_d}\gamma_A\left(I_{\text{tip-}A} + I_{cur-A}\right) + IF_A - OF_A - J_{\text{ai-A}} + J_{\text{desp-A}} - \sum_{\ell AB} k_\ell n_A n_{iB} + \sum_{QBA} k_Q n_B n_{iA}, \quad (6.12)$$

$$\frac{\partial n_B}{\partial t} = \alpha_B n_e n_{iB} - \beta_B n_B + \frac{n_{cnf}}{\lambda_d}(1-\gamma_{iB})\left(I_{\text{tip-}iB} + I_{cur-iB}\right) - \frac{n_{cnf}}{\lambda_d}\gamma_B\left(I_{\text{tip-}B} + I_{cur-B}\right) + IF_B - OF_B - J_{\text{ai-B}} + J_{\text{desp-B}} + J_{\text{thd}} - \sum_{QBA} k_Q n_B n_{iA} + \sum_{\ell AB} k_\ell n_A n_{iB}, \quad (6.13)$$

where β_j is the coefficient of ionization of neutral atoms [33], α_j is the coefficient of recombination of electrons and positively charged ions [34], n_e is the electron number density, n_{ij} is the ion number density (i.e., number of ions per unit volume), n_j is the neutral atom density, n_{cnf} is the number density (i.e., number of CNFs per unit area) of CNFs, and $\lambda_d \left(= 3\times10^{-3}\,\text{cm}\right)$ is the plasma sheath width, γ_{ij} is the ion sticking coefficient, $J_{\text{ai-j}}$ is the adsorption flux on the catalyst substrate surface, $J_{\text{desp-j}}$ is the desorption flux from the catalyst substrate surface, J_{thd} is the hydrogen ion flux due to thermal dehydrogenation, I_{tip-ij} and I_{cur-ij} are the ion collection currents at the tip and curved surface of the CNF, $I_{\text{tip-j}}$ and $I_{cur-\text{j}}$ are the neutral atom collection currents at the tip and curved surface of the CNF [See chapter 3], $IF_j \left(= 4.4\times10^{17}\times f_j / V\right)$ and $OF_j \left(= R_p \times n_j / V\right)$ are the j^{th} species inflow rate and outflow rate into/from the plasma chamber, respectively. f_j is the inlet flow of corresponding gas,

Ravi Gupta, *Department of Applied Physics, Delhi Technological University, Delhi, India*

$V\left(\approx 2\times10^{4}\ \mathrm{cm}^{3}\right)$ is the volume of the chamber, and R_p is the pumping rate [35], k_j is the ion-neutral reaction rate coefficient.

The Eqs. (6.12) & (6.13) denote the growth of neutral species of type A and B in the bulk plasma on account of increase in number density due to electron-ion recombination (first term), decrease in number density due to ionization of neutral species (second term), increase in number density due to neutralization of ions collected at the CNF surface (third term), decrease in number density due to the accretion of neutrals at the CNF surface (fourth term), inflow and outflow rate of neutral species from plasma chamber (fifth & sixth term), adsorption of neutrals to the catalyst surface (seventh term) and desorption of neutrals from the catalyst surface (eighth term). The Ninth term of Eq. (6.13) corresponds to gain in hydrogen ion number density in the plasma per unit time due to thermal dehydrogenation [22, 28]. The remaining terms correspond to the increase and decrease in neutral atoms number density due to the ion-neutral reactions considered in the present model [17] (see Table 6.3).

6.3.5 Balance equation of positively charged ions

$$\frac{\partial n_{iA}}{\partial t} = \beta_A n_A - \alpha_A n_e n_{iA} - \frac{n_{cnf}}{\lambda_d}\left(I_{\mathrm{tip}\text{-}iA} + I_{cur\text{-}iA}\right) + \sum_{\ell AB} k_\ell n_A n_{iB} - \sum_{QBA} k_Q n_B n_{iA}, \tag{6.14}$$

$$\frac{\partial n_{iB}}{\partial t} = \beta_B n_B - \alpha_B n_e n_{iB} - \frac{n_{cnf}}{\lambda_d}\left(I_{\mathrm{tip}\text{-}iB} + I_{\mathrm{cur}\text{-}iB}\right) + \sum_{QBA} k_Q n_B n_{iA} - \sum_{\ell AB} k_\ell n_A n_{iB}, \tag{6.15}$$

The Eqs. (6.14) and (6.15) denote the growth rate of positively charged species of type A and B, respectively in the bulk plasma on account of ionization of neutral species (first term), electron-ion recombination (second term), ion collection current at the CNF surface (third term), and reaction

between positively charged ions and neutrals in the plasma at different reaction rates (fourth & fifth terms).

Table 6.3. Ion-neutral reactions in the bulk plasma considered in the present model. The reaction rates of these reactions have been adopted from the Ref. [41].

Reaction	Reaction Rate (cm^3/s)
$C_2H + C_4H_2^+ \rightarrow C_6H_2^+ + H$	1.30×10^{-9}
$C_2H_2 + C_2H^+ \rightarrow C_4H_2^+ + H$	1.20×10^{-9}
$C_2H_2 + C_2H_3^+ \rightarrow C_4H_2^+ + H_2$	2.40×10^{-10}
$C_2H_2 + C_4H_2^+ \rightarrow C_6H_4^+$	1.40×10^{-10}
$C_2H_2 + C_2H_2^+ \rightarrow C_4H_3^+ + H$	9.50×10^{-10}
$C_2H_2 + C_2H_2^+ \rightarrow C_4H_2^+ + H_2$	1.20×10^{-9}
$C_2H_2^+ + H_2 \rightarrow C_2H_3^+ + H$	1.00×10^{-11}
$C_2H_2^+ + C_6H_2 \rightarrow C_6H_2^+ + C_2H_2$	5.00×10^{-10}
$C_2H_2^+ + C_2H_3 \rightarrow C_4H_3^+ + H_2$	3.30×10^{-10}
$C_4H_2^+ + C_2H_3 \rightarrow C_6H_4^+ + H$	1.20×10^{-9}
$C_4H_3^+ + C_2H_3 \rightarrow C_6H_4^+ + H_2$	5.00×10^{-10}
$C_2H_3^+ + H \rightarrow C_2H_2^+ + H_2$	6.80×10^{-11}
$H^+ + C_2H_2 \rightarrow C_2H_2^+ + H_2$	4.30×10^{-9}
$H^+ + C_4H_2 \rightarrow C_4H^+ + H_2$	2.00×10^{-9}
$H_2^+ + H \rightarrow H^+ + H_2$	6.40×10^{-10}
$H_2^+ + C_2H_2 \rightarrow C_2H_2^+ + H_2$	5.30×10^{-9}
$H_2 + C_2H^+ \rightarrow C_2H_2^+ + H$	1.70×10^{-9}

6.3.6 Balance equation of electrons

$$\frac{\partial n_e}{\partial t} = \sum_A \beta_A n_A + \sum_B \beta_B n_B - \sum_A \alpha_A n_e n_{iA} - \sum_B \alpha_B n_e n_{iB} - \gamma_e \frac{n_{cnf}}{\lambda_d}\left(I_{\text{tip-e}} + I_{\text{cur-e}}\right), \quad (6.16)$$

Ravi Gupta, Department of Applied Physics, Delhi Technological University, Delhi, India

The Eq. (6.16) illustrates the growth of electron number density in the bulk plasma on account of gain in electron number density per unit time due to ionization of neutral species of type A & B (first & second term), decay rate due to electron-ion recombination (third & fourth term) and electron collection current at the CNFs surface (last term).

6.3.7 Charged developed over the CNF surface

$$\frac{\partial Z}{\partial t} = \sum_j I_{tip-ij} + \sum_j I_{cur-ij} - \gamma_e \left(I_{tip-e} + I_{tip-e} \right), \qquad (6.17)$$

where Z is the charge number developed on the CNF surface due to the accumulation of positively charged species (first two terms) and negatively charged electrons (last term) from the plasma.

6.4 Results and discussion

In the present chapter, an analytical model has been developed to provide the better insight into the catalyzed growth of CNF via PECVD process. The fragmentation of metal catalyst thin film into the catalyst particles, dissociation of hydrocarbons on the catalyst surface to generate carbon species, diffusion of carbon species through the catalyst, precipitation of carbon species, and deformation of catalyst particle during growth have been incorporated in the present paper.

In this section, the numerical solution of model equations illustrated in Sec. 6.3 is used to explore the consequences of catalyst nanofilm on the plasma-assisted growth of CNF. In particular, we investigate the role of catalyst nanofilm on the number density and size of nucleation seeds and further its repercussions on the CNF growth. The first order simultaneous differential equations have been solved using the MATHEMATICA software for experimentally determined initial conditions [8, 9] and glow discharge plasma parameters [17, 20] listed in Table 6.4.

Table 6.4(a). Initial values of number density of numerous plasma species considered in the present computation on the basis of the literature Refs. [17, 18] specifying the plasma composition of the C_2H_2/H_2 gas in the glow discharge.

Parameter	Description	Initial Value
n_e	electron number density	1.45×10^{10} cm^{-3}
n_{ij}	Ion number density	
	C_2H^+	0.05×10^{10} cm^{-3}
	$C_2H_2^+$	0.15×10^{10} cm^{-3}
	$C_2H_3^+$	0.1×10^{10} cm^{-3}
	$C_4H_2^+$	0.15×10^{10} cm^{-3}
	$C_4H_3^+$	0.15×10^{10} cm^{-3}
	$C_6H_2^+$	0.07×10^{10} cm^{-3}
	$C_6H_4^+$	0.08×10^{10} cm^{-3}
	H^+	0.35×10^{10} cm^{-3}
	H_2^+	0.35×10^{10} cm^{-3}
n_j	Neutral atom number density	
	C_2H	1×10^{10} cm^{-3}
	C_2H_2	0.4×10^{14} cm^{-3}
	C_2H_3	0.7×10^{13} cm^{-3}
	C_4H_2	0.3×10^{13} cm^{-3}
	C_4H_3	0.2×10^{12} cm^{-3}
	C_6H_2	0.4×10^{12} cm^{-3}
	C_6H_4	0.5×10^{11} cm^{-3}
	H	0.2×10^{14} cm^{-3}
	H_2	1×10^{15} cm^{-3}

Table 6.4(b). Initial values of the various parameters considered in the present computation on the basis of the experimentally determined initial conditions Refs. [8,9].

Parameter	Description	Initial Value
T_e	electron temperature	2 eV
T_i	ion temperature	0.15 eV
T_n	neutral atom temperature	0.15 eV
A_{cf}	Area of catalyst film	1 cm^2
ρ_{ct}	Density of nickel catalyst	8.96 g/cm^3
$\alpha_{10} \approx \alpha_{20}$	electron-ion recombination coefficient	1.12×10^{-7} cm^3/sec
T_s	substrate temperature	550 ^{0}C
γ_e	electron sticking coefficient	1
γ_{ij}	ion sticking coefficient	1
γ_j	neutral atom sticking coefficient	1
θ_t	total surface coverage	0.01
$f_{C_2H_2}$	C_2H_2 gas flow rate	50 sccm
f_{H_2}	H_2 gas flow rate	200 sccm
U_s	substrate potential	-300 V

Ravi Gupta, Department of Applied Physics, Delhi Technological University, Delhi, India

Figure 6.1(a) shows the time evolution of nanoparticle surface number density as a function of nanofilm thickness during plasma pre-treatment. The number density of nanoparticles increases with time due to continuous bombardment of highly energetic species on the film surface from the plasma during the pre-treatment and attains the saturation when nanofilm get completely transformed into a large number of nanoparticles. However, the surface number density of these nanoparticles decreases with increase in initial thickness of the nanofilm and therefore the size of the nanoparticle increases (see Fig. 6.1(b)).

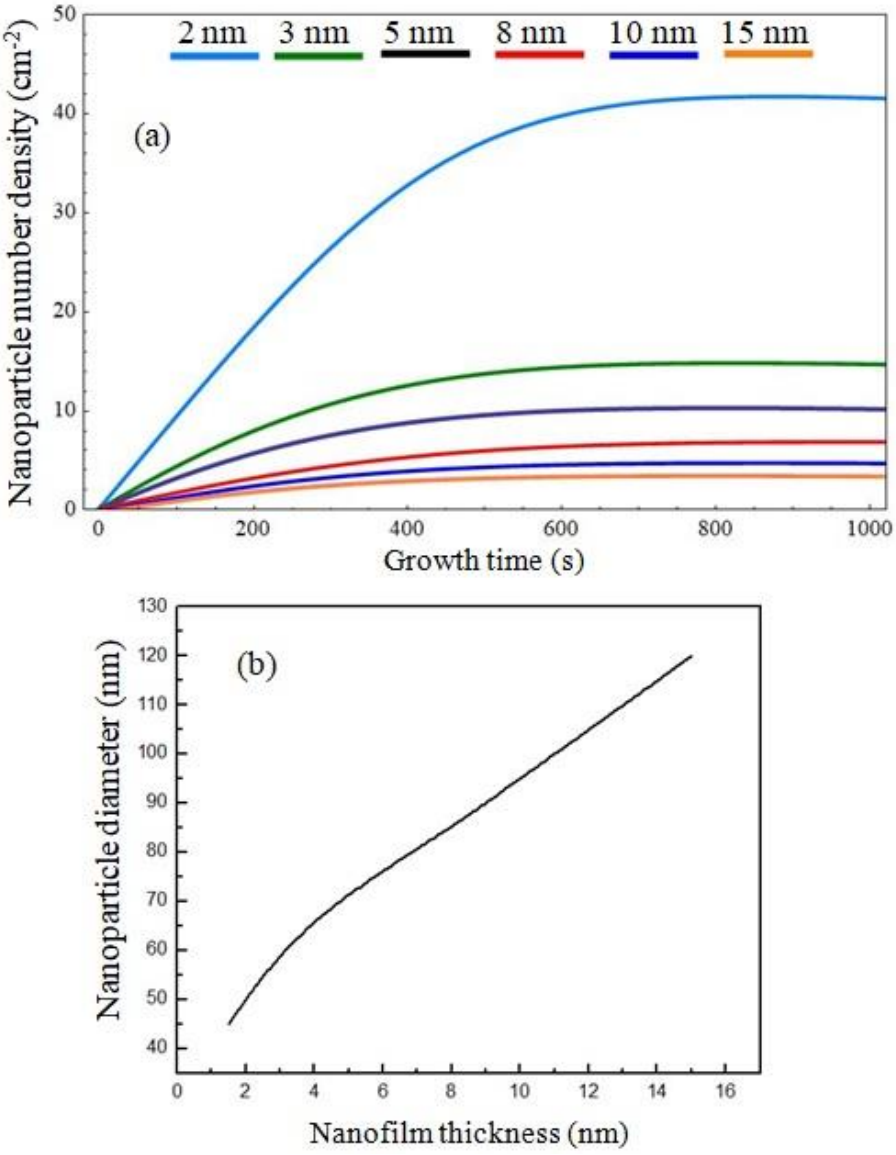

Fig. 6.1. Dependence of (a) catalyst nanoparticles number density and (b) size of catalyst nanoparticle on the catalyst thin film thickness during plasma pre-treatment.

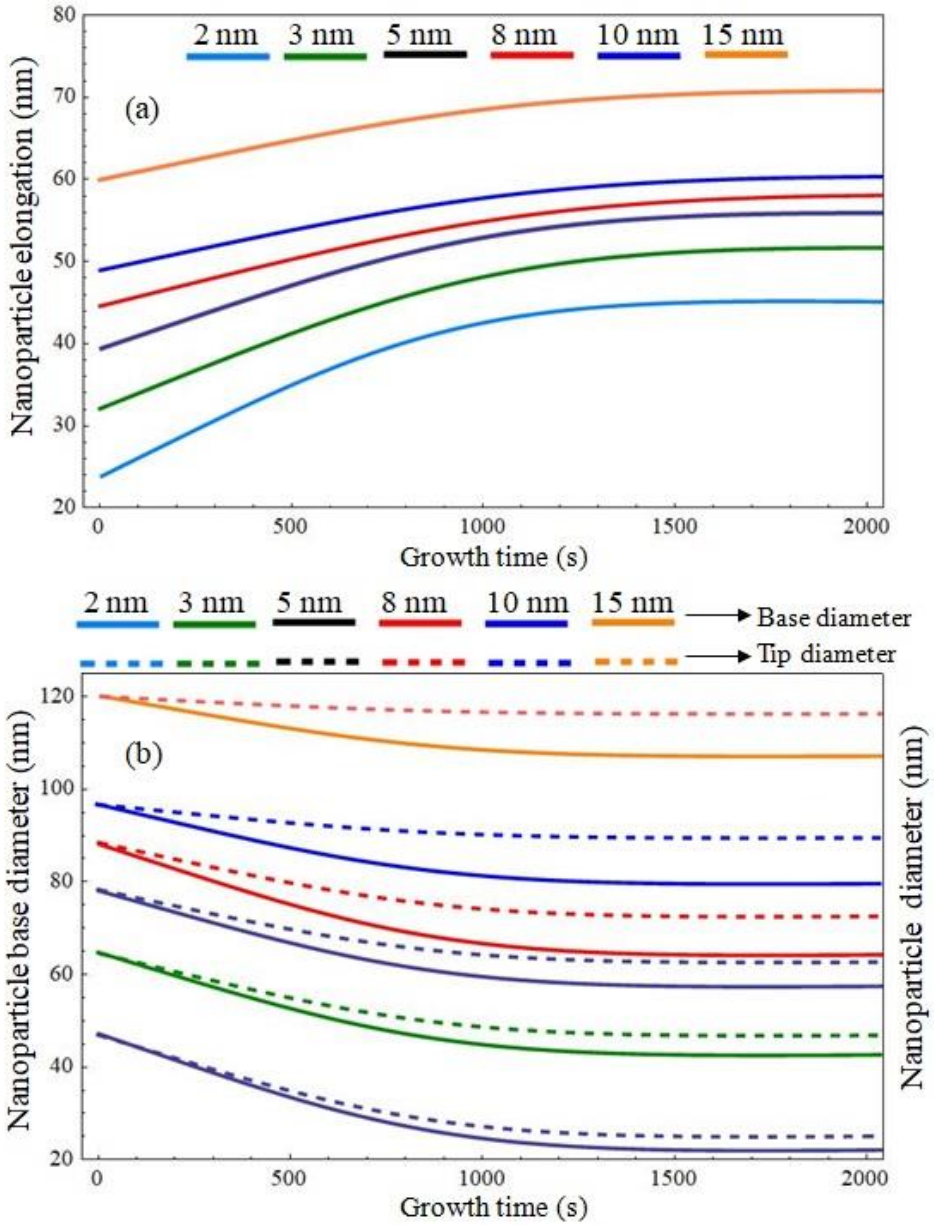

Fig. 6.2. Growth time variation of (a) elongation produced in catalyst and (b) catalyst base and tip diameter for different catalyst film thickness.

Figure 6.2 shows the restructuring of catalyst nanoparticle during the CNF growth. At the CNF nucleation stage, catalyst particle is assumed to be hemispherical. During the CNF growth, continuously formed graphene layers around the catalyst surface exert significant compressive stress on the catalyst particle which results in the elongation of the catalyst particle [see Fig. 6.2(a)]. The introductory length of the catalyst is assumed to be the half of the particle size. As catalyst particle elongates during the growth, the length of the catalyst increases with growth time and finally attains saturation. However, elongation

produced leads to the decreases in catalyst particle base as well as tip diameter [see Fig. 6.2(b)]. It can be seen from Fig. 6.2(b) that base diameter of the catalyst decreases at the higher rate as compared to the tip diameter. The carbon species generated at the active surface (front face) of the catalyst nanoparticle precipitate at the rear surface after their diffusion through the catalyst. Thus, the stress produced by the graphene layers adding one to the other between the catalyst and the existing graphene layers is much more near the rear surface of the catalyst. Additionally, one can see from Fig. 6.2 that restructuring catalyst is continuous during the growth and also depend on the thickness of the nanofilm. The different catalyst size results from the different catalyst nanofilm thickness lead to the different distortion behaviour. It is found that small nanoparticles deform quickly as compared to the large nanoparticles.

To comprehend the reliance of the CNF growth on the catalyst film thickness, the families of curves have been shown in Fig. 6.3-6.6. With the increase in nanofilm thickness, size of the nanoparticle increases which leads to increase the catalyst activity for the hydrocarbons dissociation on the active front face of the catalyst. Thus, a large number of carbon species generates on the catalyst surface (see Fig. 6.3) and ultimately increases the carbon precipitation rate. Large catalyst particles have more tendencies to shadow the graphene layers from carving by hydrogen species. Therefore, carbon species after diffusion through catalyst precipitate in the form of new graphene layers in the region shadowed by the catalyst, consequently, number of graphene layers increases (see Fig. 6.4). However, small catalyst particles are comparatively less proficient to shadow the graphene layers from carving by hydrogen, and thus carbon species precipitate in a manner to encourage the vertical growth of existing graphene layers resulting in the higher CNF growth (see Fig. 6.5). Furthermore, CNF nucleates from different nanofilm (varying in thickness) show different growth saturation behaviour. The small catalyst nanoparticles are characterized by a smaller active surface for hydrocarbons dissociation, which are found to be poisoned quickly due to the progressive formation of amorphous carbon layer at the catalyst nanoparticle surface, whereas larger nanoparticles maintain their catalytic activity for quite long time (see Fig. 6.6). Thereby,

resulting in the faster saturation of the CNFs grew over small catalyst particles as compared to the large catalyst particles.

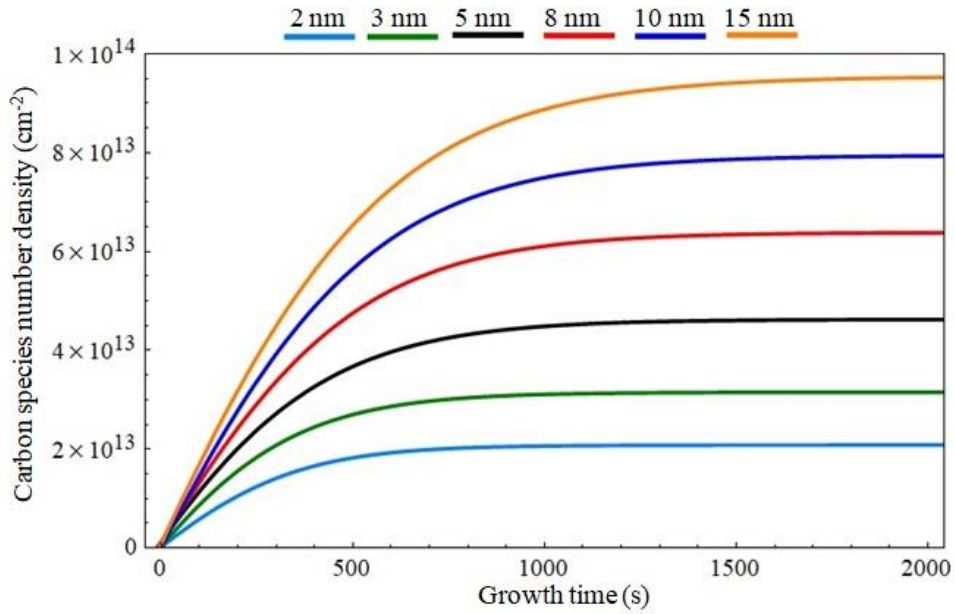

Fig. 6.3. Growth time variation of number of carbon species generated on catalyst nanoparticle front face as the function of nanofilm thickness.

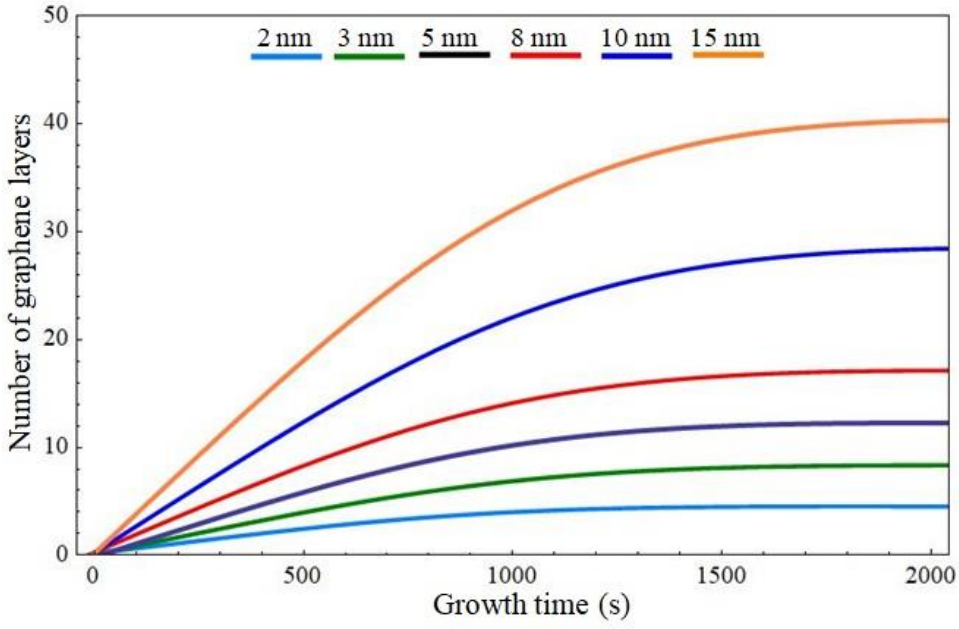

Fig. 6.4. Dependence of number of graphitic shells (graphene layers) formed during CNF growth on the catalyst film thickness.

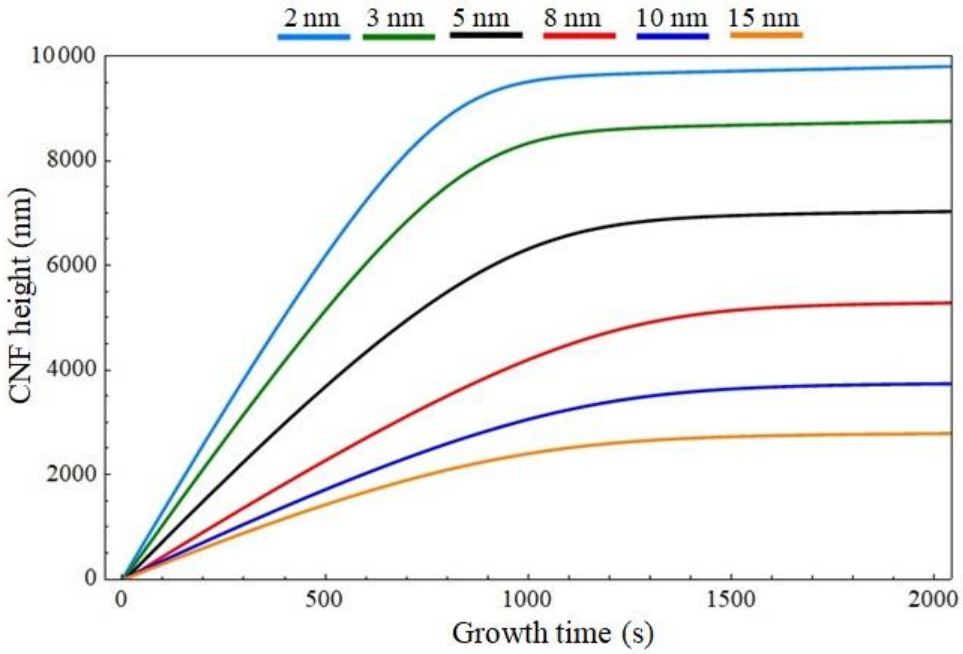

Fig. 6.5. Growth time variation of CNF height for different catalyst film thickness.

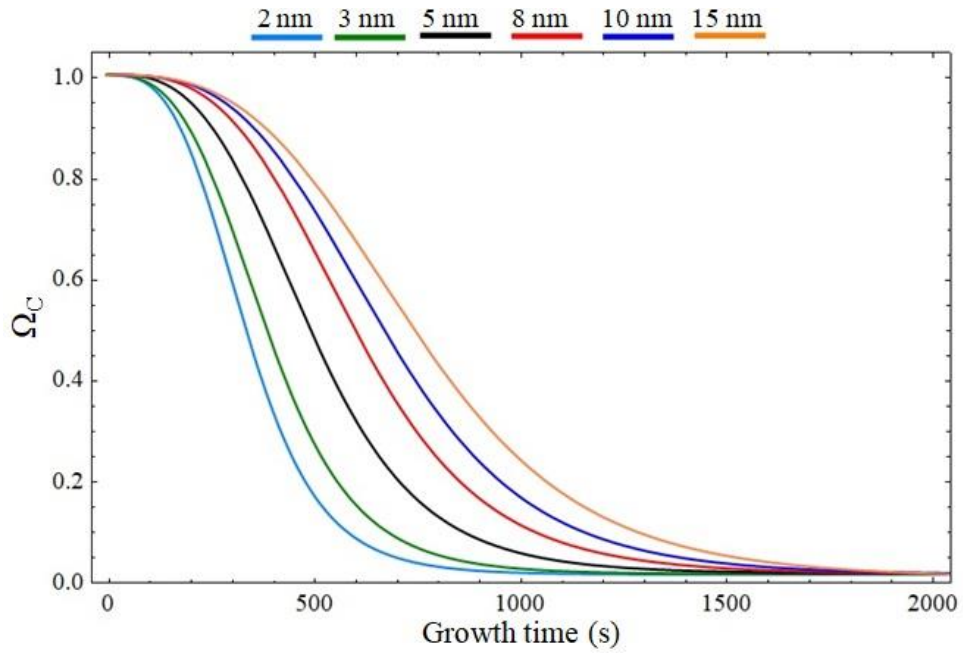

Fig. 6.6. Growth time variation of blocking function (poisoning of catalyst) as a the function of catalyst film thickness.

As schematically shown in Fig. 6.7, the correlation between CNF inner and outer diameters with the catalyst nanoparticle base diameter and tip diameters, respectively, strongly depends on the catalyst nanoparticle restructuring during PECVD growth of CNFs. The continuous deformations of catalyst particle during the growth lead to the reduction in base diameter (see Fig. 6.2) and thereby, decrease in inner diameter. Thus, the thickness of the CNF wall increases during the growth or more precisely say the number of graphitic shells increases during the growth (see Fig. 6.4) from bottom to the top of the CNF. It is believed that outer diameter of the CNFs/CNTs remains uniform throughout the growth, and there is 1:1 correlation between the catalyst diameter and CNFs/CNTs outer diameter [8]. However, from the present study one can notice the reduction in the outer diameter of the CNF during the growth [8] (see Fig. 6.2). Thus, one can predict the upper limit of the CNF/CNT outer diameter from the catalyst nanoparticle size, whereas, in reality, the outer diameter of the CNF/CNT depends on the extent up to which the catalyst nanoparticle can restructure itself during the growth.

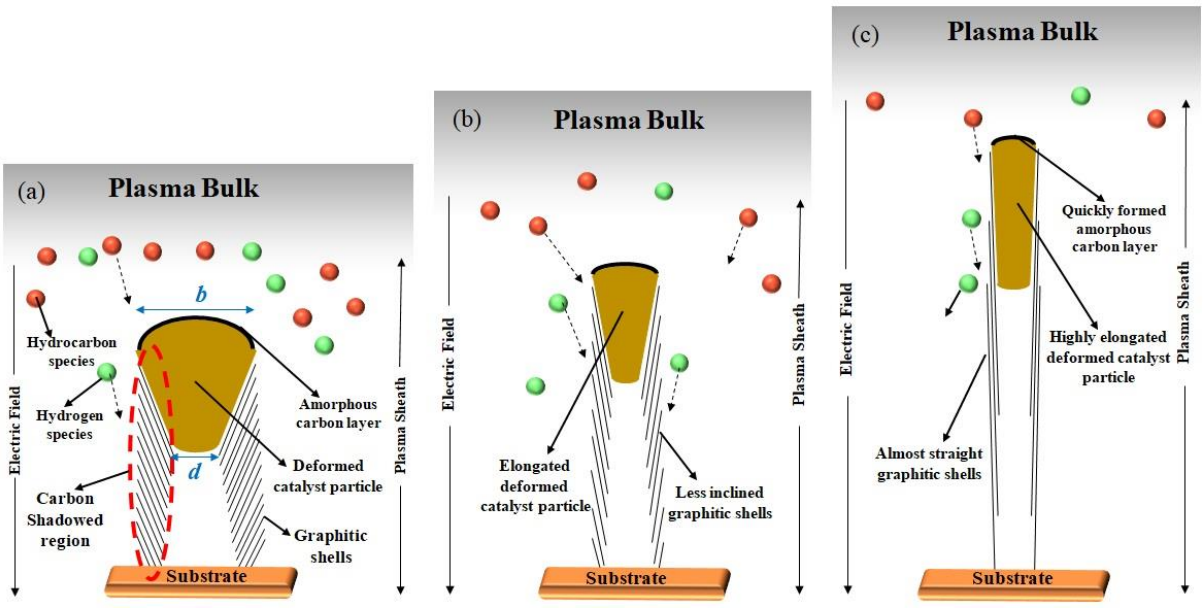

Fig. 6.7. Schematic of the restructuring of catalyst particle during CNF growth over (a) thick catalyst film (thickness around 10 nm or more), (b) thin catalyst film (thickness around 5 nm), and (c) ultrathin films (thickness around 2 nm or less). The dotted arrows show the flux of hydrocarbons and hydrogen species on the catalyst and CNF walls.

The schematic Fig. 6.8 shows the dependence of the alignment of the graphitic shells on the catalyst nanoparticles obtained from the different catalyst nanofilms (nanofilms having different thickness). In the previous chapters, we reported the strong dependence of the graphitic shell inclination angle on the geometry of the deformed catalyst nanoparticle i.e., $tan\,\theta = \frac{b-d}{2l}$, where θ is the inclination angle of the graphitic shells with the vertical growth axis. From this relation, one can see that straighter or less inclined graphitic shells are formed if elongation produced in the catalyst is higher and the difference between tip and base diameter of the deformed catalyst is lesser.

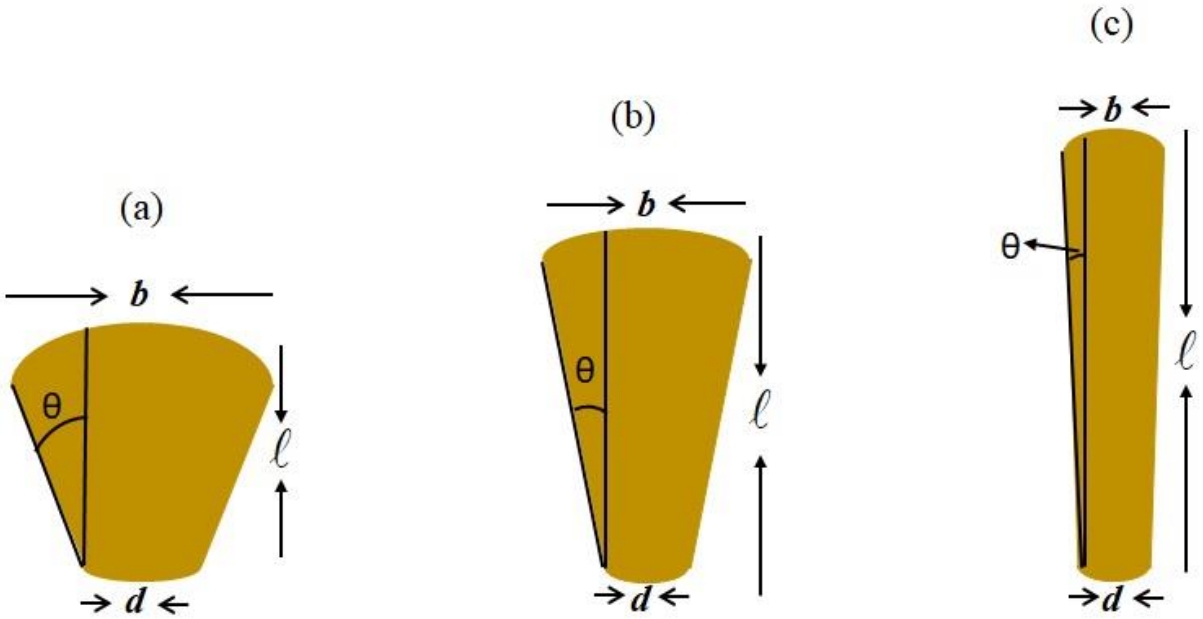

Fig. 6.8. Schematic of the dependence of graphene layers inclination on the restructuring of the catalyst during CNF growth over (a) thick catalyst film (thickness around 10 nm or more), (b) thin catalyst film (thickness around 5 nm), and (c) ultrathin films (thickness around 2 nm or less).

In the present chapter, we account the restructuring of the catalyst nanoparticle to evaluate the deformation produced (elongation produced the change in tip and base diameter) in the catalyst nanoparticle during the CNF growth in the plasma environment. The results of the present investigation show that the ultra-thin catalyst nanofilms lead to the formation of smaller catalyst nanoparticles (see Fig. 6.1). The difference between the tip and the base diameter of the deformed catalyst nanoparticle is found to be less for nanoparticles obtained from the thin nanofilm and increases with increase in nanofilm thickness [see Fig. 6.9 (a)].

Therefore, the catalyst nanoparticles obtained from thin nanofilm undergo higher elongation as compared to the nanoparticles obtained from the thick nanofilms [see Fig. 6.9 (b)]. Thus, less inclined graphitic shells are formed when nucleated over the small nanoparticles obtained from the thin catalyst nanofilms. Furthermore, from the above-detailed discussion (see Figs. 6.1 to 6.9), one can also notice the transition of thick CNFs containing a large number of graphitic shells to the thin CNFs/CNTs containing few graphitic shells when thickness on nanofilm decreases (see Fig. 6.8).

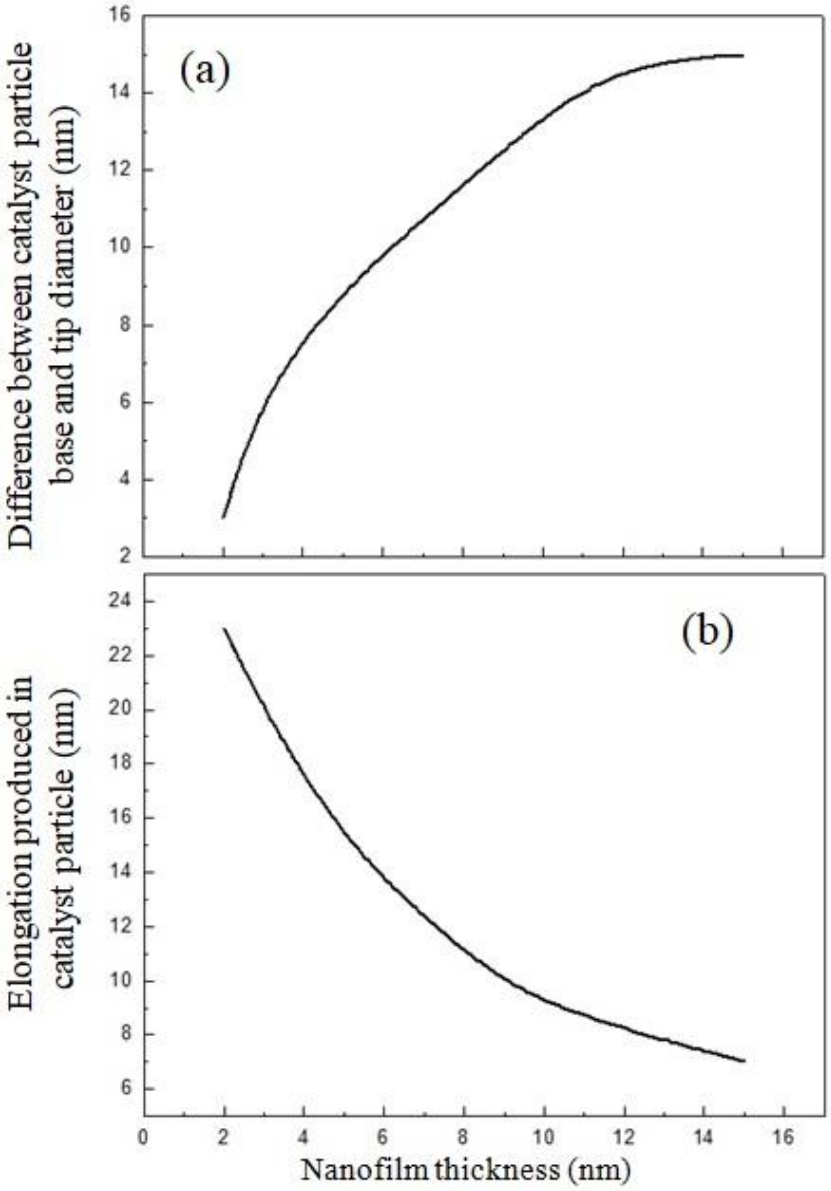

Fig. 6.9. Variation of (a) difference between catalyst tip and base diameter and (b) elongation produced in the catalyst with catalyst film thickness.

These theoretical findings obtained are in good agreement with the available experimental observations as follows. Chhowalla *et al.* [10] observed the dependence of nanoparticle size and their number density on catalyst film thickness for plasma enhanced CVD case, and Jang *et al.* [36] observed the similar trend for thermal CVD case. Many experimental works of literature report the restructuring of catalyst particle during CNF/CNT growth [8-9, 37-40]. Cantoro *et al.* [8] and Hofmann *et al.* [9] observed the dependence of catalyst deformation on the catalyst film thickness and its consequent effect on growth and the structure of the resulting nanostructure. Sharma *et al.* [13] have reported that the number of graphene layers (graphitic shells) in CNT increases with increase in catalyst film thickness. Moreover, He *et al.* [12] observed the correlation between graphene layers inclination angle and the catalyst particle deformation.

References

[1] V. I. Merkulov, D. H. Lowndes, and R. L. Baylor, J. Appl. Phys. **89,** 1933 (2001).

[2] M. A. Guillorn, A. V. Melechko, V. I. Merkulov, E. D. Ellis, C. L. Britton, M. L. Simpson, D.H. Lowndes, and L. R. Baylor, Appl. Phys. Lett. **79**, 3506 (2001).

[3] H. Murakami, M. Hirakawa, C. Tanaka, and H. Yamakawa, Appl. Phys. Lett. **76**, 1776 (2000).

[4] Z. F. Ren, Z. P. Huang, J. W. Xu, J. H. Wang, P. Bush, M. P. Siegal, and P. N. Provencio, Science **282**, 1105 (1998).

[5] V. I. Merkulov, A. V. Melechko, M. A. Guillorn, M. L. Simpson, D. H. Lowndes, J. H. Whealton, and R. J. Raridon, Appl. Phys. Lett. **80**, 4816 (2002).

[6] H. W. Wei, K. C. Leou, M. T. Wei, Y. Y. Lin, and C. H. Tsai, J. Appl. Phys. **98**, 044313 (2005).

[7] C. J. Lee, J. Park, J. A. Yu, Chem. Phys. Lett. **360**, 250 (2002).

[8] M. Cantoro, S. Hofmann, S. Pisana, C. Ducati, A. Parvez, A.C. Ferrari, J. Robertson, Diam. Relat. Mater. **15**, 1029 (2006).

[9] S. Hofmann, M. Cantoro, B. Kleinsorge, C. Casiraghi, A. Parvez, J. Robertson, C. Ducati, J. Appl. Phys. **98**, 034308 (2005).

[10] M. Chhowalla K. B. K. Teo, C. Ducati, N. L. Rupesinghe, G. A. J. Amaratunga, A. C. Ferrari, D. Roy, J. Robertson, and W. I. Milne, J. Appl. Phys. **90**, 5308 (2001).

[11] J. H. Ting, C. Y. Su, F. Y. Huang, C. L. Hsu, and S. Samukawa, Jpn. J. Appl. Phys. **45**, 8406 (2006).

[12] Z. B. He, J. L. , C.S. Lee , A. Gohier, D. Pribat, P. Legagneux, and C.S. Cojocaru, CARBON **49**, 435 (2011).

[13] H. Sharma, D. C. Agarwal, M. Sharma, A. K. Shukla, D. K. Avasthi, and V. D. Vankar, J. Phys. D: Appl. Phys. **46**, 315301 (2013).

[14] I. B. Denysenko, S. Xu, J. D. Long, P. P. Rutkevych, N. A. Azarenkov, and K. Ostrikov, J. Appl. Phys. **95**, 2713 (2004).

[15] D. J. Dagel, C. M. Mallouris, and J. R. Doyle, J. Appl. Phys. **79**, 8735 (1996).

[16] C. Deschenaux, A. Affolter, D. Magni, C. Hollenstein, and P. Fayet, J. Phys. D: Appl. Phys. **32**, 1876 (1999).

[17] M. Mao and A. Bogaerts, J. Phys. D: Appl. Phys. **43**, 205201 (2010).

[18] [18] J. Benedikt, J. Phys. D: Appl. Phys. **43**, 043001 (2010).

[19] [19] J. R. Doyle, J. Appl. Phys. **82**, 4763 (1997).

[20] H. Mehdipour, K. Ostrikov, and A. E. Rider, Nanotechnology **21,** 455605, (2010).

[21] M. A. Lieberman, and A. J. Lichtenberg, Principles of Plasma Discharges and Material Processing (*Wiley-Interscience, New York*, 1994).

[22] I. Denysenko, and K. Ostrikov, J. Phys. D: Appl. Phys. **42,** 015208 (2009).

[23] R. T. K. Baker, M. A. Barber, R. J. Waite, P. S.Harris, and F. S. Feates, J. Catal. **26,** 51 (1972).

[24] M. S. Sodha and S. Guha, Physics of Colloidal Plasmas, A. Simon and W. B. Thomson (*New York: John Wiley & Sons*) p. 219 (1971).

[25] S. C. Sharma and N. Gupta, Phys. Plasmas **22,** 123517 (2015).

[26] I. Denysenko, and N. A. Azarenkov, J. Phys. D: Appl. Phys. **44,** 174031 (2011).

[27] I. Denysenko, K. Ostrikov, M. Y. Yu, N. A. Azarenkov, J. Appl. Phys. **102,** 074308 (2007).

[28] L. Vattuone,Y. Y. Yeo, R. Kose, and D. A. King, Surf. Sci. **447,** 1 (2000).

[29] Z. Marvi, S. Xu, G. Foroutan, and K. Ostrikov, Phys. Plasmas **22,** 013504 (2015).

[30] M. Yudasaka, R. Kikuchi, T. Matsui, Y. Ohki, S. Yoshimura, and E. Ota, Appl. Phys. Lett. **67,** 2477 (1995).

[31] O. A. Louchev, T. Laude, Y. Sato, and H. Kanda, J. Chem. Phys. **118,** 7622 (2003).

[32] See (http://matter.org.uk/matscicdrom/manual/df.html) for metal atom diffusion coefficient

[33] M.S. Sodha, S. Misra, and S. K. Misra, Phys. Plasmas **17,** 113705 (2010).

[34] M. S. Sodha, S. Misra, S. K. Misra, and S. Srivastava, J. Appl. Phys. **107,** 103307 (2010).

[35] Y. T. Jang, J. H. Ahn,Y. H. Lee, and B. K. Ju, Chem. Phys. Letts. **372**, 745 (2003).

[36] S. Hofmann, R. Sharma, C. Ducati, G. Du, C. Mattevi, C. Cepek, M. Cantoro, S. Pisana, A. Parvez, F. C. Sodi, A. C. Ferrari, R. D. Borkowski, S. Lizzit, L. Petaccia, A. Goldoni, and J. Robertson, Nano let. **7,** 602 (2007).

[37] M. J. Behr, K. A. Mkhoyan, and E. S. Aydil, ACS nano **4**, 5087 (2010).

[38] C. S. Cojocaru, A. Senger, and F. L. Normand, Journal of nanoscience and nanotechnology **6**, 1331 (2006).

[39] H. Cui, X. Yang, M. L. Simpson, D. H. Lowndes, and M. Varela, Appl. Phys. Lett. **84**, 4077 (2004).

[40] UMIST http://www.udfa.net/

7

Parametric study of plasma characteristics and carbon nanofibers growth in PECVD system: Numerical modeling

7.1 Brief outline of the chapter

In this chapter, we studied the PECVD process in inductively coupled plasma (ICP) chamber reactor in which growth of CNFs occurred on nickel nanoparticles located on a substrate surface. The growth model contains two different models, one corresponds to the gas discharge model which accounts all volumetric reactions in the bulk plasma, and other corresponds to the surface deposition model that accounts all the surface reactions of various gaseous species on the catalyst surface. The plasma model accounts sheath equations that are solved for electron density, electron temperature, gas (ions and neutrals) density, and gas temperature to get the better insight of various operating plasma parameters. The surface deposition model accounts the fluxes of gaseous species from the plasma to the catalyst surface, their decomposition, diffusion, and precipitation on/through/around catalyst surface, respectively, via various complex processes. To get more insight into the plasma modification (i.e., change in density and temperature of plasma species) due to the change in process parameters, the COMSOL Multiphysics 5.2 simulation software is utilized to simulate the changes of densities and temperatures of the plasma species due to the change in plasma power and gas pressure in the plasma reactor. The simulation results and model validation was conducted against the experimental observations, and computational results available in the literature and analysis was focused onto the impact of the plasma power and gas pressure on the CNF growth rate and resulting structure.

Submitted work of the present chapter:

1. **Ravi Gupta** and Suresh C. Sharma, submitted to Plasma Sources Science and Technology

7.2 Introduction

Carbon nanofibers (CNFs) and carbon nanotubes (CNTs) characterize the unique forms of carbon in nanometer regime. Their exceptional properties such as high aspect ratios, high mechanical strength, and high chemical stability make them to be promising as field emission devices [1-5]. To obtain the enhanced field emission characteristics, the vertically oriented CNFs/CNTs are grown on catalyst substrate surface by plasma enhanced chemical vapor deposition (PECVD) technique [6-7]. PECVD process uses electrical energy to generate a glow discharge (plasma) in which the energy is transferred into a gas mixture. This transforms the gas mixture into reactive radicals, ions, neutral atoms, molecules, and other highly excited species. The areas with uncompensated surface charges, i.e., plasma sheaths are formed near the boundaries of the plasma exposed surfaces (i.e., catalyst-substrate surface and chamber walls). Therefore, nanostructures are grown in the plasma sheath region rather than bulk plasma. The electric field due to the plasma sheath near the catalyst-substrate surface has the significant role in the growth process. The strength of the electric field at the surface controls the kinetics of the ionized species and their deposition on the catalyst surface. The plasma sheath width affects the strength of the electric field near the surface, changing in the plasma parameters significantly affects the sheath width which consequently affects the electric field strength [8-11].

The growth characteristics (i.e., nanostructure height and diameter) and resulting structure of CNFs/CNTs depend on the fluxes and the energies of the radicals, ions, and neutral species from the bulk plasma to the catalyst nanoparticle surface. These fluxes and energies can be controlled by many operating parameters such as; plasma power, gas pressure, gas ratio, substrate temperature, and substrate bias, etc. Among them, gas pressure and plasma power directly influence the plasma sheath width, the strength of the electric field in the sheath region, densities, temperature, and energies of plasma species, and collision between plasma species, which in turn affects the growth characteristics of the CNFs and CNTs [12-30].

7.3 Model

The plasma enhanced chemical vapor deposition of the CNFs onto the nickel catalyst nanoparticles placed over silicon substrate via acetylene, hydrogen, and argon in the plasma reactor has been investigated through the analytical as well as the computational model. The ionized and neutral species accounted in the present model on the basis of experimentally specified plasma chemistry of the acetylene, hydrogen, and argon gas mixture [20, 31-36] are presented in Table 7.1. The volumetric reactions between these plasma species in the bulk plasma accounted in the present model are obtained from the refs. [20, 36].

Table 7.1: Species considered in the present model.

Type	Neutrals	Positively charged species
X	C_2H, C_2H_2, C_2H_3, C_4H, C_4H_2, C_4H_3 C_6H, C_6H_2, C_6H_4, C_8H, C_8H_2, C_8H_4, $C_{10}H$, $C_{10}H_2$,	C_2H^+, $C_2H_2^+$, $C_2H_3^+$, C_4H^+, $C_4H_2^+$, $C_4H_3^+$ C_6H^+, $C_6H_2^+$, $C_6H_4^+$, C_8H^+, $C_8H_2^+$, $C_8H_4^+$, $C_{10}H^+$, $C_{10}H_2^+$,
Y	H_2, H	H_2^+, H^+

7.3.1 Computational approach

The computational model to simulate the plasma modifications was constructed in the COSMSOL Multiphysics modeling suite. The 2D axisymmetric inductively coupled plasma (ICP) module is used to couple drift-diffusion interface for electron density and electron temperature; heavy species transport interface for non- electron species; and electrostatics interface for the electric field, space charge density, and induction current in a frequency transient domain sketched schematically in Fig. 7.1. The mesh with Finer standard size settings consisting quadratic triangle elements is applied to the geometries created in the present computation. All the input parameters feed to the computational domain are listed in Table 7.2.

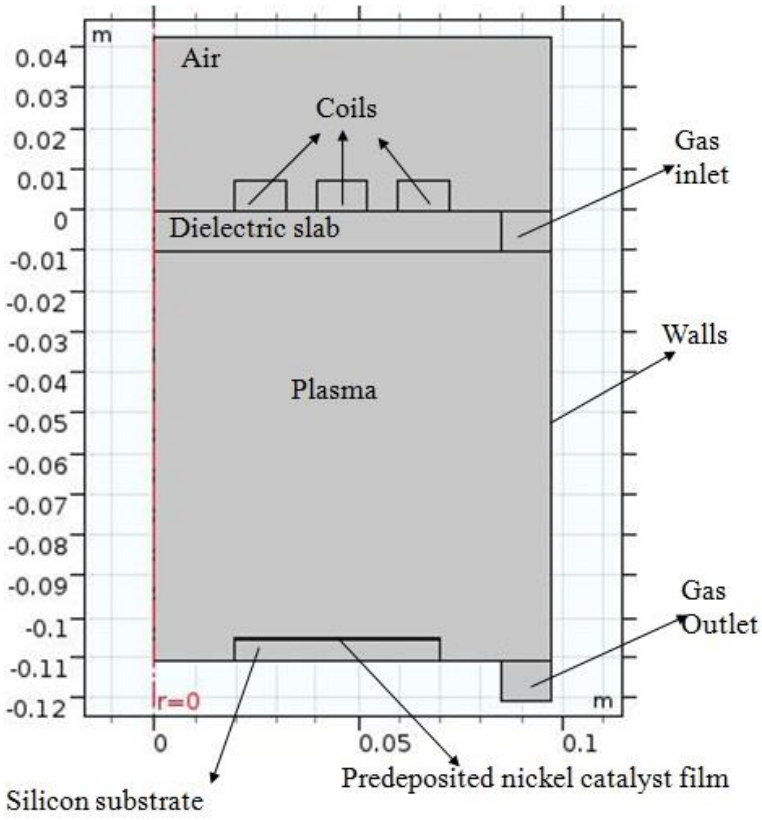

Fig. 7.1. Geometry of the model constructed in the COMSOL modeling suite which includes five turn inductive coils (source of inductively coupled plasma) connected to 13.56 MHz generator. A dielectric material is used between the coils and plasma reactor. The applied power to the coils reaches to the plasma reactor through this dielectric material. The predeposited nickel catalyst film over the silicon substrate is placed at the bottom of the plasma reactor.

Table 7.2. Parameters fed into the computational model developed in the COMSOL Multiphysics modeling suite.

Parameter	Value
Relative permittivity of vacuum	1
Relative permittivity of dielectric material	4.2
Relative permittivity of silicon substrate	12
Relative permeability of vacuum	1
Electrical conductivity of vacuum	0
Electrical conductivity of coils	6×10^{7} S/m
Electrical conductivity of dielectric material	0
Gas temperature	500 K
Reduced electron mobility	4×10^{24} $V^{-1}m^{-1}s^{-1}$

7.3.2 Analytical approach

In the PECVD synthesis technique, the CNFs and other carbon nanostructures are grown in the plasma sheath region formed between the bulk plasma and the substrate surface. The processes in the plasma and on the catalyst substrate surface affect the nanostructure nucleation and formation. The sheath model is used to find the number density, temperature, and energies of the plasma species in the plasma environment. However, the interaction of the plasma species with the catalyst substrate surface and the growth of CNFs have been accounted in the surface deposition model. The outcomes of sheath equations serve the initial values for the surface deposition model. The sheath model accounts the continuity equation (Eqs. 7.1 & 7.2), momentum equation (Eqs. 7.3 & 7.4), and Poisson's equation (Eq. 7.5) to investigate the dynamics of the plasma species [8, 37],

$$\frac{d}{dz}(n_e u_e) = v_i n_e, \tag{7.1}$$

$$\frac{d}{dz}(n_i u_i) = v_i n_i, \tag{7.2}$$

where n_e and n_i are the number densities of electrons and positively charged species considered (assumed to be singly charged) in the present model, respectively, u_e and u_i are the velocities of electrons and positively charged species along the plasma sheath, respectively, $v_i (= \varepsilon_i r_i n_n)$ is the ionization frequency of the ions, ε_i is the ionization potential of the positively charged species, r_i is the j^{th} gas pressure to total gas pressure ratio $\left(\frac{p_j}{p_T}\right)$ or i^{th} type positively charged species number density to electron density ratio $\left(\frac{n_i}{n_e}\right)$, n_n is the neutral atoms number density considered in the present model.

$$\frac{d}{dz}(u_e) = -\frac{e}{u_e}\frac{d\phi}{dz} - \frac{T_e}{n_e u_e}\frac{dn_e}{dz} - m_e v_{en}, \tag{7.3}$$

$$\frac{d}{dz}(u_i) = \frac{e}{u_i}\frac{d\phi}{dz} - \frac{T_i}{n_i u_i}\frac{dn_i}{dz} - m_i v_{in}, \tag{7.4}$$

$$\frac{d^2}{dz^2}(\phi) = 4\pi e(n_e - \sum r_i n_i), \tag{7.5}$$

where $v_{en}\left(=\sigma n_n \mathrm{v}_e\right)$ and $v_{in}\left(=\sigma n_n \mathrm{v}_i\right)$ are the collision frequencies of the electrons and ions with the neutrals, respectively, σ is the collision cross-section, $\mathrm{v}_e\left(=\sqrt{\frac{8k_B T_e}{m_e \pi} + u_e^2}\right)$ and $\mathrm{v}_i\left(=\sqrt{\frac{8k_B T_i}{m_i \pi} + u_i^2}\right)$ are the mean velocities of electrons and ions, ϕ is the sheath potential.

The above-mentioned sheath equations have been solved for appropriate boundary conditions such as; $u_e = 0$, $u_i = \sqrt{\frac{T_e}{m_i}}$, $n_e = \sum r_i n_i$ (quasi- neutrality condition), $\sum r_i = 1$, $0 < r_i < 1$, $\phi = 0$, $\frac{d\phi}{dz} = -\frac{T_e}{e\lambda_i}$, $\lambda_i\left(=\frac{T_n}{\sigma p_T}\right)$ is the mean free path of the positively charged species.

The synthesis of the CNFs involves three main steps; (i) nucleation stage, in which carbon-containing precursors (species from plasma) dissociates on the catalyst front surface that is exposed to plasma, (ii) surface and bulk diffusion of carbon species generated on the catalyst surface, and (iii) precipitation of diffused carbon species in the form of graphitic shells at the catalyst interface [38]. The CNF growth model incorporates numerous terms and equations corresponding to various complex processes and growth stages. The flux of the hydrocarbon and hydrogen species (ions and neutrals) from the plasma sheath on the catalyst surface generates carbon species and hydrogen radicals on the catalyst surface via various complex processes. The Eq. (7.6) corresponds to the number of carbon species per unit area per unit time generated on the catalyst active surface due to the hydrocarbon neutrals adsorption on the catalyst active surface (first term), thermal dissociation of adsorbed hydrocarbon neutrals on the catalyst active surface (second term), ion induced dissociation of hydrocarbon neutrals (third term), dissociation of incoming ions of the plasma sheath (fourth term), interaction of hydrocarbon

ion and hydrogen ion (fifth term), loss of adsorbed hydrocarbons due to interaction with incoming hydrogen from the plasma (sixth term), carbon species evaporation from the catalyst surface (seventh term), desorption of hydrocarbon neutrals from catalyst surface (eighth term), and interaction between carbon and hydrogen species generated on the catalyst nanoparticle surface (ninth term) [9-11].

The number of carbon species generated on catalyst surface is one of the growth rate determining factors, a possible explanation for the change in growth rate is the correlation between the generations of the carbon species to the growth of amorphous carbon layer on the active surface of the catalyst. The rapid increase in number of carbon species enhances the growth of amorphous carbon layer which ultimately poisons the catalyst and slows down the dissociation rate of incoming hydrocarbon species. The term $\frac{d\Omega_c}{dt}\left(=1-n_c\pi D^2\right)$ in Eq. (7.6) denotes the growth rate of the amorphous carbon layer on the catalyst surface.

$$\frac{\partial n_C}{\partial t}=\left[\sum_X J_X(1-\theta_t)+\sum_X n_{sX}\upsilon\exp\left(\frac{-\varepsilon_{td}}{k_BT_S}\right)+\sum_{iX}\left(\sum_X\frac{n_{sX}y_d}{\upsilon_0}\right)J_{iX}+\sum_{iX}J_{iX}\right.$$
$$+\sum_{iY}\left(\sum_{iX}\frac{J_{iX}\sigma_{ads}}{\upsilon}\right)J_{iY}-\sum_Y\left(\sum_X n_{sX}\sigma_{ads}\right)J_Y-n_C\upsilon\exp\left(\frac{-\varepsilon_{ev}}{k_BT_S}\right)$$
$$\left.-\sum_X n_X\upsilon\exp\left(\frac{-\varepsilon_{dhc}}{k_BT_S}\right)-n_C\sigma_{ads}\upsilon n_H\right]\times\frac{d\Omega_C}{dt}, \qquad (7.6)$$

where n_C is the surface concentration of carbons, $J_j\left(=\frac{n_j}{4}\sqrt{8k_BT_j/\pi m_j}\right)$ and $J_{ij}=n_{ij}\sqrt{k_BT_e/m_{ij}}$ are the neutrals and ions flux, respectively [10] (where j refers to the species of type X and Y), $n_{sj}\left(=\theta_j\upsilon_0\right)$ is the surface concentration of neutral species adsorbed on the catalyst surface from the plasma sheath [9-11], θ_j is the surface coverage by j^{th} species, υ_0 is the adsorption sites per unit area, υ is the thermal vibration frequency,

$\sigma_{ads}\left(=6.8\times10^{-16}\,\mathrm{cm}^2\right)$ is the cross-section for the interaction among various species [10], $\varepsilon_{td}(=2.1\,eV)$ is the hydrocarbons dissociation energy, $\varepsilon_{\mathrm{ev}}(=1.8\ \mathrm{eV})$ carbon evaporation energy, $\varepsilon_{dhc}\left(=1.8\ \mathrm{eV}\right)$ is the hydrocarbon desorption energy [39], and *D* is the diameter of the catalyst nanoparticle.

The relative number of hydrogen radicals generated on the catalyst surface is also an important parameter to change the growth process. These highly reactive hydrogen radicals interact with the adsorbed hydrocarbons and carbon species and prevent the early poisoning of the catalyst by slowing down the growth of formation of the amorphous carbon layer. The Eq. (7.7) is indicative to the number of hydrogen radicals per unit time generated on the catalyst surface due to the adsorption of hydrogen species on the catalyst surface from the plasma [9] (first term), ion-induced dissociation of hydrogen (second term), generation of hydrogen radicals due to the thermal dissociation of hydrocarbons (third term) [39], direct hydrogen ion flux (fourth term), desorption of hydrogen radicals from catalyst (fifth term), interaction of hydrogen radicals with carbon species generated on the catalyst surface (sixth term), and interaction of adsorbed hydrogen radicals with influx of hydrogen neutrals and ions from the plasma (seventh & eight term) [39].

$$\begin{aligned}\frac{\partial n_H}{\partial t} = &\sum_Y J_Y(1-\theta_t)+\sum_{iX}\left(\sum_X \frac{n_{sX}y_d}{\upsilon_0}\right)J_{iX}+\sum_Y n_{sY}\upsilon\exp\left(\frac{-\varepsilon_{td}}{k_BT_S}\right)\\ &+\sum_{iY}J_{iY}-\sum_Y n_{sY}\upsilon\exp\left(\frac{-\varepsilon_{dH}}{k_BT_S}\right)-n_C\sigma_{ads}\upsilon n_H\\ &-\sum_Y n_{sY}\sigma_{ads}J_Y-\sum_Y n_{sY}\sigma_{ads}J_{iY},\end{aligned}\qquad(7.7)$$

where n_H is the surface concentration of hydrogen radicals, $\delta E_{dH}(=1.8\ \mathrm{eV})$ is the hydrogen atom desorption energy [39].

After the nucleation stage, the growth of the CNF is initiated that includes various processes which are clearly explained in volumetric growth

rate equation of CNF (Eq. 7.8). The carbon species n_C dissolve in and diffuse through catalyst nanoparticle (first and second term), and then carbon layers precipitate from the rear sides of the catalyst nanoparticle to from inclined graphitic shells (third term). These graphitic shells, i.e., precipitated carbon species exert varying compressive stress on the catalyst nanoparticle due to which it undergoes shape deformation [40, 41]. The restructuring of the catalyst particle during the CNF growth is the crucial phenomenon this is because the extents up to which catalyst particle can reconstruct itself determine the diameter (*d*) of the CNF and number of graphitic shells in the CNF. Therefore, the first three terms of Eq. (7.8) are multiplied by the stress (P) applied by the growing graphitic shells. Moreover, self-diffusion of atoms of metal catalyst nanoparticle along the growth direction also makes catalyst to reconstruct itself (fourth term). Apart from the carbon deposition process, the etching by hydrogen is also an important step in CNF growth (last term). The hydrogen radicals etch carbons atoms present at the edges of the shells; however, carbon atoms under the geometrical shadow region of the catalyst particle contribute to the vertical growth of the graphitic shells.

$$\frac{d}{dt}\pi(D^2-d^2)h=\left[D_{b0}\exp\left(\frac{-\varepsilon_b}{k_BT_S}\right)+D_{S0}\exp\left(\frac{-\varepsilon_S}{k_BT_S}\right)+A_k\exp\left(\frac{-\delta\varepsilon_{inc}}{k_BT_S}\right)\nu D\right]\times\frac{P(4\pi D)n_C}{\nu\rho_{cnf}I_{ix}}+\left[\frac{D_m}{\pi D^2}+n_H(\pi D^2)\sum_Y I_{iY}\right]\times\frac{m_{cat}}{\rho_{cat}},\qquad(7.8)$$

where *D* and *h* are the diameter of the catalyst nanoparticle and height of the CNF, respectively, $D_{b0}=\nu D/2\pi$, ε_b (=1.6 eV) is the energy barrier for carbon species bulk diffusion through catalyst nanoparticle, $D_{S0}=a_0^2\nu$, $a_0(=0.34\ nm)$ is the carbon atoms inter-atomic distance, ε_S (=0.3 eV) is the energy barrier for carbon species diffusion through the catalyst nanoparticle surface [9-11], $A_k=a_0\nu$, $\delta\varepsilon_{inc}(=0.4\ eV)$ is the carbon species energy barrier to diffuse along the nanofiber-catalyst interface [42], P $(\approx 20\ GPa)$ is

the pressure exerted by graphene layers on catalyst nanoparticle [43], ρ_{cnf} is the nanofiber density, m_{cat} is the mass of the metal catalyst particle, and ρ_{cat} is the density of metal catalyst nanoparticle. $D_m = D_{m0}\exp\left(-\varepsilon_{SD}/k_B T_S\right)$ is the metal atoms diffusion coefficient [44], D_{m0} is the constant, ε_{SD} is the metal atoms self-diffusion activation energy.

Due to the continuous accumulation of positively charged species (first & second term) and electrons (last term) on the growing CNF surface over the negatively biased substrate surface, a charge is developed with growth time on the CNF surface that is represented by the Eq. (7.9).

$$\frac{dZ}{dt} = \sum_j I_{tip-ij} + \sum_j I_{cur-ij} - \gamma_e\left(I_{tip-e} + I_{cur-e}\right), \qquad (7.9)$$

where Z is the charge number, I_{tip-ij} and I_{cur-ij} are the ions collection current due to j^{th} species at the tip as well as the curved surface of the CNF, respectively [see chapter 3]. I_{tip-e} and I_{cur-e} are the electron collection current at the tip as well as the curved surface of the CNF, respectively [see chapter 3], and γ_e is the sticking coefficient of electrons.

The plasma species (electrons, ions, and neutrals) from the plasma sheath, accumulate and deposit on the catalyst surface and growing CNF surfaces, however, some of the species desorbs from the surface and move in the plasma again. Thus, it is also important to evaluate how the number densities of plasma species decay in plasma with growth time.

$$\frac{dn_e}{dt} = \sum_j \beta_j n_j - \sum_j \alpha_j n_e n_{ij} - \gamma_e \frac{n_{cnf}}{\lambda_d}\left(I_{\text{tip–e}} + I_{\text{cur–e}}\right), \qquad (7.10)$$

$$\frac{dn_{ij}}{dt} = \beta_j n_j - \alpha_j n_e n_{ij} - \frac{n_{cnf}}{\lambda_d}\left(I_{\text{tip-}ij} + I_{cur-ij}\right) + \sum k_\ell n_j n_{ij'} - \sum k_Q n_{j'} n_{ij}, \qquad (7.11)$$

Ravi Gupta, Department of Applied Physics, Delhi Technological University, Delhi, India

$$\frac{dn_j}{dt} = \alpha_j n_e n_{ij} - \beta_j n_j + \frac{n_{cnf}}{\lambda_d}\left(1-\gamma_{ij}\right)\left(I_{tip-ij} + I_{cur-ij}\right) - \frac{n_{cnf}}{\lambda_d}\gamma_j\left(I_{tip-j} + I_{cur-j}\right) + IF_j - OF_j - J_{ai-j} + J_{desp-j} + J_{thd} - \sum k_Q n_j n_{ij'} + \sum k_\ell n_{j'} n_{ij}, \quad (7.12)$$

where n_e, n_{ij}, n_j are the number density of electrons, positively charged ions, and neutrals of j^{th} species, respectively. β_j is the ionization coefficient of neutral atoms [45], α_j is the recombination coefficient of electrons and positively charged ions [46], n_{cnf} is the surface density of CNFs, and $\lambda_d \left(=3\times10^{-3}\,\text{cm}\right)$ is the plasma sheath width, γ_{ij} is the sticking coefficient of positively charged ions, $J_{\text{ai-j}}$ is the adsorption flux of neutrals on the catalyst surface, $J_{\text{desp-j}}$ is the desorption flux of neutrals from the catalyst substrate surface, J_{thd} is the hydrogen flux from the catalyst surface due to thermal dehydrogenation, $IF_j \left(=4.4\times10^{17}\times f_j \times V^{-1}\right)$ and $OF_j \left(=R_p \times n_j \times V^{-1}\right)$ are the j^{th} neutrals species inflow rate and outflow rate into/from the plasma chamber, respectively. f_j is the inlet flow of corresponding gas, $V\left(\approx 2\times10^4\ \text{cm}^3\right)$ is the volume of the chamber, and R_p is the pumping rate [47], k_j is the reaction rate coefficient of the reactions that are accounted in the present model.

The Eq. (7.10) represents the decay rate of electron number density in the plasma due to the gain in electron number density per unit time due to ionization of neutral species (first term), decay rate due to electron-ion recombination and electron collection current at the CNFs surface (second and last term). The Eq. (7.11) represent the decay rate of positively charged species in the plasma due to ionization of neutral species (first term), electron-ion recombination (second term), ion collection current at the CNF surface (third term), and reactions between different plasma species at

different reaction rates (fourth & fifth terms). The Eq. (7.12) represent the decay rate of neutral species in the plasma on account of various processes such as; electron-ion recombination (first term), decrease in number density due to ionization of neutral species (second term), increase in number density due to neutralization of ions collected at the CNF surface (third term), decrease in number density due to the accretion of neutrals at the CNF surface (fourth term), inflow and outflow rate of neutral species from plasma chamber (fifth & sixth term), adsorption of neutrals to the catalyst surface (seventh term) and desorption of neutrals from the catalyst surface (eighth term). The ninth and eight terms represent the increase and decrease in neutral atoms number density due to the various reactions considered in the present model [20, 36]. The last term of Eq. (7.12) is corresponds to gain in hydrogen ion number density in the plasma due to thermal dehydrogenation of hydrocarbons on the catalyst surface [10].

The all above equations solved simultaneously for appropriate experimentally determined boundary conditions and initial parameters [8, 20] that are listed in Table 7.3 and Table 7.4.

Table 7.3. Initial conditions fed into the analytical model.

Parameter	Description	Initial Value
D	Diameter of the catalyst nanoparticle	40 nm
T_e	electron temperature	3 eV
T_i	ion temperature	0.17 eV
T_n	neutral atom temperature	0.17 eV
ρ_{ct}	Density of nickel catalyst	8.96 g/cm^3
$\alpha_{10} \approx \alpha_{20}$	electron-ion recombination coefficient	1.12×10^{-7} cm^3/sec
T_s	substrate temperature	550 ^{0}C
γ_e	electron sticking coefficient	0.99
γ_{ij}	ion sticking coefficient	0.99
γ_j	neutral atom sticking coefficient	0.99
θ_t	total surface coverage	0.01
$f_{C_2H_2}$	C_2H_2 gas flow rate	50 sccm
f_{H_2}	H_2 gas flow rate	200 sccm
U_s	substrate potential	-300 V

Table 7.4. Initial number density of the species fed into the analytical model.

Species Considered	Initial Values (cm^{-3})
n_e **(electron number density)**	4.18×10^{11}
n_{ij} **(Ion number density)** $\times 10^{11}$ cm^{-3}	
C_2H^+	0.002
$C_2H_2^+$	0.95
$C_2H_3^+$	0.084
C_4H^+	0.91×10^{-3}
$C_4H_2^+$	0.66
$C_4H_3^+$	0.54
C_6H^+	0.02×10^{-3}
$C_6H_2^+$	0.008
$C_6H_4^+$	0.097
C_8H^+	0.005×10^{-4}
$C_8H_2^+$	1.55×10^{-3}
$C_8H_4^+$	0.61×10^{-3}
$C_{10}H^+$	0.008
$C_{10}H_2^+$	0.56×10^{-3}
H_2^+	1.45
H^+	0.38
n_j **(Neutral species number density)**	
C_2H	2.25×10^{11}
C_2H_2	5.15×10^{14}
C_2H_3	6.06×10^{13}
C_4H	9.12×10^{9}
C_4H_2	9.22×10^{12}
C_4H_3	1.85×10^{12}
C_6H	4.55×10^{9}
C_6H_2	3.42×10^{12}
C_6H_4	2.48×10^{13}
C_8H	1.11×10^{9}
C_8H_2	8.33×10^{11}
C_8H_4	4.24×10^{10}
$C_{10}H$	7.01×10^{8}
$C_{10}H_2$	6.14×10^{11}
H_2	1.48×10^{15}
H	2.54×10^{14}

7.4 Results and discussion

The effect of input process parameters such as gas pressure and input plasma power on the plasma characteristics have been investigated in the present study using the computational approach as well as analytical approach and their repercussions on the growth characteristics of the CNFs have been studied. The computational results of electron density and temperature at different gas pressures are shown in Figs. 7.2 & 7.3, respectively. At low pressure, i.e., about 50 mTorr, the electron density in the plasma and near the substrate was found to be 3.94×10^{17} m^{-3} and 1.87×10^{17} m^{-3}, respectively. And the electron temperature in the plasma and near the substrate was found to be 3.6 eV and 2.74 eV, respectively. When gas pressure is increased up to 5 Torr, the electron density in the plasma and near the substrate is found to be reduced to 2.67×10^{16} m^{-3} and 0.04×10^{16} m^{-3}, respectively. And the electron temperature in the plasma and near the substrate is found to be reduced to 2.64 eV and 2.34 eV, respectively. Moreover, the temporal variation of electron density and electron temperature obtained from the analytical model incorporated in the Sec. 7.3.1 are shown in Figs. 7.4(a) and 7.4(b), respectively. It can be seen from Fig. 7.4 that electron density and electron temperature decreases with time and with gas pressure. With the increase in gas pressure, the mean free path of electrons decreases which in turn increase the collision between electrons and neutral species and make electrons to lose their energy faster and leads to decrease in the electron density in the plasma. The reduction in electron density decreases the electric field in the plasma, thereby decreasing the electron temperature. Moreover, due to the continuous collision between electrons and other species, the energy and number of electrons decay with space and time. Harilal *et al.* [21] experimentally found the decrease in electron density and temperature with time in the laser produced carbon plasma. Many studies also report the reduction in electron density and temperature when the gas pressure in the plasma is raised [18, 20, 22].

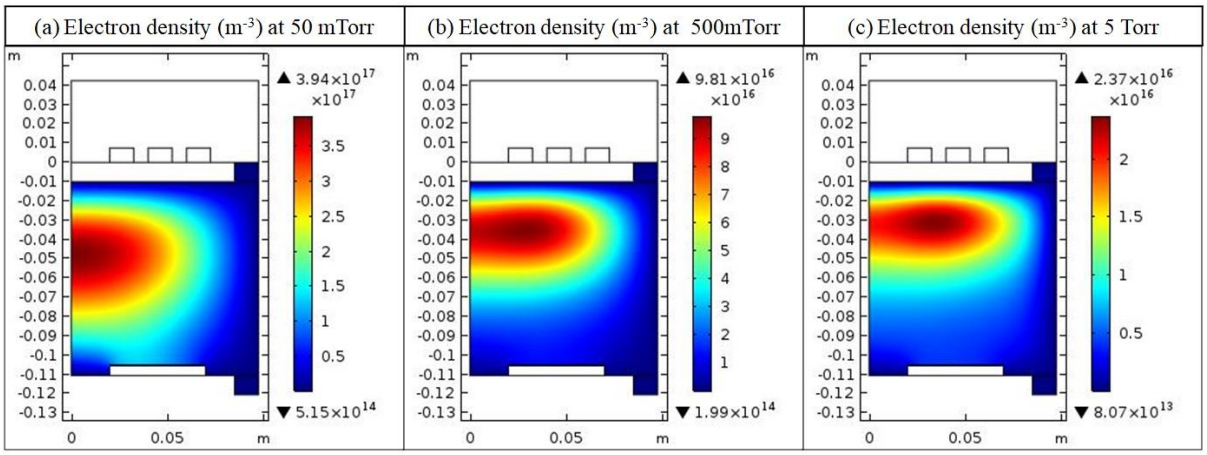

Fig. 7.2. Electron density spatial distribution in the plasma obtained from the computational model for different gas pressures, i.e., (a) 50 mTorr, (b) 500 mTorr, and (c) 5 Torr.

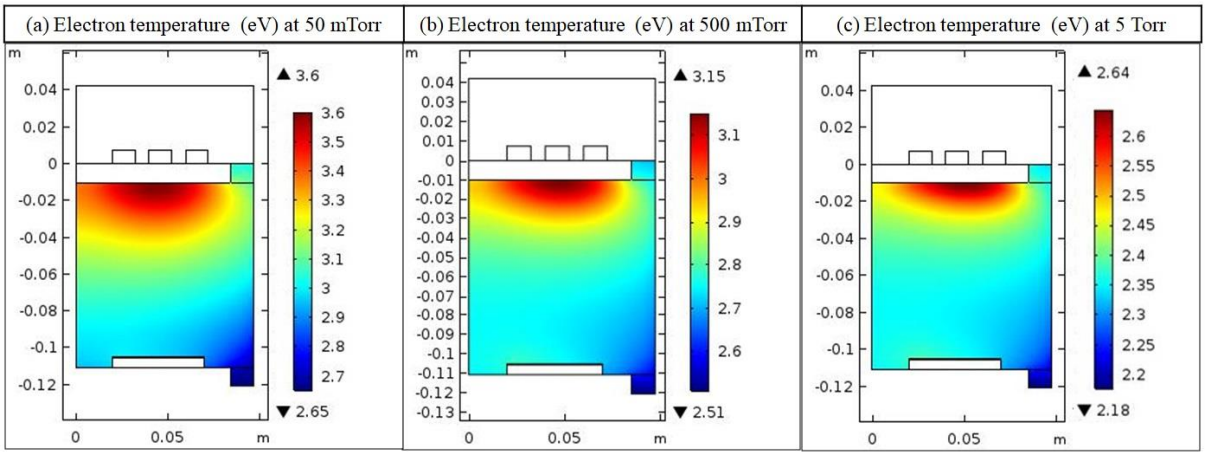

Fig. 7.3. Electron temperature spatial distribution in the plasma obtained from the computational model for different gas pressures, i.e., (a) 50 mTorr, (b) 500 mTorr, and (c) 5 Torr.

The number density distributions of the various neutral species in the bulk plasma region and substrate surface obtained from the computational model at different gas pressures are shown in Fig. 7.5. The number density of neutral species drops as one go from bulk plasma region to the substrate surface due to the ionization of neutral species, dissociation of the neutral species and various reactions between ion and neutral species. From Fig. 7.5, one can see that the number density of carbon-bearing species near the substrate surface is related to the gas pressure [23]; when gas pressure is raised, the number densities of neutral species increase and decay at the slower rate in the plasma. This can be ascribed to the fact that with an increase in pressure, plasma becomes more collisional due to which species lose their energy faster and, therefore, temperature and energy of the neutral species decrease. The rates of reactions

between ions and neutrals also depend on the temperature of the respective species. A large number of collisions at higher pressure decreases the neutral temperature, and thereby, decreasing the reaction rates. The reduction in electron number density with increase in pressure also leads to the lower ionization of neutral species. Thus, the concentration of neutral species increases in the plasma as gas pressure is raised.

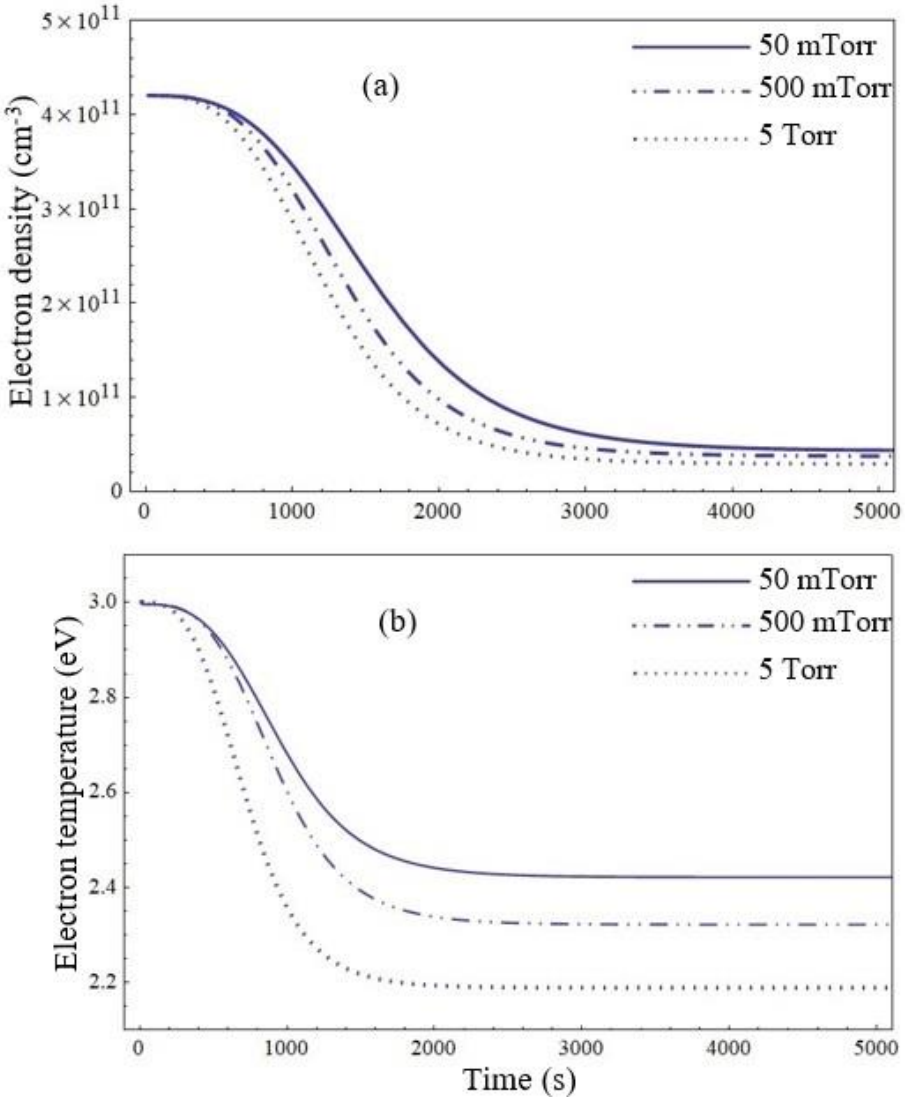

Fig. 7.4. Variation of (a) electron density and (b) electron temperature with growth time in the plasma for different gas pressures, i.e., 50 mTorr, 500 mTorr, and 5 Torr keeping other parameters constant that are given in the text.

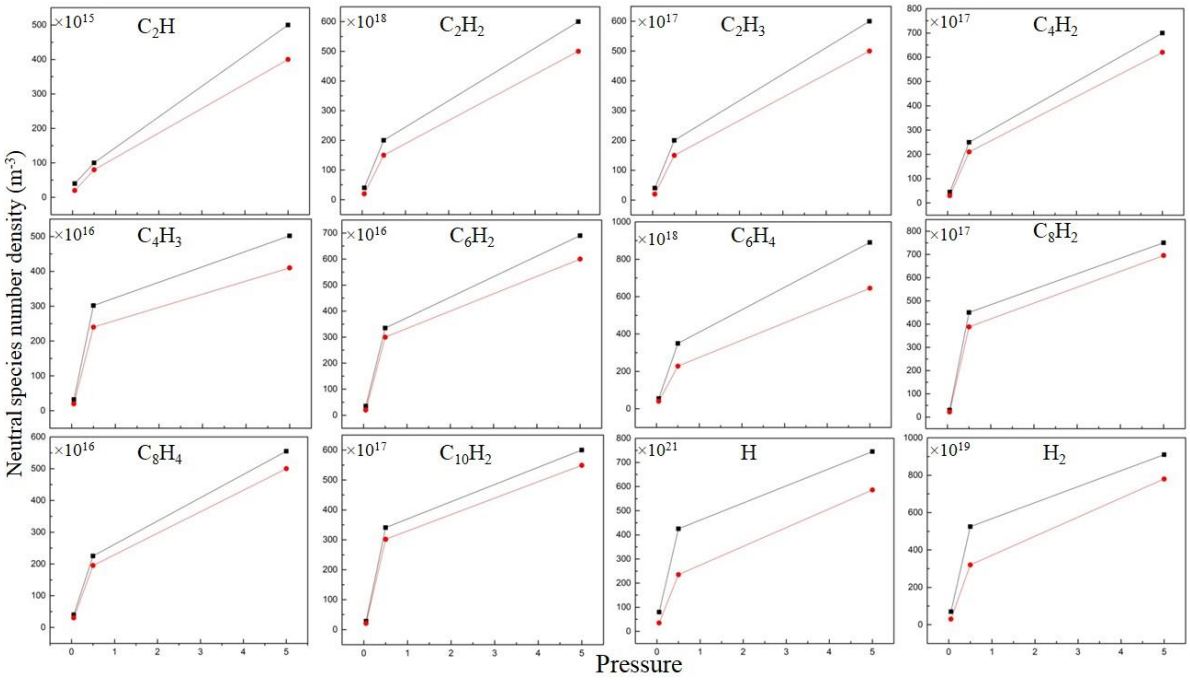

Fig. 7.5. Density distribution of the neutral species in the bulk plasma region (black dots) and near the substrate surface (red dots) obtained from the computational model for different gas pressures i.e., 50 mTorr, 500 mTorr, and 5 Torr.

In Fig. 7.6(a) and 7.6(b), the temporal variation of CNF height and diameter, respectively, has been carried out at different gas pressures in the plasma. From Fig. 7.6(c) & 7.6(d), one can see that the decomposition of various carbon-bearing species on the catalyst surface depends on the gas pressure. Moreover, the surface concentration of the carbon species over the catalyst surface changes with gas pressure. With increase in gas pressure, the neutral density in the plasma increases (see Fig. 7.5) due to which flux of hydrocarbon neutrals and hydrogen neutrals on the catalyst nanoparticle surface increases. Which leads to more effective generation of carbon species and hydrogen radicals on the catalyst active surface [see Fig. 7.6(c) & 7.6(d)] and thus, enhance the CNF growth (height per unit deposition time). Whereas, at sufficiently high pressure (around and above 50 Torr), CNF growth begins to drop significantly. This is because, at much higher pressure plasma is not sufficient to dissociate hydrocarbons neutrals but able to dissociate hydrogen molecules since they require less dissociation energy as compared to the hydrocarbons neutrals. Due to which hydrocarbons neutral flux and number of carbon species on the catalyst surface increases rapidly leading to the early poisoning of the catalyst. To make it clear, the poisoning rate (variation of blocking function with the growth time)

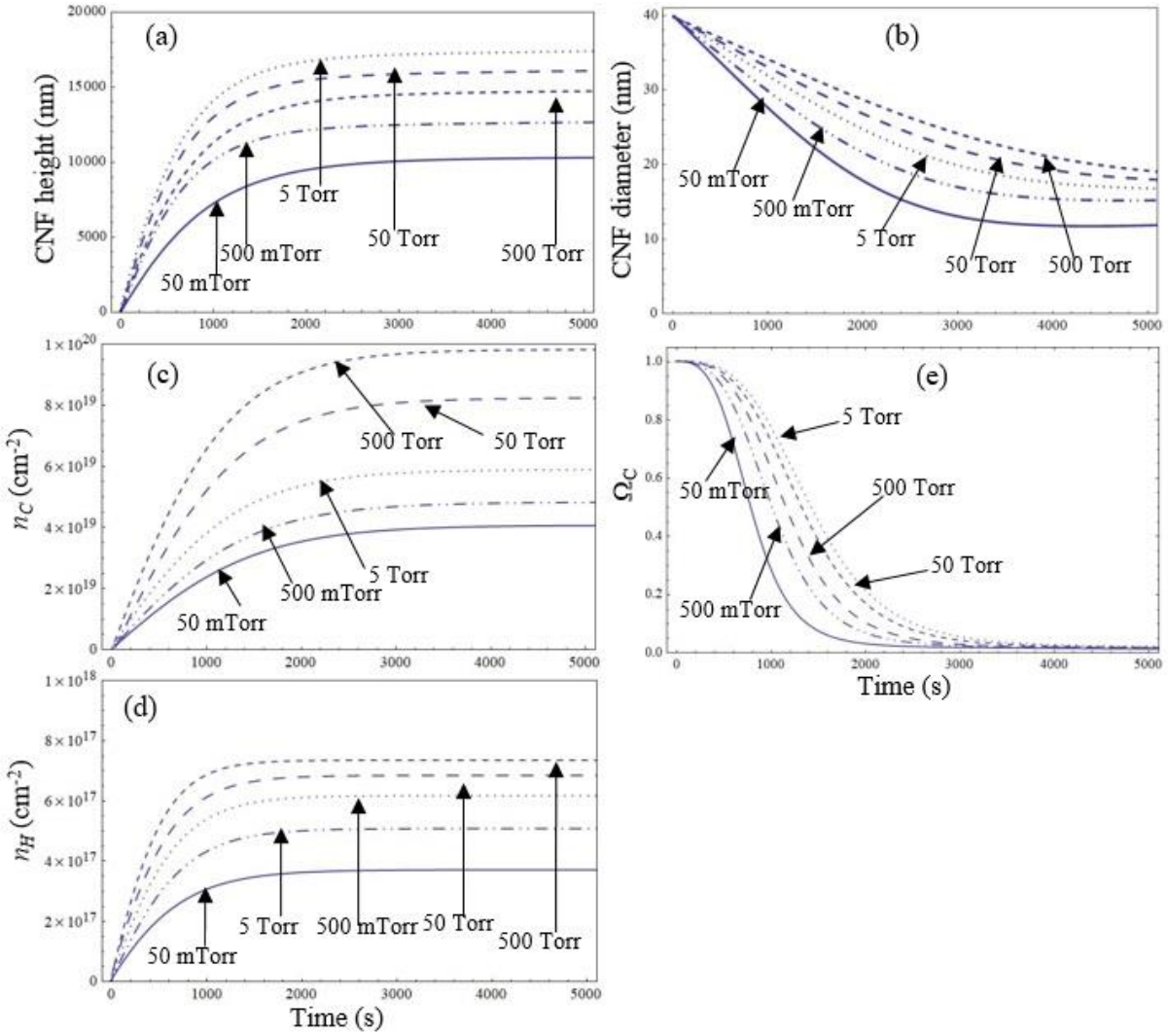

Fig. 7.6. Temporal variation of the (a) CNF height, (b) CNF diameter, (c) surface concentration of carbon species on the catalyst surface n_C, (d) surface concentration of hydrogen radicals on the catalyst surface n_H, and (e) poisoning rate of the catalyst for different gas pressures i.e., 50 mTorr, 500 mTorr, 5 Torr, 50 Torr, and 500 Torr keeping other parameter constant that are given in the text.

of the catalyst nanoparticle at different gas pressure is plotted in Fig. 7.6(e) which shows that catalyst nanoparticle maintains its activity for quite long time when gas pressure is increased up to 5 Torr. This is because of the removal of amorphous carbon layer due to the presence of sufficient number of hydrogen radicals. However, at high pressure (around and above 50 Torr), the rapid growth in surface density of carbon species is obtained [see Fig. 7.6(c)] due to which interaction between carbon species and hydrogen radicals becomes less effective. This leads to the rapid growth of the amorphous carbon layer over the catalyst active surface which in turn leads to the quick poisoning of the catalyst activity. The Fig. 7.6(b) shows the temporal variation of the CNF diameter at

different gas pressures. The initial diameter (at time t=0) of the CNF is assumed to be same as the diameter of the catalyst nanoparticle and reduction of CNF diameter with growth time is observed due to the compressive stress exerted by the growing graphitic shells and also due to the etching of CNF side walls by energetic hydrogen species (radicals and ions). Moreover, it can also be seen that CNFs having large diameters are grown when gas pressure in the plasma is increased which can be explained by two ways; (i) the rate of diffusion and precipitation of carbon species over the growing walls of the CNFs increases due to the availability of large number of carbon species, (ii) at higher pressure, ions lose their energy due to large of collisions and thus, fewer energetic ions reach near the substrate surface and, consequently, etching is reduced [23]. The results obtained in Fig. 7.6(a) and 7.6(b) are in good agreement with the available experimental observations discussed as follows; Wei *et al*. [7] experimentally investigated the effect of pressure in the plasma on the CNF length and observed that the length of the CNF increases with increase in pressure (0-30 Torr) and decrease when pressure is increased further (cf. 7.6(a) ref. [7]). Wang *et al*. [17] investigated the growth of CNTs via PECVD technique at two different gas pressures i.e. 15 Torr, and 30 Torr and found that average length of the CNF grown at 30 Torr is smaller than that at pressure 15 Torr. Li *et al*. [24] studied the effect of gas pressure on the structure and growth of the CNTs via chemical vapor deposition (CVD) technique and observed that CNTs grow with shorter in length and larger in diameter at high pressure (50-760 Torr). Ganjipour *et al*. [14] observed the increase in CNTs diameter when gas pressure in the PECVD system is increased (0-500 Torr). Pint *et al*. [25] investigated the effect of pressure on the CNT growth via CVD process and found the increase in CNT height with increase in pressure (0-15 Torr). Tsakadze *et al.* [26] studied the effect of the pressure on the field emission properties of the CNTs grown via thermally CVD system and observed the length of the CNTs is decreased at high pressure range (300-700 Torr). Tanemura *et al.* [27] have tried to optimize the PECVD process parameters to enhance the growth of CNTs and found that diameter of the CNTs increases when pressure of C_2H_2 gas is raised in the growth environment. Chhowalla *et al.* [12] investigated the PECVD growth process conditions of the vertically aligned CNTs and observed the increase in

the length of the CNTs with increase in the pressure (0-10 Torr). Hinkov *et al.* [28] found the increase in the growth rate of plasma grown single-walled CNTs with increase in the pressure (0-1000 mbar). Cruden *et al.* [19] reported the increase in the CNFs length with increase in pressure (2 Torr, 3 Torr, and 8 Torr) in the DC PECVD growth process of CNFs. From the results obtained in the present study and from the above specified experimental literature, one can conclude that CNFs grow at slower rate when pressure is very low and very high. However, the optimum pressure range for the enhanced CNFs growth is about the one order of the magnitude in the units of Torr.

Figures 7.7, 7.8, and 7.9 show the computational results of the electron number density, electron temperature, number densities of positively charged species in the bulk plasma region and near the substrate surface at different input plasma powers, respectively. From the computational plots obtained at 200 W input plasma power, the electron density and temperature in the bulk plasma region is found to be 1.22 $\times 10^{17}$ m^{-3} and 3.6 eV, respectively, which reduced to 0.42 $\times 10^{17}$ m^{-3} and 3.07 eV, respectively, near the substrate surface. However, at 1000 W, the electron density and temperature are found to be 8.56 $\times 10^{17}$ m^{-3} and 5.81 eV, respectively, in the bulk plasma region and 5.89 $\times 10^{17}$ m^{-3} and 5.24 eV, respectively near the substrate surface. Moreover, from the spatial distribution of the densities of various species, we have obtained the reduction in the ion densities from bulk plasma region to substrate surface due to the collisions with the neutral species in the plasma as discussed before. The Figs. 7.10(a) and 7.10(b) shows the analytical results of the electron number density and electron temperature with the growth time in the plasma at different input plasma powers, respectively. When input plasma power is increased, the volume of the plasma region increases which goes into the increase in electric field in the plasma, and consequently, electron number density and electron temperature in the plasma increases. Collison *et al.* [22] experimentally observed the increase in the electron density and temperature when plasma power in the plasma system is increased. The increase in the electron density with input plasma power also leads to more ionization of the neutral species, thereby, increasing the ion densities in the plasma [see Fig. 5.9]. Therefore, ion densities decay at the slower rate in the plasma with the increase in input plasma

power. Thus, ion-induced decomposition process and ion dissociation process on the catalyst nanoparticle surface becomes dominant due to which large number of carbon species and hydrogen radicals are produced on the active catalyst surface as shown in Fig 7.11(a) and 7.11(b), respectively.

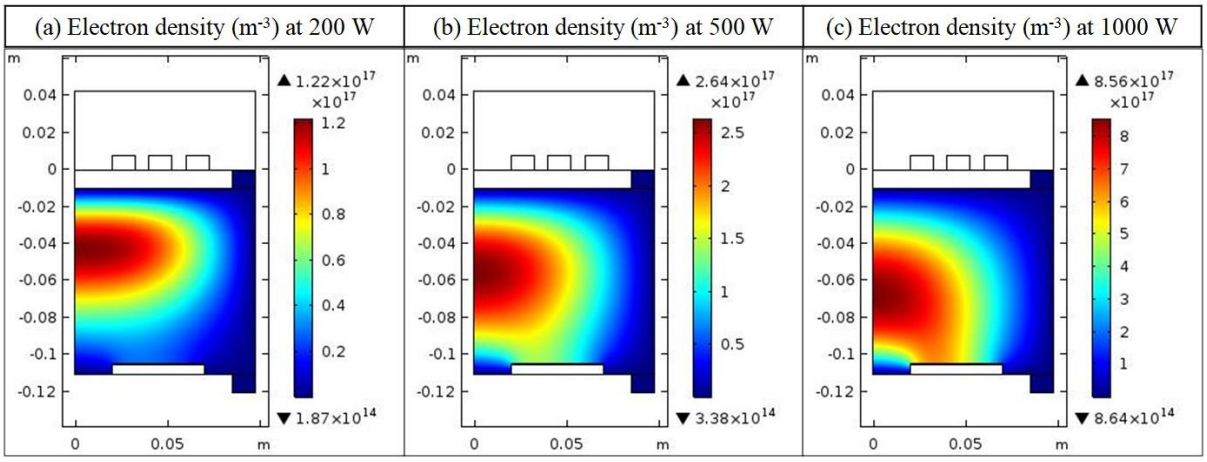

Fig. 7.7. Electron density distribution in the plasma obtained from the computational model for different input plasma powers, i.e., (a) 200 W, (b) 500 W, and (c) 1000 W.

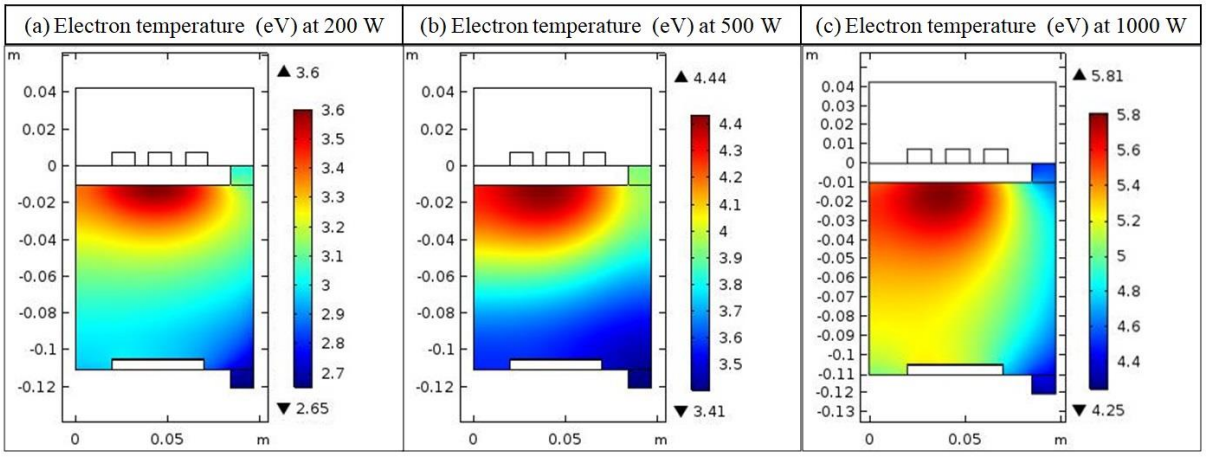

Fig. 7.8. Electron temperature spatial distribution in the plasma obtained from the computational model for different plasma powers, i.e., (a) 200 W, (b) 500 W, and (c) 1000 W.

To understand the effect of power on the distribution of plasma species and their repercussion on the growth of CNFs, blocking function versus growth time curve is plotted for different input plasma powers in Fig. 7.11(c). As input plasma power is increased, poisoning rate of the catalyst becomes slower which is somewhat surprising because one would think of faster poisoning of the catalyst due to the availability of a large number of carbon species on the catalyst surface. However, reverse trend is followed in reality, this is because a

large number of hydrogen radicals are also produced at the same time on the catalyst surface and interacts with amorphous carbons and preserve the activity of the catalyst for quite longer time, thereby, increasing the growth of the CNF [see Fig. 7.11(d)]. Moreover, at high input plasma power, the highly energetic hydrogen ions and radicals also etch walls of the CNF which leads to decrease in CNF diameter [see Fig. 7.11(e)]. The results obtained in the Fig. 7.11(d) and 7.11(E) are in line with the available experimental observations as follows; Chang *et al*. [29] synthesized the CNTs at low temperature using microwave plasma and found the considerable reduction in the diameter of the CNT when input plasma power is raised (700-1000 W). Merkulov *et al.* [30] found the reduction in the diameter of the CNFs when plasma power of the DC PECVD system is increased. Wei *et al.* [7] also observed the increase in the CNF length with an increase in the plasma power (0-2000 W).

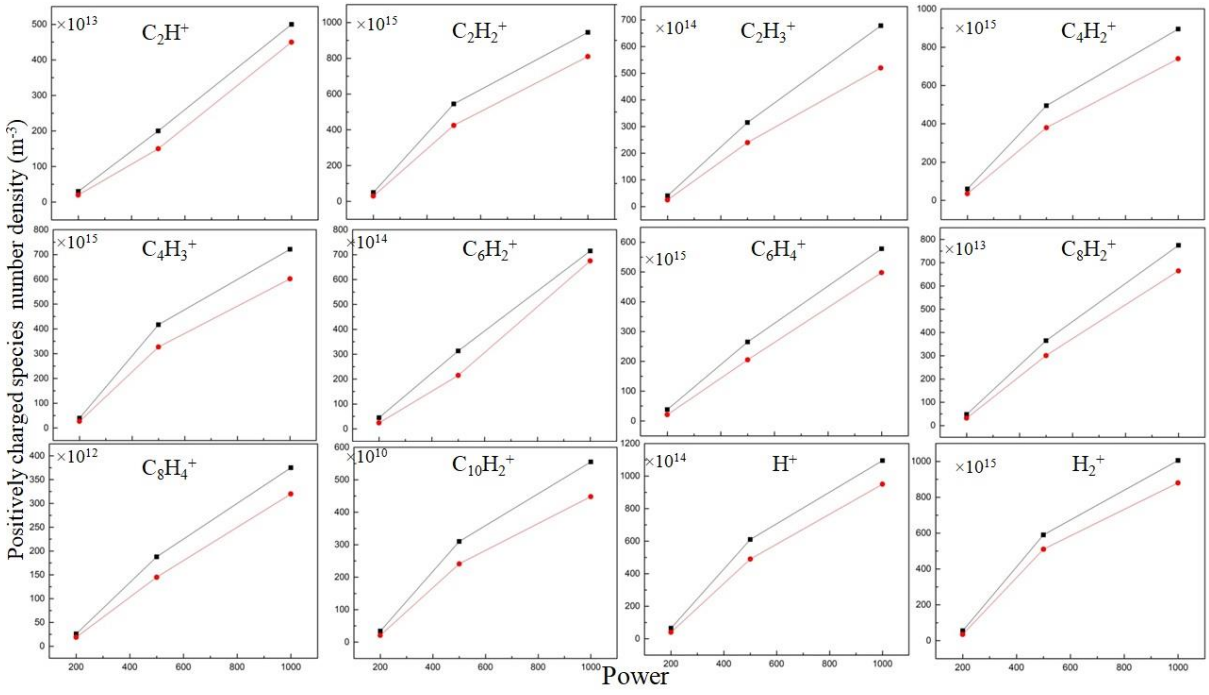

Fig. 7.9. Density distribution of the positively charged species (ions) in the bulk plasma region (black dots) and near the substrate surface (red dots) obtained from the computational model for different input plasma powers, i.e., 200W, 500W, and 1000W.

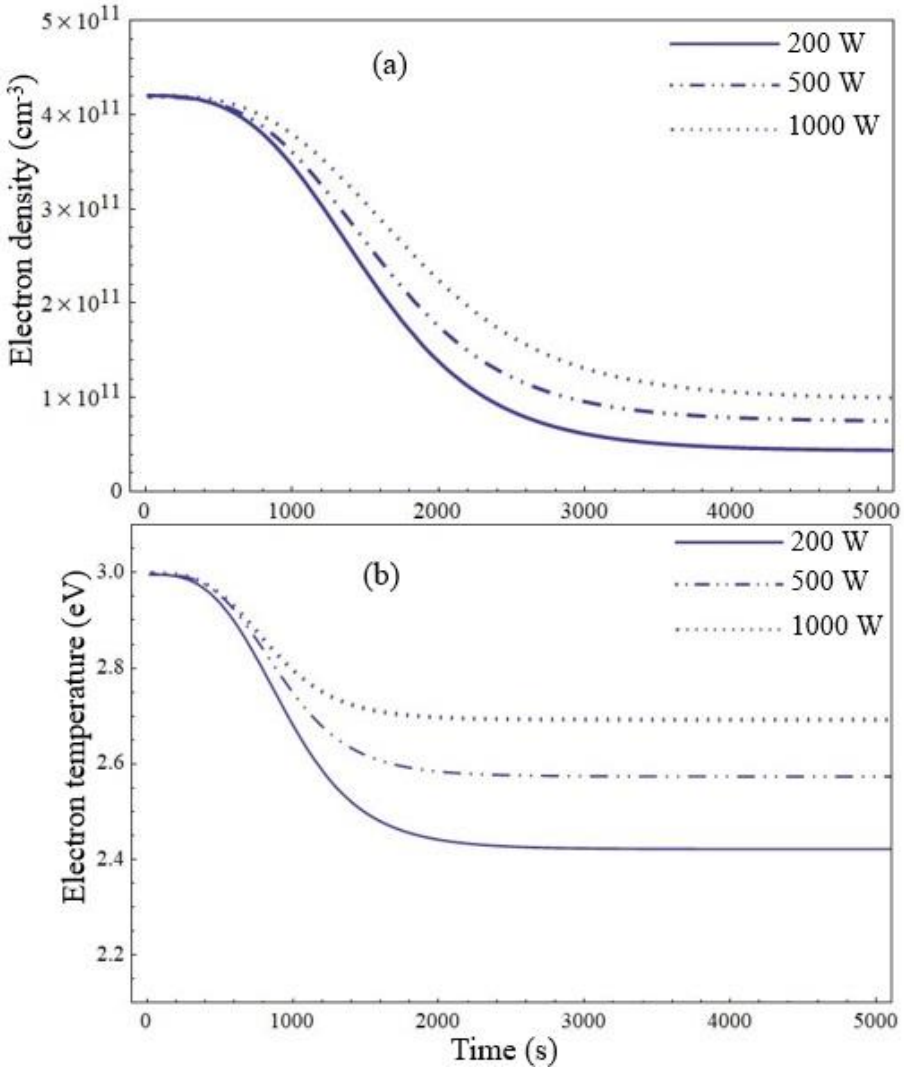

Fig. 7.10. Variation of (a) electron density and (b) electron temperature with growth time in the plasma for different gas pressures i.e., 50 mTorr, 500 mTorr, and 5 Torr keeping other parameters constant that are given in the text.

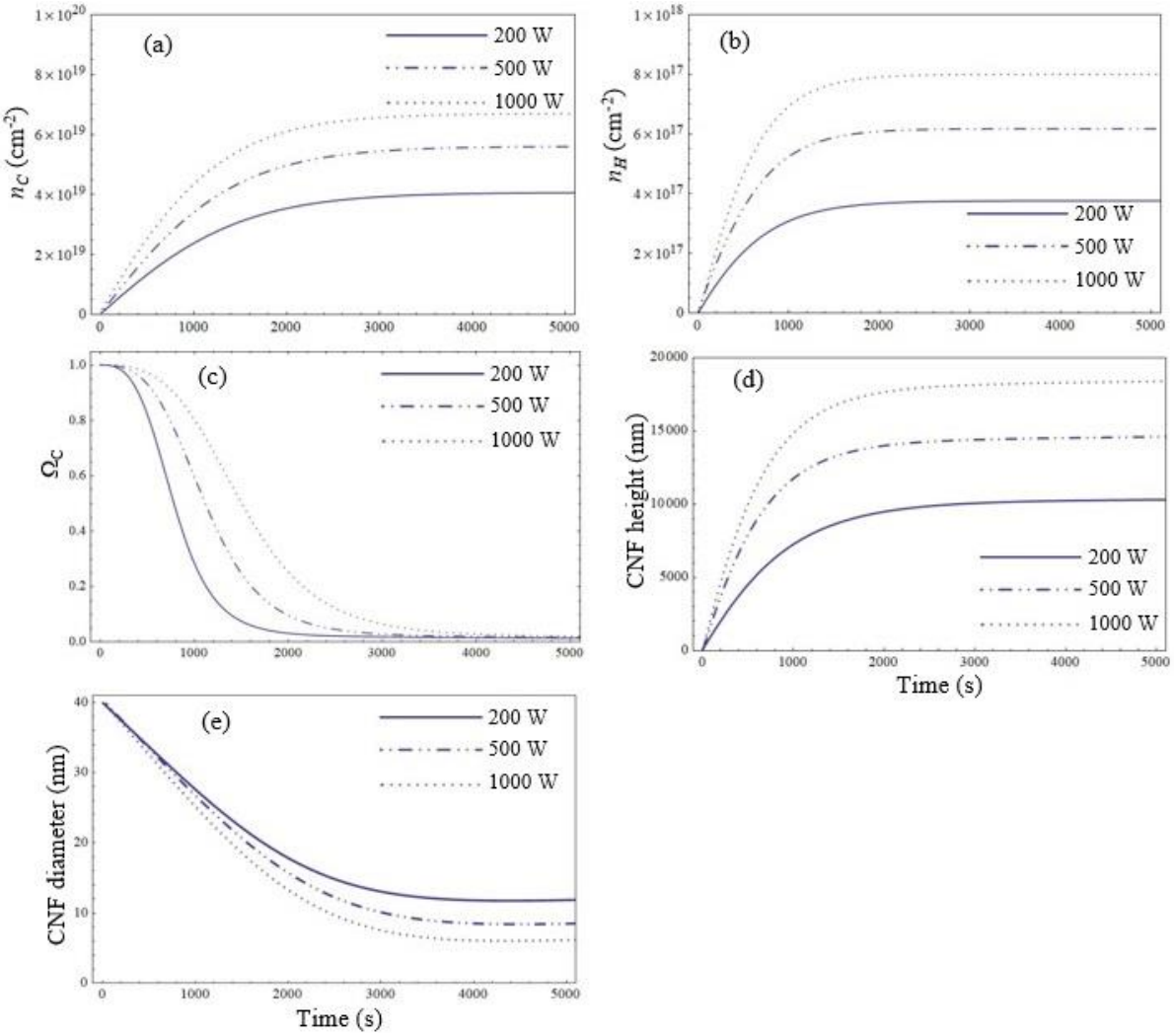

Fig. 7.11. Temporal variation of the (a) surface concentration of carbon species on the catalyst surface n_C, (b) surface concentration of hydrogen radicals on the catalyst surface n_H, (c) poisoning rate of the catalyst, (d) CNF height, and (e) CNF diameter for different input plasma powers i.e., 200 W, 500 W, and 1000 W.

References

[1] Choi W B, Jin Y W, Kim, H Y, Lee S J, Yun M J, Kang J K, Coi Y S, park N S, Lee N S and Kim J M 2001 *Appl. Phys. Lett.* 78 1547Appl. Phys. Lett. **78**, 1547 (2001).

[2] C. Niu, E. K. Sichel, R. Hoch, D. Moy, and H. Tennent, Appl. Phys. Lett. **70**, 1480 (1997).

[3] R. Saito, G. Dresselhaus, and M. S. Dresslhaus, *Physical Properties of Carbon Nanotubes,* Imperial College Press, London, (1998).

[4] F. L. Darkrim, P. Malbrunot, and G. P. Tartaglia, Int. J. Hydrogen Energy **27**, 193 (2002).

[5] M. A. Guillorn, A. V. Melechko, V. I. Merkulov, E. D. Ellis, and M. L. Simpson, J. Vac. Sci. Technol. B **19**, 2598 (2001).

[6] V. I. Merkulov, A. V. Melechko, M. A. Guillorn, M. L. Simpson, D. H. Lowndes, J. H. Whealton, and R. J. Raridon, Appl. Phys. Lett. **80** 4816 (2002).

[7] H. W. Wei, K. C. Leou, M.T. Wei, Y. Y. Lin, and C. H. Tsai, J. Appl. Phys. **98** 044313 (2005).

[8] H. Mehdipour, K. Ostrikov, and A. E. Rider, Nanotechnology **21**, 455605, (2010).

[9] I. Denysenko, and N. A. Azarenkov, J. Phys. D: Appl. Phys. **44,** 174031 (2011).

[10] I. Denysenko, and K. Ostrikov, J. Phys. D: Appl. Phys. **42,** 015208 (2009).

[11] I. Denysenko, K. Ostrikov, M. Y. Yu, N. A. Azarenkov, J. Appl. Phys. **102,** 074308 (2007).

[12] M. Chhowalla, K. B. K. Teo, C. Ducati, N. L. Rupessinghe, G.A. J. Amaratunga, A. C. Ferrari, D. Roy, J. Robertson, and W. I. Milne, J. Appl. Phys. **90**, 5308 (2001).

[13] Y. Catherine and P. Couderc, Thin solid Films **144**, 265 (1986).

[14] B. Ganjipour, S. Mohrajerzadeh, H. Hesamzadeh and A. Khodadadi, Fullerenes, nanotubes, and carbon nanostrcutures **13**, 365 (2005).

[15] L. Delzeit, I. McAninch, B. A. Cruden, D. Hash, B. Chen, J. Han, and M. Meyyappan, J. Appl. Phys. **91**, 6027 (2002).

[16] H. W. Wei, K. C. Leou, M. T. Wei, Y. Y. Lin, and C. H. Tsai, J. Appl. Phys. **98**, 044313 (2005).

[17] B. B. Wang, S. Lee, X. Z. Xu, S. Choi, H. Yan, B. Zhang, and W. Hao, Applied surface science **236**, 6 (2004).

[18] G. Shivkumar, S. S. Tholeti, M. A. Alrefae, T. S. Fisher, and A. A. Alexeenko, J. Appl. Phys. **119**, 113301 (2016).

[19] B. A. Cruden, A. M. Cassell, D. B. Hash, and M. Meyyappan, J. Appl. Phys. **96**, 5284 (2004).

[20] M. Mao and A. Bogaerts, J. Phys. D: Appl. Phys. **43**, 205201 (2010).

[21] S. S. Harilal, C. V. Bindhu, R. C. Issac, V. P. N. Nampoori, and C. P. G. Vallabhan, J. Appl. Phys. **82**, 2140 (1997).

[22] W. Z. Collison, T. Q. Ni, and M. S. Barnes, J. Vac. Sci. Technol. A **16**, 100 (1998).

[23] A. V. Melechko, V. I. Merkulov, T. E. McKnight, M. A. Guillorn, K. L. Klein, D. H. Lowndes, and M. L. Simpson, J. Appl. Physics **97,** 041301 (2005).

[24] W. Z. Li, J. G. Wen, Y. Tu, and Z. F. Ren, Appl. Phys. A **73**, 259 (2001).

[25] C. L. Pint, N. Nicholas, S. T. Pheasant, J. G. Duque, A. N. G. P. Vasquez, G. Eres, M. Pasquali, and R. H. Hauge, J. Phys. Chem. C **112**, 14041 (2008).

[26] Z. L. Tsakadze, K. Ostrikov, C. H. Sow, S. G. Mhaisalkar, and Y. C. Boey, J. Nanosci. Nanotechnol. **10**, 6575 (2010).

[27] M. Tanemura, K. Iwata, K. Takahashi, Y. Fujimoto, and F. Okuyama H. Sugie, and V. Filip, J. Appl. Phys. **90,** 1523 (2001).

[28] I. Hinkov, S. Farhat, and C. D. Scott, Carbon **43**, 2453 (2005).

[29] S. C. Chang, T. C. Lin, C. Y. Pai, Microelectronics Journal **38,** 657 (2007).

[30] V. I. Merkulov, D. K. Hensely, A. V. Melechko, M. A. Guillorn, D. H. Lowndes, and M. L. Simpson, J. Phys. Chem. B **106**, 10570 (2002).

[31] D. J. Dagel, C. M. Mallouris, and J. R. Doyle, J. Appl. Phys. **79**, 8735 (1996).

[32] I. B. Denysenko, S. Xu, J. D. Long, P. P. Rutkevych, N. A. Azarenkov, and K. Ostrikov, J. Appl. Phys. **95**, 2713 (2004).

[33] C. Deschenaux, A. Affolter, D. Magni, C. Hollenstein, and P. Fayet, J. Phys. D: Appl. Phys. **32**, 1876 (1999).

[34] J. Benedikt, J. Phys. D: Appl. Phys. **43**, 043001 (2010).

[35] J. R. Doyle, J. Appl. Phys. **82**, 4763 (1997).

[36] K. Ostrikov, H. J. Yoona, A. E. Rider, S. V. Vladimirov, Plasma Process. Polym. **4**, 27 (2007).

[37] H. Mehdipour, K. Ostrikov, A. E. Rider, and Z. Han, Plasma Process. Polym. **8**, 386 (2011).

[38] C. S. Cojocaru, A Senger, and F. L. Normand, J. Nanosci. Nanotechnol. **6**, 1 (2006).

[39] Z. Marvi, S. Xu, G. Foroutan, and K. Ostrikov, Phys. Plasmas **22,** 013504 (2015).

[40] M. Cantoro, S. Hofmann, S. Pisana, C. Ducati, A. Parvez, A.C. Ferrari, J. Robertson, Diam. Relat. Mater. **15**, 1029 (2006).

[41] S. Hofmann, M. Cantoro, B. Kleinsorge, C. Casiraghi, A. Parvez, J. Robertson, C. Ducati, J. Appl. Phys. **98**, 034308 (2005).

[42] O. A. Louchev, T. Laude, Y. Sato, and H. Kanda, J. Chem. Phys. **118,** 7622 (2003).

[43] M. Yudasaka, R. Kikuchi, T. Matsui, Y. Ohki, S. Yoshimura, and E. Ota, Appl. Phys. Lett. **67,** 2477 (1995).

[44] See (http://matter.org.uk/matscicdrom/manual/df.html) for metal atom diffusion coefficient

[45] M.S. Sodha, S. Misra, and S. K. Mishra, Phys. Plasmas **17,** 113705 (2010).

[46] M. S. Sodha, S. Misra, S. K. Misra, and S. Srivastava, J. Appl. Phys. **107,** 103307 (2010).

[47] I. B. Denysenko, S. Xu, J. D. Long, P. P. Rutkevych, N. A. Azarenkov, and K. Ostrikov, J. Appl. Phys. **95,** 2713 (2004).

8

Conclusion and future scope

8.1 Conclusion

The work carried out in the present thesis aims to develop the analytical model to elucidate the mechanisms of the nucleation and growth of carbon nanofibers (CNFs) in the reactive plasma environment. The model incorporated in the present thesis comprises the plasma sheath equations to investigate the energy and fluxes of the plasma species (neutrals and charged species), charge neutrality equation, energy and particle balance equations of all the plasma species (neutrals and charged species), dissociation of the plasma species over the catalyst nanoparticle active surface to generate building species (carbon species) and hydrogen radicals via various complex surface processes, surface and bulk diffusion of building species through the catalyst surface, incorporation of carbon species in the form of graphitic shells, deformation of catalyst nanoparticle due to the stress exerted by the graphitic shells, etching of graphene layers, alignment of graphitic shell, and vertical growth of CNFs under the inclusion of electric field induced in the plasma sheath. The present work of the thesis may help to understand the better insights of the plasma parameters, operating process parameters, and gaseous sources on the growth characteristics of the CNFs. In brief, the work done in the present thesis can be summarized as follows:

- The plasma parameters strongly influence the plasma pre-treatment of the metal catalyst film. The diameter and surface concentration of the catalyst nanoparticles increases when ions of the etching species (hydrogen ions) in the plasma and input plasma power increases. Moreover, it has been

found that the plasma species transfer their momentum to the substrate film surface and raise the substrate temperature.

- The growth rate of CNF increases with decrease in catalyst nanoparticle size. In addition, it is observed that upon an increase in hydrocarbon number density, the CNF length gets increased. Moreover, we have also shown the effect of hydrogen on the CNF tip diameter, CNF growth, and the inclination angle of graphene layers to the fiber axis. It is found that the tip diameter and CNF growth decreases and the graphene layers tilt away from the growth axis as hydrogen content in the growth atmosphere increases.
- An analytical model to study the effects of nitrogen doping on the growth of CNFs and hence the plasma-assisted growth model of nitrogen contained carbon nanofibers (N-CNFs) is developed, and its field emission properties have been estimated. From the results obtained, it can be seen that, on nitrogen doping, the height and the tip diameter of the CNFs decreases. The field enhancement factor β calculated from these results reveals that nitrogen-doped CNFs have enhanced field emission characteristics than undoped CNFs. Moreover, it has also been observed that C_2H_2/NH_3 gas ratio is the crucial parameter for the N-CNFs growth. The N-CNF growth rate increases and the tip diameter decreases with a decrease in the C_2H_2/NH_3 gas ratio. These results have been explained on the basis of variation in the number density of etchant species in the reactive plasma.
- The CNF growth in three different plasmas, i.e., $C_2H_2+H_2$ plasma, $C_2H_2+H_2+H_2O$ plasma, and $C_2H_2+H_2+O_2$ plasma has been investigated. From the results obtained, it is found that the CNF growth in normal $C_2H_2+H_2$ plasma terminates faster due to the formation of the amorphous carbon layer on the catalyst active surface. However, on the addition of water in $C_2H_2+H_2$ the reactive plasma, i.e., in $C_2H_2+H_2+H_2O$ plasma, water molecules etch the amorphous carbon by means of $C+H_2O \rightarrow CO+H_2$ from the catalyst surface and thus preserve the catalyst activity and enhance the CNF growth. On the other hand, the CNF growth

rate is found to be maximum in $C_2H_2+H_2+O_2$ plasma. This is because of the dual role played by the oxygen during the CNF growth; (i) etching of amorphous carbon layer from the catalyst surface and (ii) removal of hydrogen species from the catalyst surface which act as the sink for carbon species. Also, in the present study, we found that tip diameter is minimum for CNF grown in $C_2H_2+H_2+O_2$ plasma followed by $C_2H_2+H_2+H_2O$ and $C_2H_2+H_2$ plasmas. Moreover, relative concentrations of oxidizers in the reactive plasma significantly influence the CNF growth, i.e., CNF growth rate increases when the concentration of oxidizers increases up to some optimum level after that CNF growth rate decreases rapidly. This is because of the oxidation of the carbon species generated on the catalyst surface that might have ultimately diffused and precipitated in the form of the graphene layers around the catalyst nanoparticle.

- The role of thin metal catalyst film thickness on the nucleation and growth of CNFs/CNTs in the hydrogen-diluted acetylene plasma have been studied. It is observed that nanostructuring of thin nanofilms leads to the formation of small nanoparticles. In addition, it is also found that catalyst nanoparticle goes under shape deformation during CNFs/CNTs growth and restructuring rate of nanoparticle significantly depends on the nanofilm thickness. The CNFs/CNTs nucleated from thin nanofilms contain few graphitic shells with the small opening angle and show faster growth with early saturation compared to those nucleated from thick nanofilms. Moreover, the reduction in CNF inner and outer diameters has been found with growth time as well as with nanofilm thickness.

- The numerical simulations have been carried out using COMSOL Multiphysics 5.2 simulational software to investigate the properties of $Ar+H_2+C_2H_2$ reactive plasma as the function of process parameters and their impact on the growth dynamics of the CNFs have been studied using analytical model. From the numerical data obtained, we found that temperature and number density distributions of the electrons and other species (neutrals and positively charged) in the plasma are non-uniform

i.e., densities of each species decreases from bulk plasma region to substrate surface and from the analytical model. It is found that the temperature and density of electrons and other species decay in the plasma due to collisions and dissociation/ionization reactions among various species. Moreover, we have also found that the electron density and temperature in the plasma decreases when gas pressure is raised and increases when input plasma power is raised and the densities of neutral and charged species are related to the concentration and energy of the electrons in the plasma. From the surface deposition model, we have obtained that the dissociation rate of the carbon bearing species on the catalyst active surface to generate carbon-hydrogen species are related to the gas pressure and input plasma power; when gas pressure is raised (50 mTorr to 5 Torr), the growth rate of CNF increases. However, at very high pressure, i.e., above and around 50 Torr, the growth of the CNF decreases due to the quick poisoning of the catalyst whereas, the diameter of the CNF increases within the entire pressure range. Thus, we can conclude that the optimum pressure for the enhanced growth of the CNFs is about one order of the magnitude in the units of Torr. Moreover, when input plasma power is raised (200 W to 1000 W), the growth rate of the CNF increases, however, the CNF diameter decreases due to more effective etching of the energetic ions.

8.2 Future scope of the present work

The present work of the thesis can be extended to fabricate the thin and long vertically oriented carbon nanofibers for their potential applications in the field emitters as the superior field emission from carbon nanostructures (CNTs and CNFs) comes from their geometry rather than their crystalline structure.

The present work incorporates most of the important aspects for the deterministically controlled nucleation and growth of CNFs in reactive plasma. However, there are some aspects which can be deepened further for the future development of the synthesis of the plasma grown CNFs.

- During the PECVD growth of CNFs, the CNFs are not exactly normal to the substrate surface. The alignment mechanism of the CNFs during PECVD growth can be investigated to enhance the field emission properties.

- The contribution of higher hydrocarbon species, i.e., $C_{12}H$, $C_{12}H_4$, $C_{12}H_6$, $C_{12}H_8$ etc. on the resulting structure of the CNF.

APPENDIX A

Graphene layers (graphitic shells) inclination angle with the growth axis

The geometry of the catalyst nanoparticle size is shown in Fig. A1, where *l* is the length of the truncated cone, *D* is the diameter of the catalyst nanoparticle and *d* is the diameter of the CNF tip. From Fig. A1, the angle between graphene layers and the growth axis can be calculated in terms of the tip diameter of the CNF and the diameter of the particle size. Initially, catalyst nanoparticle have spherical shape and finally transforms to pear drop like shape i.e., hemispherical + truncated cone shape. Here, we are assuming that the volume of the catalyst nanoparticle remains constant during the CNF growth. Therefore, initial volume must be equal to the final volume of the catalyst nanoparticle.

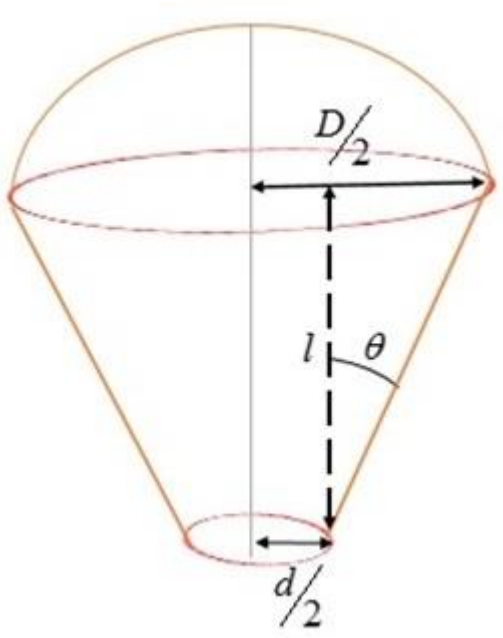

Fig. A1. Geometrical representation of the deformed catalyst particle at the tip of the Carbon Nanofiber.

Volume of sphere = volume of hemisphere + volume of truncated cone

$$\frac{1}{6}\pi D^3 = \frac{1}{12}\pi d^3 + \frac{1}{12}\pi\left(D^2 + D.d + d^2\right)l,$$

and $\tan\theta = \frac{D-d}{2l}$,

therefore, $\tan\theta = \frac{1}{2}\left[1 - \frac{d}{D} + \left(\frac{d}{D}\right)^2 - \left(\frac{d}{D}\right)^3\right]$

or

$$\theta = \tan^{-1}\left(\frac{1}{2}\left[1 - \frac{d}{D} + \left(\frac{d}{D}\right)^2 - \left(\frac{d}{D}\right)^3\right]\right)$$